Resonant and Nonresonant All-Optical Switching Devices in GaAs/GaAlAs

by

Kadhair A. Al-hemyari M.Sc., B.Sc.

July 1992

A Thesis submitted to the Faculty of Engineering
of the University of Glasgow for the degree of
Doctor of Philosophy

ProQuest Number: 10992047

![ProQuest logo]

ProQuest 10992047

IN THE NAME OF ALLAH THE BENEFICENT, THE MERCIFUL:
READ* IN THE NAME OF THY LORD, WHO HATH CREATED ALL THINGS*
WHO HATH CREATED MAN OF CONGEALED BLOOD*
READ BY THY MOST BENEFICENT LORD*
WHO TAUGHT THE USE OF THE PEN*
WHO TEACHETH MAN THAT WHICH HE KNOWETH NOT*

SURAT AL ALAQ (CONGEALED BLOOD)

DEDICATION

To my parents, my brothers and my sisters

ACKNOWLEDGEMENTS

TABLE OF CONTENTS

Journal Publications

Conferences

Abstract

Chapter 1
Introduction

Chapter 2
Nonlinear Optical Properties of GaAs/GaAlAs Semiconductors

Chapter 3
Modelling and Design of GaAs/GaAlAs Quantum Well Waveguides

Chapter 4
Growth and Characterisation Techniques of GaAs/GaAlAs Single and Multiple Quantum Well Materials

Chapter 5

Fabrication and Linear Characterisation of GaAs/GaAlAs Waveguides

Chapter 6
Nonlinear Characterisation of GaAs/GaAlAs Waveguides

Chapter 7
Nonlinear Integrated Asymmetric Mach-Zehnder Interferometer

Chapter 8
Nonlinear Integrated Directional Coupler

Chapter 9
Conclusions and Future Work

JOURNAL PUBLICATIONS

1) K. Al-hemyari, J.S. Aitchison, C.N. Ironside, G.T. Kennedy, R.S. Grant and W. Sibbett, "Ultrafast All-Optical Switching in a GaAlAs integrated interferometer in the 1.55 µm Spectral Region", Electron. Lett., Vol. 28(12), p. 1090 (1992).

2) K. Al-hemyari, C.N. Ironside and J.S. Aitchison, "Resonant Nonlinear Optical Properties of GaAs/GaAlAs single Quantum Well Waveguide and a Nonlinear Asymmetric Mach-Zehnder Interferometer", to be published in October 1992, IEEE Journal of Quantum Electronics.

3) K. Al-hemyari, C.D.W. Wilkinson and G.F. Doughty, "Dependence of End Facet Reflectivity of GaAs/GaAlAs Rib Waveguides on Tilt Angle", to be published in Journal of Lightwave Technology.

4) K. Al-hemyari, G.F. Doughty and C.D.W. Wilkinson, "Optical Loss Measurements on GaAs/GaAlAs Single-Mode Waveguide Y-Junctions and Waveguide Bends", to be published in Journal of Lightwave Technology.

CONFERENCES

1) K. Alhemyari, B.S. Bhumbra and C.N. Ironside, "Nonlinear Optical Properties of a Single Quantum-Well Waveguide and a Nonlinear Asymmetric Interferometer", OSA Topical meeting *Nonlinear Guided-Wave Phenomena*, Cambridge, England, TuB5-2, 1991.

2) C.N. Ironside, K. Al-hemyari, J.S. Aitchison (Univ. of Glasgow/Scotland), G.T. Kennedy, R. Grant, W. Sibbett (Univ. of St. Andrews/Scotland), "Nonlinear Optical Properties of GaAs/GaAlAs integrated asymmetric Mach-Zehnder Interferometer", OSA Topical meeting *Integrated Photonics Research*, New Orleans, LA, USA, WA3, 1992.

3) K. Al-hemyari, J.S. Aitchison, C.N. Ironside, G.T. Kennedy, R.S. Grant and W. Sibbett, "Low-Loss Ultrafast All-Optical Switching in a GaAlAs integrated interferometer at Half the Band-Gap", OSA Annual meeting Symposium on Ultrafast Nonlinear Guided Wave Phenomena and Optical Switching, Albuquerque/ New Mexico, U.S.A., 20-25 September 1992.

4) J.S. Aitchison, K. Al-hemyari, C.N. Ironside (Univ. of Glasgow/Scotland), A. Villeneuve, G.I. Stegeman (CREOL/U.S.A.), G.T. Kennedy, R. Grant and W. Sibbett (Univ. of St. Andrews), "Ultrafast Switching in AlGaAs Waveguide Devices", OSA Annual meeting Symposium on Ultrafast Nonlinear Guided Wave Phenomena and Optical Switching, Albuquerque/ New Mexico, U.S.A., 20-25 September 1992.

Abstract

The resonant refractive and absorptive optical nonlinearity of a GaAs/GaAlAs single quantum well waveguide are characterised; hh and lh excitons are well resolved at room temperature. The unsaturated resonant nonlinear refractive index coefficient n_2 was 1.4×10^{-8} cm^2/W, measured using the external Mach-Zehnder interferometric technique. It has been shown that the recovery time of the resonant nonlinearity is reduced to 125 ps (1/e recovery time), by placing the single quantum well close to the top surface. All-optical switching of an integrated asymmetric Mach-Zehnder interferometer is demonstrated and it was shown experimentally and theoretically that due to the absorption saturation, a complete switching is not possible.

The nonresonant nonlinear optical properties of GaAlAs waveguide were characterised at photon energy below half the band gap. The nonresonant nonlinear refractive index coefficient n_2 was calculated from the spectral broadening measurements due to self-phase modulation effect in GaAlAs waveguides, and it was found to be $\approx (5.4 \pm 0.5) \times 10^{-14}$ cm^2/W. The two-photon absorption coefficient, below half the band gap, was $\beta = 0.14$ cm/GW.

We report the first observation of ultrafast all-optical switching in an integrated asymmetric Mach-Zehnder interferometer, using the nonresonant nonlinearity in Ga$_{0.82}$Al$_{0.18}$As below half the band gap. A relative switching fraction of more than 80% has been achieved using 330 fs pulses at around 1.55 μm from a coupled-cavity mode-locked colour centre laser.

Chapter 1

Introduction

Optical data transmission systems offer the potential of operating at extremely high data rates, the frequency of the optical carrier is on the order of 10^{14} Hz. The transmission medium, single mode optical fibre, having an attenuation loss as low as 0.2 dB/Km at 1.55 μm and 1.3 μm with zero dispersion is used for long-haul telecommunications. For these optical wavelengths, a single mode fibre transmission system can be operated at a 20 to 100 Gbit/s data rate over a distance over 100 Km [1]. Some of the components required for such an optical system operating at 100 GHz are available, at least in the laboratory, e.g. mode-locked semiconductor laser [2] and ion implanted photodetector [3]. Using these extremely fast opto-electronic components, it is possible to convert a high-speed electrical signal into an optical signal, transmit that optical signal over a long distance, and then reconvert the optical signal back into an electrical signal. However, doing the signal processing in the electrical domain has its fundamental speed limitation at about 1 GHz for silicon integrated circuits and at about 10 GHz for less matured GaAs integrated circuits. The ability of performing logic operations in the optical domain will enhance the flexibility and speed of such system.

These optical logic devices are known as all-optical switches and are based on the optically induced nonlinear material effects. These nonlinear effects results in the optical output depending nonlinearly on the optical input. The nonlinear optical effects usually take place at very high optical intensities, and the index of refraction is described by;

$$n = n_0 + n_2 I$$

where n_0 is the linear refractive index and the second term, $n_2 I$, is the nonlinear contribution, I is the optical intensity inside the medium. Another nonlinear material effect that can be employed is saturable absorption, a term applied to the phenomenon where the absorption of a material decreases with the increasing incident optical intensity, and at some point the absorption of the material saturates and therefore becomes dependent on the incident optical intensity.

For the utilisation of the full fibre bandwidth many data formats are imaginable including frequency or time division multiplexing (FDM or TDM). FDM could be implemented by using a number of modulated semiconductor lasers operating at different wavelengths

which are simultaneously transmitted. This technique takes the advantage of the tuning properties of semiconductor lasers as well as the relative simplicity with which the channels may be sorted by using a frequency selective element, e.g. grating. The use of TDM involves the use of one laser, and the high rate data pulses could be used with the information serially encoded by modulation of the pulse stream. Several data streams could of course be interleaved. This scheme takes advantage of the ability to mode-lock semiconductor lasers to produce a stream of short, intense pulses. TDM has the added advantage that the high peak intensity of the optical pulses can be allowed to interact in a nonlinear optical medium.

The most pressing needs in the area of nonlinear optics are the identification of new materials as well as the reassessment and improvement of the existing ones. The important parameters of nonlinear optical materials, include the second-order or third-order nonlinear response and saturation level, are the relaxation time and the damage threshold. In addition, availability or ease of fabrication play an important role in the choice of materials. Recently an intense research effort has been aimed at the development of organic and polymeric materials. These materials are attractive because of the demonstration that large nonresonant nonlinear responses can be found among certain structural classes [4]. At the moment, however, the field of organics is minimally developed. On the other hand, semiconductors have been extensively researched, which possess large resonantly enhanced third-order nonlinearities. Semiconductors will have a particularly dominant role to play in the future of nonlinear optics since material and fabrication techniques are well developed in both the electronics and linear optics industries. Essentially every guided-wave device currently used for electro-optic switching and modulation, beam-splitting, etc...., can be made into an all-optical switch by using waveguide materials with nonlinear optical properties.

Intensity dependent refraction has been observed in 1964 in liquids by Maker et al. [5], they measured values of up to 10^{-2} esu for $\chi^{(3)}$. In 1966, Patel et al. [6] measured values of $\chi^{(3)}$, using a Q-switched CO_2 laser, for InAs, InSb and GaAs of 1.8×10^{-10} esu, 8×10^{-14} esu and 7×10^{-12} esu respectively. However, saturated absorption in GaAs was reported as long ago as 1965 by Michel and Nathan [7], they observed an increase in the transmission by a factor of up to 14 in Mn doped GaAs at high intensity. Although observations of nonlinear refraction in various materials continued to be reported, general interest in this field was low over this period since it was felt that the nonlinearities were too small to produce a useful all-optical device. However in 1978, Miller et al. [8] measured $\chi^{(3)}$ values of up to 10^{-2} esu in InSb for frequencies just below the band edge.

There are a wide range of materials can be used for nonlinear optical devices, but more work is focused on III-V semiconductors due to the attraction of possible integration of

such devices with other optical elements, e.g. lasers and detectors. Therefore the nonlinear optical properties of such materials have been investigated, and it is now generally accepted that MQW structures produce enhanced nonlinearities over bulk material. D. Chemla [9] have shown that MQWs made of GaAs/GaAlAs have great potential for use as a nonlinear material in optical switching and signal processing devices.

Optical bistable devices were first produced in 1979 by two groups, Gibbs et al. [10] and Miller et al. [11], using an etalon which consisted of a GaAs/GaAlAs epitaxial layers structure grown by MBE with 90% reflectivity coatings. A laser source continuously tunable in the wavelength range 770 nm to 870 nm was used and bistability was observed from 5 °K to 120 °K. The values of $\chi^{(3)}$ deduced from these experiments were from 10^{-5} to 10^{-4} esu. Miller et al. [11] observed nonlinear transmission in a plane parallel InSb crystal, the Fabry-Perot interferometer was formed by the natural reflectivity of its surfaces. The value of $\chi^{(3)}$ deduced was 1 esu at a temperature of 5 °K. These bistable etalons can be used to operate as all-optical modulators with or without hysteresis. A bistable etalon without hysteresis was shown to exhibit an optical transistor action [12]. The hysteresis provided the required condition for a memory device. In 1982 another important achievement was reported by Gibbs [13] of demonstrating a room temperature bistable etalon in multiple quantum well material. The layer structure of the MQWs consisted of 336 Å thick of GaAs well and 401 Å thick of GaAlAs barrier. Later in the same year, it was reported another bistable etalon in GaAs at room temperature. It was shown that the required switching power was lower in the MQW material and also the hysteresis loop was wider.

The attractive features of using waveguides for implementing efficient nonlinear interactions were recognised in the early days of integrated optics [14]. The key factors are; firstly the high power density due to the optical confinement offered by the waveguide small cross-sectional area and secondly, the diffractionless propagation in two dimensions which leads to long interaction lengths. Much of the work on the fabrication of thin film waveguides was made possible by the rapid development of photolithographic techniques and by the motivation to built integrated optical circuits. In early 80 's, it was realised that standard integrated optics devices could be operated in an all-optical mode by introducing waveguide media with intensity dependent refractive indices [15-17]. Now it is believed that such devices can be used for all-optical signal processing at speeds limited only by the "turn-off" time of the nonlinearity.

In 1982 Jensen [18] proposed a nonlinear directional coupler useful for optical processing but not bistable device. This device has subsequently been examined in detail and many interesting regimes of operation have been predicted [19-21]. K. Kitayama and S. Wang [22] proposed the use of the nonlinear directional coupler for optical pulse compression

caused by the intensity dependent refractive index property in the interaction region. Their theoretical calculations predict that the pulse compression to less that 1/5 of the original pulse width is achievable. In 1985 P. LiKamWa [23] demonstrated a nonlinear directional coupler in a MQW waveguide. A partial switching of power between the two coupled waveguides was achieved by varying the intensity of the input light beam. The sample was cooled to 180 °K to reduce the large absorption of the MQWs close to the band edge. In the following year LiKamWa et al. [24] observed an all-optical switching in a passive GaAs/GaAlAs MQW waveguide resonator at room temperature and have shown that the mechanism responsible for the switching was not due to thermal effects.

In 1983, an all-optical logic device was reported [17], the device based on the Mach-Zehnder interferometer. The principle of operation was demonstrated in a LiNbO$_3$ substrate. The experiments were performed with a near-infrared dye laser which produced 5 ps pulses at λ=840 nm. The possible applications of the device structure were as an all-optical inverter, an XOR gate and an AND gate. It was suggested [25] that a similar device made in GaAs or a MQW structure would operate at a lower power level.

The discovery that an active MQW laser structures emits radiation at an energy below the band gap of the passive MQW waveguide [26] means that lasers and waveguide devices can be fabricated on the same chip [27]. The nonlinearity associated with room temperature exciton absorption of the MQWs can be saturated at powers and wavelengths compatible with the semiconductor laser diodes. One of the most important parameters which characterises a nonlinear optical element is the temporal response. The typical recovery time of the absorption in GaAs is $\approx$10 ns and in GaAs/GaAlAs MQW $\approx$5 ns [28]. Waveguide geometry may shorten the recovery time of the resonant nonlinearity due to the diffusion and surface recombination of the photogenerated carriers [29]. Y. Silberberg et al. [30] showed that a proton bombardment of GaAs/GaAlAs MQWs shorten the recovery time of the excitonic absorption to 150 ps without affecting the absorption characteristics or the saturation energy of the MQWs. P. LiKamWa et al. [31] demonstrated an all-optical switching action in a nonlinear directional coupler fabricated in GaAs/GaAlAs MQW with a recovery time of 130 ps. The large reduction in the switching recovery time was obtained by the application of an external DC bias which swept out the carriers from the QWs.

To implement nonlinear waveguide devices it is important to measure the waveguide nonlinearity, including its magnitude, sign and speed. The measurement techniques of the waveguide nonlinear optical properties are the nonlinear prism and grating coupling, degenerate four wave-mixing, pump-probe transmission measurements, intensity dependent birefringence and external Mach-Zehnder interferometers.

Y.J. Chen and G.M. Carter [32] developed the nonlinear grating coupling technique to measure the magnitude and sign of the intensity dependent refractive index change in GaAs and Si at a wavelength of 1.05 µm and 1.11 µm respectively. J.D. Valera et al. [33] used the nonlinear prism coupling technique to measure the optical nonlinearity in thin film liquid crystals. Nonlinear prism and grating coupling have been widely used to investigate nonlinearities in Polydiacetylene, Si, GaAs, GaAs/GaAlAs MQWs, liquid crystal, semiconductor doped glass, silicon on sapphire, ZnS and ZnO waveguides [34-40].

The degenerate four-wave mixing technique has been used to measure the magnitude and the "turn-off" time of nonlinearities in waveguides. This technique does not yield the sign of the nonlinearity and was used in liquid carbon disulphide [41] and ion-exchanged semiconductor doped glass waveguide [42].

The pump-probe technique is appropriate for studying nonlinearities related to absorption changes by monitoring the power dependence of the guided wave attenuation [43]. This technique has been applied to channel waveguides made from semiconductor doped glass [43, 44].

The external Mach-Zehnder interferometric technique was first used to measure the nonlinearities in MQW GaAs/GaAlAs strain-induced waveguide [24] and ion-exchanged semiconductor doped glass waveguides. This technique yields the magnitude and the sign of the nonlinearity. D. Cotter et al. [45], used the pump-probe interferometric technique to measure the refractive and absorptive optical nonlinearities in semiconductor-doped fibers with picosecond time resolution.

Layout of the Thesis:

The aim of the research carried out during the course of this investigation was the experimental observation of switching action in all-optical devices based on the nonlinear asymmetric Mach-Zehnder interferometer AM-ZI and directional coupler NLDC in GaAs/GaAlAs semiconductor structures. Chapter 1 is intended to provide a broad introduction to the motivation behind nonlinear integrated optics research. It includes a discussion of the materials that have favourable properties for integrated optics. Chapter 2 contains a brief introduction to quantum wells and the linear and nonlinear optical properties of the bulk and QW semiconductors. It includes a description of the electro-optic properties of these semiconductor materials. Chapter 3 outlines the theory of the one and two dimensional waveguides. It includes the design steps of GaAs/GaAlAs heterostructure and MQW waveguides, and the calculation of the QW hh and lh excitonic transitions. Chapter 4

5

describes the growth and spectroscopic characterisation techniques of GaAs/GaAlAs epitaxial structures. It includes the photocurrent and photoluminescence spectroscopy. In this chapter we present a study of the disordering techniques of GaAs/GaAlAs MQW band structure. Chapter 5 presents the experimental results of the linear characterisation of stripe waveguides. Chapter 6 contains the experimental measurements of the magnitude, size and recovery time of the resonant and nonresonant nonlinear optical properties of GaAs/GaAlAs waveguides. The measurement techniques were the pump-probe and external Mach-Zehnder interferometer. It includes the investigations of the electro-refractive and absorptive effects in GaAs/GaAlAs p-i-n QW waveguides. Chapter 7 presents the theoretical model and experimental studies of the electro-optic, the resonant and nonresonant nonlinear integrated AM-ZI device. Chapter 8 contains the theoretical and experimental studies of the electro-optic, the resonant and nonresonant nonlinear integrated directional coupler device. Chapter 9 presents the conclusions of the thesis research and suggestions for future research.

References:

[1] C. Lin and D. Marcuse, *"Dispersion in single mode fiber: The question of maximum transmission bandwidth"*, Paper TUC5, IOOC81, San Francisco (1981).

[2] J.P. Van der Ziel, W.T. Tsang, R.A. Logan, R.M. Mikulyak and W.M. Augustyniak, *"Subpicosecond pulses from passively mode-locked GaAs buried optical guide semiconductor lasers"*, Appl. Phys. Lett., Vol. 39, p. 525 (1981).

[3] P.R. Smith, D.H. Auston, A.M. Johnson and W.M. Augustyniak, *"Picosecond photoconductivity in radiation-damaged silicon-on-sapphire films"*, Appl. Phys. Lett., Vol. 38, p. 47 (1981).

[4] J.L. Oudar, *"Optical nonlinearities of conjugated molecules: Stilrene derivatives and highly polar aromatic compounds"*, J. Chem. Phys., Vol. 67, p. 446 (1977).

[5] P.D. Maker, R.W. Terhune, C.M. Savage, *"Intensity dependent changes in the refractive index of liquids"*, Phys. Rev. Lett., Vol. 12, p. 507 (1964).

[6] C.N.K. Patel, R.E. Slusher, P.A. Fleury, *"Optical nonlinearities due to mobile carriers in semiconductors"*, Phys. Rev. Lett., Vol. 17, p. 1010 (1966).

[7] A.E. Michel and M.I. Nathan, *"Saturation of the optical absorption in GaAs"*, Appl. Phys. Lett., Vol. 6, p. 101 (1965).

[8] D.A.B. Miller, M.H. Mozolowsky, A. Miller, S.D. Smith, *"Nonlinear optical effects in InSb with a CW CO laser"*, Optics Commun., Vol. 27, p. 133 (1978).

[9] D.S. Chemla, D.A.B. Miller, P.W. Smith, A.C. Gossard and W. Wiegmann, *"Room temperature excitonic nonlinear absorption and refraction in GaAs/GaAlAs multiple quantum well structures"*, IEEE J. Quantum Electron., QE-20, p. 265 (1984).

[10] H.B. Gibbs, S.L. McCall, T.N.C. Venkatesan, A. Passner, A.C. Gossard and W. Wiegmann, *"Saturation of the free exciton resonance in GaAs"*, Sol. St. Commun., Vol. 30, p. 271 (1979).

[11] D.A.B. Miller, S.D. Smith, A. Johnston, *"Optical bistability and signal amplification of new low-power nonlinear effects in InSb"*, Appl. Phys. Lett., Vol. 35, p. 658 (1979).

[12] D.A.B. Miller, S.D. Smith, A. Johnston, *"Two beam optical signal amplification and bistability in InSb"*, Opt. Commun., Vol. 31, p. 101 (1979).

[13] H.M. Gibbs, S.S. Tarng, J.L. Jewell, D.A. Weinberger, K. Tai, A.C. Gossard, S.L. McCall, A. Passner, W. Wiegmann, *"Room temperature excitonic bistability in GaAs/GaAlAs super lattice etalon"*, Appl. Phys. Lett., Vol. 41, p. 221 (1982).

[14] D.B. Anderson and J.T. Boyd, *"Wide-band CO_2 laser second harmonic generation phase matched in GaAs thin-film waveguides"*, Appl. Phys. Lett., Vol. 19, p. 266 (1971).

[15] W. Sohler, *"Nonlinear integrated optics: in new directions in guided wave and coherent optics"*, D.B. Ostrawsky and E. Spitz, Eds. (NATO ASI Series 78) The Hague, The Netherlands: Martinus Nijhoff, p. 449 (1984).

[16] S.M. Jensen, *"The nonlinear coherent coupler"*, IEEE J. Quantum Electron., Vol. QE-18, p. 1580 (1982).

[17] A. Lattes, H.A. Haus, F.J. Leonberger and E.P. Ippen, *"An ultrafast all-optical gate"*, IEEE J. Quantum Electron., Vol. QE-19, p. 1718 (1983).

[18] S.M. Jensen, *"The nonlinear coherent coupler"*, IEEE J. Quantum Electron., Vol. QE-18, p. 1580 (1982).

[19] B. Daino, G. Gregori and S. Wabnitz, *"Stability analysis of nonlinear coherent couplings"*, J. Appl. Phys., Vol. 58, p. 4512 (1985).

[20] S. Wabnitz, E.M. Wright, C.T. Seaton and G.I. Stegeman, *"Instabilities and all-optical phase-controlled switching in a nonlinear directional coherent coupler"*, Appl. Phys. Lett., Vol. 49, p. 838 (1986).

[21] S. Trillo and S. Wabnitz, *"Nonreciprocal and stochastic all-optical switching in nonlinear coherent couplers"*, in Tech. Dig. CLEO, Washington, Paper THK30, p. 260 (1987).

[22] K. Kitayama and S. Wang, *"Optical pulse compression by nonlinear coupling"*, Appl. Phys. Lett., Vol. 43, p. 17 (1983).

[23] P. LiKamWa, J.E. Stich, N.J. Mason, J.S. Roberts and P.N. Robson, *"All optical multiple-quantum well waveguide switch"*, Electron. Lett., Vol. 21, p. 26 (1985).

[24] P. LiKamWa, P.N. Robson, J.P.R. David, G. Hill, P. Mistry, M.A. Pate and J.S. Roberts, *"All-optical switching effects in a passive GaAs/GaAlAs multiple-quantum well waveguide resonator"*, Electron. Lett., Vol. 22, p. 1129 (1986).

[25] H.A. Haus, N.A. Whitaker and Jr., *"All-optical logic in optical waveguides"*, Phil. Tran. R. Soc. Lond., Vol. A313, p. 311 (1984).

[26] S. Tarucha, Y. Horikoshi, H. Okamoto, *"Optical absorption characteristics of GaAs-GaAlAs multi-quantum well heterostructure waveguides"*, Jap. J. Appl. Phys., Vol. 22, p. L482 (1983).

[27] S. Tarucha, H. Iwamura, H. Kobayashi, H. Okamoto, *"Optical properties of GaAs-GaAlAs multi-quantum well lasers/waveguides"*, IEEE Trans. Electron. Dev., Vol. ED-30, p. 1575 (1983).

[28] D.A.B. Miller, D.S. Chemla, D.J. Eilenberger, P.W. Smith, A.C. Gossard and W.T. Tsang, *"Large room-teperature optical nonlinearity in GaAs/GaAlAs multiple quantum well structures"*, Appl. Phys. Lett., Vol.41, p. 679 (1982).

[29] W.M. Gibbons and D. Sarid, *"Effect of carrier diffusion on the nonlinear response of optical waveguides"*, Optics Lett., Vol. 12, p. 564 (1987).

[30] Y. Silberberg, P.W. Smith, D.A.B. Miller, B. Tell, A.C. Gossard and W. Wiegmann, *"Fast nonlinear optical response from proton-bombarded multiple quantum well structures"*, Appl. Phys. Lett., Vol. 46, p. 701 (1985).

[31] P. LiKamWa, A. Miller, J.S. Roberts and P.N. Robson, *"130 ps recovery of all-optical switching in a GaAs multiquantum well directional coupler"*, Appl. Phys. Lett., Vol. 58, p. 2055 (1991).

[32] Y.J. Chen and G.M. Carter, *"Measurement of third order nonlinear susceptibilities by surface plasmons"*, Appl. Phys. Lett., Vol. 41, p. 307 (1982).

[33] J.D. Valera, C.T. Seaton, G.I. Stegemann, R.L. Shoemaker, Xu Mai and C. Liao, *"Demonstration of nonlinear prism coupling"*, Appl. Phys. Lett., Vol. 45, p. 1013 (1984).

[34] R.M. Fortenberry, R. Moshrefzadeh, G. Assanto, Xu Mai, E.M. Wright, C.T. Seaton and G.I. Stegeman, *"Power-dependent coupling and switching in prism and grating coupling to ZnO waveguides"*, Appl. Phys. Lett., Vol. 49, p. 6987 (1986).

[35] F. Pardo, H. Chelli, A. Koster, N. Paraire and S. Laval, *"Experimental and theoretical study of ultrafast optical switcing using guided mode excitation in silicon on sapphire"*, IEEE J. Quantum Electron., Vol. QE-23, p. 545 (1987).

[36] G. Assanto, V. Svensson, D. Kuchibhatla, U.J. Gibson, C.T. Seaton and G.I. Stegeman, *"Prism coupling in ZnS waveguides: A classical example of a nonlinear coupler"*, Opt. Lett., Vol. 11, p. 644 (1986).

[37] G.M. Carter, Y.J. Chen and S.K. Tripathy, *"Intensity-dependent refractive index of refraction in multilayers of polydiacetylene"*, Appl. Phys. Lett., Vol. 43, p. 891 (1983).

[38] Y.J. Chen, G.M. Carter, G.J. Sonek and J.M. Ballantyne, *"Nonlinear optical coupling to planar GaAs/AlGaAs waveguides"*, Appl. Phys. Lett., Vol. 48, p. 272 (1986).

[39] S. Patela, H. Jerominek, C. Delisle and R. Tremblay, *"Nonlinear prism coupling in waveguide structures deposited on to semiconductor-doped glass"*, Electron. Lett., Vol. 22, p. 411 (1986).

[40] G. Vitrant and P. Arlot, *"Demonstration of optical bistability with a nonlinear prism coupler"*, J. Appl. Phys., Vol. 61, p. 4744 (1987).

[41] C. Karaguleff, G.I. Stegeman, R. Zanoni and C.T. Seaton, *"Degenerate four wave mixing in planar CS_2 covered waveguides"*, Appl. Phys. Lett., Vol. 7, p. 621 (1985).

[42] A. Gabel, K.W. Delong, C.T. Seaton and G.I. Stegeman, *"Efficient degenerate four-wave mixing in an ion-exchange semiconductor-doped glass waveguide"*, Appl. Phys. Lett., Vol. 51, p.1682 (1987).

[43] C.N. Ironside, T.J. Cullen, B.S. Bhumbra, J. Bell, W.C. Banyai, N. Finlayson, C.T. Seaton and G.I. Stegeman, *"Nonlinear optical effects in ion-exchanged semiconductor doped glass waveguides"*, J. Opt. Soc. Amer. B, Vol. 7, p. 492 (1988).

[44] T.J. Cullen, C.N. Ironside, C.T. Seaton and G.I. Stegeman, *"Semiconductor doped glass ion-exchanged waveguides"*, Appl. Phys. Lett., Vol. 49, p. 1403 (1986).

[45] D. Cotter, C.N. Ironside, B.J. Ainslie and H.P. Girdlestone, *"Picosecond pump-probe interferometric measurement of optical nonlinearity in semiconductor-doped fibers"*, Opt. Lett., Vol. 14, p. 317 (1989).

Chapter 2

Nonlinear Optical Properties Of GaAs/GaAlAs Semiconductors

2.1 Introduction:

Almost all materials exhibit optical nonlinearity when they are excited with a very intense laser beam. However, in most cases the size of the nonlinear effect is so small that it is virtually non-existent. In semiconductors an enhancement of the nonlinearity occurs near resonance and the effect can become significant. The nonlinear optical properties of semiconductor materials can be explained using the classical picture of nonlinear optics. In this chapter we will discuss the microscopic origins of the optoelectronic and optothermal nonlinear effects in GaAs/GaAlAs semiconductors and the enhanced optical nonlinearity in MQWs due to the two-dimension quantum confinement effect (excitonic effect). Finally the electro-optic effects in semiconductor QWs are described. These effects were used in our proposed all-optical switching devices (in chapter 7 and 8) to reduce the relaxation time of the resonant nonlinearity and to improve the throughput of these devices.

2.2 Classical Description of Optical Nonlinearity:

When a dielectric medium is exposed to a beam of light, the electron orbital is elongated along the axis of the electric field and induces a small dipole component into the electron charge distribution, and they are affected (polarised) by the external field. This in turn may influence the propagation of the light waves in that medium.

In terms of a simple classical model in which an electron is visualised as a classic particle of mass m oscillating in one-dimensional harmonic potential $bx^2/2$, the equation of motion describing the response (polarisation) of the electron to an external field of a given frequency ω is [1]:

$$m\frac{\partial^2 x}{\partial t^2} + \sigma\frac{\partial x}{\partial t} + b x = -e\varepsilon_0 \exp(i\omega t) \qquad (2.1)$$

where b is the classical restoring force, σ is the damping coefficient, e is the electron charge and x is the displacement. Assuming that the solution to Eq. (2.1), x(t), is a harmonic function with amplitude x_0 such that:

$$x(t) = \text{Re}\left[x_0(\omega)\exp(i\omega t)\right] \qquad (2.2)$$

where Re means that we take the real part of the expression. By substituting Eq. (2.2) into Eq. (2.1) and differentiate it, gives the amplitude x_0 as:

$$x_0(\omega) = -\frac{e\,\varepsilon_0}{m}\cdot\frac{1}{\omega_0^2 - \omega^2 + i\omega\sigma} \qquad (2.3)$$

where $\omega_0 = (b/m)^{1/2}$ is the resonant frequency. The polarised electron by the external field induces a dipole -ex, and for N electrons in a unit volume, the total polarisation is:

$$P(\omega) = -Nex_0 \qquad (2.4)$$

The electronic susceptibility $\chi(\omega)$ is defined as the ratio of the complex amplitude of the induced polarisation to the amplitude of the external field multiplied by ε_0:

$$\chi(\omega) = \frac{P(\omega)}{\varepsilon_0\varepsilon_0} \qquad (2.5)$$

$$\chi(\omega) = \frac{Ne^2}{\varepsilon_0 m}\cdot\frac{1}{\omega_0^2 - \omega^2 + i\omega\sigma} \qquad (2.6)$$

$\chi(\omega)$ has a real and imaginary parts, i.e. $\chi(\omega)=\chi'(\omega)-i\chi''(\omega)$ where:

$$\chi(\omega) = \frac{Ne^2 / \varepsilon_0 m}{\left(\omega_0^2 - \omega^2\right)^2 + \left(\frac{\sigma}{m}\omega\right)^2}\left[\left(\omega_0^2 - \omega^2\right) - i\frac{\sigma}{m}\omega\right] \qquad (2.7)$$

Fig. 2.1 shows a normalised plot of $\chi'(\omega)$ and $\chi''(\omega)$, the real part represents the optical wave dispersion (refractive index) and the imaginary part represents the absorption. With reference to Fig. 2.1, at resonant frequency $\omega=\omega_0$, the absorption is at its maximum and the dispersion goes to zero, also the dispersion is still high at frequencies away from resonance at which the absorption is very small.
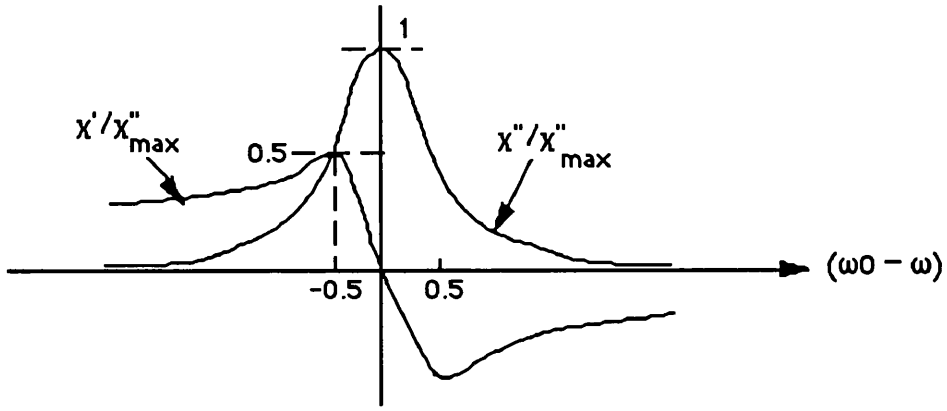
Fig. 2.1 *A plot of the real (χ') and imaginary (χ'') parts of the electronic susceptibility.*

For any material, the real and imaginary parts of the susceptibility are linked by the Kramers-Kronig transformation [2,3]:

$$\chi(\omega) = \frac{2}{\pi} \, \Pi \int_0^\infty \frac{\Omega}{\Omega^2 - \omega^2} \, \chi'(\Omega) \, d\Omega \qquad (2.8)$$

$$\chi'(\omega) = \frac{2}{\pi} \, \Pi \int_0^\infty \frac{\omega}{\Omega^2 - \omega^2} \, \chi'(\Omega) \, d\Omega \qquad (2.9)$$

where Π denotes the principal part of the integral. This transformation implies that the χ' (refractive index) can be calculated at any frequency from a knowledge of the χ'' (absorption) at all frequencies. The change in the refractive index Δn at any frequency can be related to the change in absorption $\Delta \alpha$ at all frequencies by using the following expression [4]:

$$\Delta n(\omega) = \frac{2}{\pi} \, \Pi \int_0^\infty \frac{\Delta \alpha(\Omega)}{\Omega^2 - \omega^2} \, d\Omega \qquad (2.10)$$

This relation indicates that any change in absorption results in a change in refractive index of the material and vice-versa.

In semiconductor materials, the electron and hole particles have energy levels that are calculated from the Schrodinger equation, and when absorption of photon takes place (at resonance), electrons make jumps between these quantum states across the semiconductor forbidden gap E_g. It is possible to apply the above classical model to an intrinsic

13

semiconductor by putting $\omega_0 = E_g/\hbar$. The semiconductor band gap play an important part in determining the polarisation properties of the material even when the frequency of the applied field is much smaller than the $E_g/\hbar$. Therefore it is necessary to have a good knowledge of the band structure of the bulk and QW semiconductor materials, which will be outlined in the next section.

From Eq. (2.5), the polarisation is a linear function of the external applied field. When the semiconductor material is subject to an intense optical field, the polarisation will not be a linear function of the applied field, and can be expressed as a Taylor series in power of the optical field [5]:

$$P = \sum_n \epsilon_0 \, \chi^{(n)}(\omega) \, \epsilon_0^n \tag{2.11}$$

where $\chi^{(n)}$ is the nth order susceptibility,

$$\epsilon_0^n \equiv \epsilon_0(k_1, \omega_1) \, \epsilon_0(k_2, \omega_2) \ldots \epsilon_0(k_n, \omega_n) \tag{2.12}$$

each component of the electromagnetic field is characterised by its wave vector k and frequency ω. $\chi^{(n)}$ can be derived in the same manner as $\chi^{(1)}$, Eq. (2.6), by adding higher order terms to the harmonic potential in Eq. (2.1), $\chi^{(n)}$ is a multiple function of the linear electronic susceptibility $\chi^{(1)}$.

The second order susceptibility $\chi^{(2)}$ describes nonlinear effects such as the second harmonic generation, three-wave mixing, parametric amplification/oscillation, frequency up-conversion, optical rectification and Pockels electro-optic effect [6]. These effects are beyond the scope of this work, except the last effect. The third order coefficient $\chi^{(3)}$ describes nonlinear effects such as four-wave mixing, optical phase conjugation, Kerr electro-optic effect, stimulated Raman/Brillouin scattering, two-photon absorption and the field or intensity dependent refractive index change. The effects emerge from the field (intensity) dependent refractive index change are: self-phase modulation, self focusing, soliton propagation and optical bistability. The field (intensity) dependent refractive index change can be expressed as:

$$n = n_0 + n_2|\epsilon(t)|^2$$

or

$$n = n_0 + n_2 I(t) \tag{2.13}$$

14

where n_0 is the linear refractive index, I is the optical intensity and n_2 is the nonlinear refractive index coefficient. n_2 is expressed as [7]:

$$n_2(SI) = \frac{\chi^{(3)}}{2cn_0^2\epsilon_0}$$

(2.14)

c is the velocity of light and ϵ_0 is the free space permittivity. The nonlinearities which are investigated in this project arise from $\chi^{(3)}$, which can give rise to both the nonlinear absorption and refraction effects in the semiconductor materials.

In the above description of nonlinear effects, only the classical nonlinear effects have been considered. However, in semiconductors additional effects which occur. When photon energies close to or above the band gap are incident on the semiconductor, then the photons will be absorbed and photogenerated carriers will be induced which modifie the dielectric constant and consequently alter the semiconductor refractive index. These effects are known as *resonant nonlinear* effects, while other effects which do not involve generation of real carriers are known as *nonresonant nonlinear* effects.

In the following sections, the microscopic origins of the nonlinear effects are discussed for both GaAs/GaAlAs bulk and multiple quantum well MQW materials.

2.3 Microscopic Origins of Optical Nonlinearity in Semiconductors:

In semiconductors, there are various mechanisms which contribute to the nonlinear effects. The dominant contribution to n_2 depends on number of factors such as the material band structure, photon energy, intensity and temperature. These mechanisms are divided into two sections, optoelectronic and optothermal nonlinearities.

2.3.1 Optoelectronic Nonlinearity in GaAs:

2.3.1.1 Band Filling:

When photons with an energy corresponding to the band gap of a semiconductor are absorbed, electrons are promoted from the valence band to the conduction band. These photo-excited carriers rapidly relax within the band, intraband transition (50fsec), to form a thermal distribution. Recombination between bands (interband transition) occurs on a

much longer time scale than intraband transition processes, e.g. in GaAs it is about 12nsec. Therefore, these photo-generated carriers will occupy energy levels at the band extrema and block any further transition to these states, via Pauli exclusion principle. This will shift the semiconductor effective band gap to larger energies, this is known as the Dynamic Burstein-Moss shift [8]. This shift in the band gap will be followed by a change in the photon absorption. From the Kramers-Kronig (K-K) relationships, this will induce a change in the refractive index of the material. The nonlinear coefficient n_2, caused by the band filling effect, is expressed as [8]:

$$n_2 = \frac{-8\sqrt{\pi}}{3} \cdot \frac{e^2 h^2}{m} \cdot \frac{\mu}{m_c} \cdot \frac{mP^2}{h^2} \cdot \frac{1}{n_0} \cdot \frac{1}{kT}$$

$$\frac{\alpha(h\omega)\tau_r}{(h\omega)^3} \cdot J\left[\frac{\mu(h\omega - E_g)}{m_c kT}\right] \qquad (2.15)$$

where

$$J(a) = \int_0^\infty \frac{x^{1/2} e^{-x}}{x - a} \, dx$$

here m_c is the conduction band effective mass, μ is the electron-hole reduced effective mass ($\mu = m_c m_v/(m_c+m_v)$), τ_r is the carrier recombination time, k is the Boltzmann constant and P is the momentum matrix element. J(a) is a dimensionless resonance function, the resonant behaviour of J(a) is shown in Fig. 2.2. As the detuning from the band edge is decreased the value of n_2 increases through the function J(a).
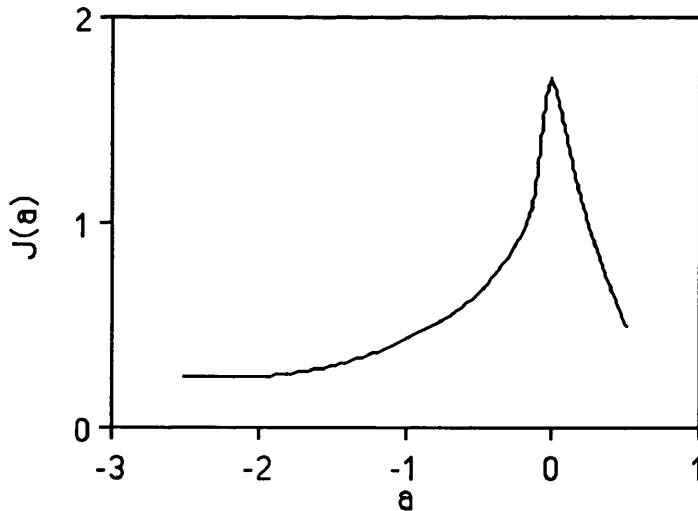
Fig. 2.2 *The resonant function J(a), dimensionless, plotted against* a=μ(hω-E$_g$)/m$_c$kT *(after ref. 8).*

16

2.3.1.2 Plasma Effects:

The photo-generated carriers also contribute to the refractive index through the plasma effect, the plasma induced nonlinear refractive index coefficient n_2 is expressed as [9];

$$n_2(\text{plasma}) = -\frac{\alpha \tau_r e^2}{2\hbar\omega^3 \varepsilon_0 n_0 m^*} \qquad (2.16)$$

where m^* is the effective mass of the carriers, e is the electron charge and α is the absorption coefficient. It can be seen that there is no resonant term in $n_2(\text{plasma})$. Close to the band edge, the plasma effect is usually small compared to other nonlinear mechanisms.

2.3.1.3 Nonlinear Excitonic Effect in GaAs:

In the previous sections the coulombic interaction between the photo-excited carriers has been neglected. The inclusion of such effects gives rise to other potential sources of optoelectronic nonlinearity.

The electrons in the conduction band and holes in the valence band, as electrically charged particles, interact through the Coulomb potential. This interaction is repulsive for equally charged quasiparticles and is attractive for oppositely charged quasiparticles. The attractive interband interaction causes a strong correlation between electrons and holes and may lead to the formation of bound states (excitons). These excitons may be regarded as hydrogen atom-like quasiparticles which are characterised by the Bohr radius, expressed as:

$$a_{3D} = \frac{4\pi \in \hbar^2}{\mu e^2} \qquad (2.17)$$

where μ is the reduced mass of the electron-hole pair ($\mu = 1/m_e + 1/m_h$), where m_e and m_h are the electron and hole masses respectively. The binding energy of the ground state exciton is given by:

$$B_{3D} = -\frac{e^4 \mu}{8 \in^2 \hbar^2} \qquad (2.18)$$

The negative value of B_{3D} is the Rydberg constant, R_y, (i.e. $B_{3D} = -R_y$). There is an infinite series of exciton levels, and the energy of the nth level is given by:

$$E_n^{3D} = E_g - \frac{R_y}{n^2} \qquad\qquad (2.19)$$

where E_g is the band gap energy and n is an integer (n=1, 2, 3 ...). In GaAs the Bohr radius and binding energy of the ground state are 140 Å and 4.2 meV, respectively [10]. The exciton effect is seen as a sharp peak, in the absorption spectrum of the semiconductor material, just below the band edge as shown in Fig. 2.3.
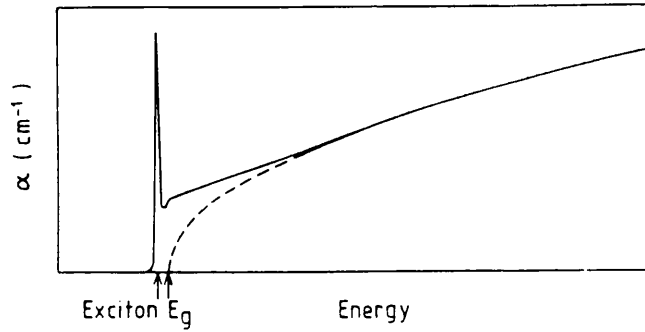
Fig. 2.3 *The absorption coefficient* α *(cm^{-1}) as a function of photon energy for a bulk GaAs, the exciton line is just below the onset of the band-to-band transitions across the forbidden gap* E_g.

When the carrier density is increased, the Coulomb interaction will be screened and the exciton will ionise. Therefore, photogenerated carriers cause screening of the Coulombic potential and result in a change in the absorption spectrum followed by a change in the refractive index.

Gibbs [11] used a two-level transitions model to calculate the nonlinear refractive index coefficient, which is given by:

$$n_2 = \frac{\alpha_{ex} \tau}{4 \pi I_s} \cdot \frac{\Delta}{\left(1 + \Delta^2\right)^2} \qquad\qquad (2.20)$$

where Δ is the detuning from resonance, I_s is the saturation intensity and α_{ex} is the exciton absorption coefficient. At low temperature, the dominant mechanism of resonant nonlinearity in GaAs has been shown to be due to the exciton saturation [12]. As the temperature is increased, the excitonic peak is thermally broadened due to the scattering with the longitudinal optical LO phonons, and at room temperature the excitonic resonances are not seen in the absorption spectrum.

2.3.2 Opto-Electronic Nonlinearity in GaAs/GaAlAs MQWs:

It has been found that the magnitude of the electronic nonlinearity may be enhanced over that found for bulk semiconductors by the use of quantum wells. In order to understand the electronic nonlinearities in the semiconductor QW structures, it is vital to present the concept of quantum well band structures.

2.3.2.1 GaAs/GaAlAs QW Band Structure:

These QW structures consist of a thin layer of GaAs sandwiched between two layers of GaAlAs. This double heterostructure system is referred to as QW, because their band structure form a well (GaAs) with a barrier (GaAlAs). The height of the barrier in the conduction and valence bands is given by ΔE_c and ΔE_v respectively, as shown in Fig. 2.4. The well width is chosen to be thick enough ($W_w > 20$ Å) that the layers have the characteristic properties of a GaAs crystal, and thin enough ($W_w < 300$ Å) to ensure that W_w is shorter than the mean free path. When the two intrinsic semiconductors have similar lattice structures and constants, then the band discontinuity at the GaAs-GaAlAs heterojunctions can be considered abrupt enough so that it is possible to model the QW as a finite square well.
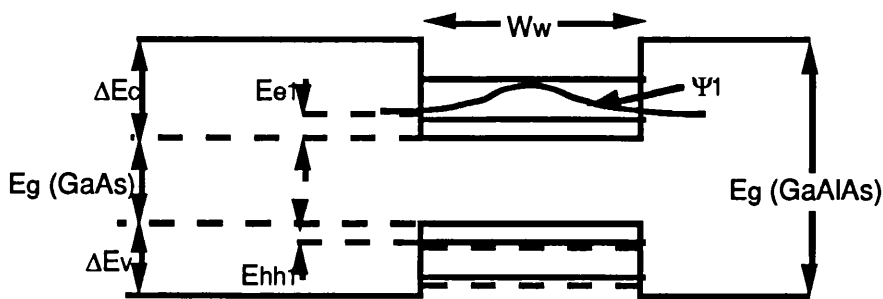
Fig. 2.4 *Schematic diagram of the conduction and valence bands structure of GaAs/GaAlAs quantum well.*

The confined electrons and holes in the well are free to move in the plane of the well (x-y plane) while its motion is limited by the formed barriers in the z-direction. The confinement effect gives rise to electron and hole bound states which can be described by solving the time-independent Schroedinger equation:

$$H \Psi(z) = E \Psi(z) \qquad\qquad (2.21)$$

where $\Psi(z)$ is the wavefunction of the particle in question and E is the energy of the particle. The Hamiltonian H, for a finite potential well, is given by:

$$H = -\frac{h^2}{2m^*} \frac{d^2}{dz^2}$$

for the region in the well, and

$$H = -\frac{h^2}{2m^*} \frac{d^2}{dz^2} + V_0$$

outside the well, where h is Planck's constant divided by 2π, m^* is the effective mass of the particle in question and V_0 is the height of the potential barrier. As described in section 3.6, the electron and hole effective masses depend on the composition of the material, therefore two different masses $\left(m^*_{e,h}\right)_w$ in the well and $\left(m^*_{e,h}\right)_b$ in the barrier were used.

Equation (2.21) has a finite number of bound-state wavefunction solutions which are sinusoidal within the well and decay exponentially outside it. Thus:

$$\Psi(z) = A e^{k_1 z} \qquad\qquad z < -W_w/2$$

$$\Psi(z) = B \sin k_2 z + C \cos k_2 z \qquad |z| < W_w/2 \qquad (2.22)$$

$$\Psi(z) = D e^{k_3 z} \qquad\qquad z > W_w/2$$

$$k_1 = k_3 = \left[\frac{2 m^*_b (V_0 - E)}{h^2}\right]^{1/2}$$

$$k_2 = \left[\frac{2 m^*_w E}{h^2}\right]^{1/2}$$

where A, B, C, and D are constants obtained by setting the boundary conditions such that Ψ and its derivative are equal at $z = \pm W_w/2$. The solution to Eq. (2.21), for a finite square well, is given by [13]:

$$\left(\frac{2m^*_w E}{\hbar^2}\right)^{1/2} W_w - \tan^{-1}\left[\frac{m^*_w}{m^*_b}\cdot\left(\frac{V_0 - E}{E}\right)^{1/2}\right] - n\pi = 0 \qquad (2.23)$$

which is solved numerically to calculate the nth eigenvalue E. Each of these solutions is characterised by a quantum number n and has a discrete energy E_n. Fig. 2.5 shows a sketch of the wavefunctions for the lowest three energies. The exponential decay of the wavefunctions outside the well depends strongly on the difference V_0-E, and is equal to zero for an infinite square well.
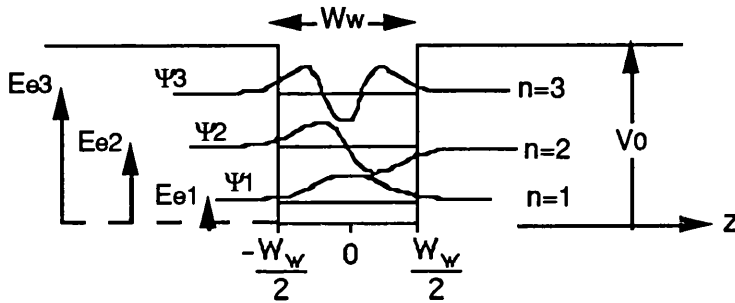
Fig. 2.5 *Schematic diagram of the conduction band structure of a quantum well, the well width and the barrier height are W_w and V_0, respectively. n_i and Ψ_i are the ith quantum energy level and electron wavefunction, respectively.*

The three dimensional dispersion relation (energy E versus wave vector k) of a particle (electron or hole) in a quantum well is given by:

$$E = E_n + \frac{\hbar^2 k_x^2}{2m^*} + \frac{\hbar^2 k_y^2}{2m^*} \qquad (2.24)$$

where E_n is the nth quantization energy level in the z direction, which is found from the solution of the Schrodinger equation, and k_x and k_y are the De Broglie wave numbers in the x-y plane of the well. Fig. 2.6a shows the energy sub-bands, in the conduction band, as a function of the wave vector k. The density of states of electrons ρ, associated with the sub-bands, is shown in Fig. 2.6b as a function of the energy E. The dash curve is for the bulk (three-dimensional) parabolic band where the density of states goes as $E^{1/2}$. The solid line represents the density of states for the QW (two-dimensional) which has a step-like form.

In the valence band, the same above picture can be followed to draw the energy sub-bands of the holes in the QW. The energy levels are measured from the top of the valence band. The position of these levels is not the same as that in the conduction band because both the barrier height ΔE_v and the effective mass of the hole are in principle different from the height of ΔE_c and the electron effective mass.

(a)   (b)
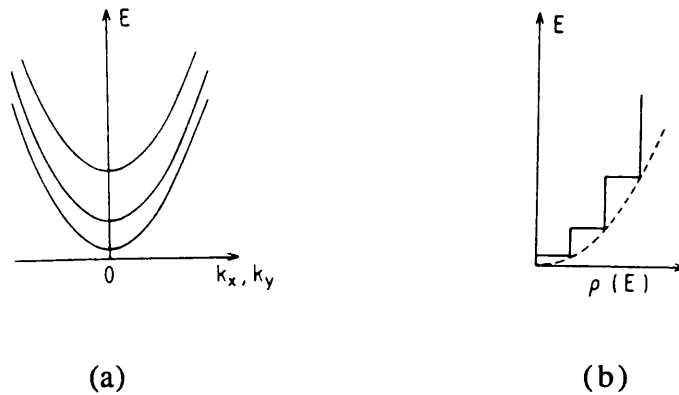
Fig. 2.6 a) *the construction of the total energy dispersion electron in the conduction band of a quantum well structure, Z is the direction perpendicular to the QW,* b) *The density of the states of a QW, the broken line indicates the form of* ρ *for a bulk crystal.*

With reference to Eq. (2.23), the difference in the effective masses of the heavy hole hh and light hole lh gives two different eigenvalue states. Therefore the degeneracy of the hh and lh sub-bands at k=0, in bulk GaAs semiconductor, is lifted in the QW structure due to the quantum confinement effect.

From the band structure picture of the QWs, it is clear that the required photon energy to lift an electron from the valence band to the conduction band, of the lowest states, should be greater than that of the bulk gap of the GaAs, i.e. $E_g(QW)=E_g(GaAs)+E_{e1}+E_{hh1}$, where E_{e1} and E_{hh1} are the energies of the lowest confined electron and heavy hole states, respectively. The allowed transitions across the forbidden gap are only possible between the states of the same quantum number, these possible transitions follow the selection rule [14] which require zero difference between the initial and final quantum states (i.e. $\Delta n=0$). The optical transitions depends on the density of states and the selection rule, and hence the absorption coefficient $\alpha(h\omega)$ shows a step-wise increase in absorption as the photon energy increases above the band gap.

2.3.2.2 Excitons in GaAs/GaAlAs QWs:

We have seen in bulk GaAs, that the exciton radius is of the order of 140 Å with a small binding energy ≈ 4.2 meV. In QWs, the exciton binding energy is modified significantly due to the quantum confinement effect. Solving Schrödinger wave equation in two-dimensional space gives an exciton binding energy as [3]:

$$B_{2D} = -\frac{R_y}{\left(n - \frac{1}{2}\right)^2} \qquad\qquad (2.25)$$

Therefore the reduction of the dimensions of the electron and hole distributions has increased the binding energy of the exciton. Hence the 2D formed ground state exciton (n=1) would have four times the energy ($4R_y$) and half the radius of the 3D exciton. In practice, due to the finite barrier potential, the penetration of the electron and hole wavefunctions into the barrier increases as the well width decreases, therefore for a very thin wells the exciton binding energy and radius tend to that of the 3D exciton of the barrier material. There is an optimum layer thickness that corresponds to a maximum binding energy, this optimum is typically found for $a_{3D}/2 < W_w < a_{3D}$ for which $-3R_y < B_{e1-hh1} < -2R_y$ [15]. Greene et al. [16] calculated that, for $Ga_{0.7}Al_{0.3}As$ barrier, the hh-exciton binding energy increases to 9.5 meV as the well width is decreased to 40 Å and then decreased for narrower wells.

In the absorption spectrum of the QWs, the excitonic peaks appear at photon energies just below the QW band-to-band transitions, i.e. $\hbar\omega = E_g(QW) - B_{ex}$, as shown in Fig. 2.7.

Fig. 2.7 *The absorption coefficient α (cm^{-1}) for a QW structure as a function of photon energy, α can be seen to follow the step-like character of the density of states. The sharp feature near the edge of each step is the exciton contribution to α.*

An interesting property of QW structures is that, due to the quantum confinement effect the band-to-band transitions are predicted to be anisotropic for light propagating parallel to the plane of the layers [17]. This property arises from the nature of the light and heavy hole valence sub-bands. As predicted by the selection rules for absorption, the interaction of the hh and lh excitons with a linearly polarised light is strongly dependent on the polarisation direction. The oscillator strengths of the hh and lh band-to-band transitions are predicted to be 3/4 and 1/4 respectively for light polarised in the plane of the layers (TE), and 0 and 1 for light polarised perpendicular to the layers (TM). These assignments have been qualitatively verified by spin polarization measurements [18,19]. The highly anisotropic optical absorption of the QWs was explained in term of the crystal symmetry and the angular momentum of the sub-bands [14]. Measurements of the polarisation dependent absorption in a SQW waveguide structure, for both the TE- and TM-modes, confirmed the predictions of the selection rules [40]. Similar results have been obtained during the course of this project on a SQW GaAs/GaAlAs waveguides for both polarisations.

2.3.2.3 Enhanced Optical Nonlinearity in QWs:

The enhanced dynamic nonlinear effects in MQW structures result from the strong excitonic binding energy due to the quantum confinement effect. This nonlinear effect is resonant and is largest at photon energies equal to or above the excitonic peaks.

When electron and hole are injected into the semiconductor QW exciton is formed, as described above. As the density of the carriers is increased, e.g. by exposing the material to intense light, a phase transition occurs from the insulating excitonic phase to a metallic phase of electron-hole plasma. The electron-hole plasma occurs when the separation of the excitons becomes comparable with the exciton radius, and the exciton wave functions are overlapped. The phase transition will be accompanied by broadening of the exciton line, reduction of the band gap energy (band gap renormalisation) and decrease of the excitonic oscillator strength [10,14,20]. The presence of the electron-hole plasma screens the Coulomb interaction between electrons and holes, and the excitonic absorption peak is effectively removed, and a corresponding change in the refractive index will result.

The screening or ionisation time of the exciton, in GaAs-GaAlAs MQW is ≈150 fsec [10], this is of the same order as that in GaAs [21]. While the recombination time of the plasma carriers is of the order of nanoseconds, this limits the application of resonant nonlinearity for a usable ultrafast all-optical switching devices.

24

2.3.3 Optothermal Nonlinearity:

Under continuous illumination conditions, thermal effects in semiconductors usually dominate over the optoelectronic nonlinearities. The contribution of thermal effect on n_2 is opposite to that due to the electronic effects. Therefore, precautions must be taken to avoid heating, for example heat sinking of the sample and using a pulsed input beam.

As already discussed above, the photoexcited carriers, electrons and holes, survive for a short time before they recombine again. The recombination of these carriers is of two types; either radiative or non-radiative recombinations. Radiative recombination involves the production of photons with energy equal the interband transition energy levels. In the second type of recombination, the energy of the photo-generated carriers goes to the lattice in the form of heat.

Nonradiative recombination can occur through traps and dislocation in the crystal structure [22], defects, surface recombination [23] and auger recombination [24] which involves an emission of third particle (phonon). As a result of the nonradiative processes, the temperature of the sample increases. This leads to a shift in the band gap E_g due to the expansion of the lattice. The variation of E_g with temperature in GaAs has been measured as [25];

$$E_g(T)_{GaAs} = 1.519 - \frac{5.405 \times 10^{-4} T^2}{204 + T} \qquad (eV) \qquad (2.26)$$

An increase in temperature results in a decrease in the energy-gap and a consequent shift of the absorption spectrum to longer wavelength (red shift). This change in absorption, via K-K relation, cause a change in refractive index of the semiconductor. The sign of the index change is positive and as a consequence competes with the negative contribution arising from the electronic effects.

2.4 Electro-Absorption Effects in Semiconductor QWs:

The effects induced by applying an electrostatic field on the absorption of QWs have been extensively studied and well documented [26]. The electric field can be applied either parallel to or perpendicular to the plane of the QWs. Let us consider first the case of the field applied parallel to the QW layers because it is qualitatively similar to the case of bulk material [27].

In bulk semiconductor, the electric field induced effect on the absorption edge is dominated by the Franz-Keldysh effect [28]. This effect induces a general broadening in the absorption edge, when a uniform DC electric field ($\approx 10^5$ V/cm) is applied to a semiconductor crystal. A tail is induced in the absorption edge, at photon energies below the band gap, and oscillations are induced in the absorption spectrum, at photon energies above the absorption edge. The Franz-Keldysh effect neglect any effect arising from the Coulomb interaction between electrons and holes (i.e. excitonic effect). At low temperature, the excitonic effect forms a sharp peak in the absorption spectrum and was seen to broaden rapidly and shift slightly in energy with the applied field strength [29]. The exciton broadening is due to the ionisation effect of the exciton in the presence of the electric field, which tend to tear the electron-hole pair a part.

In MQWs, the applied field parallel to the plane of the QWs, induces absorption effect very similar to that in bulk material [14]. The only difference compared to the case of bulk material is that the exciton binding energy and the in plane-wave function are slightly modified. In both cases, the dominant effect is a broadening of the exciton resonance with applied field that results from the shortening of the exciton life time due to field ionisation. Fig. 2.8 shows the spectra of the QW absorption for various electric field strength applied in the plane of the GaAs/GaAlAs QWs (after ref. 27).
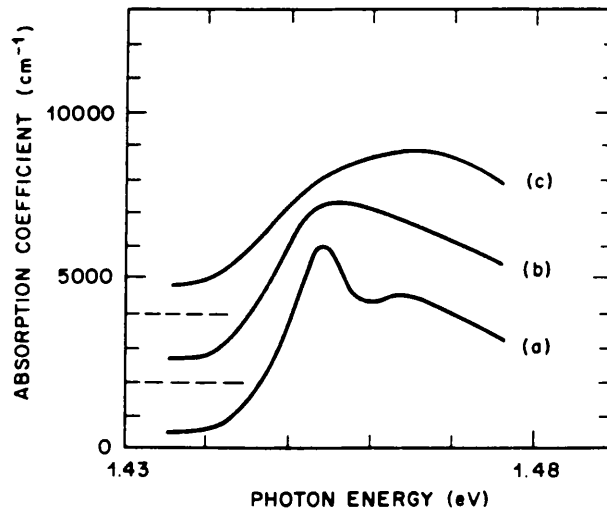
Fig. 2.8 *The absorption spectra of a QW for various electric fields applied in the plane of the GaAs/GaAlAs QW layers:* a) 0 V/cm, b) 1.6×10^4 V/cm and c) 4.8×10^4 V/cm. *(after ref. 27)*

When the electric field is applied perpendicular to the plane of the QWs (z-direction), then the induced effects are qualitatively different from that in bulk material. In this geometry, the applied field tilt the band of the QW as shown in Fig. 2.9. The electron and hole wave

functions peak move to opposite ends of the well, in the region where the potential is more attractive for the particle in question.
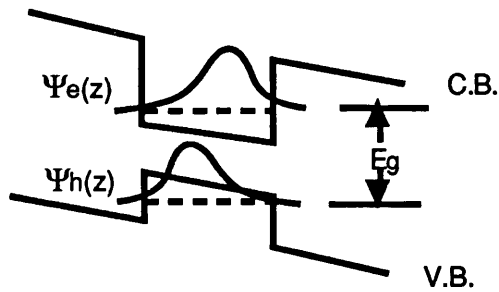
Fig. 2.9 *Schematic diagram of the tilt of the conduction and valence bands of a QW with applied electric field perpendicular to the plane of the well.*

The same happens to an electron-hole pair forming an exciton. This reduces the attraction between the two particles, i.e. the exciton binding energy becomes smaller. However, the walls of the well prevent ionisation by constraining the particles within the well. Ionisation and hence exciton peak broadening, can only occur when the particles tunnel out of the well. The electric field induced effects in MQW structures is known as the quantum confinement Stark effect QCSE [27,30,31], for field applied perpendicular to the plane of the QWs. The QCSE induces two effects, broadening and shift to lower energies of the excitonic resonances. The broadening is due to the penetration of the electron and hole wave functions into the barriers, due to the finite barrier height. The excitonic peaks will be removed from the absorption spectrum when these particles tunnel through the barriers. However, the excitonic resonances remain resolved at very high fields (e.g. 100 times the classical ionisation field). Weiner et al. [32] and Miller et al. [33] measured the electro-absorption spectra of GaAs/GaAlAs QW in a waveguide geometry, at different applied electric field strengths, for both the TE- and TM-modes. Their results showed not only a large shift in the absorption spectra but also the exciton peaks remained well resolved for high field strengths.

2.5 Electro-Optic Effects in Semiconductor QWs:

When a transparent material is subject to an electric field, the material may experience a change in refractive index. The effect leading to such a change is known as the electro-optic E-O effect [34].

At photon energies well below the semiconductor absorption edge the E-O effect arises from two components, the linear and quadratic E-O effects. The linear E-O effect or

Pockels effect is exhibited by non-centrosymmetric crystals and is a linear change in the refractive index with applied electric field. The E-O effect is defined as [1]:

$$\Delta B_{ij} = \sum_k r_{ijk} E_k \tag{2.27}$$

where

$$\Delta B_{ij} = \frac{\epsilon_0}{\epsilon_{ij}}$$

ΔB_{ij} is the dielectric tensor, r_{ijk} is the linear electro-optic tensor and is a 6¥3 matrix, i, j and k represent directions 1=x, 2=y and 3=z. In GaAs, with point group symmetry 43m [1], there are three equal non zero terms r_{41}, r_{52} and r_{63}.

For an electric field applied perpendicular to the plane of the wells, the index change can be expressed as [1]:

$$\Delta n(E) = \pm \frac{1}{2} n_0^3 r_{63} E_3 \tag{2.28}$$

where n_0 is the refractive index at zero field, r_{63} is the linear E-O coefficient which gives the index change experienced by light polarised in the x-y plane. In QW structures, this is referred to a light polarised in the plane of the well. As there is no component of the electro-optic coefficient in the direction perpendicular to the plane of the well, the refractive index change experienced by a light polarised perpendicular to the QWs is zero. The sign of the linear E-O coefficient is positive for light propagating along [1$\underline{1}$0] and negative for light propagating along [110].

The quadratic E-O effect is exhibited by all transparent materials, and leads to a change in refractive index proportional to the square of the electric field strength. In a non-centrosymmetric crystal the quadratic E-O effect is very small compared to the linear E-O effect.

At photon energies close to the materials absorption edge, the refractive index change induced by applied electric field perpendicular to the QW is enhanced by the electro-absorptive effect. The change in the electro-refractive effect, at a frequency ω, is calculated from knowing the change in absorption in the spectral region close to ω [35]. The electro-refractive effect is predicted to have a quadratic dependence on the applied field strength, such that the change in refractive index in a waveguide geometry can be expressed as [36]:

28

$$\Delta n(E) = \frac{1}{2} n_0^3 \left[\pm \Gamma_1 r_{63} E_z + \Gamma_2 S E_z \right] \qquad (2.29)$$

where S is the quadratic electro-optic coefficient and Γ_1 and Γ_2 are the confinement factors of the optical field in the active region of the waveguide for the linear and quadratic E-O effects respectively. It has been shown that a large change in the refractive index is associated with the Stark shift of the exciton resonance in MQWs [37,38]. The electro-refractive effect is highly polarisation dependent [39], this is due to the anisotropic polarisation dependence of the absorption of the QW structures [40].

2.6 Conclusions:

The optical properties of semiconductors is a large subject, therefore the review presented in this chapter was limited to the work presented in this thesis. The linear and nonlinear optical properties of the bulk and MQW structures have been discussed. This included the band gap structure of these materials and the enhanced nonlinearity due to the excitonic effect specially in the MQW structure. The electro-refractive and -absorptive effects in these materials were briefly discussed.

References:

[1] A. Yariv, "Optical electronics", Holt Saunders, 3rd ed., p. 135 (1985).

[2] F. Stern, "Solid state physics", Edited by F. Seitz and D. Turnbull, Academic, NewYork, Vol. 5, p. 299 (1963).

[3] D.S. Chemla, D.A.B. Miller, P.W. Smith, A.C. Gossard and W. Wiegmann, "Room temperature excitonic nonlinear absorption and refraction in GaAs/GaAlAs multiple quantum well structures", IEEE J. Quantum Electron, Vol. QE-20, p. 265 (1984).

[4] J.S. Weiner, D.A.B. Miller and D.S. Chemla, "Quadratic electro-optic effect due to the quantum-confined Stark effect in quantum wells", Appl. Phys. Lett., Vol. 50, p. 842 (1987).

[5] A. Miller, D.A.B. Miller and S.D. Smith, "Advances in physics", Vol. 30, p. 697 (1981).

[6] H.M. Gibbs, "Optical Bistability: Controlling Light With Light", Academic Press (1985).

[7] B. Jensenm and A. Torabi, "Quantum theory of the dispersion of the refractive index near the fundamental absorption edge in compound semiconductors", IEEE J. Quantum Electron., Vol. QE-19, p. 448 (1983).

[8] D.A.B. Miller, C.T. Seaton, M.E. Prise and S.D. Smith, *"Band-gap-resonant nonlinear refraction in III-V semiconductors"*, Phys. Rev. Lett., Vol. 47, p. 197 (1981).

[9] D.A.B. Miller, S.D. Smith and B.S. Wherrett, *"The microscopic mechanism of third-order nonlinearity in InSb"*, Opt. Commun., Vol. 35, p. 221 (1980).

[10] N. Peyghambarian and H.M. Gibbs, *"Optical nonlinearity, bistability and signal processing in semiconductors"*, J. Opt. Soc. Am. B, Vol. 2, p. 1215 (1985).

[11] H.M. Gibbs, *"Optical bistability: Controlling light with light"*, Academic press (1985).

[12] H.M. Gibbs, A.c. Gossard, S.L. McCall, A. Passner, W. Wiegmann and T.N.C. Benkatesan, *"Saturation of the free exciton resonance in GaAs"*, Solid state commun., Vol. 30, p. 271 (1979).

[13] B.S. Bhumbra, *"Nonlinear optical waveguide devices in GaAs/GaAlAs"*, Ph.D. Thesis, University og Glasgow (1990).

[14] D.S. Chemla and D.A.B. Miller, *"Romm-temperature excitonic nonlinear optical effects in semiconductor quantum well structures"*, J. Opt. Soc. Am. B, Vol. 2, p. 1155 (1985).

[15] R.L. Greene and K.K. Bajaj, *"Binding energy of Wannier excitons in GaAs-GaAlAs quantum well structures"*, Solid state commun., Vol. 45, p. 831 (1983).

[16] R.L. Greene , K.K. Bajaj and D.E. Phelps, *"Energy levels of Wannier excitons in GaAs-GaAlAs quantum well structures"*, Phys. Rev. B, Vol. 29, p. 1807 (1984).

[17] D.D. Sell, S.E. Stokowski, R. Dingle and J.V. DiLorenzo, *"Polariton reflectance and photoluminescence in high-purity GaAs"*, Phys. Rev. B, Vol. 7, p.4568 (1973).

[18] R.C. Miller, D.A. Kleinman, W.A. Nordland, Jr. and A.C. Gossard, *"Luminescence studies of optically pumped quantum wells in GaAs-Al$_x$Ga$_{1-x}$As multilayer structures"*, Phys. Rev. B, Vol. 22, p. 863 (1980).

[19] C. Weisbuch, R.C. Miller, R. Dingle, A.C. Gossard and W. Wiegmann, *"Intrinsic radiative recombination from quantum states in GaAs-Al$_x$Ga$_{1-x}$As multiple-quantum well structures"*, Solid State Commun., Vol. 37, p. 219 (1981).

[20] D.S. Chemla, A.B. Miller and S. Schmitt-Rink, *"Optical nonlinearities and instabilities in semiconductors"*, Edited by H. Haug, Academic, p. 83 (1988).

[21] C.V. Shank, R.L. Fork, R.F. Leheny and J. Shah, *"Dynamics of photoexcited GaAs band-edge absorption with subpicosecond resolution"*, Phys. Rev. Lett., Vol. 42, p. 112 (1979).

[22] K. Ando, C. Amano and H. Sugiura, *"Nonradiative e-h recombination characteristics of mid-gap electron trap in $Al_xGa_{1-x}As(x=0.4)$ grown by molecular beam epitaxy"*, Jap. J. Appl. Phys. 26, L266 (1987).

[23] D. Frank and B. S. Wherrett, *"Influence of surface recombination on optically bistable semiconductor devices"*, J. Opt. Soc. Am. A. 4, p. 25 (1987).

[24] A.R. Beattie and P.T. Landsberg, *"One-dimentional overlap functions and their application to Auger recombination in semiconductors"*Proc. Roy. Soc. Lon. A258, p.486 (1960).

[25] H. Kawai, K. Kaneko, N. Watanabe, *"Photoluminescence Of GaAs/GaAlAs Quantum Wells Grown By Metalorganic Chemical Vapor Deposition"*, J. Appl. Phys., Vol. 56, p.-- (1984).

[26] D.A.B. Miller, J.S. Weiner and D.S. Chemla, *"Electric-field dependence of linear optical properties in quantum well structures: waveguide electroabsorption and sum rules"*, IEEE J. Quantum Electron., Vol. 22, p. 1816 (1986).

[27] D.A.B. Miller, D.S. Chemla, T.C. Damen, A.C. Gossard, W. Wiegmann, T.H. Wood and C.A. Burrus, *"Electric field dependence of optical absorption near the band gap of quantum-well structures"*, Phys. Rev. B, Vol. 32, p. 1043 (1985).

[28] L.V. Keldysh, *"The effect of a strong electric field on the optical properties of insulating crystals"*, Soviet Phys. JETP, Vol. 34, p. 788 (1958).

[29] J.D. Dow and D. Renfield, *"Electroabsorption in semiconductors: The excitonic absorption edge"*, Phys. Rev. B1, p. 3358 (1970).

[30] D.A.B. Miller, D.S. Chemla, T.C. Damen, A.C. Gossard, W. Wiegmann, T.H. Wood and C.A. Burrus, *"Band-edge electroabsorption in quantum well structures: The quantum confined Stark effect"*, Phys. Rev. Lett., Vol. 53, p. 2173 (1984).

3 1

[31] J.A. Brum and G. Bastard, "*Electric-field-induced dissociation of excitons in semiconductor quantum wells*", Phys. Rev. B31, p. 3893 (1985).

[32] J.S. Weiner, D.A.B. Miller, D.S. Chemla, T.C. Damen, T.H. Wood, A.C. Gossard and W. Wiegmann, "*Strong polarization-sensitive electroabsorption in GaAs/GaAlAs quantum well waveguides*", Appl. Phys. Lett., Vol. 47, p. 1148 (1985).

[33] D.A.B. Miller, J.S. Weiner and D.S. Chemla, "*Electric-field dependence of linear optical properties in quantum-well structures: waveguide electroabsorption and sum rules*", IEEE J. Quantum Electron., Vol. QE-22, p. 1816 (1986).

[34] Nye, "*Physical properties of crystals*", Clarendon Press, Oxford (1957).

[35] M. Whitehead, G. Pasry, K. Woodbridge, P.J. Dobson and G. Duggan, "*Experimental confirmation of a sum rule for room temperature electroabsorption in GaAs/GaAlAs multiple quantum well structures*", Appl. Phys. Lett., Vol. 52, p. 345 (1988).

[36] M. Glick, F.K. Reinhart, G. Weimann and W. Schlapp, "*Quadratic electro-optic light modulation in a GaAs/GaAlAs multiquantum well heterostructure near the excitonic gap*", Appl. Phys. Lett., Vol. 48, p. 989 (1986).

[37] D.S. Chemla, I. Bar-Joseph, J.M. Kuo, T.Y. Chang, C.K. Lingshien, G. Livescu and D.A.B. Miller, "*Modulation of absorption in field-effect quantum well structures*", IEEE J. Quantum Electron., Vol. QE-24, p. 1664 (1988).

[38] T. Hiroshima, "*Electric field induced refractive index changes in GaAs/GaAlAs quantum wells*", Appl. Phys. Lett., Vol. 50, p. 968 (1987).

[39] J. Shimizu, T. Hiroshima, A. Ajisawa, M. Sugimoto and Y. Ohta, "*Measurements of the polarisation dependence of field-induced refractive index changes in GaAs/GaAlAs multiple quantum well structures*", Appl. Phys. Lett., Vol. 53, p. 86 (1988).

[40] J.S. Weiner, D.S. Chemla, D.A.B. Miller, H.A. Hause, A.C. Gossard, W. Wiegman and C.A. Burrus, "*Highly anisotropic optical properties of single quantum well waveguides*", Appl. Phys. Lett., Vol. 47, p. 664 (1985).

Chapter 3

Modelling and Design Of GaAs/GaAlAs Quantum Well Waveguides

3.1 Introduction:

In this chapter, the theoretical modelling of optical waveguides is described. This includes the effective index method EIM, variational method, and finite difference method. The accuracy of these methods are also discussed. In the second part of this chapter, the design of GaAs/GaAlAs MQW waveguides is studied. This includes the calculation of the excitonic resonant peaks transitions and the refractive index of the MQWs as a function of the well width and height (i.e. Al mole fraction in GaAlAs barrier).

3.2 One-Dimensional Waveguide Theory:

The simplest form of integrated optical components is the passive step-index slab waveguide illustrated in Fig. 3.1. It consists of a dielectric layer of thickness d and refractive index n_2, sandwiched between two semi-infinite layers of refractive indices n_1 and n_3. Layers 1 and 3 are known as the lower and upper cladding regions respectively, and layer 2 as the guiding region. Optical confinement in a such structure is only in the X-direction (transverse direction).

Optical guiding in such structure can be explained by using the geometrical optics. With reference to Snell's law, if a ray is incident upon the structure with an angle θ which is smaller than the critical angle θ_c at either of the two material interfaces, then the ray will experience an internal reflection at the interfaces. If θ is larger than θ_c then the ray will be transmitted to the cladding layers. The critical angle $\theta_{c1,3}$ is given by;

$$\theta_{cl,3} = \sin^{-1}\left(\frac{n_2}{n_{1,3}}\right)$$
(3. 1)

The slab waveguide can be analysed by using the simple ray optic approach as well as the more rigorous approach using Maxwell's equations. Both methods are consistent and have been described in many text books [1-3], therefore only the latter approach is outlined in this chapter.
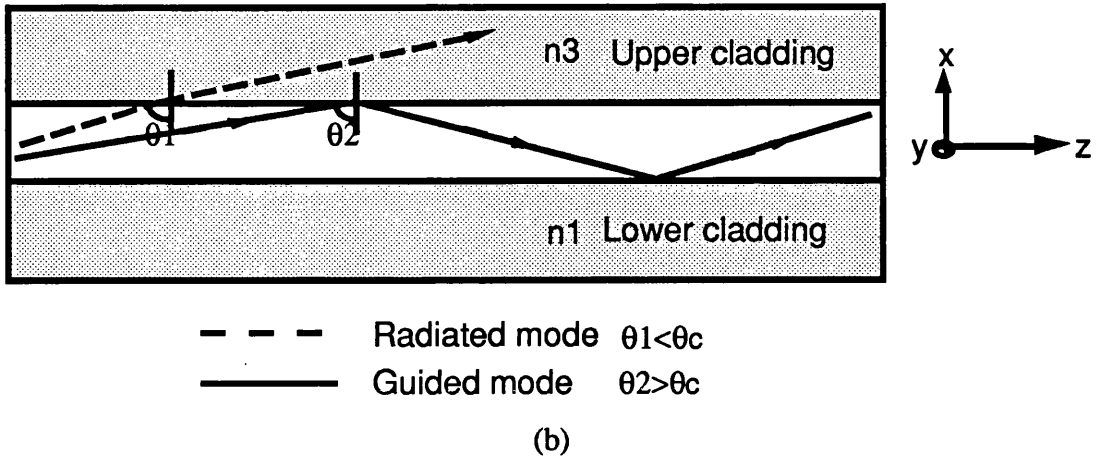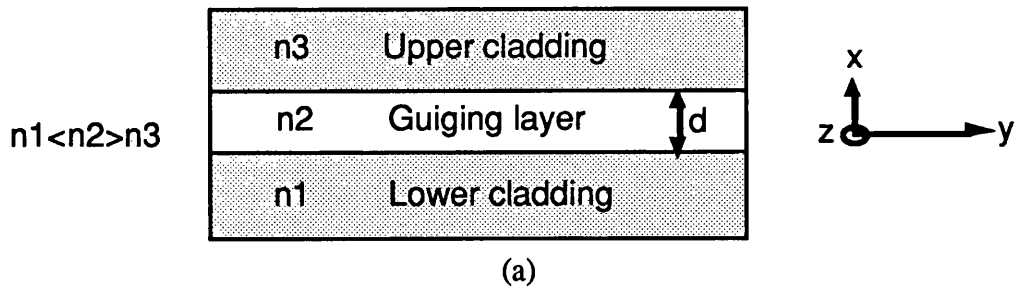
Fig. 3.1 *Schematic diagrams of* (a) *passive step-index slab waveguide* (b) *the guided and radiated modes.*

3.2.1 Maxwell's Equations:

Maxwell's equations in an isotropic, homogeneous and source free medium can be written as;

$$\nabla \cdot D = 0 \qquad\qquad \nabla \cdot B = 0$$

$$\nabla \times E = -\mu \frac{\partial H}{\partial t} \qquad\qquad \nabla \times H = \epsilon \frac{\partial E}{\partial t}$$

where

D: electric displacement ($D = \epsilon E$).

B: magnetic displacement ($B = \mu H$).

E and H: electric and magnetic field vectors.

ϵ and μ: permittivity and permeability of the medium.

In a nonmagnetic medium $\mu = \mu_0$, where μ_0 is the permeability of free space and in a lossless medium $\epsilon = \epsilon_0 \epsilon_r = \epsilon_0 n^2$, n is a real number representing the refractive index of the medium and ϵ_0 is the permittivity of free space.

For a monochromatic wave travelling in the Z-direction, the $\underline{E}$ and $\underline{H}$ fields take the following forms:

$$\underline{E} = \underline{E}(x, y) e^{i(\omega t - \beta z)} \qquad (3.2)$$

$$\underline{H} = H(x, y) e^{i(\omega t - \beta z)} \qquad (3.3)$$

where ω is the angular frequency and β is the propagation constant in the Z-direction. Combining Maxwell's equations, the electric field (or its magnetic equivalent) wave equation is given by:

$$\nabla^2 E(x, y) + \omega^2 \mu \, \epsilon E(x, y) = 0 \qquad (3.4)$$

In the one dimensional slab waveguide, shown in Fig 3.1, two self consistent types of solutions exist where $\partial/\partial y = 0$. The first is referred to as transverse electric field TE with zero component in the Z-direction, its finite components are E_y, H_x and H_z. The second is referred to as transverse magnetic field TM and contains only H_y, E_x and E_z components. Therefore, for the TE mode, Eq.(3.4) is reduced to the form:

$$\frac{\partial^2 E_y}{\partial x^2} + \left(n_i^2 k_0^2 - \beta^2 \right) E_y = 0 \qquad (3.5)$$

and for the TM-mode:

$$n_i^2 \frac{\partial}{\partial x} \left[\frac{1}{n_i^2} \cdot \frac{\partial H_y}{\partial x} \right] + \left(n_i^2 k_0^2 - \beta^2 \right) H_y = 0 \qquad (3.6)$$

where

$$k_0^2 = \mu_0 \, \epsilon_0 \, \omega^2$$

n_i is the refractive index of the ith layer. If n_i is constant within each layer, then Eq. (3.5) and (3.6) are written as:

$$\frac{\partial^2 \psi_y}{\partial x^2} + \left(n_i^2 k_0^2 - \beta^2 \right) \psi_y = 0 \qquad (3.7)$$

where $\psi_y = E_y$ or H_y.

Applying the boundary conditions to Eq. (3.7) for guided modes in the slab waveguide lead to the dispersion relations which contain all the parameters required to define the behaviour of light in the slab. The boundary conditions are $\psi_y \to 0$ as $x \to \pm\infty$, E_y and $\partial E_y/\partial x$ (for the TE-mode) and H_y and $(1/n_i)(\partial H_y/\partial x)$ (for the TM-mode) are continuous at each interface. The dispersion relations for the TE- and TM-mode are:

$$k_2 d = \tan^{-1}\left[\frac{\eta_1 k_1}{\eta_2 k_2} \right] + \tan^{-1}\left[\frac{\eta_3 k_3}{\eta_2 k_2} \right] + m\pi \qquad (3.8)$$

where

$$k_1 = k_0 \left(n_{eff}^2 - n_1^2 \right)^{1/2} \qquad (3.9)$$

$$k_2 = k_0 \left(n_2^2 - n_{eff}^2 \right)^{1/2} \qquad (3.10)$$

$$k_3 = k_0 \left(n_{eff}^2 - n_3^2 \right)^{1/2} \qquad (3.11)$$

m=0,1,2,3...

$n_{eff}=\beta/k_0$ is the effective refractive index of the guided mode. The terms η_i takes into account the two sets of boundary conditions for the TE- and TM-modes.

$$\eta_i = 1 \qquad \text{for the TE fields.}$$
$$\eta_i = 1/n_i^2 \qquad \text{for the TM fields.}$$

The guided mode solutions can be obtained by solving Eq. (3.7) for discrete modes, where m=0 gives the propagation constant ($\beta=k_0 n_{eff}$) of the fundamental mode. The propagation constant of all the guided modes must lie in the range $n_{1,3}k_0 < \beta < n_2 k_0$. The forms of the fields, the solutions to Eq. (3.7), within each layer is given by:

Layer 1 (x>d)

$$\psi_y = A e^{-k_1(x-d)} \qquad\qquad \beta > n_1 k_0$$

Layer 2 ($0 \leq x \leq d$)

$$\psi_y = B \cos(k_2 x) + C \sin(k_2 x) \qquad \beta \langle n_2 k_0 \qquad (3.12)$$

Layer 3 (x<0)

$$\psi_y = D e^{k_3 x} \qquad \beta \rangle n_3 k_0$$

The field is oscillating in the guiding region d and decays outside it. A, B, C and D are constants. Fig. 3.2 shows a sketch of the three lowest order TE modes of the slab waveguide.

TE0   TE1   TE2
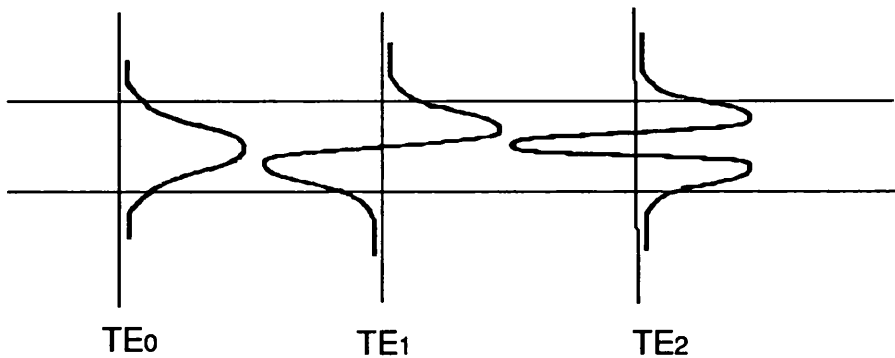
Fig. 3.2 *The transverse electric field profile of the lowest three guided mode.*

The degree of the optical confinement in a waveguide can be represented using the normalised thickness V parameter, where V is given by [4]:

$$V = k_0 d \sqrt{(n_2^2 - n_1^2)} \qquad (3.13)$$

V parameter can be adjusted by either changing the guiding layer thickness or changing the refractive index difference between the guiding and cladding layers. Therefore the optical confinement can be increased by either increasing the guiding layer thickness or, for a thin guiding layer, increasing the step index difference between the guiding and the cladding layers. The increase in the optical confinement, generally, results in an increase in the number of the guided modes. In the case of a symmetrical slab waveguide (i.e. $n_1 = n_3$), $V < \pi$ for a single mode guide.

The cut-off thickness for the TE guided mode to be radiated to the substrate is when $n_{eff}=n_1$, and is given by:

$$d_{cut-off} = \frac{1}{2\pi} \cdot \frac{\lambda_0}{\sqrt{\left(n_2^2 - n_1^2\right)}} \tan^{-1}\left[\frac{k_3}{k_2}\right] + m\pi \qquad (3.14)$$

Theoretically, this means that a symmetrical slab waveguide always support at least one TE-mode even with zero guiding layer thickness.

In a multilayer slab waveguides, the dispersion relations of the modes can be derived using the transfer matrix method [5]. For the four layers slab waveguide shown in Fig. 3.3, the dispersion relation is given by:

$$k_2 d_2 = \tan^{-1}\left[\frac{\eta_1 k_1}{\eta_2 k_2}\right]$$

$$+ \tan^{-1}\left[\frac{\eta_3 k_3}{\eta_2 k_2} \cdot \frac{(\eta_3 k_3 + \eta_4 k_4)e^{k_3 d_3} - (\eta_3 k_3 - \eta_4 k_4)e^{-k_3 d_3}}{(\eta_3 k_3 + \eta_4 k_4)e^{k_3 d_3} + (\eta_3 k_3 - \eta_4 k_4)e^{-k_3 d_3}}\right]$$

$$+ m\pi \qquad (3.15)$$

where

$$k_4 = k_0\left(n_{eff}^2 - n_4^2\right)^{1/2} \qquad (3.16)$$

n4	Top caldding
n3	Upper cladding d3
n2	Guiaing layer d2
n1	Lower cladding d1
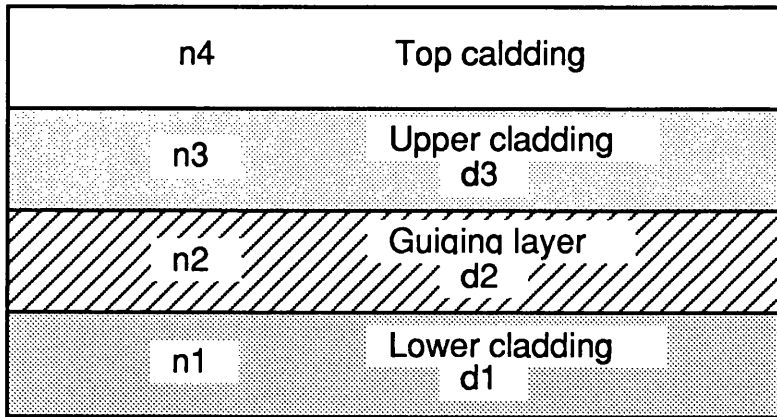
Fig. 3.3 *Schematic diagram of four layers slab waveguide.*

It is possible to use Eq. (3.15) in a three layers slab waveguide, by setting $d_3 = 0$. By applying this equation to a four or three layers waveguide, an optimum design for a single mode waveguide geometry can be achieved. A computer program in turbo pascal was written by Dr. B. Buhambra to calculate the propagation constant of a given mode from the dispersion equation by using the Bisection Method [6].

3.3 Two-Dimensional Waveguide Theory:

The planar waveguide discussed in the previous section is useful in many integrated optic applications in spite of the fact that it provides confinement of the optical field in only one dimension. However, other applications require optical confinement in two dimensions. Strip waveguides which confine light in both directions perpendicular to the propagation direction are used. There are many different methods of obtaining such two-dimensional confinement, and Fig. 3.4 shows several different step-index, rectangular waveguide structures. The embedded channel guide laterally confines light through its real lateral refractive index step. In the rib and strip loaded guides, lateral confinement occurs due to the high refractive index under the ridge.
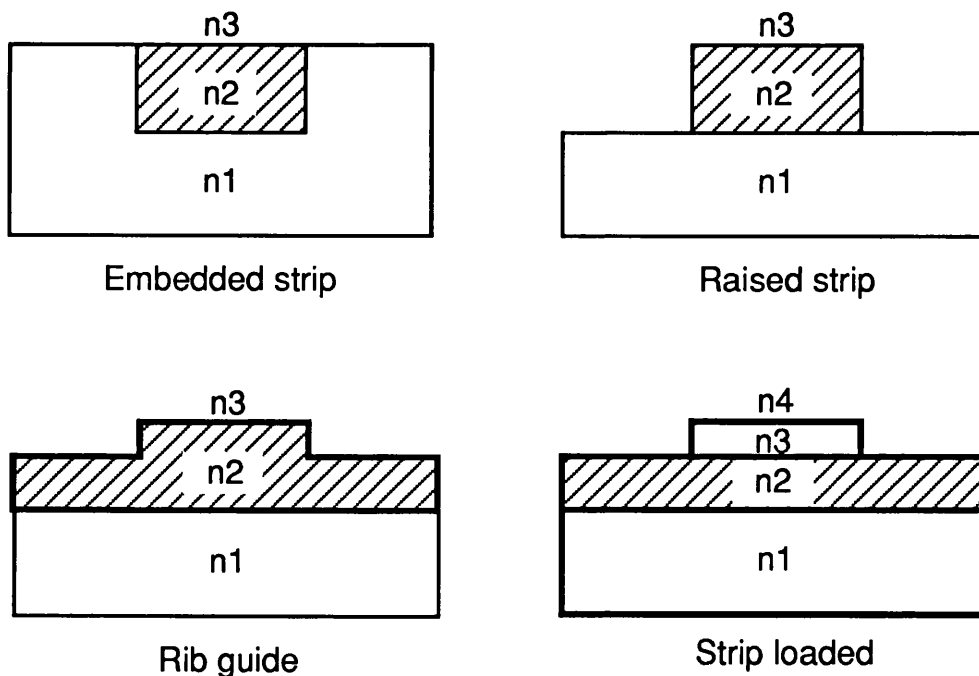
Fig. 3.4 *Cross section of four types of strip waveguides.*

In the one-dimensional slab waveguides, the wave equation was solved with no approximations. One uses solutions to the vector wave equations of the electric field or magnetic field inside and outside the slab and matches the boundary conditions on the slab surfaces, giving the eigenvalue equations for the TE and TM modes. This is often carried over to two-dimensional guides but it is not strictly correct.

The rectangular two-dimensional waveguide is far more complex structure to analyse than the slab guide. This is due to the propagating modes being hybrid (TE-TM), and pure TE or TM modes being impossible in these structures. To overcome this particular problem, a full vector analyses is necessary [7]. This requires a great deal of computer time to find the solutions.

During the term of this work, three different approaches have been used to obtain approximate solutions. The first approach was to reduce the two-dimensional problem into two one-dimensional problems by using the effective index method EIM [8,9]. The second approach was to use a numerical calculation to the variational version of the scalar wave equation to obtain an estimate of both, the modal propagation constant and the modal field profile [10]. The third approach was to solve the vector wave equation and obtain the solution for the modal propagation constant and the field profile [11]. The three methods are outlined in this chapter and a comparison is made between them.

3.3.1 Effective Index Method:

EIM is an approximate method which converts the analyses of a two-dimensional waveguide into two one-dimensional problems. This is illustrated in Fig. 3.5. The rib waveguide cross-section is divided into three regions each represents a slab waveguide of finite width. Regions I and III are slab guides of thickness t and region II a slab guide of thickness d. The effective refractive indices for each region are then found using the model of the slab guide described in section 3.2. These effective indices are then used in an equivalent symmetric three media slab guide with a thickness W to find the effective index of the original rib waveguide.

If one applied the TE boundary conditions in the first part of the problem, then the TM boundary conditions should be applied in the second part and vice versa. However, for guides with small index difference between media there is only a marginal difference in results when using TE or TM boundary conditions in the lateral direction. The disadvantages of the EIM are that, it can not be used to obtain the field intensity distribution. A plot of the modal field distribution is useful since it shows qualitatively the

degree of confinement and how this is affected as the waveguide geometry is altered. Another disadvantage is the EIM becomes progressively more inaccurate as t decreases and breaks down completely when t is below cutoff.
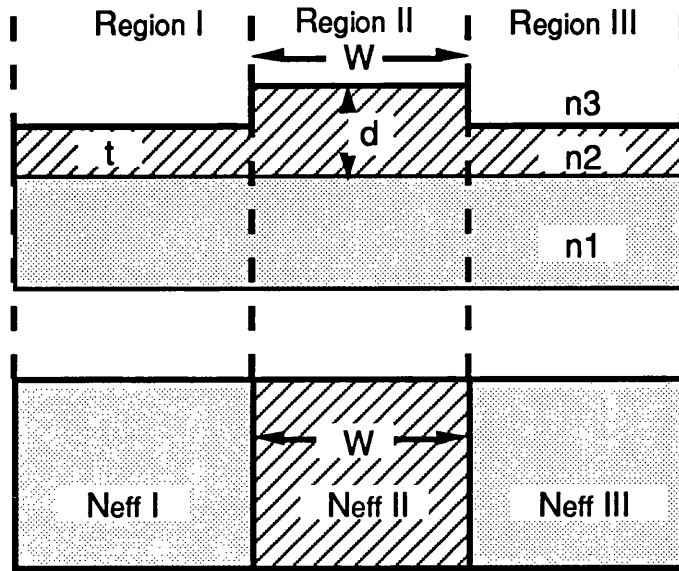
Fig. 3.5 *Configuration of the rib waveguide for the effective index method analysis.*

3.3.2 The Variational Method:

The variational method provides an analytical procedure for obtaining solutions in the form of functions which are close to the exact solution of the boundary value problem. For a boundary value problem in two dimensional space, the general variational problem is:

$$F(\psi) = \iint_R J(\psi) \, dR \qquad (3.17)$$

where $\psi(x,y)$ is specified on the boundary ∂R of the domain R in which the solution is required. Substitution of various trial functions, ψ, into the variational expression yields approximation to the functional, $F(\psi)$. The trial function which produces a stationary functional as ψ is varied, i.e. $\partial F/\partial \psi = 0$, is the best approximate solution for the form of trial function used.

The Rayleigh-Ritz method is used to find the extremum of the functional, here the trial function to be put in the variational expression is a linear combination of Ritz basis functions ψ_i, i=1,2,3,...,n:

$$\psi = \sum_{i=1}^{n} a_i \psi_i \tag{3.18}$$

where a_i are variable scalar parameters known as the Ritz parameters. To find the best combination of ψ_i, the functional is differentiated with respect to any one a_i to give $\partial F/\partial a_i$. The best minimizing combination gives $\partial F/\partial a_i=0$. This is true for all a_i and therefore there are n such equations (with i=1,2,3,...,n) in n unknowns ($a_1,a_2,...,a_n$). The solution to these equations gives an approximate solution to ψ.

NWAVE:

NWAVE is a computer program based on the variational method described above. This variational method yields accurate solutions of the propagation constants and is capable of analysing isolated rib waveguides as well as directional couplers. The analysis was developed by Prof. C.D.W. Wilkinson and Dr. J.A.H. Wilkinson and later modified by R.G. Walker to model the step-index strip waveguides [12].

NWAVE program solves the Helmholtz scalar wave equation for quasi-TE modes:

$$\nabla^2_{x,y} E_y + k_0^2 \left[n^2(x,y) - n^2_{\text{eff}} \right] E_y = 0 \tag{3.19}$$

where

$$E_y = E_y(x,y) \qquad \text{and} \qquad \nabla^2_{x,y} = \left(\partial^2 / \partial x^2 \right) + \left(\partial^2 / \partial y^2 \right)$$

The Raleigh-Ritz procedure is used with a variational expression to obtain the solution to the wave equation. The scalar variational expression which is used for the propagation constant can be restated as follows [13]:

$$F(E_y) = \beta^2 = \frac{\int\int_{-\infty}^{\infty} \left(\nabla^2 E_y + k^2(x,y) E_y \right) E_y \, dxdy}{\int\int_{-\infty}^{\infty} E_y E_y \, dxdy} \tag{3.20}$$

The trial function $\psi(x,y)$ selected to approximate E_y is a series of orthogonal basis functions. The basis functions used are the parabolic cylinder (Hermite-Gaussian) functions. These functions resemble the modes of a waveguide. They go to zero at $\pm\infty$ and are orthogonal. Because a dimensional field is required, each term of the series is a product of an x-direction and a y-direction function. These functions are scaled and normalised and because the waveguide is asymmetric about the y-axis, a zero shift y_0 is required. The trial function is substituted for E_y in the variational expression, in Eq. (3.20). The coefficients a_{ij}, in Eq.(3.18) for two dimensional case, are then varied until a stationary value of the variational expression is obtained. This is done by simultaneously setting $\partial F/\partial a_{ij}=0$ for all i, j.

Although the trial function may more closely approximate E_y by using more and more basis functions, the computational time increases approximately as the square of the product of the basis functions in the x and y directions. Therefore the number of basis functions must be minimized but also must be selected to yield eignvalues of the required accuracy. 10 basis functions in the y direction and 8 in the x direction give accurate results, to the fifth decimal, for an isolated rib waveguide. While for a directional coupler 9 basis functions in the y direction and 14 basis functions in the x direction.

Results:

As mentioned in the previous section, the accuracy of the effective index method decreases as the discontinuities at the sides of the guide become more pronounced and the method breaks down completely when the slab thickness is below cut-off. The effect of increasing the relative height of the rib by etching away more and more of the adjacent slab layer was studied using the variational program. As well as increasing the optical confinement, this has the effect of decreasing the propagation constants of the guided modes and hence reducing the number of allowable modes in the waveguide. Table 3.1 gives the effective indices of the quasi-TE guided modes of a rib waveguide with W=2 μm, as shown in Fig. 3.6, as a function of the slab height t, calculated at wavelength λ=1.15 μm. As can be seen, decreasing t decreases the effective indices and the number of guided modes. These results were obtained by using 10×7 basis functions in the y- and x-directions, respectively.

Fig. 3.7 shows the calculated effective refractive index of the fundamental TE guided mode as a function of the adjacent slab height for different rib width W. As the rib width decreases, the waveguide becomes single mode at shallower etching depth (smaller rib height).

43
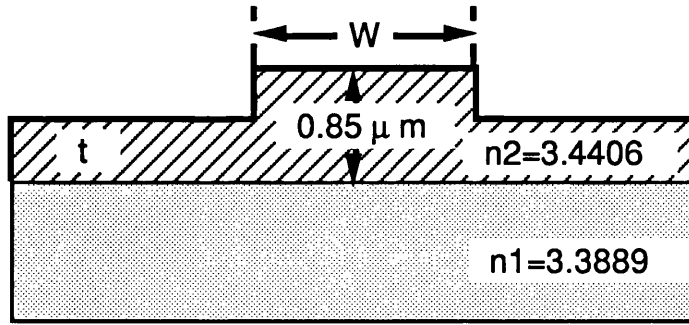
Fig. 3.6 *Schematic diagram of rib waveguide with* W=2 μm.

Table 3.1: *The effective refractive index of the first five guided mode of a GaAs/GaAlAs rib waveguide as a function of the adjacent slabs thickness t.*

t (mm)	TE_0	TE_1	TE_2	TE_3	TE_4
0.75	3.40612	3.40314	3.40222	3.40009	3.39726
0.65	3.40424	3.39618	3.39330	3.38924	
0.55	3.40270	3.38995			
0.45	3.40147				
0.35	3.40046				
0.25	3.39960				
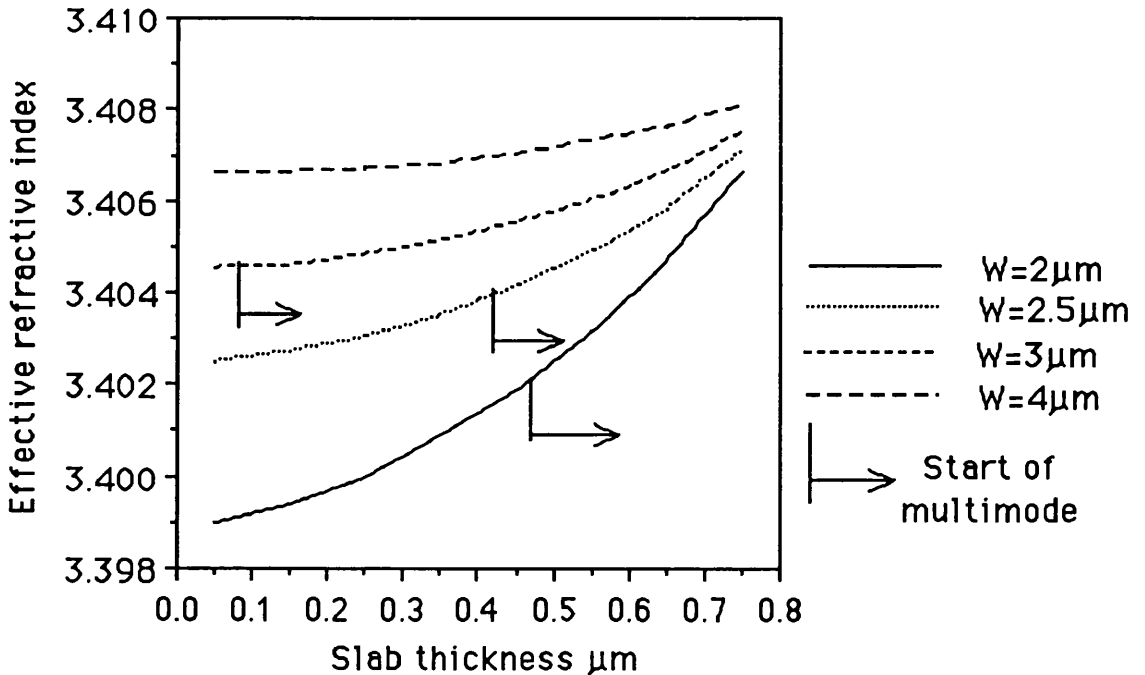
Fig. 3.7 *The effective refractive index of the* TE_0 *mode as a function of the adjacent slab thickness* t *for different rib width* W *of the waveguide shown in Fig. 3.6, calculated by* NWAVE *program.*

44

The modal field distribution for two different waveguide geometries are shown in Fig. 3.8, the rib width W=2 μm and the adjacent slab thickness t=0.5 μm, Fig. 3.8a, and t=0.2 μm, Fig. 3.8b. As can be seen, increasing the relative height of the rib increases the optical confinement.
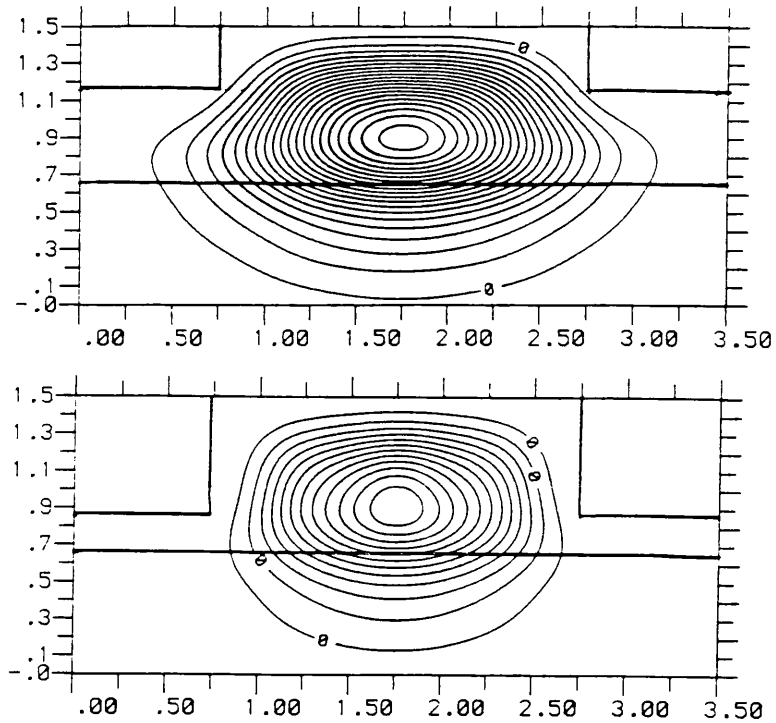
Fig. 3.8 *The modal field distributions for two different waveguide geometries (using NWAVE program) with rib width W=2 μm and height:* a) *t=0.5 μm and* b) *t=0.2 μm*

3.3.3 The Finite Difference Method:

In the finite difference method, the waveguide cross-section is divided into a large number of mesh points. The distances between neighbouring points are Δx and Δy in the x- and y-directions, respectively. The function $E_y(x,y)$ is replaced by discrete values of E_y at mesh points only and the partial derivatives of Eq. (3.4) by the expressions:

$$\frac{\partial^2 E_y}{\partial x^2} = \frac{E(I+1, J) + E(I-1, J) - 2E(I, J)}{(\Delta x)^2}$$

(3.21)

$$\frac{\partial^2 E_y}{\partial y^2} = \frac{E(I, J+1) + E(I, J-1) - 2E(I, J)}{(\Delta y)^2}$$

(3.22)

at the point $(I\Delta x, J\Delta y)$. Substituting Eq. (3.21) and (3.22) into Eq. (3.19) and rearranging for $E(I,J)$ gives:

$$E(I, J) = \frac{E(I+1, J) + E(I-1, J) + R^2\{E(I, J+1) + E(I, J-1)\}}{2(1 + R^2) - k_0^2(\Delta x)^2 \cdot \{N^2(I, J) - N_{eff}^2\}}$$

$$(3.23)$$

where $R = \Delta x / \Delta y$, $N(I,J)$ is the refractive index at the point $(I\Delta x, J\Delta y)$ and N_{eff} is the effective refractive index of the guide. A typical program can begin with an arbitrary field distribution $E(I,J)$, which is integrated using the variational expression Eq. (3.20) to provide the first estimate of the effective index $N = \beta/k_0$. This in turn, can be used in Eq. (3.23) to modify the electric field distribution. The iteration is repeated until E and N converged to the final values determined by the required accuracy.

FWAVE Program:

FWAVE is a computer program developed by Michael Tayler of this Department, to calculate the field and the refractive index at discrete mash points over the cross-sectional area of the waveguide. Effective index method EIM was used at first to estimate the initial field distribution. More accurate results of the field distribution and effective refractive index can be achieved by reducing the mesh size. This increases the computing time significantly, therefore to model waveguides with thin layers (e.g. MQWs) requires a large computing time.

Dr. Kader Dendane of this Department modified the program to calculate the field distribution and effective indices of guided modes in waveguides with thin layers (e.g. MQW waveguides). This was achieved by dividing the waveguide cross-sectional area into a nonuniform mesh with small mesh size at the thin layers. With this way, the computing time was reduced significantly.

A modal field distribution and the waveguide geometry are shown in Fig. 3.9 for GaAs/GaAlAs rib waveguide at a wavelength $\lambda = 1.15$ μm. Fig. 3.9a and 3.9b show the lowest (fundamental) TE- and TM-modes and Fig. 3.9c shows the next possible first order TE-mode of the guide, the slab thickness $t = 0.5$ μm.

In the next section, a comparison between the three methods of modelling rib waveguides is discussed.
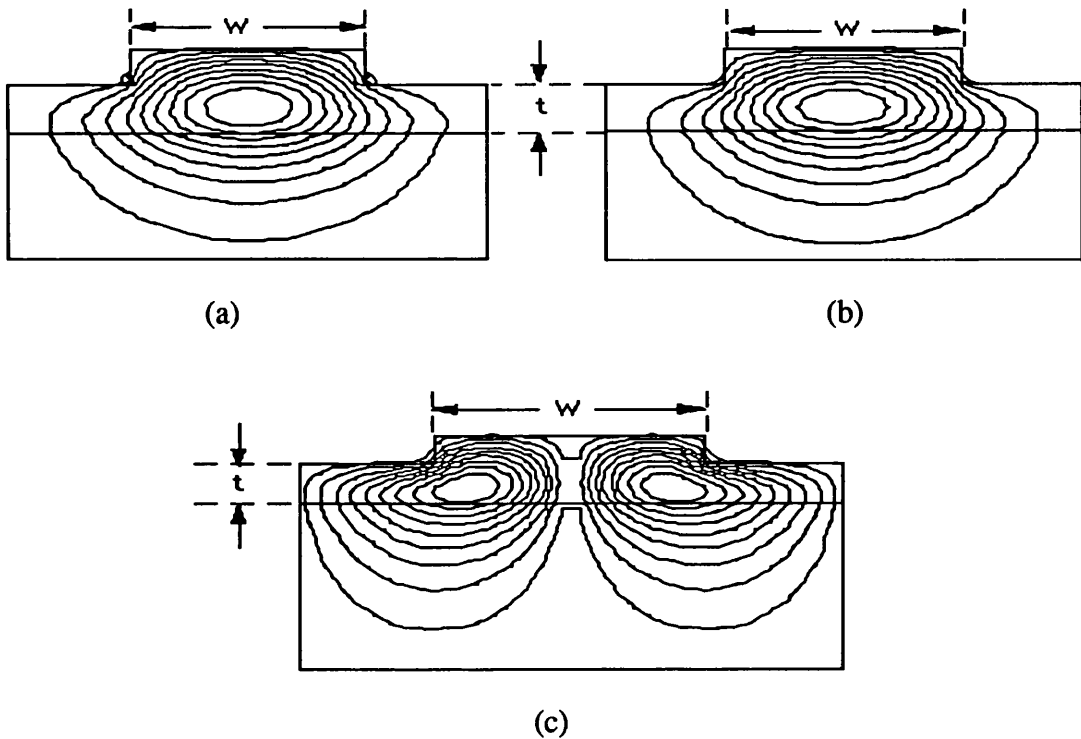
Fig. 3.9 *The modal field distributions of rib waveguide (using FWAVE program)*
with rib width W=2 μm for: a) TE_0 *mode* b) TM_0 *mode* c) TE_1 *mode.*

3.4 Comparison of the Three Models of Two-Dimension Waveguides:

The three methods of modelling rib waveguides, effective index method, variational method and finite difference method were compared. Fig. 3.10 shows the effective index of the fundamental TE mode of the rib waveguide, shown in Fig. 3.6, as a function of the adjacent slab thickness t at a wavelength $\lambda=1.15$ μm. The difference between the effective refractive indices calculated by the EIM and NWAVE program increases as the effective height of the rib increases. When the adjacent slab thickness was just above cut-off (t=0.45μm), the difference was 0.0032. Numerous guides have been analysed and the effective index method always predicated values which are higher than those predicated by the NWAVE program.

The effective indices predicated by using the finite difference method (FWAVE program) showed no significant difference with that predicated by NWAVE program, as shown in Fig. 3.10. Although the two methods are capable of yielding accurate solutions and provide the modal field distribution, the variational method does not require extensive computer calculations.
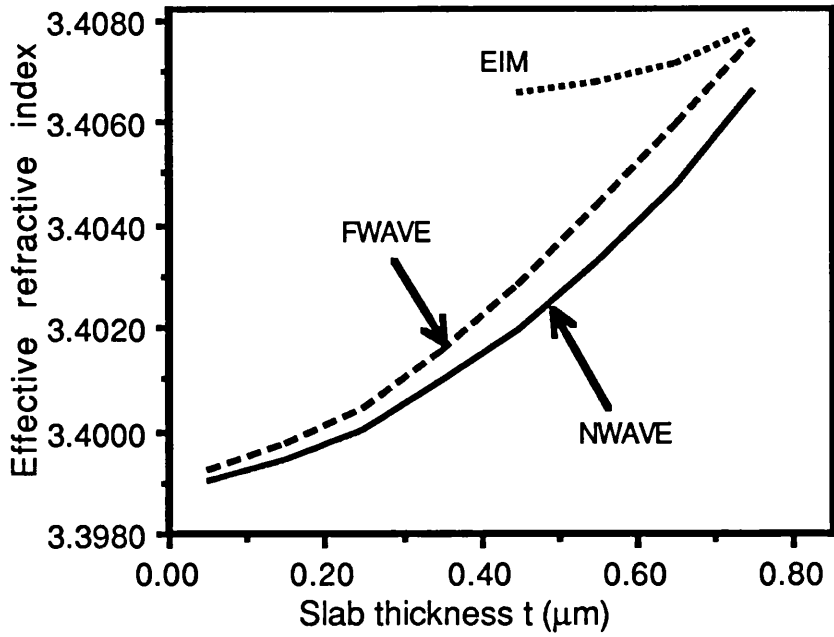
Fig. 3.10 *The effective refractive index of the TE_0 mode as a function of the adjacent slab thickness t for the waveguide shown in Fig. 3.6, calculated by using* EIM, NWAVE *and* FWAVE *programs.*

3.5 GaAs/GaAlAs Semiconductor Waveguides:

We have seen that the transverse optical confinement in waveguides is obtained in the layer of higher refractive index (guiding region). In GaAs semiconductor waveguides, the transverse refractive index change can be achieved by two means; either by changing the free carriers concentration [14] or the material composition as in the case of GaAs/GaAlAs waveguides [15]. The later approach was used in our waveguides.

GaAs and AlAs have a similar lattice constant and therefore Ga may be substituted by Al to alter the refractive index (and bandgap) without creating a substantial lattice mismatch. In the ternary system $Ga_{1-x}Al_xAs$, the bandgap increases and the refractive index decreases as the Al concentration is increased. A slab waveguide can therefore be formed by growing a GaAs guiding layer on a lower index buffer layer of GaAlAs. The change in the refractive index as a function of Al concentration is given by [15]:

$$n(x) = \left[A - 2.92x + \frac{B}{\lambda_0^2 - C(x)} - D(x)\lambda_0^2\right]^{1/2} \qquad (3.24)$$

48

where:

λ_0 :operating wavelength (μm)

A   =10.906

B   =0.97501

C   =$(0.52886 - 0.735x)^2$ x≤0.36

      =$(0.30386 - 0.105x)^2$ x>0.36

D   = 0.002467(1.41x + 1)

Figure 3.11 shows the variation of the refractive index of GaAlAs as a function of Al concentration.
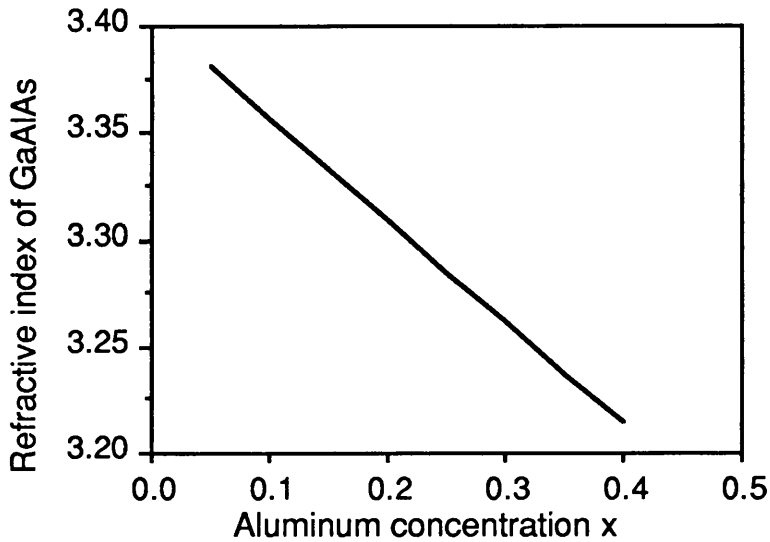
Fig. 3.11 *The change in refractive index of* $Ga_{1-x}Al_xAs$ *as a function of Al mole fraction* x.

The variation of the bandgap of GaAlAs with Al mole fraction is given by [16]:

$$E_g(x) = 1.424 + 1.594x + x(1-x)(0.127 - 1.3 \bar{x}) \qquad (3.25)$$

The knowledge of the band structure and refractive index of GaAlAs as a function of Al mole is important in designing quantum well waveguides, as we will see later in this chapter.

49

At a given wavelength single-mode GaAs/GaAlAs waveguides can be designed by a proper choice of the Al concentration in the cladding layer and thickness of the guiding layer. Fig. 3.12 shows the cut-off thickness of the first three TE modes, calculated using Eq. (3.14), as a function of the Al mole fraction in the GaAlAs cladding layer, at a wavelength $\lambda=1.15$ μm. It shows that by reducing either the Al concentration in the cladding layer (i.e. reducing the step index between GaAs and GaAlAs) or the thickness of GaAs guiding layer, a single mode waveguide can be obtained.
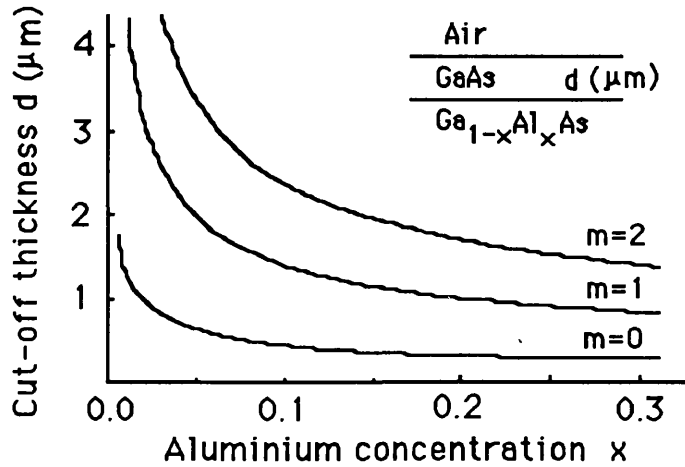
Fig. 3.12 *Plot of the cut-off thickness of a GaAs guiding layer as a function of the aluminium concentration, for various modes.*

3.6 GaAs/GaAlAs Quantum Well Waveguides:

In these structures the optical field is confined in a guiding region with QWs. This is due to the enhanced optical nonlinearity in QWs over that of the bulk material, as described in section 2.3.2. The design of MQW waveguides requires a knowledge of the resonant absorption peaks and refractive index of the MQW layers. In this section the excitonic energies and refractive index of MQW structures are determined as a function of the QW parameters (i.e. well width and height).

Excitonic Absorption Energies in GaAs/GaAlAs MQWs:

In GaAs/GaAlAs MQW structures, thin GaAs layers are sandwiched between GaAlAs layers. Owing to the larger bandgap of the GaAlAs, Eq. (3.25), virtually all the absorption

takes place in the GaAs well. Hence the absorption mechanisms in bulk GaAs are applied for the MQW layers. However, due to the small size of GaAs wells, two important differences emerge. Firstly, the electrons and holes, trapped within the wells in the direction perpendicular to the well walls, have a quantised energy levels (as discussed in section 2.3.2). Therefore the density of states distribution is altered and the bandgap energy of the GaAs wells is widened (i.e. shift to higher energy). The other effect is the increase in the exciton binding energy. The binding energy E_{ex} of exciton in MQWs is about four times larger than that of bulk material [17].

The exciton transition energies in GaAs/GaAlAs MQWs was calculated using a Turbo Pascal computer program called XTON written by Dr. B. Buhambra [18]. The program calculates the energy levels of the electrons (in the conduction band) and holes (in the valence band) in a single finite potential well, as described in section 2.3.2. The exciton energy is then calculated by summing the energies of the electron level and hole level and temperature dependent of GaAs bandgap. The hh- and lh-excitons binding energies are calculated and subtracted from the sum. Fig. 3.13 shows a schematic diagram of the energy levels in the conduction and valence bands of GaAs well.
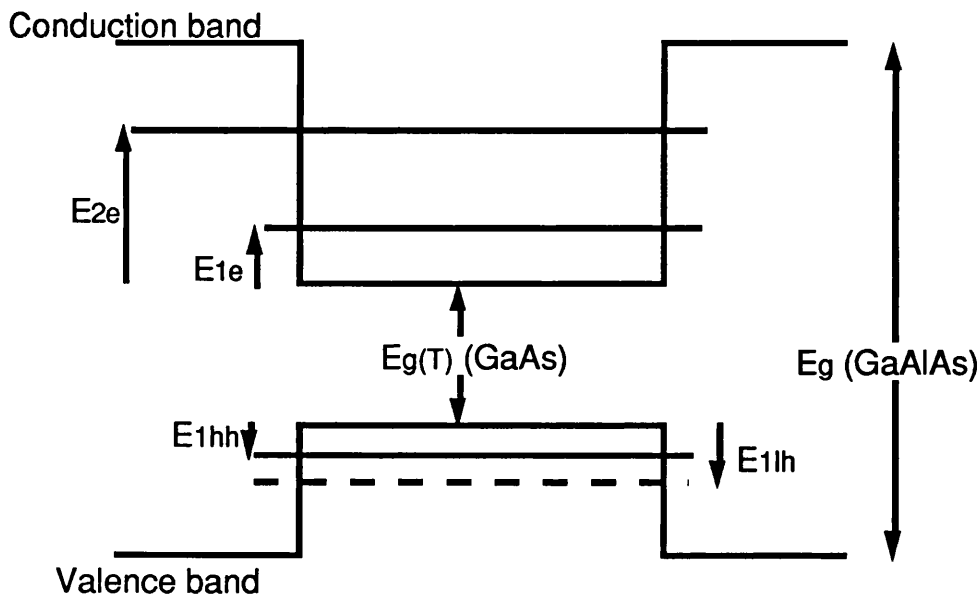
Fig. 3.13 *Schematic diagram of the energy levels in the conduction and valence band of GaAs/GaAlAs quantum well.*

The parameters used in the XTON program are outlined below:

*The temperature dependent of the energy band in GaAs is given by [19]

5 1

$$E_g(T)_{GaAs} = 1.519 - \frac{5.405 \times 10^{-4} T^2}{204 + T} \quad (eV) \qquad (3.26)$$

*The conduction and valence band offsets for GaAs well with $Ga_{1-x}Al_xAs$ barrier (where x<0.45) are [20]

$$V_v = 0.55x\Delta E_g \qquad (3.27)$$

$$V_c = (1 - 0.55x)\Delta E_g \qquad (3.28)$$

where ΔE_g is the difference between the well and barrier bandgaps.

*The Al dependent bandgap of $Ga_{1-x}Al_xAs$ is given in Eq. (3.25).

*The effective mass of electron in the conduction band, and hh and lh in the valence band as a function of Al concentration are given by [21,22]

$$m_e^*(x) = 0.0665 + 0.0835x \qquad (3.29)$$

$$m_{hh}^*(x) = 0.34 + 0.45x \qquad (3.30)$$

$$m_{lh}^*(x) = 0.087 + 0.063x \qquad (3.31)$$

*The binding energy of the hh and lh excitons as a function of the well width are given by [23]

$$\text{hh-exciton BE (meV)} = 14.47 - 0.0645L - 0.000141L^2 \qquad (3.32)$$

$$\text{lh-exciton BE (meV)} = 15.74 - 0.0611L - 0.000119L^2 \qquad (3.33)$$

where L in Å

The above parameters were used with the finite square well theory to calculate the expected bound state energies of the QWs used in this work.

The effect of changing the well width and barrier height on the quantization energy levels in the conduction and valence bands are investigated. Fig. 3.14a,b shows the calculated electron energy level (from the bottom of the conduction band) and the hh and lh energy levels (from the top of the valence band). These energy levels shift to higher energy as the well width decreases and the barrier height increases. Fig. 3.15a,b shows the hh- and lh-excitonic binding energies (meV) and the transition energies (eV) as a function of the well

width. From these results it was possible to tune the excitonic transition energies in GaAs/GaAlAs quantum wells by varying the well width and barrier height. Although narrower wells enhance the binding energies of excitons, in practice the excitons resonant peaks becomes broader due to the fluctuation in the well width.

(a)   (b)
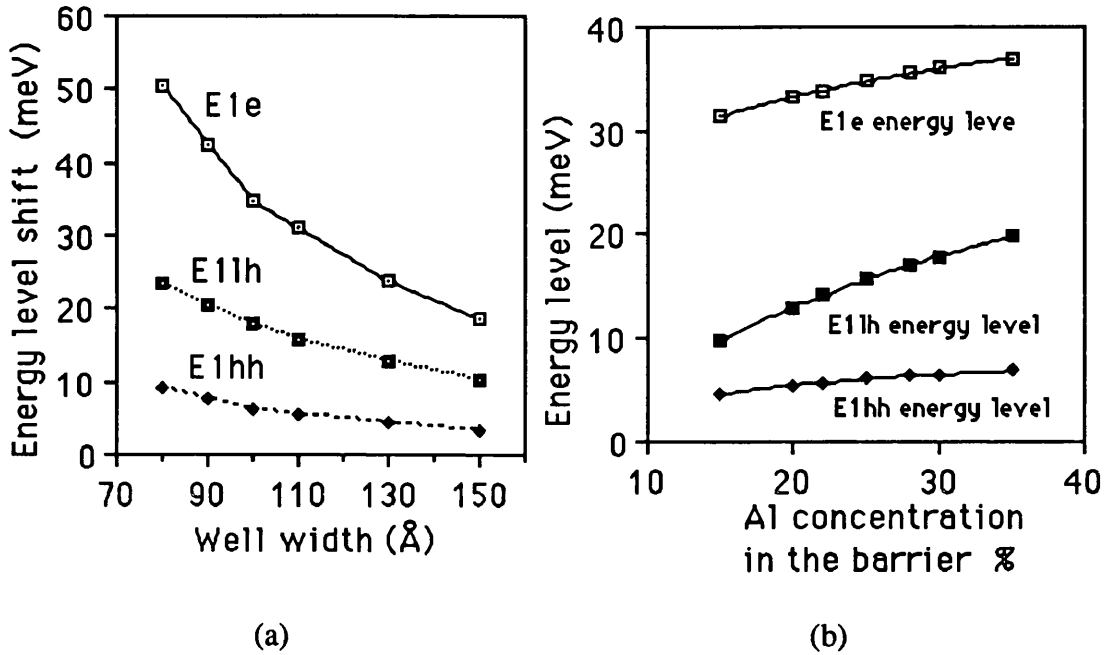
Fig. 3.14 *The energy shift of the 1e (with respect to the bottom of the conduction band), and 1hh and 1lh (with respect to the top of the valence band) as a function of the* a) *well width* b) *barrier height.*

(a)   (b)
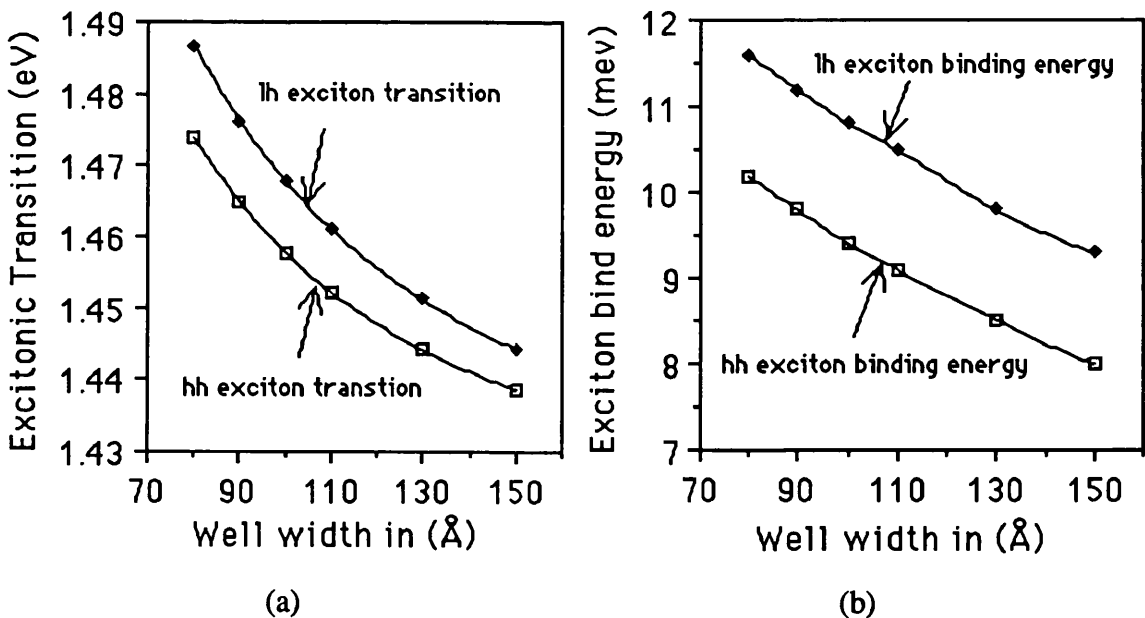
Fig. 3.15 a) *The hh- and lh-excitonic transitions and* b) *binding energies as a function of the well width.*

Refractive Index of GaAs/GaAlAs MQWs:

The effective refractive index of the MQW structure, with well width L_w and refractive index n_w and barrier width L_b with refractive index n_b, is given by [24]:

$$n_{TE} = \left[\frac{n_w^2 L_w + n_b^2 L_b}{L_w + L_b} \right]^{1/2} \tag{3.34}$$

$$n_{TM} = \left[\frac{n_w^2 n_b^2 (L_w + L_b)}{L_w n_b^2 + L_b n_w^2} \right]^{1/2} \tag{3.35}$$

for light field polarised parallel to and perpendicular to the QW layers, respectively. The polarisation dependence of these equations is due to the difference in boundary conditions for the two situations. The refractive index for the TE polarisation is greater than that for the TM polarisation ($n_{TE} > n_{TM}$).

Although FWAVE program, described in section 3.3.3, is capable to model MQW stripe waveguides with large number of layers (about 100 layer) and handle thin layers (≈ 20 Å). The computing time was reduced dramatically with no significant difference in the results, by using the approximation of the refractive index of the MQW region in Eq. (3.34) and (3.35).

3.7 Conclusions:

The modelling of slab (one-dimension) and rib (two-dimension) waveguides have been described in details. Analytical solution, using EIM, and numerical solution, using the variational and finite difference methods, were obtained for rib waveguides. The accuracy of the predicted solutions were discussed and compared for a given GaAs/GaAlAs waveguide. It was found that the variational method yields an accurate solution and provides a modal field distribution for the two-dimensional waveguide but it does not require extensive computational time.

Design of MQW structures and the method for determining the layers parameters (well width and barrier height) have been outlined. The exciton transition energies were tuned by changing the well width and barrier height.

The effective refractive index of MQW structures was calculated by using an approximate method. This reduced the computation time to find an accurate solution for the MQW rib waveguides, using the finite difference method.

XTON program (to calculate the exciton transition in GaAs/GaAlAs QWs) and NWAVE program (to calculate the propagation constant of the TE modes in rib waveguides) were an effective tools in designing single mode waveguides.

References:

[1] T. Tamir, *"Integrated optics"*, Springer-Verlag, Berlin (1975).

[2] D. Marcuse, *"Theory of dielectric optical waveguides"*, Academic press, New York (1974).

[3] N.S. Kopany and J.J. Burke, *"Optical waveguides"*, Academic press, New York (1972).

[4] H. Kogelnik, V. Ramaswamy, *"Scaling rules for thin-film optical waveguides"*, Appl. Opt., vol. 13, no. 8, p. 1857 (1974).

[5] J. Chilwell and I. Hodgkinson, *"Thin-film field-transfer matrix theory of planar multilayer waveguides and reflection from prism-loaded waveguides"*, J. Opt. Soc. Am. A1, p. 742 (1984).

[6] E. Kreyszig, *"Advanced engineering mathematics"*, 5th Ed., John Wiley and Sons (1983).

[7] M. Koshiba and M. Suzuki, *"Vectorial wave analysis of dielectric waveguides for optical-integrated circuits using equivalent network approach"*, J. of Lightwave Tech., LT4, no. 6, p. 656 (1986).

[8] H. Diestel, *"A method for calculating the guided modes of strip-loaded optical waveguides with arbitrary index profile"*, IEEE J. of Quantum Electronics, QE-20, no. 11, p. 1288 (1984).

[9] G.B. Hocker and W.K. Burns, *"Mode dispersion in diffused channel waveguides by the effective index method"*, Appl. Opt., vol. 16, no. 1, p. 113 (1977).

[10] M. Matsuhara, *"Analysis of TEM modes in dielectric waveguides by a variational method"*, J. of Opt. Soc. Am., vol. 63, no. 12, p. 1514 (1973).

[11] M.S. Stern, *"Semivectorial polarised finite difference method for optical waveguides with arbitrary index profiles"*, Proc. IEE J., vol. 135, p. 56 (1988).

[12] R.G. Walker, C.D.W. Wilkinson and J.A.H. Wilkinson, *"Intergrated optical waveguiding structures made by silver-ion exchange in glass. 1:The propagation characteristics of stripe ion-exchanged waveguides; a theoretical and experimental investigation"*, Appl. Opt., vol. 22, p. 1923 (1983).

[13] A. Sharma, P.K. Mishra and A.K. Ghatak, *"Analysis of single mode waveguides and directional couplers with rectangular cross-section"*, Proceedings of the 2nd European Conference, IEE Conference Publication, p. 9, Florence (1983).

[14] E. Garmire: NEREM 72, *"Proceedings of the solid state circuits"*, p. 115-118, NEREM, Boston (1972).

[15] V. Evtuhov and A. Yariv, *"GaAs and GaAlAs devices for integrated optics"*, IEEE Trans. Microwave Therory Tech., MTT-23, p. 44 (1978).

[16] D.E. Aspnes, S.M. Kelso, R.A. Logan and R. Bhat, *"Oprical properties of $Ga_{1-x}Al_xAs$"*, J. Appl. Phys., vol. 60, no. 2, p. 754 (1986).

[17] D.S. Chemla, D.A.B. Miller, P.W. Smith, A.C. Gossard and W. Weigmann, *"Room-temperature excitonic nonlinear absorption and refraction in GaAl/GaAlAs multiple quantum well structures"*, IEEE J. Quantum Electronic, QE-20, no. 3 (1984).

[18] B. Buhambra, *"Nonlinear optical waveguide devices in GaAs/GaAlAs"*, Ph.D. thesis, Glasgow University (1991).

[19] H. Kawai, K. Kaneko and N. Watanabe, *"Photoluminescence of GaAs/GaAlAs quantum wells grown by metalorganic chemical vapor deposition"*, J. Appl. Phys., vol. 56, no. 2 (1984).

[20] J. Batey, S.L. Wright and D.J. DiMaria, *"Energy band-gap discontinuities in GaAs:(Ga,Al)As heterojunctions"*, J. Appl. Phys., vol 52, p. 484 (1985).

[21] G. Duggan, H.I. Ralph and K.J. Moore, "*Reappraisal of the band-edge discontinuity at the $Al_xGa_{1-x}As/GaAs$ heterojunctions*", Phys. Rev. B32, p. 8395 (1985).

[22] S. Adachi, "*GaAs, AlAs and GaAlAs: material parameters for use in research and device applications*", J. Appl. Phys., vol. 58, R1 (1985).

[23] E.S. Koteles and J.Y. Chi, "*Experimental exciton binding energies in GaAs/GaAlAs quantum wells as a function of well width*", Phys. Rev. B, vol. 37, no. 11, p. 6332 (1988).

[24] R.A. Sammut and I.M. Skinner, "*Effective index models for MQW waveguides*", Opt. Comm., vol. 76, p. 213 (1990).

Chapter 4

Growth and Characterisation Techniques of GaAs/GaAlAs Single and Multiple Quantum Well Materials

4.1 Introduction:

In this chapter, we will high-light the growth techniques used to grow GaAs/GaAlAs single and multiple quantum well structures (SQW and MQW). The linear characterisation techniques of these materials are presented, this includes the photoluminescence and photocurrent spectroscopy. In the last section, we will discuss the band structure disordering of the SQW and MQW materials, this included the impurities induces disordering IID and vacancies induced disordering techniques.

4.2 Growth Techniques:

Epitaxial growth technique allows the fabrication of single-crystalline films for integrated optical devices. It has been a big challenge to material scientists to refine the growth technique such that low loss waveguide devices can be constructed. There are three main techniques to grow epitaxial semiconductor structures, liquid phase epitaxy LPE, metal organic vapour phase epitaxy MOVPE and molecular beam epitaxy MBE. The growth of multiple quantum well structures for optical devices require low loss waveguides with strong quantum properties. In certain cases, crystal defects and impurity concentrations are crucial for low loss waveguide formation. In MQW structures, roughness in the interfaces of the layers increases the scattering loss in a waveguide. The quantum properties require abrupt heterojunctions between layers with fluctuation in wells width being less than a few atomic layers.

LPE can produce high quality materials but abrupt interfaces and thickness control of the layers are difficult to obtain. Therefore the other two techniques (MOVPE and MBE) were used to grow GaAs/GaAlAs QW structures, and are outlined in the following sections.

58

4.2.1 Metal Organic Vapour Phase Epitaxy MOVPE:

In MOVPE, the deposited materials are carried by a gas, usually H_2. For GaAs growth, the gallium source is an organic compound either trimethylgallium (TMG) or triethylgallium (TEG). The arsenic source is normally arsine (AsH_2). For GaAlAs growth, the aluminium source is trimethylaluminium (TMA). The ratio of TMA and TMG mixture determines the Al mole fraction x in $Ga_{1-x}Al_xAs$ layer. Fig. 4.1 shows a schematic diagram of the MOVPE reactor. The TMG and TMA are held in bubbler and hydrogen passes through them to transport the vapour to the reactor, while arsine is held in a gas cylinder. All the gases are mixed and fed into the reactor chamber where the substrate is placed. The substrate is heated to temperatures from 600 °C to 850 °C by mounting it on a graphite susceptor heated with an RF induction coil. The susceptor is tilted at an angle 2°-5° to improve the flow dynamics of the gases in the reactor.
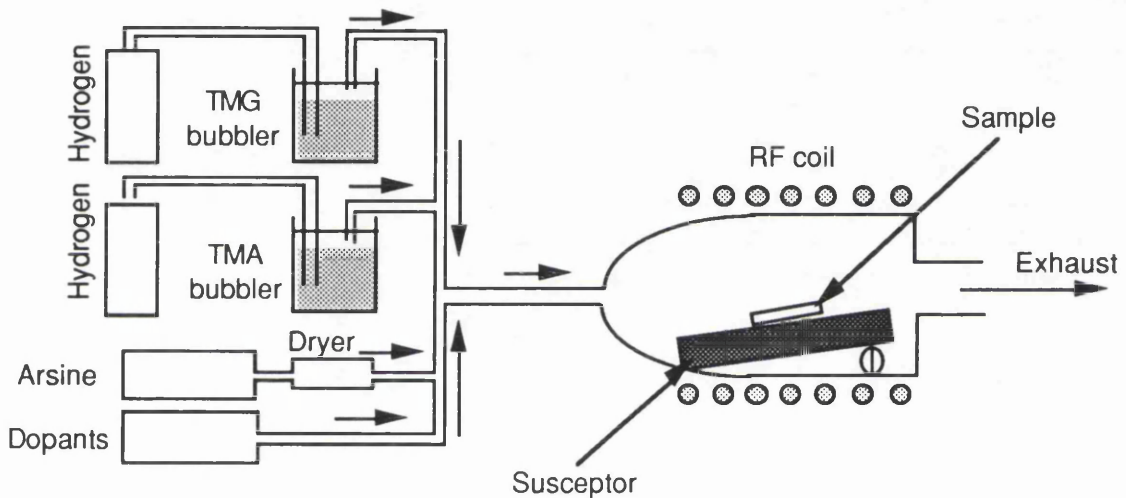
Fig. 4.1 *Schematic diagram of a MOVPE system.*

The deposition rate is slower than that of the LPE method, which allows greater control of thickness and doping profile of each deposited layer. This technique is capable of producing very thin layers with good morphology, and lower cost compared to the MBE growth system.

MOVPE epitaxial materials suffer from two major impurities. First is carbon which is present in the reactor in the form of methyl groups. This some times incorporate into the growth layer, and act as a donor. In GaAs, this can be reduced by reducing the growth temperature to around 600 °C. It is difficult to obtain a doping density lower than 10^{14} cm^{-3} [1]. In GaAlAs, the problem is worse due to the strong Al-C bond. Second is the oxygen incorporation in GaAlAs due to the strong Al-O bond. To reduce the oxygen incorporation,

the reactor must be leak free. One other disadvantage with the MOVPE is that the source chemicals are either extremely toxic or inflammable in air, therefore rigorous safety precautions are required.

4.2.2 Molecular Beam Epitaxy:

Molecular beam epitaxy MBE is a powerful technique for growing single crystal films with precise control of stoichiometry, thickness, growth rate and dopant concentration. Growth is performed in a high-vacuum chamber where the substrate is kept at an elevated growth temperature. Molecular species are evaporated and directed toward the substrate by separate source chambers.

Fig. 4.2 shows a schematic diagram of an MBE system. The compounds or elements are heated in crucibles and deposited onto the surface of the substrate. The growth temperature of the substrate is an important parameter, if it is too low then the deposited atoms will have insufficient motion across the surface to find the best site which may results in poor crystal quality. If the temperature is too high, then the problem of interlayer diffusion may occur and species can be re-evaporated from the surface. For GaAs the growth temperature is from 550 °C to 650 °C and for GaAlAs around 680 °C. The slow growth rates allow process control down to a film thickness of a few atomic layers. An electron gun is used to assess the surface roughness from the diffraction of the high energy electron beam. The electron beam is incident at a very shallow angle to the substrate surface and the diffracted beam form a characteristic pattern on a fluorescent screen (RHEED) which provides an information of the morphology.
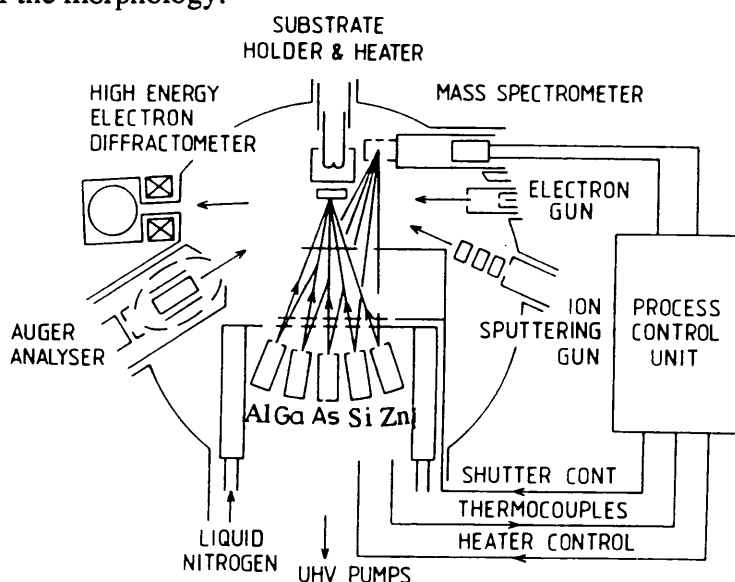
Fig. 4.2 *Schematic diagram of a MBE system (after ref. 27).*

By rotating the specimen at a rate slower than the growth rate of one monolayer, a high uniform growth can be obtained [2].

4.3 GaAs/GaAlAs QW Wafers used in this project:

A number of GaAs/GaAlAs QW and GaAlAs waveguide structures were grown using mainly the MBE technique, at the author's Department. These structures were designed to meet the requirements of electro-optic and all-optical switching devices, e.g. p-i-n, single mode, low propagation losses and large nonlinear optical properties. The wafers included in this chapter has been limited to those used successfully to demonstrate the optical switching devices. The theory to design single mode QW and heterostructure waveguides are presented in chapter 3. The wafers employed are schematically described below with some high lights of the key points in their design:

A187 SQW:

This wafer was grown by MBE technique, and Fig. 4.3 shows a schematic diagram of the layers structure of the A187 SQW wafer. The relatively thick lower cladding layer of $Ga_{0.7}Al_{0.3}As$ was to isolate the evanescent field of the guided mode from the high refractive index GaAs substrate. The SQW was placed only 400 Å below the top surface, this was to enhance the recovery time of the resonant nonlinearity due to the surface recombination of the photogenerated carriers. The price paid in return was that the overlap integral of the SQW with the confined optical field was not at its maximum.
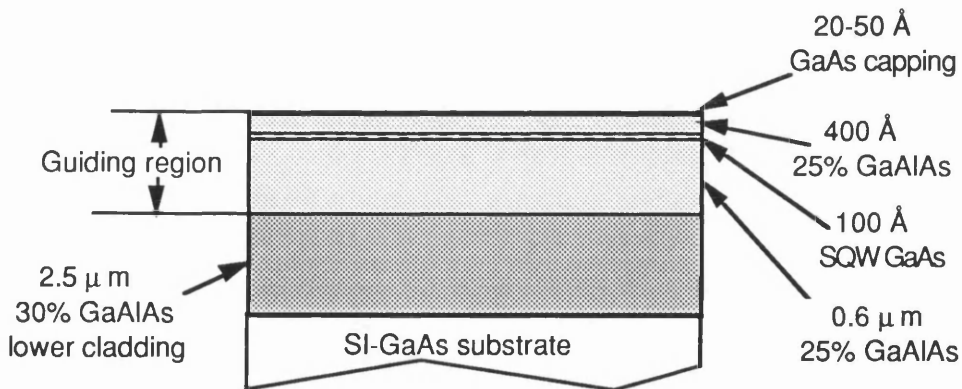
Fig. 4.3 *Schematic diagram of the epitaxial layers of A187 GaAs/GaAlAs SQW waveguide structure grown by MBE. The GaAs well is only 400 Å below the top surface. All the layers are undoped and grown on SI-GaAs substrate.*

61

QT147 p-i-n SQW:

This wafer was grown by MOVPE technique at the SERC Central Facility for III-V semiconductors, Sheffield University. Fig. 4.4 shows a schematic diagram of the epitaxial layers structure of the QT147 p-i-n SQW wafer. The SQW was placed in the centre of the symmetrical p-i-n waveguide structure. This was to ensure a maximum overlap integral of the SQW with the confined optical field. The recovery time of the resonant nonlinearity can be enhanced by sweeping the photogenerated carriers out of the guiding region when an electric field is applied across the intrinsic region [3]. The i-region was extended to the p-type (0.4 μm) and the n-type (0.4 μm) upper and lower cladding regions to reduce the free carriers absorption and also to provide an electrical isolation of the electrodes (in active devices) without the need to etch through the guiding region.
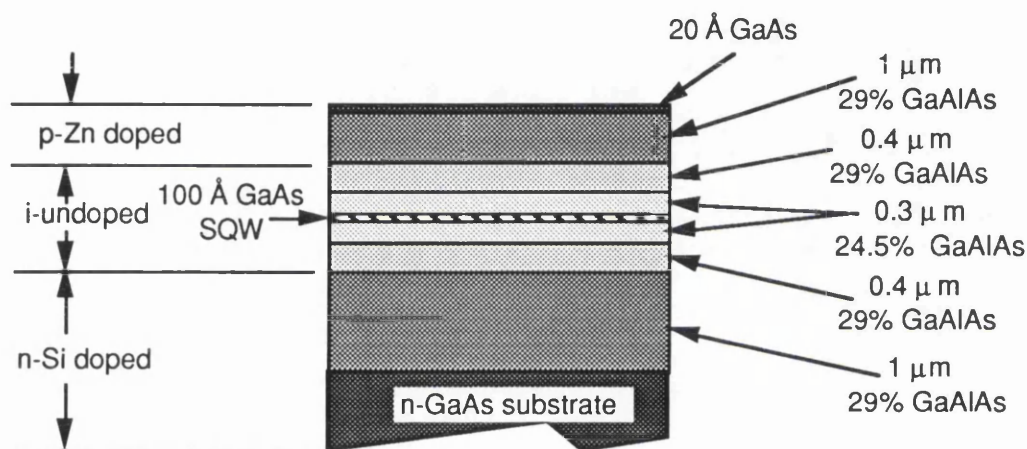
Fig. 4.4 *Schematic diagram of the epitaxial layers of QT147 GaAs/GaAlAs p-i-n SQW waveguide structure grown by MOVPE. The GaAs well is in the middle of the guiding region.*

A163 p-i-n MQW:

The wafer was grown by MBE technique at the author's Department. The wafer was designed by Dr. A. Jennings to investigate the electro-optic effects in MQW waveguides [4]. Fig. 4.5 shows a schematic diagram of the layers structure of A163 p-i-n MQW wafer, the guiding region was formed of 25 wells and 26 barriers, the large number of QWs was to provide a large nonlinear effects.
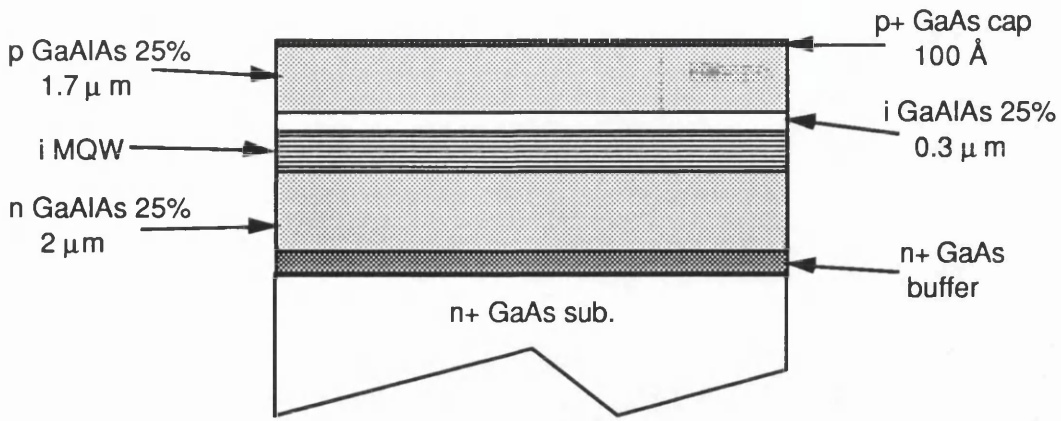
Fig. 4.5 *Schematic diagram of the epitaxial layers of A163 GaAs/GaAlAs p-i-n MQW waveguide structure grown by MBE. The guiding region is formed of the intrinsic MQW layers.*

A293 GaAlAs:

This wafer was grown by MBE technique and Fig. 4.6 shows a schematic diagram of the layers structure of A293 GaAlAs wafer. It consisted of a 1.5 μm thick $Ga_{0.82}Al_{0.18}As$ guiding region, a 1.5 μm thick $Ga_{0.75}Al_{0.25}As$ upper cladding layer and a 4 μm thick $Ga_{0.75}Al_{0.25}As$ lower cladding layer. The epitaxial layers were grown on a semi insulating (SI) GaAs substrate.
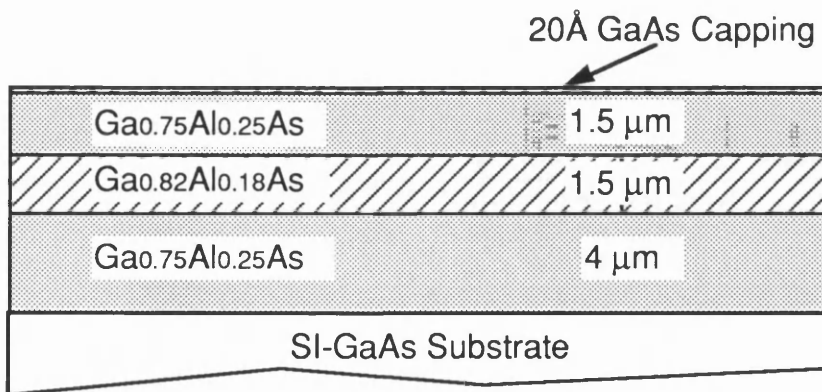
Fig. 4.6 *Schematic diagram of the epitaxial layers of A293 GaAlAs heterostructure waveguide.*

4.4 Photoluminescence Spectroscopy:

Photoluminescence PL measurement technique is an effective way to study the band structure and the quality of the semiconductor materials [5]. The possible information which can be extracted from the PL spectra are the Al mole fraction in GaAlAs and the well width of the quantum well structures.

The basic idea behind the PL spectroscopy is to generate carriers (electrons and holes) in a semiconductor, by illumination with high energy photones, and then detect the emission spectrum of the recombined carrieres. There are many possible states that photogenerated carriers may occupy and there are a corresponding number of relaxation transitions which may occur. Each of these has a characteristic energy which can be identified from the photoluminescence PL spectrum of the material.

The Al mole fraction in the GaAlAs cladding layers can be extracted from the optical transition peaks associated with the bound excitons, using the following expression [6]:

$$x = b[E_g(x) - E_g(0)]$$

where x is the Al mole fraction, $E_g(x)$ is the bound exciton transition in $Ga_{1-x}Al_xAs$, b=0.6872 and $E_g(0)$=1.512 for 0<x<0.35. The well width was estimated from the e1-hh1 exciton transition in QWs by using the XTON program described in section 3.6.

The PL system used in this work is a part of the analysis equipment in the department, run by Mr. J. Cochrane. Samples were mounted in a cryostat, cooled to a temperature as low as 10 K and excited (illuminated) with a He-Ne laser source (λ=632.8 nm). The PL from the sample was collected by a collimating lenses and focused onto the slit of a monochrometer. The luminescence spectrum was measured by scanning through a wavelength range, the output signal of the monochrometer was detected with a Ge detector. The laser source was chopped at 1 KHz and the detected signal was amplified using a lock-in amplifier, then the output signal was recorded in a chart recorder. PL spectroscopy was also used during the term of this project to investigate the vacancies induced disordering in GaAs/GaAlAs quantum well materials, via the shift in the exciton transitions of the QWs.

PL Results of A187 SQW Wafer:

Fig. 4.7 shows the PL spectrum for an A187 SQW sample, obtained at a temperature of 19 K. There were five peaks, the two peaks at 1.493 eV and 1.514 eV were due to donor

bound excitonic recombination and to a free-to-bound transition involving a carbon acceptor respectively [7], in GaAs capping layer. The two peaks at 1.838 eV and 1.902 eV were referred to the GaAlAs guiding and cladding layers, respectively. From these two transitions, the Al% was calculated to be 26% and 30% respectively. The peak at 1.549 eV was referred to the e1-hh1 exciton transition in the SQW, the well width was estimated to be 97 Å (using XTON program).
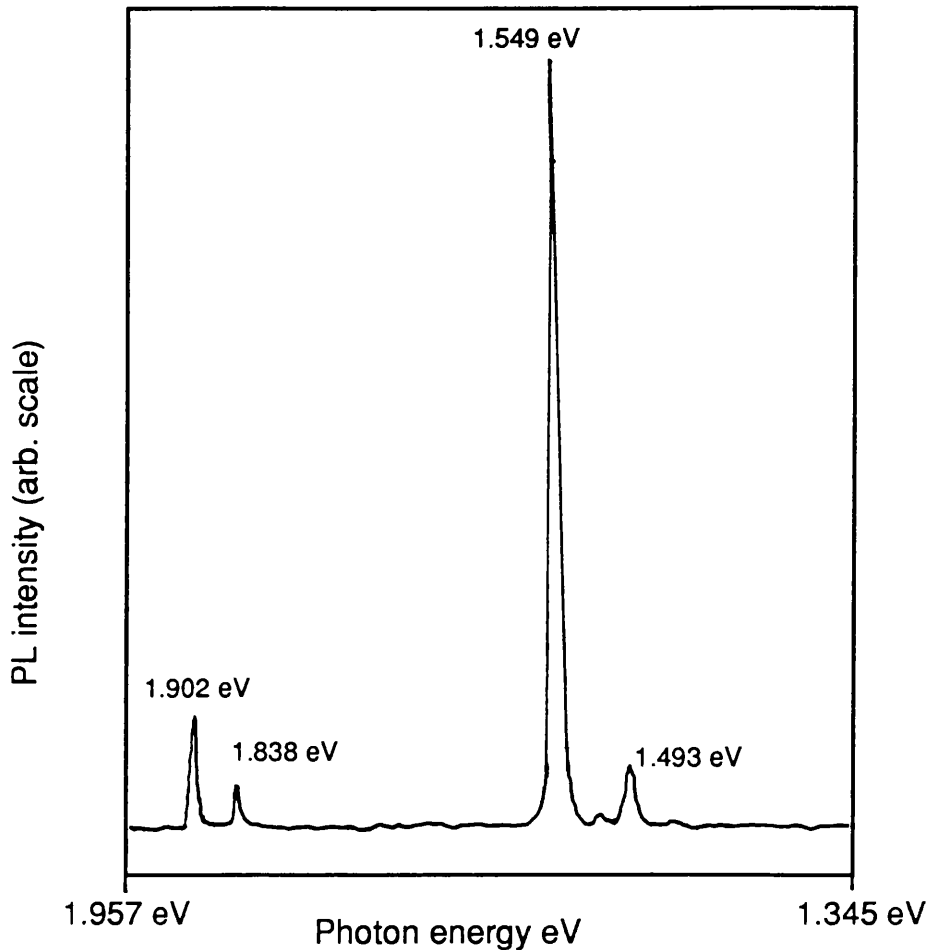
4.7 *Photoluminescence spectrum of A187 GaAs/GaAlAs SQW wafer, at a temperature 19 K.*

PL Results of QT147 SQW Wafer:

Fig. 4.8 shows the PL spectrum for a QT147 SQW sample, at a temperature of 12 K. It showed two peaks, the broad peak at 1.484 eV was most likely due to transition associated with deep impurity level. The other peak at 1.543 eV was referred to the SQW, from this peak the well width was estimated to be 94 Å.

65
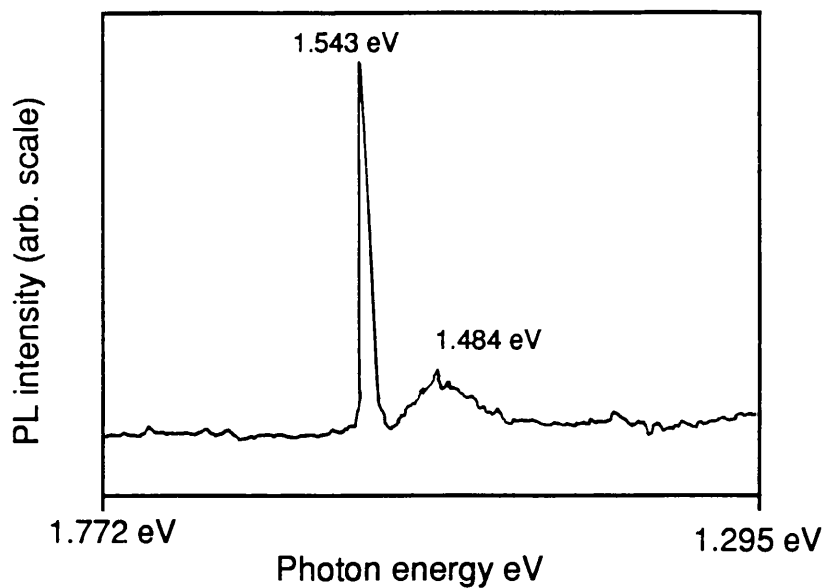
Fig 4.8 *Photoluminescence spectrum of QT147 GaAs/GaAlAs p-i-n SQW wafer, at a temperature 12 K.*
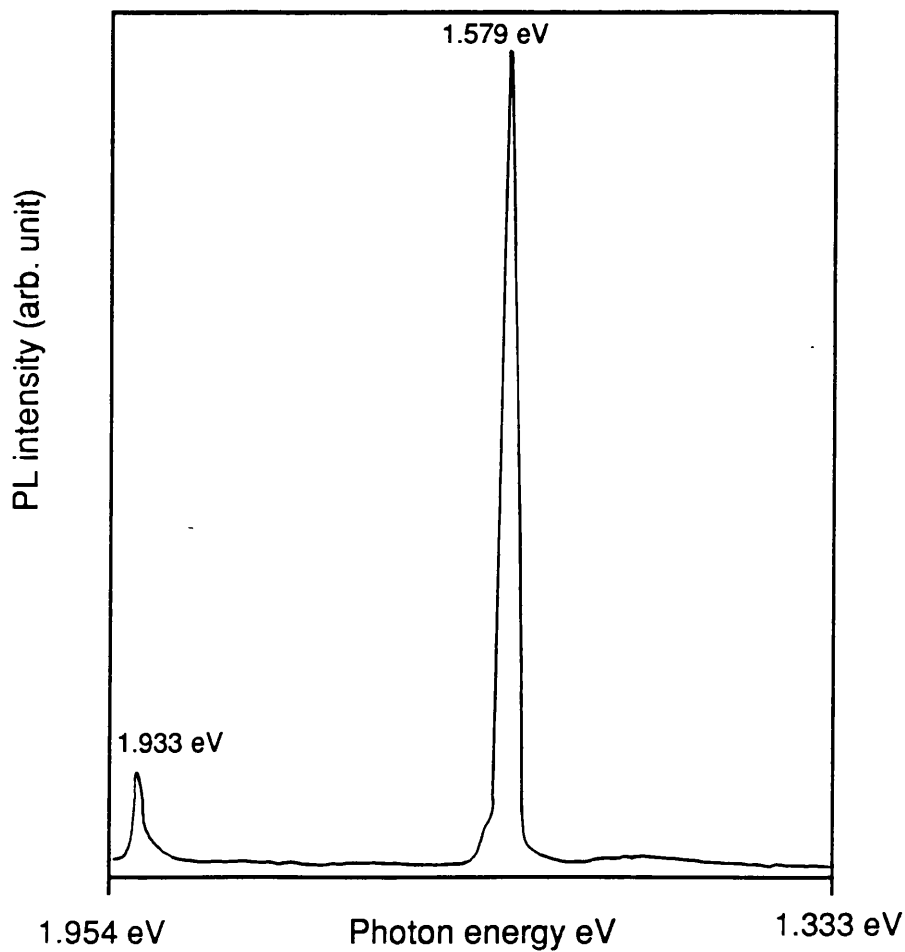
Fig. 4.9 *Photoluminescence spectrum of A163 GaAs/GaAlAs p-i-n MQW wafer, at a temperature 25 K.*

PL Results of A163 MQW Wafer:

Fig. 4.9 shows the PL spectrum for a A163 MQW sample, at a temperature of 12 K. The peak at 1.933 eV was associated with the bound exciton in the GaAlAs cladding layer, the Al% was calculated to be 30%. The peak at 1.578 eV was referred to the e1-hh1 exciton transition in the MQW layer, the well width was estimated to be 94 Å.

PL Results of A293 GaAlAs Wafer:

Fig. 4.10 shows the PL spectrum for a A293 GaAlAs sample, at a temperature of 12 K. The peak at 1.839 eV was associated with the bound exciton in the GaAlAs guiding layer; the Al% was calculated to be 22%, this is larger than the requested Al mole fraction of 18%. The peak at 1.892 eV was associated with the bound exciton in the GaAlAs cladding layer, the Al% was calculated to be 26%.
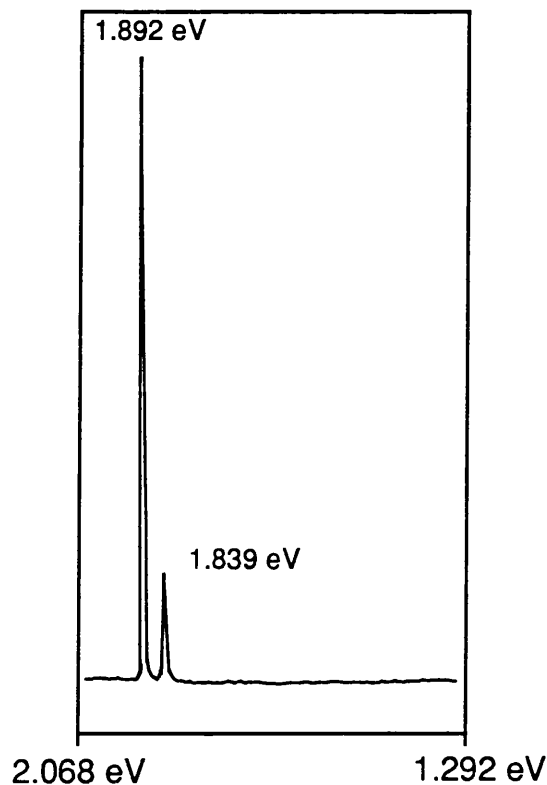
Fig. 4.10 *Photoluminescence spectrum of A293 GaAlAs wafer, at a temperature 12 K.*

4.5 Photocurrent Spectroscopy:

Photocurrent spectroscopy is an effective technique to investigate the absorption and electro-absorption properties of a p-i-n semiconductor structures [8-10]. It has the advantage, over the transmission spectrum measurements, of giving a large signal at the high absorption spectral regions. Measurements were carried out on p-i-n GaAs/GaAlAs single and multiple quantum well materials, and provided an assessment of the band edge structure of the QWs and also a study of the electro-absorption effect due to the quantum confinement Stark effect [11]

4.5.1 Theory Of Photocurrent Spectroscopy:

A p-i-n structure can be used as a detector when it operates under a reverse bias voltage smaller than the breakdown voltage. The detection capability arises from the absorption of an incident photon and creation of an electron and hole pair. These photo-generated carriers are normally (with zero electric field) recombine within a diffusion length. When an electric field is present across the depletion region, then these carriers are swept apart by the electric field. The transport of the carriers out of the QWs is by tunnelling through the barriers. These carriers contribute to the total reverse current, therefore the detected current will change from I_0 (the dark current) to $I_0 + I_{ph}$ due to the detection of the light. I_{ph} is the detected photocurrent, and is given by [8];

$$I_{ph}(h\omega, F) = P_i(h\omega) \ (1 - R) \left(\frac{e\lambda}{hc}\right) \eta(F) . (1 - e^{-\alpha(h\omega, F)d}) \qquad (4.1)$$

$P_i(h\omega)$ = incident power at a photon energy $h\omega$.
R = surface reflection coefficient.
η = internal quantum efficiency.
d = total depletion depth.
$e\lambda/hc$ = conversion from watts to amps.
F = electric field strength.

The thickness of the depletion region d depends on the applied reverse bias voltage, and becomes independent of voltage when the whole intrinsic region is depleted. The internal quantum efficiency η of the diode depends on the electric field strength [12] as well as the thickness of the barrier width [10]. This is due to the tunnelling of the photogenerated carriers through the QW barriers. η increases rapidly with the increase in the electric field strength and it becomes independent of the applied voltage when $\eta=1$. This is because,

initially the intrinsic region is partially depleted and the photo-generated carriers recombine at the low electric field region before being swept out. At high voltages, the whole region is depleted and the strong electric field across the depletion region sweep the photo-generated carriers out. When $\alpha d \ll 1$, the photocurrent is directly proportional to the absorption coefficient of the material.

Photocurrent measurement technique has been used by Miller et al. [9] to investigate p-i-n MQW diode at a variety of bias voltages. It was experimentally demonstrated the proportional relationship between I_{ph} and $\alpha(h\omega)$. It was found that η was independent of wavelength. Photocurrent measurements were also achieved in a waveguide geometry [8], the light was propagating in the plane of the QWs. This gave the advantages of examining the electro-absorption effect for both the TE- and TM-modes. In the case of a waveguide geometry, the photocurrent is related to the total propagation loss of the waveguide where:

$$I_{ph}(h\omega, F) = P_i(h\omega) \, \gamma \, (1- R) \left(\frac{e\lambda}{hc}\right) \eta(F) . \left(\alpha_{abs}(h\omega, F) \, / \, \alpha_{total}(h\omega, F)\right)$$
$$. \left(1 - e^{-\alpha(h\omega, F)d}\right) \qquad (4.2)$$

L = the waveguide length.
α_{total} = total propagation loss (absorption, scattering etc).
α_{abs} = contribution to α_{total} due to absorption only.
γ = coupling coefficient to the waveguide.

In this project the photocurrent spectroscopy was used to characterise the GaAs/GaAlAs p-i-n single and multiple QW materials and to determine the position of the excitonic peaks of the QWs. This technique also enabled us to measure the red shift in the absorption edge with applied electric field across the QW via the quantum confined Stark effect (QCSE) [11].

4.5.2 Device Fabrication:

Chrome masks designed by Sheffield University were used to fabricate photodetectors for photocurrent measurements. It consisted of a pattern of discs of 400 μm, 200 μm and 100μm outer diameters with aperture in the centre of diameter 150 μm, 100 μm and 50 μm respectively. This mask was used to form p-type ohmic contacts on the top of the samples, using optical lithography and lift-off processes, as described in sections 5.3 and 5.4. Mesa structures were formed by etching through the epitaxial layers to a depth below the i-n junction to isolate the individual devices. The p-type ohmic contact discs and apertures were

69

protected with photoresist ridges, the resist ridges were aligned on the top of the ohmic contact discs using a mask aligner. The mesa structures containing individual devices were formed by wet etching the sample in a solution of $H_2SO_4:H_2O_2:H_2O$ (1:8:1) for 15 seconds. The p-type (on the top) and n-type (on the bottom) ohmic contacts were annealed at $360°C$ for 45 seconds. The sample was bonded onto a p.c.b. mount with silver epoxy and individual devices were connected by ultrasonically bonded aluminium wire from the top contact of the device to the p.c.b. mount. Fig. 4.11 shows an SEM photograph of complete devices. Fig. 4.12 shows a schematic diagram of the experimental set-up and the equivalent circuit diagram of the photocurrent device. The I-V characteristics of devices fabricated on samples of QT147 p-i-n SQW and A163 p-i-n MQW wafers, showed a breakdown voltage of 38 V and a dark current $I_0 \approx 20$ nA.
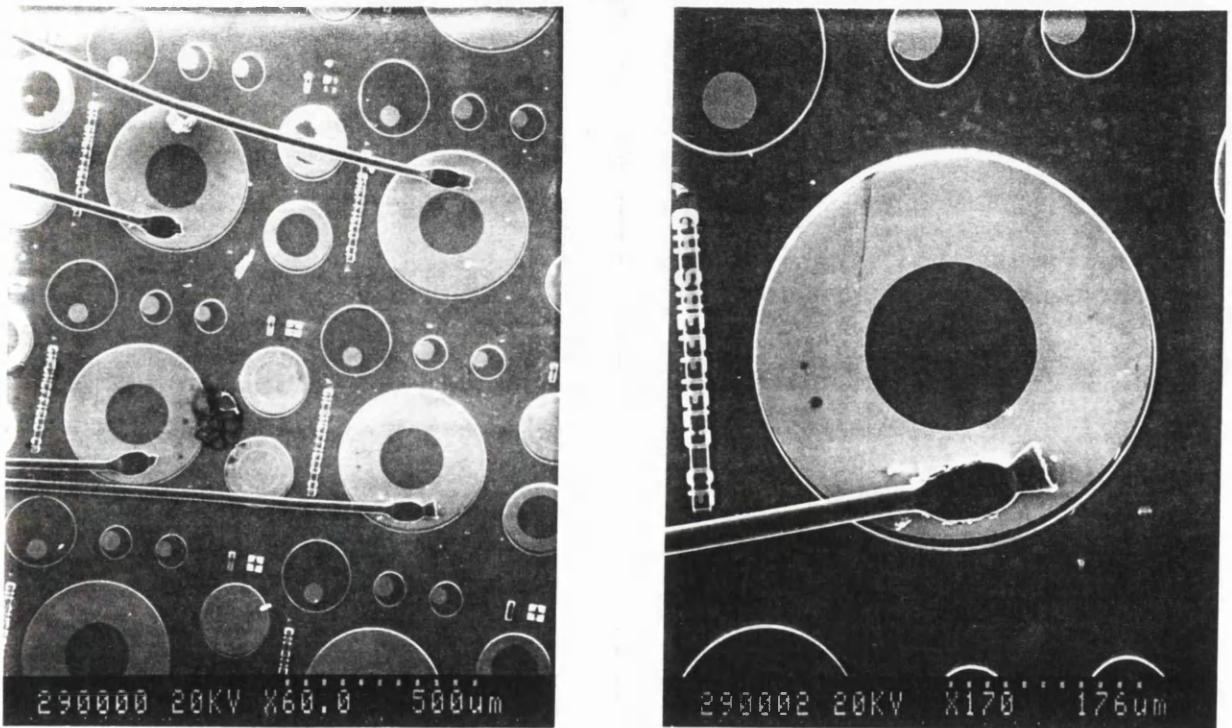
Fig. 4.11 *SEM micrograph of a bonded photocurrent device.*

4.5.3 Experimental Arrangement:

The experimental arrangement for the photocurrent measurements is described in section 5.7.2. The laser source was a tunable Ti:sapphire laser, described in section 5.8.2. The laser beam was focused onto the aperture of the device (at normal incidence) using a microscope objective mounted horizontally on an optical bench. The objective turrets, containing 10×, 20×, 50× and 80× objectives, which allowed to change the size of the

beam spot. A He-Ne laser, $\lambda=0.633$ µm, was used to align the Ti:sapphire laser with respect to the aperture of the device. The eyepiece of the microscope could be used to ensure that the alignment of the visible laser beam was on the device aperture. The wavelength of the Ti:sapphire laser was changed continuously by a motorised driver unit attached to the micrometer controller of the birefringent filter. The laser was chopped at 1 kHz and a lock-in amplifier was used to measure the photocurrent at the load resistor. The output of the lock-in amplifier was connected to a data logging computer. The power of the laser incident on the sample was kept low ($\leq$50 µW) and focused to a spot of diameter 50 µm. This is to prevent the nonlinear effect and saturation of absorption [26]. The absorption of the light in the p-type GaAlAs cladding layer will not contribute to the photocurrent, due to the absence of an electric field outside the depletion region of the p-i-n structure.
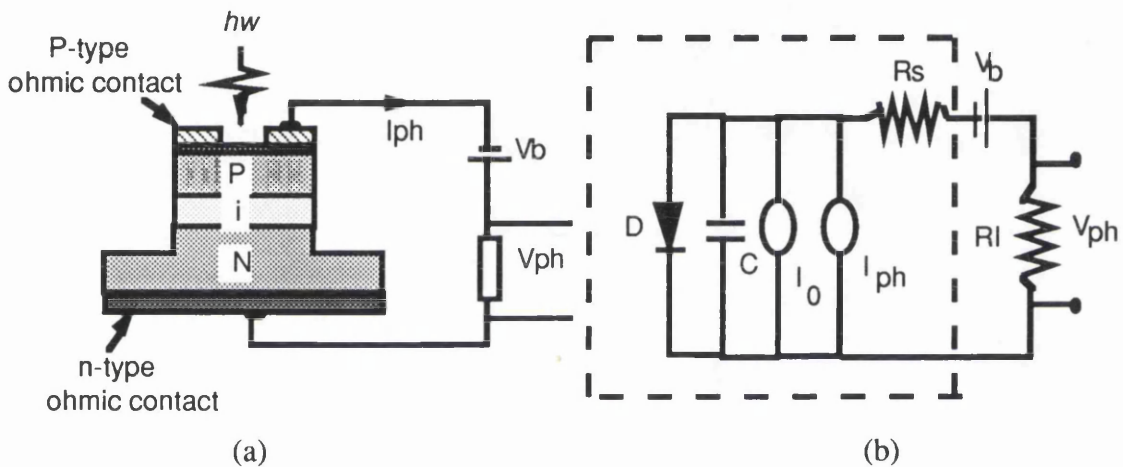
Fig. 4.12 a) *Schematic diagram of the experimental arrangement of the photocurrent spectroscopy of a p-i-n device,* b) *The equivalent circuit diagram of the p-i-n photocurrent device.*

4.5.4 Experimental Results:

The photocurrent spectrum was measured in devices fabricated on wafers QT147 SQW and #A163 MQW. Fig 4.13 shows the photocurrent spectrum of the QT147 at zero reverse bias voltage. It shows clearly the excitonic absorption peaks. The e1-hh1 and e1-lh1 exciton transitions were resolved at photon energies 1.562 eV and 1.566 eV respectively. At high photon energies, the photocurrent signal was noisy due to the instability of the laser output transverse mode when the wavelength is continuously tuned.

The electro-absorption effect in the quantum well (QCSE) was measured in these devices. Fig 4.14 shows the photocurrent absorption spectra at different reverse bias voltages. The spectra are off-set from each other for clarity. A progressive shift of the excitonic peaks to lower energies (red shift) with broadening at large electric fields [13]. A shift in the e1-hh1 exciton of about 20 meV at a reverse bias voltage of 8 V.
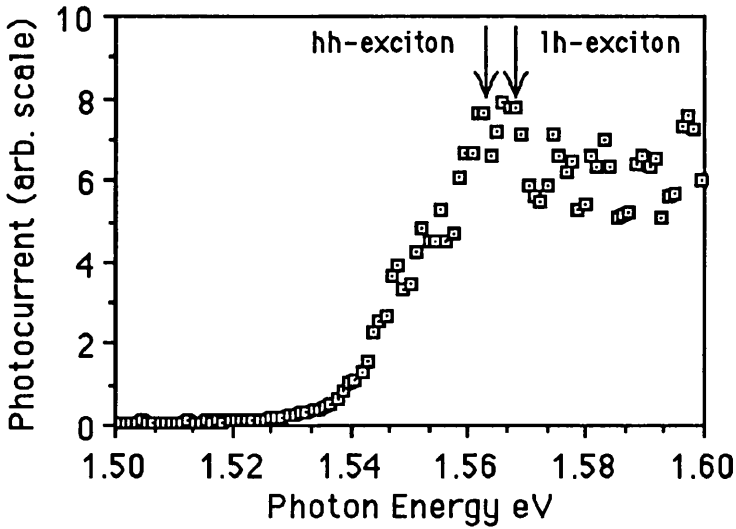
Fig. 4.13 *The photocurrent spectrum of the QT147 SQW diode at a zero bias voltage, a hh and lh excitonic peaks are shown at photon energies 1.562 eV and 1.566 eV, respectively.*
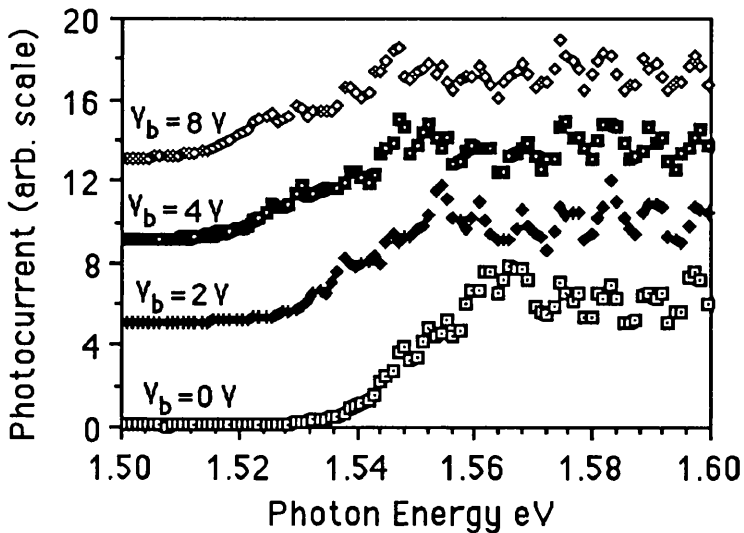
Fig. 4.14 *The photocurrent spectra of the QT147 SQW diode at different bias voltages, the hh and lh excitonic peaks are shifted to lower energies due to the quantum confinement Stark effect (QCSE).*

The absorption spectrum of a photocurrent device fabricated on wafer #A163 MQW is shown in Fig. 4.15 at zero bias voltage. The e1-hh1 and e1-lh1 excitonic transitions were resolved at photon energies 1.508 eV and 1.515 eV respectively. The electro-absorption effect in the quantum well (QCSE) was measured in these devices. Fig 4.16 shows the photocurrent absorption spectra at different reverse bias voltages. A shift in the e1-hh1 exciton of about 15 meV at a reverse bias voltage 6 V was achieved.
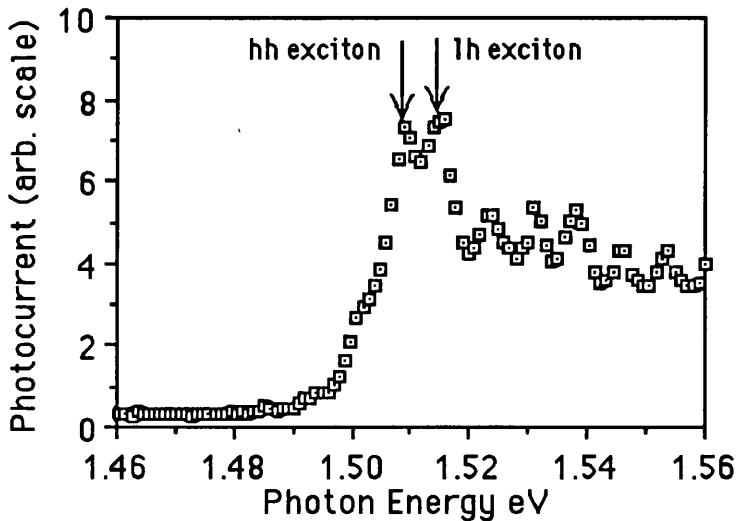
Fig. 4.15 *The photocurrent spectrum of the A163 MQW diode at a zero bias voltage, a hh and lh excitonic peaks are shown at photon energies 1.508 eV and 1.515 eV, respectively.*
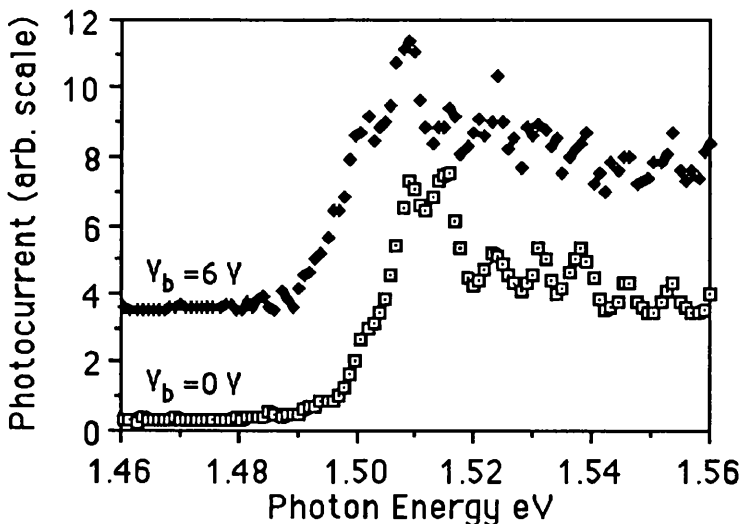
Fig. 4.16 *The photocurrent spectra of the A163 MQW diode at two different bias voltages, the hh and lh excitonic peaks are shifted to lower energies due to the quantum confinement Stark effect (QCSE).*

4.6 Vacancies Indiffusion Disordering in GaAs/GaAlAs Quantum Well Materials:

The ability to control the spatial distribution of the optical properties of a semiconductor wafer have a significant impact on the optoelectronic devices and their integration. In a quantum well material, this can be accomplished by locally control the interdiffusion of the well and the barrier and thus shift their effective band gap. This local intermixing process between the well and barrier, which alter the band structure of the QWs is known as disordering.

As proposed in chapter 7, the local (selective) disordering technique can be implemented in the nonlinear asymmetric Mach-Zehnder interferometer AM-ZI for two reasons, which are discussed in section 7.4. Firstly, to enable the fabrication of linear device with a nonlinear section in one arm of the AM-ZI, at which the π phase change can be obtained (by all-optical means). Secondly with such a device configuration, the total insertion loss due to band edge absorption can be reduced.

In the rest of this chapter, the microscopic origin and the techniques of the disordering are discussed with the experimental results.

4.6.1 Microscopic origin of GaAs/GaAlAs QWs Disordering:

The microscopic origin of GaAs/GaAlAs QWs band structure disordering is due to two mechanisms, Ga self diffusion and Al-Ga (barrier-well) interdiffusion, these are analogous diffusion phenomena [14]. The intermixing process will cause the initial finite square well to become rounded (smoothed). Therefore due to the change in the effective thickness of the quantum wells and shallower $Ga_{1-x}Al_xAs$ wells, the quantization energy levels in the conduction and valence bands shift to higher energies. This is shown in Fig. 4.17, the conduction and valence bands of the as-grown square well (dashed) and a modified potential (solid curve) after interdiffusion of Al-Ga. The bound states of the potential well are labelled e for electron states, hh and lh are for heavy hole and light hole states, respectively. The short bars indicate the energy states for the as-grown square well. The first two states moved up in energy while the third energy state moved down in energy. This is due to the increase of the effective well thickness, at the top of the well.
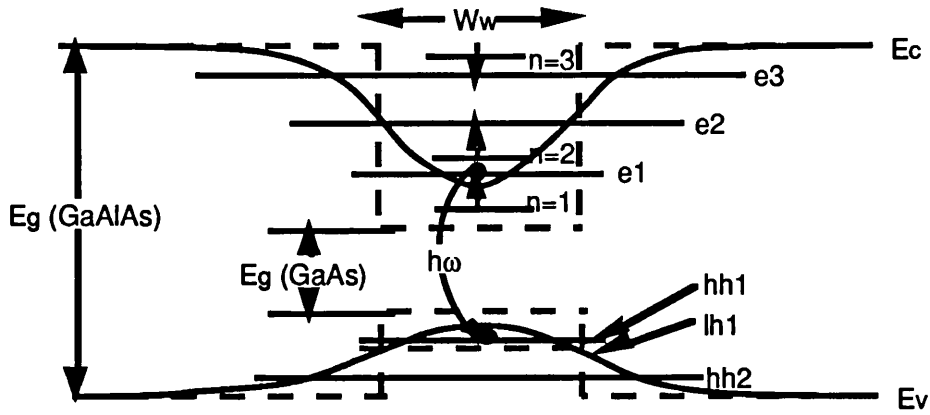
Fig. 4.17 *Schematic diagram of the QW band structure before intermixing (square well profile) and after intermixing (smooth rounded well profile). The hh and lh excitonic transitions shifted to higher energies.*

4.6.2 Disordering Techniques:

There are three techniques which can modify the band structure of GaAs/GaAlAs QWs, these are as follow:

Thermal Annealing:

This technique was used to modify the wavelength of a QW laser [15] without significant increase in threshold pumping current. The modification of the wavelength was achieved by annealing the QW material between 870 °C and 900 °C in an evacuated quartz ampoule with excess As. With this technique there was no lateral selective disordering, where the band gap of the whole chip is shifted to higher energy (i.e. blue shift).

Impurities Induced Disordering IID:

In this technique, the samples were selectively bombarded with high energetic ions to enhance the intermixing of GaAs/GaAlAs QW structures. A large number of elements were used, shallow dopants such as Zn and Si as well as other elements, e.g. Kr, F, B and As which produce only lattice damage [16-18]. The implanted samples were then capped with a dielectric film of silicon dioxide or nitried and thermally annealed at temperatures from 600°C to 900°C.

Although this technique is highly selective, the Zn and Si tend to ionize at room temperature which give rise to the free carriers optical absorption. Implantation with the other elements may result in the broadening or screening of the QWs excitonic resonances, due to the crystal damage.

Vacancies Indiffusion Disordering:

In this technique, the interdiffusion of Al-Ga (barrier-well) is enhanced by capping the samples with a silicon dioxide film and annealing them at temperatures between 800 °C to 950 °C [19-22]. The intermixing enhancement is due to the out-diffusion of Ga into the cap layer leaving behind a vacancy. These vacancies indiffuse during thermal annealing through the epitaxial layers. The Al-Ga interdiffusion is proportional to the Ga vacancies concentration and diffusivity. The relative shift in the QW band edge between the capped and uncapped areas is a function of the annealing temperature, time and to certain extend the thickness of the SiO_2 film.

The selectivity in this technique can be enhanced by using another dielectric capping film, silicon nitride to form a barrier for Ga outdiffusion. Haga et al [21] investigated the concentration of the outdiffusion of Ga and As into SiO_2 and Si_3N_4 dielectric films. This was achieved by using the Rutherford backscattering spectroscopy and particl-indused X-ray emission techniques. It was found that the SiO_2 capping is far more soluble for Ga outdiffusion than As outdiffusion, while Si_3N_4 forms a very good barrier for Ga and As, and there was no significant Si indiffusion into GaAs substrate. L. Guside et al. [19] showed that the Al-Ga interdiffusion coefficient (D_{Al-Ga}) in GaAlAs-GaAs QW heterostructure is highly dependent upon the crystal encapsulation conditions. The interdiffusion coefficient D_{Al-Ga}, using Si_3N_4 capping, is almost an order of magnitude smaller than that of either capless or SiO_2 capped samples, at temperatures from 800 °C to 875 °C. J. Ralston et al. [23] measured the electro-absorption spectra in GaAs/GaAlAs QW waveguides which have been modified via the vacancies indiffusion disordering technique. It was shown that this technique provides a permanent energy band blue shift while still retaining clearly resolved heavy and light hole excitonic peaks at room temperature. Furthermore, the QCSE was shown to be preserved in the intermixed structures.

The vacancies indiffusion disordering technique is obtainable in the author's Department and was investigated as a function of the annealing temperature and time and also as a function of the dielectric film thickness.

4.6.3 Material Description and Characterisation:

The wafer used in the investigations of the vacancies indiffusion disordering was B34 GaAs/GaAlAs three QWs structure, grown by MBE. As shown in Fig 4.18, it consisted of three QWs, the GaAs well thicknesses were 80 Å, 60 Å and 40 Å. These were referred to as SQW3, SQW2 and SQW1 respectively. The thickness of the $Ga_{0.7}Al_{0.3}As$ barrier was 200 Å (between the wells), and 800 Å in either sides of the QWs. The epitaxial layers were all undoped and grown on a SI-GaAs substrate.
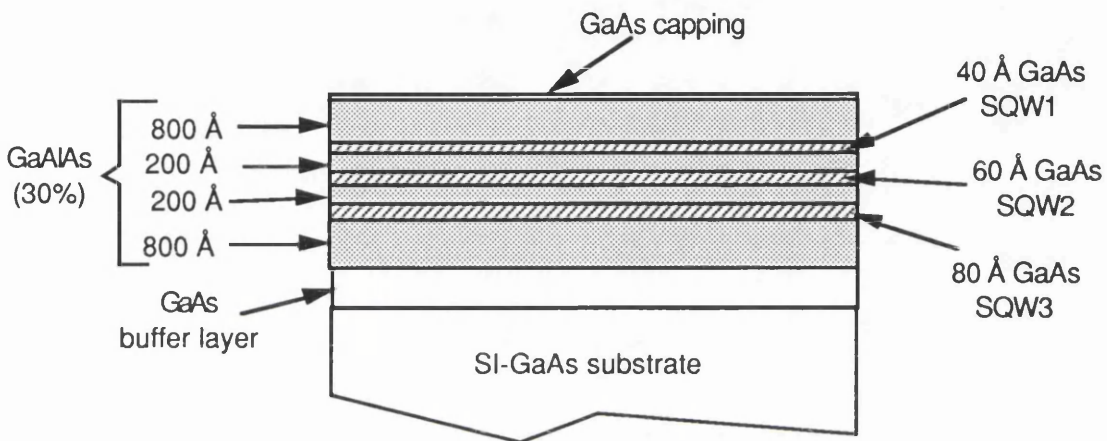
Fig 4.18 *Schematic diagram of the epitaxial layers of the B34 3QWs structure grown by MBE. The three GaAs QWs have thicknesses of 40 Å, 60 Å and 80 Å. All layers are undoped and grown on SI-GaAs substrate.*

PL technique was the effective tool used to measure the degree of the disordering of the QWs via observing the shift in the PL spectral peaks. Fig. 4.19 shows the PL spectrum of the as grown B34 material, at 12 K. The peaks at 1.647 eV, 1.595 eV and 1.567 eV were referred to the hh-excitons of SQW1, SQW2 and SQW3 respectively. The other two peaks, at 1.515 eV and 1.493 eV, were from the GaAs capping layer caused by band-to-band recombination and transitions via carbon acceptor levels, respectively [7].

It has been seen in section 3.6, that QWs with narrow well thickness (≤80 Å) are more sensitive to any fluctuation in the well thickness. Therefore, it was vital in our investigations of the vacancies disordering to examine the uniformity of the wells over the entire wafer. This was achieved by taking the PL spectra at different places in the wafer, which showed no drift in the hh-excitons positions of the three QWs.
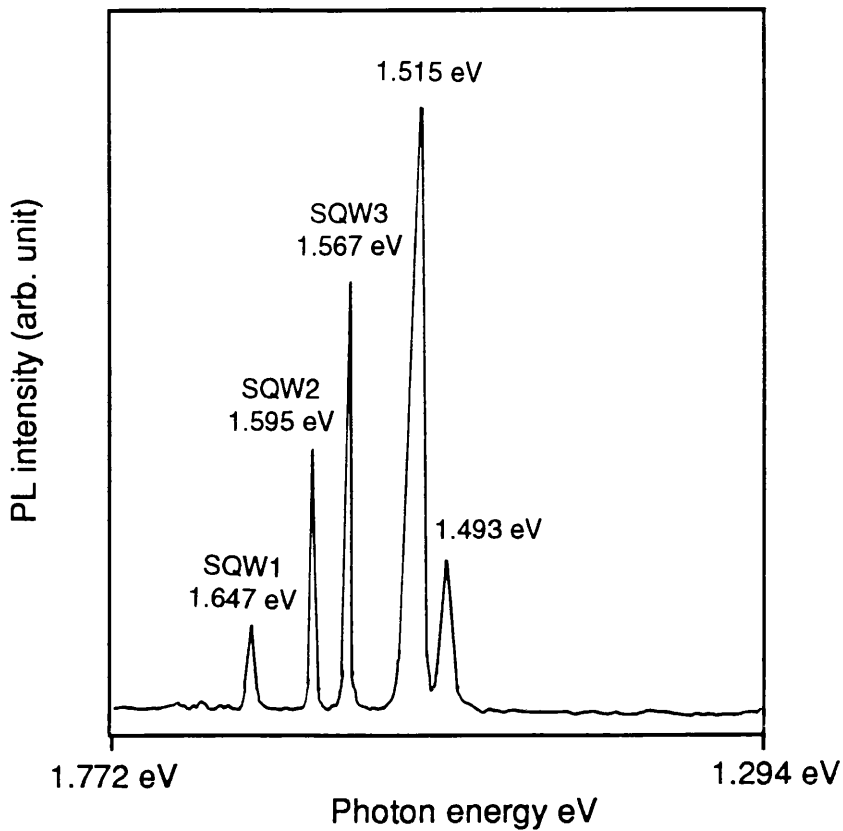
Fig. 4.19 *Photoluminescence spectrum of B34 GaAs/GaAlAs three QWs wafer, at a temperature 12 K.*

4.6.4 SiO₂ Dielectric Capping Film:

To obtain a good adhesion of SiO_2 film on GaAs substrate, samples were chemically cleaned to remove dust and other forms of airborne and human contamination. This was achieved by using the procedure described in section 5.3.1.

Amorphous silicon dioxide, SiO_2, was plasma deposited using a standard process developed by Plasmatech, the deposition conditions were:

SiH_4 flow rate = 8 sccm.

N_2O flow rate = 110 sccm.

Pressure = 250 mTorr

R.F. power = 5 W.

Substrate temperature = 300 °C.

The deposition rate was ≈65 nm/min and resulted in an even film thickness across the average sample size. The samples were capped with four different thicknesses 960 Å, 2600 Å, 4200 Å and 6200 Å.

Annealing was carried out in a conventional diffusion furnace with high-purity flowing nitrogen atmosphere. The samples were mounted inside an enclosed high-purity graphite box so that the samples top surface was uppermost and exposed to a high local vapour pressure of arsenic provided from a small volume of gallium loaded with GaAs. Samples were annealed at different temperatures 800 °C, 850 °C, 900 °C, 950 °C and 980 °C for 30 minutes.

4.6.5 Experimental Results:

The shift in the e1-hh exciton transition of the QW1, QW2 and QW3 due to intermixing of Al-Ga (barrier-well) was measured, using the PL technique, at 12 K. Fig. 4.20 shows the spectra for three samples capped with 2600 Å of SiO_2. The first spectrum was for an as grown sample and the other two spectra were for samples annealed at temperatures 900 °C and 950 °C. It shows the blue shift in the hh-exciton of the three QWs, after annealing. There was a small broadening in the excitons linewidth, and at 950 °C the SQW1 hh-exciton disappeared due to the complete intermixing of the well within the $Ga_{0.7}Al_{0.3}As$ barrier.

Fig. 4.21(a-d) shows the energy shift (meV) of the hh-excitonic peak of the three QWs as a function of the annealing temperature, for the four thicknesses of the SiO_2 films (960 Å, 2600 Å, 4200 Å and 6200 Å respectively). It shows a blue shift (to higher energy levels) of the hh-excitons as the annealing temperature increases. The energy shift is larger as the QWs were closer to the top surfaces of the material, i.e. $(\Delta E_{ex})_{SQW1} > (\Delta E_{ex})_{SQW2} > (\Delta E_{ex})_{SQW3}$. This was due to the high concentration of Ga vacancies close to the $GaAs-SiO_2$ interfaces which enhance the intermixing of the Al-Ga (barrier-well). These vacancies indiffused through the epitaxial layers as a function of the annealing temperature and time. For the SQW1, which was closest to the top surface, the hh-excitonic peak disappeared at temperatures ≥950 °C (for a SiO_2 thickness of 960 Å and 2600 Å) and at temperatures ≥900 °C (for a SiO_2 thickness of 4200 Å and 6200 Å). This was due to the complete intermixing of the well within the barrier. A blue shift of ≈120 meV, of the hh-exciton, was obtained at annealing temperature of 980 °C.

79
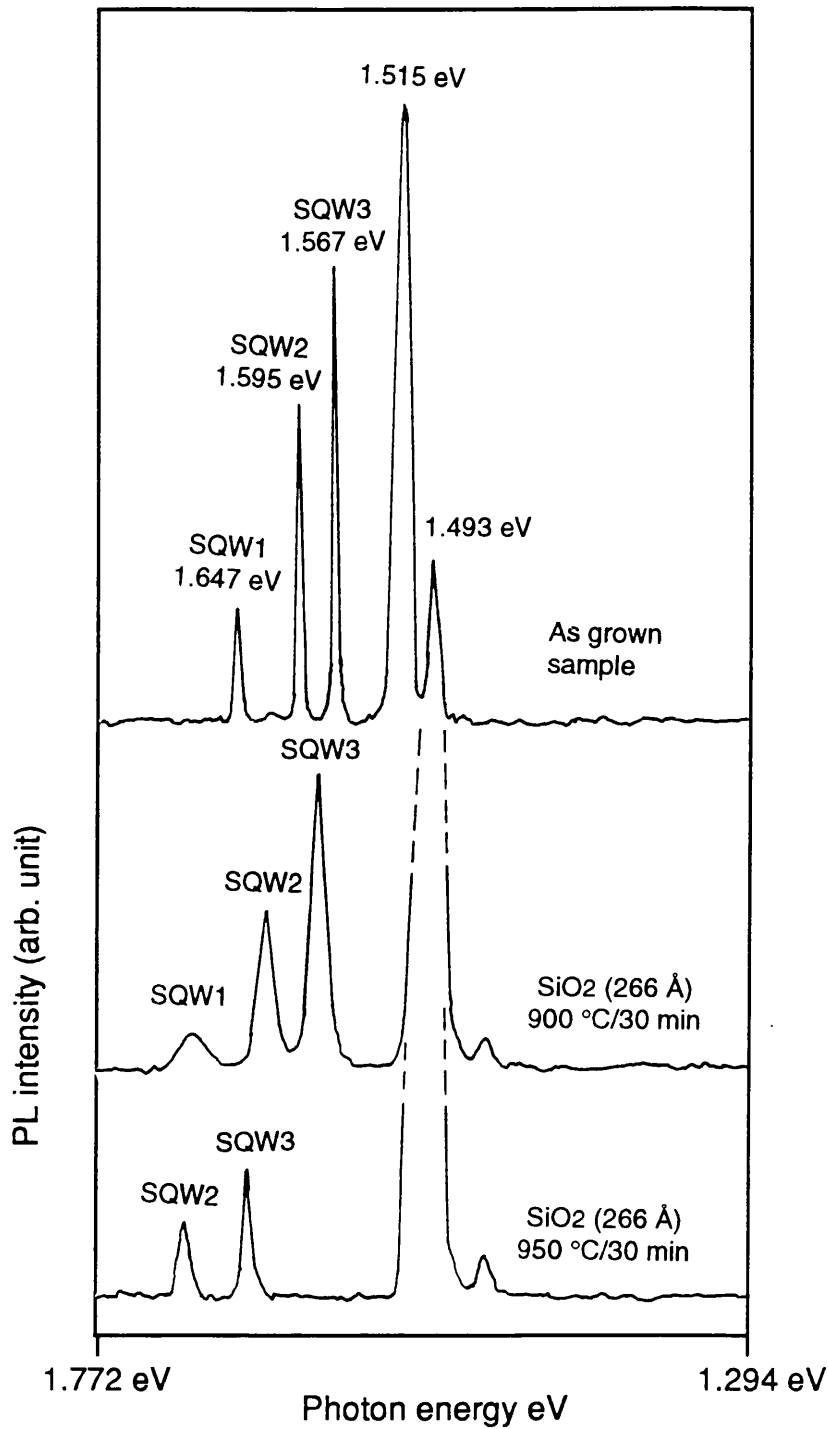
Fig. 4.20 *Photoluminescence spectrum of B34 GaAs/GaAlAs QW wafer for the as grown wafer (top), samples capped with a 2600 Å thick of SiO₂ film and annealed for 30 minutes at 900 °C (middle) and 950 °C (bottom). PL measurements were achieved at a temperature of 12 K.*
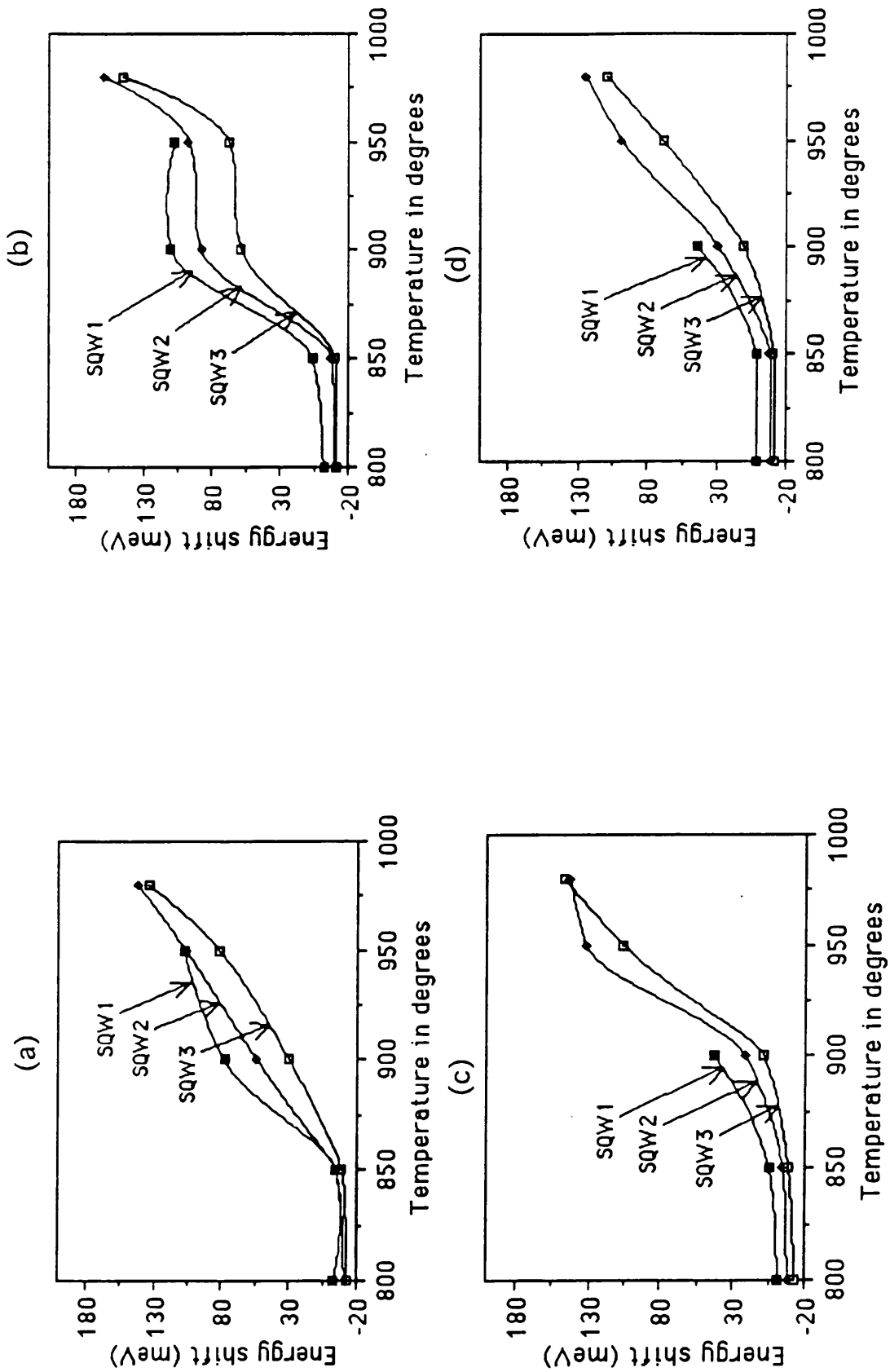
Fig. 4.21 *Energy shift (meV) of the hh exciton of SQW1, SQW2 and SQW3 as a function of the annealing temperature in samples capped with SiO₂ dielectric film of a thickness; a) 960 Å, b) 2600 Å, c) 4200 Å, d) 6200 Å.*

The shift in the QWs absorption edge was investigated as a function of the thickness of the SiO_2 capping layer. The hh-exciton energy shift, for the three QWs, did not show a consistent increase in the band edge (blue shift) with the increase in the thickness of the capping layer. This was may be due to the variation of the properties of the deposited SiO_2 film from one run to another.

4.6.6 Si3N4 Dielectric Capping Film:

A standard process developed by Plasmatech to deposit amorphous silicon nitride, Si_3N_4, was used. This gave a satisfactory deposition rate of ≈ 6 nm.min^{-1} and resulted in an even film thickness across the average sample size. The conditions for this process were:

SiH_4 flow rate = 10 sccm.
N_2 flow rate = 100 sccm.
NH_3 flow rate = 40 sccm.
R.F. power = 20 W.
Substrate temperature = 300 °C.

Unfortunately these films suffered cracking and peeling off when the samples were annealed above 600 °C. Fig. 4.22 shows an SEM photograph of a Si_3N_4 film cracked and peeled off after annealing. This was believed to be due to the large amount of stress within the amorphous Si_3N_4 layer. This stress originated during the growth process and is a strong function of the gas phase chemistry, i.e. plasma conditions.

The growth-in stress may be reduced by varying the deposition conditions. Smith et al. [24] and Hicks et al. [25], of this department, have shown that there exists at least two distinct gas phase regions for the deposition of amorphous Si_3N_4 with very different stresses. In an attempt to reduce the stress, films were deposited onto GaAs substrates using a variety of plasma conditions. It was found that the following set of conditions resulted in films that did not crack or peel even at temperatures in excess of 1000 °C, the deposition rate was 8 nm/min:

SiH_4 flow rate = 2 sccm.
NH_3 flow rate = 8 sccm.
Pressure = 0.25 torr
R.F. power = 20 W.
Substrate temperature = 300 °C.
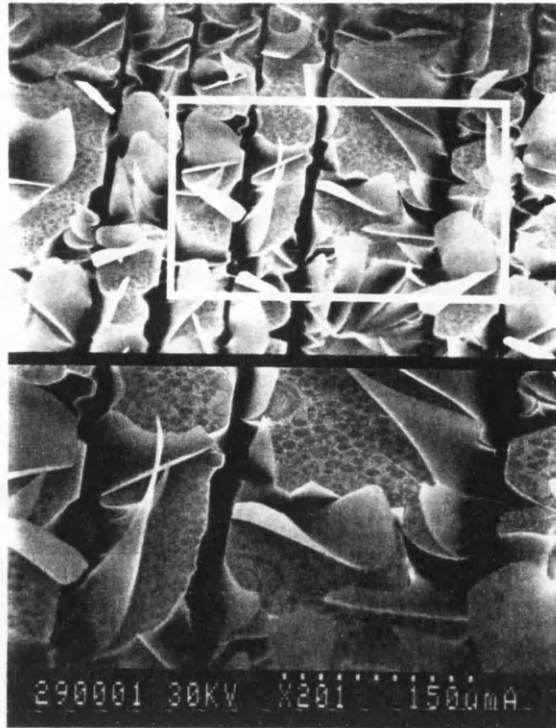
Fig. 4.22 *SEM micrograph of a GaAs/GaAlAs structure capped with Si$_3$N$_4$ dielectric film after thermal annealing, the Si$_3$N$_4$ film was peeled off at a temperature 640 °C.*

Surface preparation of the samples was also investigated, using two different procedures. Samples were cleaned using the steps described in section 5.3.1, and the others were cleaned with acetone and IPA followed by a blow drying with filtered air gun. The second set of samples showed cracks in the Si$_3$N$_4$ capping film, this was due to cleaning the samples with IPA as a final step leaves a very fine residue on the GaAs surface.

4.6.7 Vacancies Induced Selective Disordering:

In this section the degree of the differential disordering in samples capped with SiO$_2$ and Si$_3$N$_4$ has been investigated. Three sets of samples, of B34 3SQWs, were cleaned and one set was capped with SiO$_2$ (1200 Å thick) and the second set capped with Si$_3$N$_4$ (1100 Å thick) while the third set was uncapped. Samples (from each set) were annealed at the same conditions, two annealing temperatures were used 800 °C and 850 °C for 30 minutes.

Fig. 4.23 shows the energy shift of the hh-exciton of the three QWs as a function of the annealing temperature, for both the SiO$_2$ and Si$_3$N$_4$ capping film. These results were

derived from the PL measurements at 12 K. The energy shift was relative to the uncoated samples, annealed under the same conditions. A larger blue shift in the hh-exciton of the QW which is closer to the top surface was achieved, and virtually there was no shift in the band structure for samples capped with Si_3N_4 film. A differential shift of ≈ 40 meV was obtained between samples capped with SiO_2 and Si_3N_4, at annealing temperature of 850 °C.
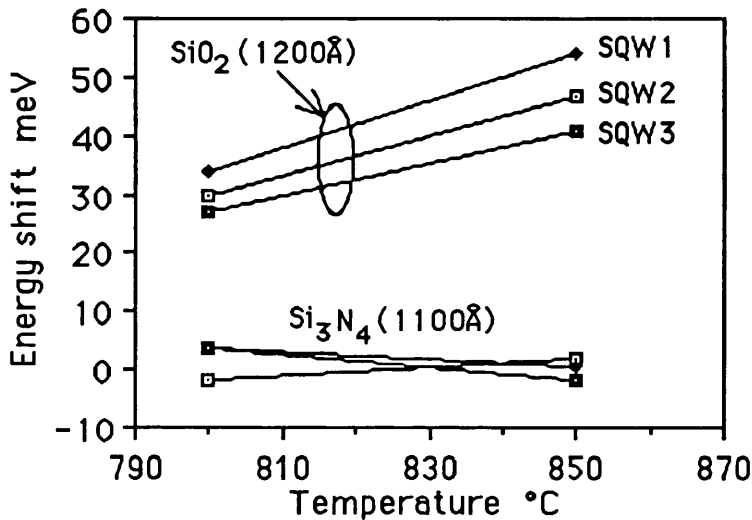
Fig. 4.23 *Energy shift of the hh exciton of the three QWs of B34, in samples capped with SiO2 and Si3N4 dielectric films, as a function of the annealing temperature. The energy shift is relative to the uncoated samples annealed at the same conditions.*

Further measurements were carried out on GaAs/GaAlAs DQWs structure. Fig. 4.24 shows a schematic diagram of the epitaxial layers, it consisted of two wells of 70 Å thick of GaAs and a barrier of 100 Å thick of $Ga_{0.76}Al_{0.24}As$, the two wells and the barrier were sandwiched between two layers of $Ga_{0.76}Al_{0.24}As$ with a 0.32 μm thickness on the top and 300 Å on the bottom. The PL spectrum of the as grown A113 DQW material was measured at 12 K and showed an excitonic transition peak at energy 1.616 eV, referred to the DQWs.

Two sets of samples were partially capped with SiO_2 and Si_3N_4 films of thicknesses of 1800 Å and 1500 Å, respectively (i.e. half of the sample area was coated with either SiO_2 or Si_3N_4 capping while the rest area uncoated). The fabrication procedure was as follow: samples were capped with a SiO_2 (or Si_3N_4), a photoresist mask was used to protect half of the capped area (using optical lithography) and the rest of the capping was etched by using RIE (using C_2F_6 gas). The etching process was performed in a Plasmatech machine using the following conditions:

C$_2$F$_6$ gas flow rate = 19 sccm.

etching pressure = 16 mtorr.

R.F. power = 100 W.

reverse bias voltage = 420 V.

This gave an etching rate of ≈50 nm.min^{-1} for Si$_3$N$_4$, and SiO$_2$. Samples from each set were annealed at temperatures, 800 °C, 850 °C and 88 °C for 30 minutes. Fig. 4.25 shows the e1-hh exciton energy as a function of the annealing temperature. The dash horizontal line, at energy 1.616 eV, indicates the energy of the hh-exciton of the as grown material before annealing. The hh-exciton experienced a blue shift as the samples annealed at temperatures ≥800 °C regardless of whether the sample was capped or not. With reference to Fig. 4.25, the Si$_3$N$_4$ capping film formed a good barrier for Ga outdiffusion, where the hh-exciton energy experienced an average blue shift of only 40 meV over the annealing temperature range. At annealing temperature of 880 °C, a blue shift of 175 meV of the hh-exciton was achieved.

Fig. 4.26 shows the relative shift in the energy of the hh-exciton of the DQWs of the samples capped with SiO$_2$ film and uncoated samples as a function of the annealing temperature. This energy shift was compared to the samples capped with Si$_3$N4. An energy shift of 147 meV and 10 meV were achieved in the samples capped with SiO$_2$ film and uncoated samples respectively, at an annealing temperature of 880 °C.
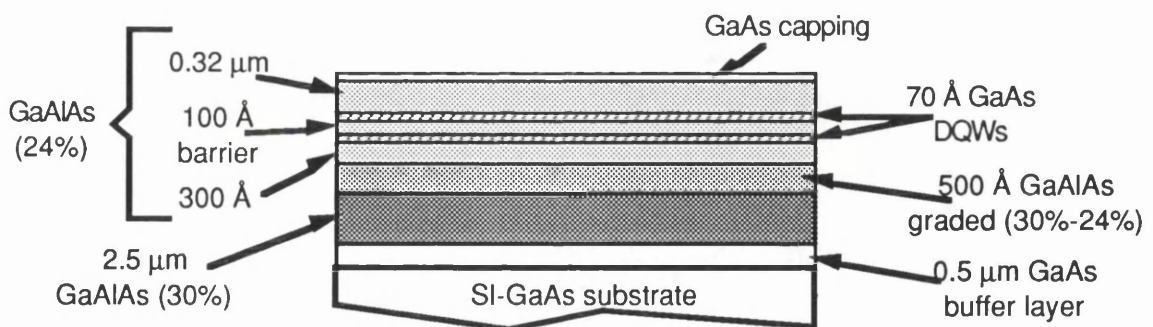
Fig. 4.24 *Schematic diagram of the epitaxial layers of A113 GaAs/GaAlAs DQW structure grown by MBE. The two GaAs QWs have thickness of 70 Å. All layers are undoped and grown on SI-GaAs substrate.*

85
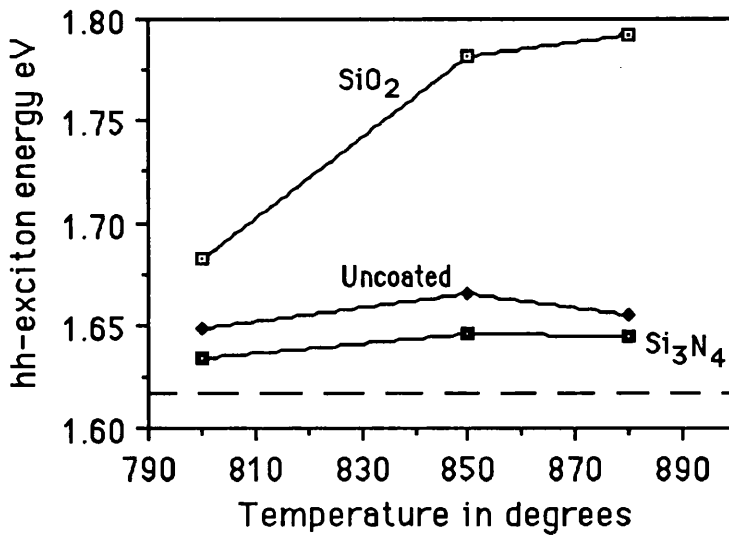
Fig. 4.25 *The hh exciton energy of the DQWs of A113 material as a function of the annealing temperature, for SiO₂ capped, Si₃N₄ capped and uncoated samples.*
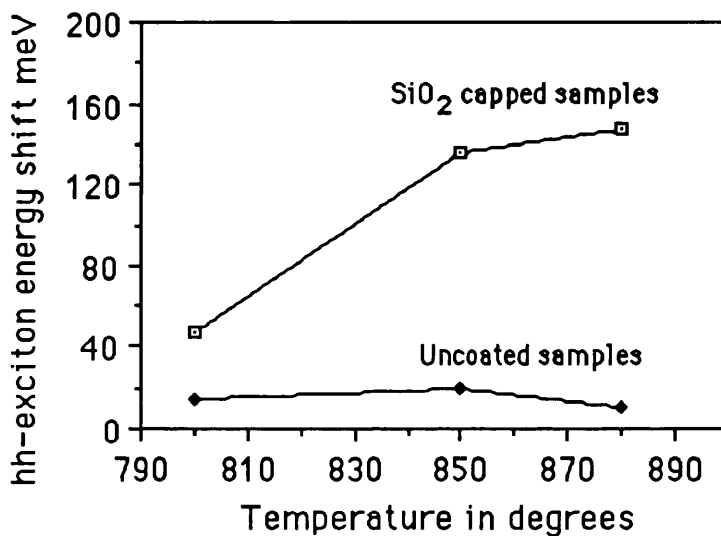
Fig. 4.26 *Energy shift of the hh exciton of the DQWs of A113, in samples capped with SiO₂ and uncoated samples, as a function of the annealing temperature. The energy shift is relative to the samples capped with Si₃N₄ dielectric film, annealed at the same conditions.*

Similar measurements were carried out on a waveguide structure, A187 GaAs/GaAlAs SQW. This material is fully described in section 4.3. Two sets of samples were prepared, one set was partially capped with SiO₂ of 2300 Å thickness and the second set was partially

capped with Si_3N_4 of 2500 Å thickness. The samples were annealed at temperatures 807 °C, 837 °C, 851 °C and 880 °C, for 20 minutes. Fig. 4.27 shows the exciton energy of the SQW as a function of the annealing temperature. In the samples capped with Si_3N_4 film, the hh- and lh-excitons were well resolved in the PL spectra and the energy split of their sub-bands in the valence band increased with the annealing temperature. These results shows no change in the hh-exciton energy, of the uncoated and Si_3N_4 capped samples, over the annealing temperature range (837 °C to 880 °C). The lh-exciton of the Si_3N_4 capped samples was blue shifted with annealing temperature. A large shift in the hh-exciton energy was achieved in the samples capped with SiO_2 film, as the annealing temperature was increased.
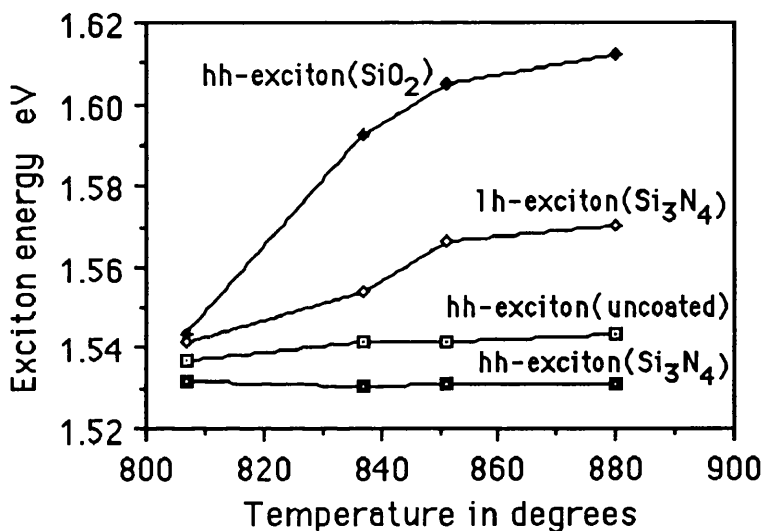
Fig. 4.27 *The hh and lh exciton energies of the SQW of A187 material as a function of the annealing temperature, for SiO_2 capped, Si_3N_4 capped and uncoated samples. The lh excitons of the uncoated and SiO_2 capped samples were not resolved in the PL spectra.*

Fig. 4.28 shows the energy shift, in meV, of the hh-exciton of the SQW of the sample capped with SiO_2 film and uncoated samples, and the lh-exciton energy shift of the samples capped with Si_3N_4 as a function of the annealing temperature. These energy shifts were compared to the hh-exciton energy of the samples capped with Si_3N_4 film which were annealed at the same conditions. At an annealing temperature of 880 °C, an energy shift in the hh-exciton of 81 meV and 10 meV were achieved in samples capped with SiO_2 and uncoated samples respectively.
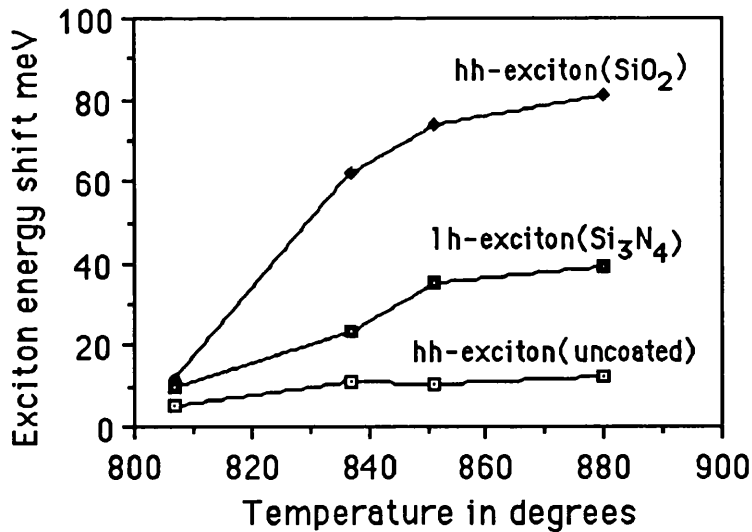
Fig. 4.28 *Energy shift of the hh and lh excitons of the DQWs of A113, in samples capped with SiO2 and uncoated samples, as a function of the annealing temperature. The energy shift is relative to the hh exciton energy of the samples capped with Si3N4 dielectric film, annealed at the same conditions.*

Further measurements were planed to investigate these results in a waveguide geometry by measuring the absorption spectrum for the TE- and TM-modes, but unfortunately we had problems of using the deposition machine due to the damage of the mass flow controllers of the gases. These measurements in a waveguide geometry and the implementation of the vacancies induced disordering technique in the all-optical switching devices are proposed as a future work, in chapter 9.

4.7 Conclusions:

The growth techniques of The GaAs/GaAlAs SQW and MQWs were outlined, and the characterisation techniques of their band structure were presented, using the photocurrent and photoluminescence spectroscopic techniques. In the last section of this chapter we discussed the possible techniques of disordering the band structure of GaAs/GaAlAs QW materials. The vacancies indiffusion disordering technique was employed in this work to obtain a lateral selective disordering and the experimental results showed the effectiveness of such technique to achieve a large shift in the QWs band structures.

References:

[1] D.D. Sell, H.C. Casey, K.W. Wecht, "*Concentration dependence of the refractive index for n- and p-type GaAs between 1.2 and 1.8 eV*", J. Appl. Phys., Vol. 45, No. 6 (1974).

[2] B. Joyce, "*Molecular beam epitaxy growth*", Low dimensional structures summer school, Nottingham (1985).

[3] P. LiKamWa, A. Miller, J.S. Roberts and P.N. Robson, "*130 ps recovery of all-optical switching in a GaAs multiquantum well directional coupler*", Appl. Phys. Lett., Vol. 58, p. 2055 (1991).

[4] J.A. Jennings, "*Electro-optic effects in multiple quantum well GaAs/GaAlAs stripe waveguides*", Ph.D. Thesis, University of Glasgow (1990).

[5] J.I. Pankove, "*Optical processes in semiconductors*", Prentic-Hall Electricall Engineering Series (1971).

[6] G.B. StringFellow, R. Linnebach, "*Photoluminescence of shallow acceptors in epitaxial $Ga_{1-x}Al_xAs$*", J. Appl. Phys., Vol. 51, No. 4 (1980).

[7] "*Properties of Gallium Arsenid*", Datareviews Series No. 2 (Inspec, London).

[8] T.H. Wood, "*Direct measurement of the electric-field-dependent absorption coefficient in GaAs/GaAlAs multiple quantum wells*", Appl. Phys. Lett., Vol. 48, p. 1413 (1986).

[9] D.A.B. Miller, D.S. Chemla, T.C. Damen, A.C. Gossard, W. Wiegmann, T.H. Wood and C.A. Burrus, "*Electric field dependence of optical absorption near the band gap of quantum-well structures*", Phys. Rev. B32, p. 1043 (1985).

[10] K. Yamanaka, T. Fukunada, K.L.I. Kobayashi and M. Ishii, "*Photocurrent spectroscopy in GaAs/GaAlAs multiple quantum wells under a high electric field perpendicular to the heterointerface*", Appl. Phys. Lett., Vol. 48, p. 840 (1986).

[11] D.A.B. Miller, D.S. Chemla, T.C. Damen, A.C. Gossard, W. Wiegmann, T.H. Wood and C.A. Burrus, "*Band-edge electroabsorption in quantum well structures: the quantum confined Stark effect*", Phys. Rev. Lett., Vol. 53, p. 2173 (1984).

[12] R.T. Collins, K.V. Klitzing and K. Ploog, "*Photocurrent spectroscopy of GaAs/GaAlAs quantum wells in an electric field*", Phys. Rev. B33, p. 4378 (1986).

[13] H. Ribot, F. Laruelle and L.A. Coldren, "*Comparison of quantum-confined Stark effect in interdiffused and abrupt GaAs/GaAlAs quantum wells*", Appl. Phys. Lett. 55, p.2526 (1989).

[14] T.Y. Tan and U. Gosele, "*Mechanisms of doping enhanced superlattice disordering and of gallium self-diffusion in GaAs*", Appl. Phys. Lett., Vol. 52, p. 1240 (1988).

[15] M.D. Camras, N. Holonyak, Jr., R.D. Burnham, W. Streifer, D.R. Scifres, T.L. Paoli and C. Lindstrom, "*Wavelength modification of $Al_xGa_{1-x}As$ quantum well heterostructure lasers by layer interdiffusion*", J. Appl. Phys., Vol. 54, p. 5637 (1983).

[16] P. Gavrilovic, D.G. Deppe, K. Meehan, N. Holonyak, Jr., J.J. Coleman and R.D. Burnham, "*Implantation disordering of $Al_xGa_{1-x}As$ superlattices*", Appl. Phys. Lett., Vol. 47, p. 130 (1985).

[17] W.D. Laidig, N. Holonyak, Jr., M.D. Camras, K. hess, J.J. Coleman, P.D. Dapkus and J. Bardeen, "*Disordering of an AlAs-GaAs superlattice by impurity diffusing*", Appl. Phys. Lett., Vol. 38, p. 776 (1981).

[18] K. Meehan, N. Holonyak, Jr., J.M. Brown, M.A. Nixon, P. Gavrilovic and R.D. Burnham, "*Disordering of an $Al_xGa_{1-x}As$-GaAs superlattice by donor diffusion*", Appl. Phys. Lett., Vol. 45, P. 549 (1984).

[19] L.J. Guido, N. Holonyak, Jr., K.C. Hsieh, R.W. Kaliski, W.E. Plano, R.D. Burnham, R.L. Thornton, J.E. Epler and T.L. Paoli, "*Effects of dielectric encapsulation and As overpressure on Al-Ga interdiffusion in AlGaAd-GaAs quantum well heterostructures*", J. Appl. Phys., Vol. 61, p. 1372 (1987).

[20] H. Ribot, K.W. Lee, R.J. Simes, R.H. Yan and L.A. Coldren, "*Disordering of GaAs/GaAlAs multiple quantum well structures by thermal annealing for monolithtic integration of laser and phase modulator*", Appl. Phys. Lett., Vol. 55, p. 672 (1989).

[21] T. Haga, N. Tachino, Y. Abe, J. Kasahara, A. Okubora and H. Hasegawa, "*Out-diffusion of Ga and As atoms into dielectric films in SiO_x/GaAs and SiN_y/GaAs systems*", J. Appl. Phys., Vol. 66, p. 5809 (1989).

[22] M. Kuzuhara, T. Nozaki and T. Kamejima, *"Characterisation of Ga out-diffusion from GaAs into SiO_xN_y films during thermal annealing"*, J. Appl. Phys., Vol. 66, p. 5833 (1989).

[23] J.D. Ralston, W.J. Schaff, D.P. Bour and L.F. Eastman, *"Room-temperature exciton electroabsorption in partially intermixed GaAs/GaAlAs quantum well waveguides"*, Appl. Phys. Lett., Vol. 54 (1989).

[24] D.L. Smith, A.S. Almonda, C.C. Chen, S.E. Ready, B. Wacker, *"Mechanism of SiN_xH_y deposition from NH_3-SiH_4 plasma"*, J. Electrochem. Soc., Vol. 137, p. 614 (1990).

[25] S.E. Hicks, *"An optical emission investigation of Glow discharge processes"*, Ph.D. Thesis, University of Dundee (1991).

[26] D.S. Chemla and D.A.B. Miller, "Romm-temperature excitonic nonlinear-optical effects in semiconductor quantum-well structures", J. Opt. Soc. Am. B, Vol. 2, p. 1155 (1985).

[27] M. Jaros, "Physics and applications of semiconductor microstrucrures", Oxford Science Publications, Clarendon Press, Oxford (1989).

Chapter 5

Fabrication and Linear Characterisation of GaAs/GaAlAs Waveguides

5.1 Introduction:

In this chapter the fabrication details of active and passive optical devices were described, this included photolithography, ohmic contacts and dry etching techniques. The linear characterisation of the straight waveguides and their experimental arrangements were presented. Finally, the high power tunable laser sources and their mode-locking techniques were discussed. These lasers were used to study the nonlinear optical properties of the straight waveguides and the all-optical switching devices.

5.2. Chrome Mask Manufacturing:

A great deal of time and effort were spend to manufacture glass shadow masks using three different approaches.

In the first approach, the layout of the pattern was generated on a Rubylith transparent film using a cutting table. This was used to produce simple patterns, e.g. straight lines. The second approach was used to produce more complicated patterns (Y-junctions and curves with S-bends), the layout of the pattern was a computer-generated on a single-matt transparent Calcomp film. A GKS.UK graphical routines were used on a Vax computer to draw the patterns on a one meter wide Calcomp plotter 1042GT. The generated patterns on these transparent films were reduced (×1/40) onto emulsion plates and then (×1/4) onto a chrome shadow plate to the final required size. In the third approach, masks were fabricated using an electron-beam writer. The required pattern was written directly onto the chrome plate. The technique was made available at the Department towards the end of this project. It produces a high quality masks with high resolution.

5.3 Fabrication of Stripe Waveguides:

Fabrication of small semiconductor devices requires a temperature and humidity controlled environment, with a limited number of dust particles since these particles could critically

mask the processed areas. Therefore fabrication of these devices was done in class 0-100 clean cabinets in a class 1000 clean room. Standard optical lithography was used to define the optical device patterns in a light sensitive resist (i.e. photoresist) spun over the samples. The photoresist can either be a positive image of the pattern which in this case serve as an etching mask or a negative image which was used for further process (lift-off). Rib waveguides were defined by dry etching through the epitaxial layers of the semiconductor material.

The steps used to fabricate GaAs/GaAlAs passive and active rib waveguides are shown in Fig. 5.1, and are as follow:

1) Surface preparation.
2) Coating.
3) Softbacking.
4) Exposure.
5) Development.
6) Etching.

5.3.1 Surface Preparation:

Samples were chemically cleaned to remove dust and other forms of airborne and human contamination. They were then force dried and given a short bake to remove residual surface moisture, permitting good resist adhesion. The samples were chemically and ultrasonically cleaned (using an ultrasonic agitator) as follows:

1) RO water.
2) Methanol (removes water vapour).
3) Trichloroethylene (removes grease).
4) Methanol (removes trichloroethylene).
5) Acetone (removes organic contamination).
6) Methanol (removes Acetone).
7) RO water (removes traces of solvents).

The last stage was followed by blow drying the sample through a 0.45 μm filtered air-gun, leaving a clean surface. The samples were then baked at 90 °C for 5 minutes to remove residual surface moisture.

Active waveguides

Passive waveguides

Coating
Exposing

UV light (dark-filed mask) — Photoresist film

UV light (light-field mask)

n-type ohmic contact

Developing

NiCr etch mask

Evaporation n-type contact then NiCr

p-type ohmic contact

etching mask

Lift-off

RIE using SiCl4 gas

Removal of the etch mask

*Thermal annealing at 360 °C for 45 s to form the p- and n-type ohmic contacts.
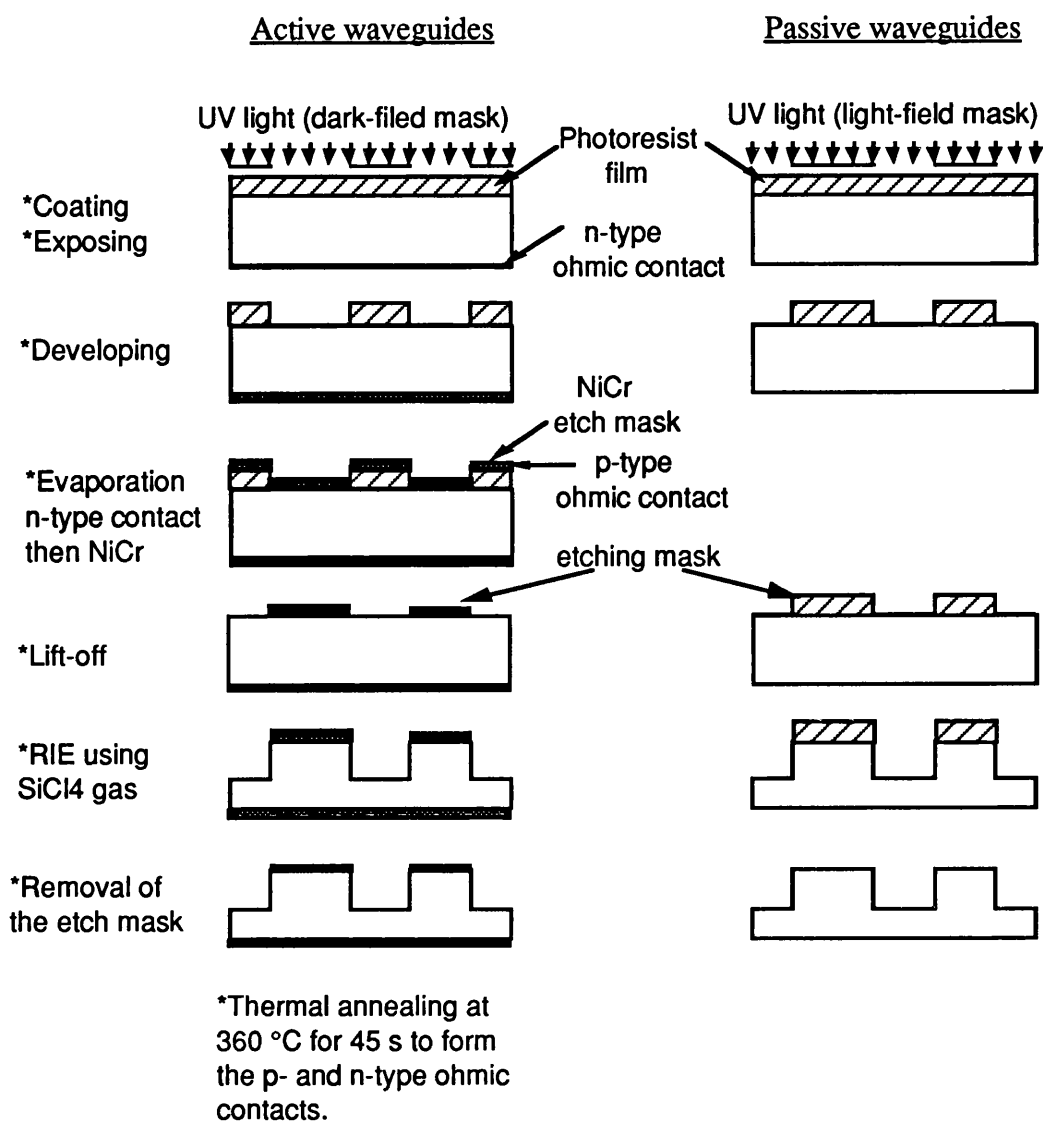
Fig.5.1 *Fabrication steps of active (to the left) and passive (to the right) waveguides.*

5.3.2 Coating:

Two different resists produced by Shipley; AZ1350J and AZ1350 were used. The photoresist was dispensed through a filter (0.45 μm and 0.2 μm respectively) over the sample and spun at 4000 r.p.m. for 30 seconds. This produced an even resist film, except at the corners of the sample, approximately 1.8 μm thick (for AZ1350J) and 0.45 μm thick (for AZ1350). These photoresist were replaced later by S1400-31 (equivalent to AZ1350J) and S1400-17 (equivalent to AZ1350). Thinner resist gives higher resolution with vertical sidewall profiles.

5.3.3 Softbaking:

The samples were softbaked in a fan oven at 90 °C for 30 minutes. During the softbake almost all the solvents were removed from the photoresist, rendering it photosensitive. This is an important part in photo-imaging and number of parameters are determined by it (e.g. adhesion, exposure and development).

Adhesion of the photoresist is partially a function of softbaking. Incomplete softbaking results in poor resist-sample bonding and subsequent lifting of resist images in the developer.

Over softbaked photoresist will degrade the photosensitivity of the resist, due to either reducing the developer solubility or destroying a portion of the sensitiser.

under softbaked resist is readily attacked by the developer in both exposed and unexposed areas.

5.3.4 Exposure:

The resist was exposed to ultra-violet light through a chrome mask using a contact printing. The contact printer arrangement is simple but effective, it involves pressing the sample down on top of the shadow mask by means of a large weight. The exposure time for the thick resist (AZ1350J and S1400-31) was 6 minutes and for thin resist (AZ1350 and S1400-17) was 4 minutes.

A mask aligner was also used in contact printing, it provides the alignment facility of the pattern with respect to the sample. The exposure time for the thick resist was 10 seconds and for thin resist was 4 seconds.

The build up of the photoresist at the sample corners (<30 μm) prevents a hard contact between the photoresist and the chrome mask, which leads to poor quality line definition because of the diffraction of light between the mask and photoresist. Therefore the resist at these corners was removed by webbing it with a cotton-bud soaked in acetone, before exposure to U.V. light.

5.3.5 Development:

The exposed photoresist was developed in a 1:1 solution of AZ developer and RO water (freshly made). After immersion for about 35 seconds, the patterns were fully developed, then rinsed in RO water and blow dried with filtered air-gun. The chrome mask was cleaned after every 2-3 exposures, where it may pick-up pieces of the resist from previous exposures.

Figure 5.2 shows ridge profile of AZ1350J and AZ1350 photoresists, the resist profile was steeper in the thin resist with vertical sidewalls. In both profiles, standing waves are shown in the sidewalls of the resist image. This was due to the periodic variation in the exposing intensity. The periodic intensity variation was caused by the interference between the incident and reflected U.V. light, from the sample surface. The standing waves can be eliminated by treating the sample surface with a thin layer of antireflection coating before coating the sample with photoresist.
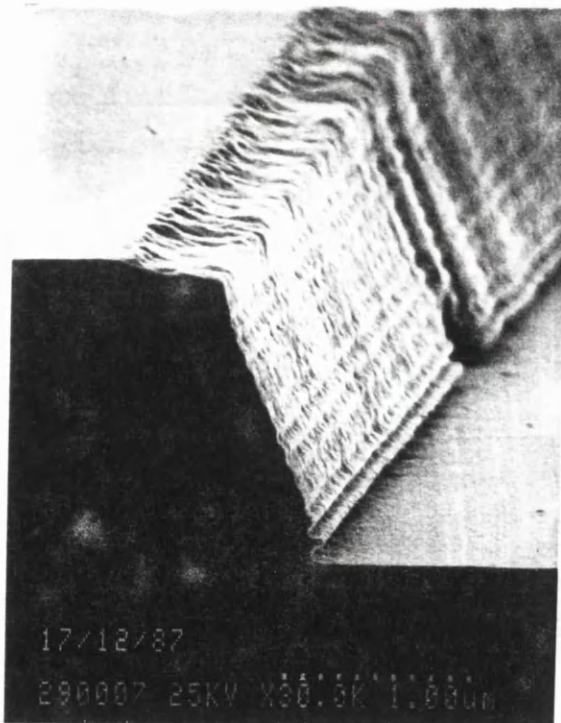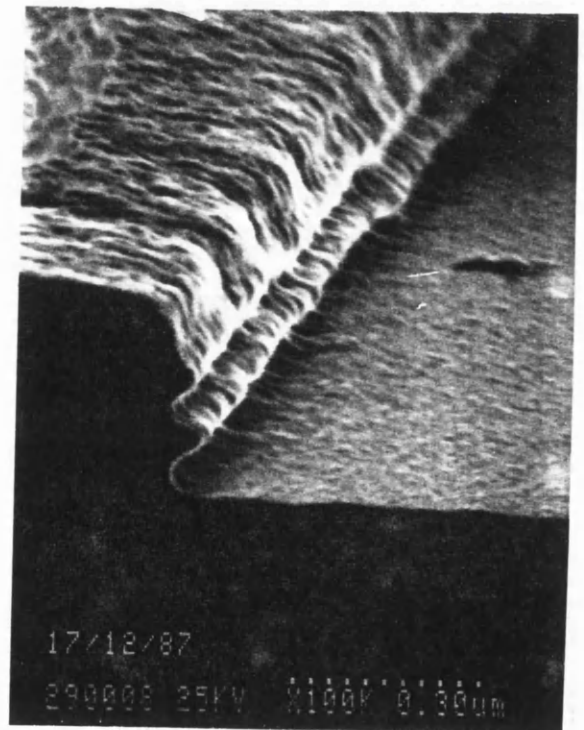
(a)   (b)

Fig. 5.2 *SEM micrograph of a developed ridge profile of a thick photoresist AZ1350J in* (a) *and a thin photoresist AZ1350 in* (b).

5.3.6 Deposition:

Metal deposition was used in two occasions, either as an etch mask (usually a 500 Å of NiCr film) or an ohmic contacts (electrodes) in active devices. The use of the NiCr film in dry etching enhance the etch selectivity between the mask and the substrate compared to the photoresist. Ohmic contacts were usually protected, during dry etching, with a NiCr deposited layer.

Standard photolithography was used to define a negative image of the pattern in the photoresist (by using a dark-field chrome mask), followed by thermal evaporation in an evacuated chamber. The chamber was evacuated down to $\approx$20 mtorr by using the rotary pump and then to $\approx 3 \times 10^{-3}$ mtorr by using the diffusion pump. Metals were placed in a tungsten coils and heated by using a high voltage power supply. Slow deposition rate of 0.2 nm/second were used to ensure uniform deposition. The thickness of the deposited metal was monitored by an Intellimetrics sensor placed close to the sample. It consisted of a crystal which oscillates at a frequency varying according to the thickness of the deposited metal.

The metal mask was $\approx$500 Å thick of nichrome (alloy of 90% nickel and 10% chromium). This gives good dry etching resistance properties and is easy to remove from the sample by wet etching (using 1:1 $HCl:H_2O$).

Lift-Off:

After metallisation the unwanted metal was removed by using a lift-off, leaving a positive image of NiCr film of the pattern on top of the sample. This was achieved by immersing the sample in acetone to dissolve the resist and lift the NiCr layer on top of it, the sample was then rinsed with methanol followed by RO water and blow drying with N_2.

5.3.7 Dry Etching:

Rib waveguide devices are highly sensitive to etch depth and ridge profile. These parameters are difficult to control with wet etching, therefore dry etching was used. Although this method is more controllable, it can produce rough sidewalls and damage in the etched surfaces. These contribute to the propagation losses of waveguides, and therefore dry etching conditions must be optimised to minimise these effects.

Dry etching techniques can be categorised according to the mechanisms involved in the etching process. Ion beam etching IBE [1] is a pure physical process, while plasma etching PE [2] is primarily a chemical process, reactive ion beam etching RIBE and reactive ion etching RIE [3] provide the two means of physical and chemical processes. Since RIE was used in this work, therefore it is described below.

Reactive Ion Etching RIE:

Fig. 5.3 shows a schematic diagram of a RIE system. It was developed from sputtering systems. RF power was applied across electrodes within a vacuum chamber producing chemically active ions plasma from a suitable single gas or mixture of gases. The sample to be etched was generally mounted on the smaller, non-grounded electrode of a pair of parallel-plate electrodes. The rectifing properties of the plasma produce a D.C. self-bias and ions were directed onto the sample across the plasma dark space.
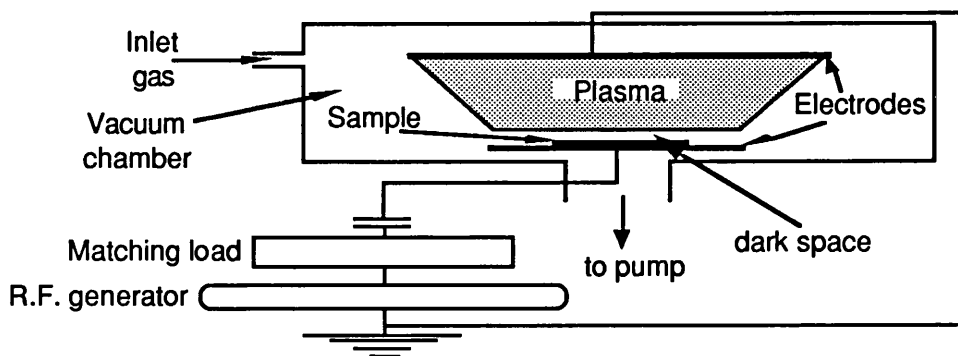
Fig. 5.3 *Schematic diagram of a simple reactive ion etching system.*

Due to chemically active gases being used, etching was partly chemical, producing a material dependent etch rate. However, the ions arrive at the sample after being accelerated across the dark-space, therefore etching is directional. The etch characteristics of RIE depends on a large number of parameters such as RF power, gases partial pressure and the bias voltage.

The patterned samples were etched in a Plasmatech RIE80 reactive ion etcher RIE using a SiCl4 gas with flow rate of 9 sccm and an etch pressure of 12 mTorr. RF power of 100 watts at 13.56 MHz was applied across plates 60 mm apart, the top plate having a diameter

of 180 mm and the bottom 170 mm. The resulting D.C. self-bias was 270 V. The bottom plate temperature was 40 °C.

Figure 5.4 shows an etched samples of GaAs/GaAlAs material using RIE (with $SiCl_4$ gas), the etching masks were AZ1350 and AZ1350J photoresists. The etch rate was 0.17 μm (for GaAs) with vertical sidewalls and smooth surface.

(a)   (b)
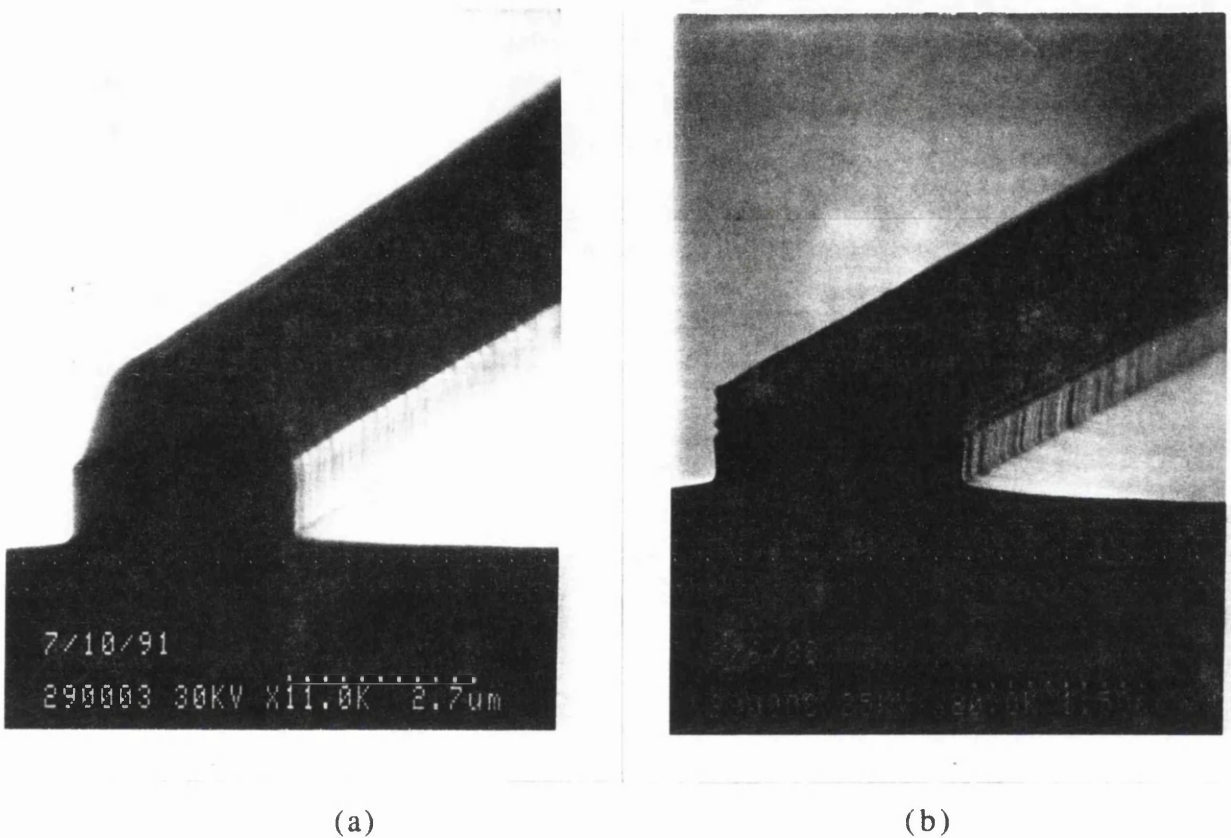
Fig. 5.4 *SEM micrograph of a GaAs/GaAlAs rib waveguide fabricated by using RIE, with $SiCl_4$ gas. The etching mask is AZ1350J in (a) and AZ1350 in (b).*

In waveguides with deep etching, the photoresist mask may deteriorate at the edges. Due to the erosion of the resist mask, the waveguide profile was not rectangular. This is shown in Fig. 5.5, the effective width of the waveguide was smaller than the linewidth of the original pattern. Therefore a metal mask (NiCr) was used, which provides a high etching resistant.

The resist mask was removed subsequently with acetone in ultrasonic agitator. While the NiCr mask was removed using wet etching by soaking the etched samples in a 1:1 mixture of $HCl:H_2O$ for 45 seconds. The samples were cleaved to produce mirror finish end facets.

99
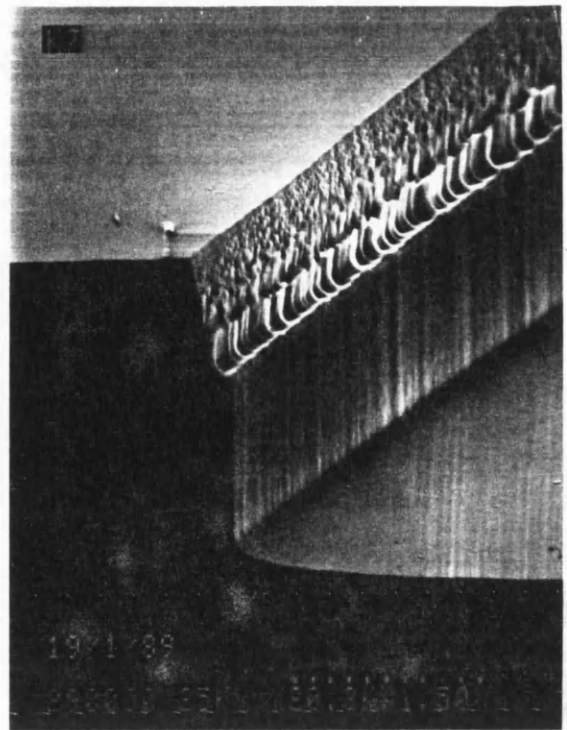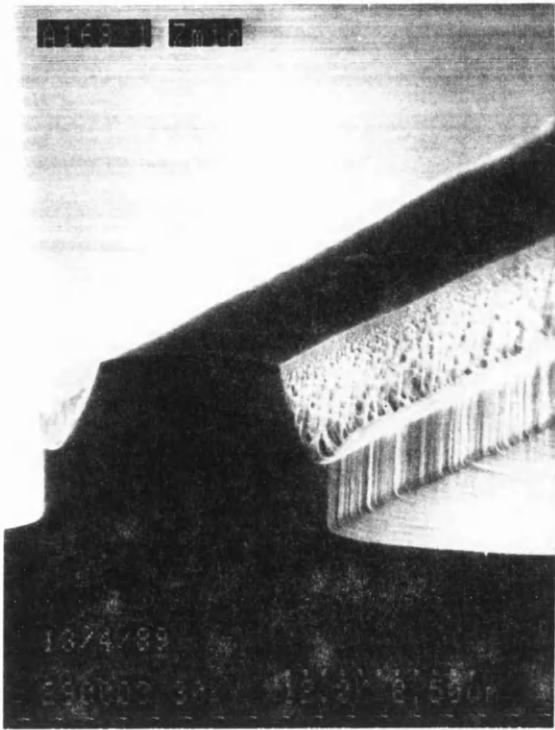
Fig. 5.5 *SEM micrograph of a GaAs/GaAlAs rib waveguide, the edges of the etching mask were deteriorated during the long etching time.*

5.4 Ohmic Contacts:

The fabrication of active optical waveguide devices required metal-semiconductor contacts to enable the application of an electrical power to the device. When a metal is brought in contact with a semiconductor, a potential barrier occurs at the interface originated from the difference in work functions between the metal and the semiconductor. Fig. 5.6a shows the energy level diagrams for a metal and an n-type semiconductor before contact, where the work function of the metal ϕ_m is greater than that of the semiconductor ϕ_s. When the two materials are brought into contact, electrons flow out of the semiconductor into the metal until thermal equilibrium is established and the fermi levels within the metal and n-type semiconductor are equal. The surface of the n-doped semiconductor adjacent to the metal is depleted of free electrons and the energy bands bend upward as shown in Fig. 5.6b. In the case of a p-doped semiconductor, the energy bands bend downwards. Although, in theory, the height of the potential barrier ϕ_B is governed by the work function of the metal, in practice, it is very nearly independent of the metal used. This is because the Fermi-level of the semiconductor is "pinned" at its surface by surface states. The potential barrier produces a rectifying properties and is known as Schottky barrier [4], and the applied voltage drops

100

across the metal-semiconductor barrier. In some active devices, the applied voltage is required to be across the device active region and not the Schottky barrier. In such devices, ohmic contacts were used where the voltage drop across the metal-semiconductor is negligible compared with that across the actual device. In order to achieve this, the doping level in the GaAs at the metal-semiconductor interface should be increased such that the barrier width is reduced and carriers can tunnel through it, as shown in Fig. 5.6c. The highly doped layer can either be grown on top of the structure and/or formed by deposition and annealing of alloy contact containing an element which acts as a donor (in n-type) or acceptor (in p-type) material.
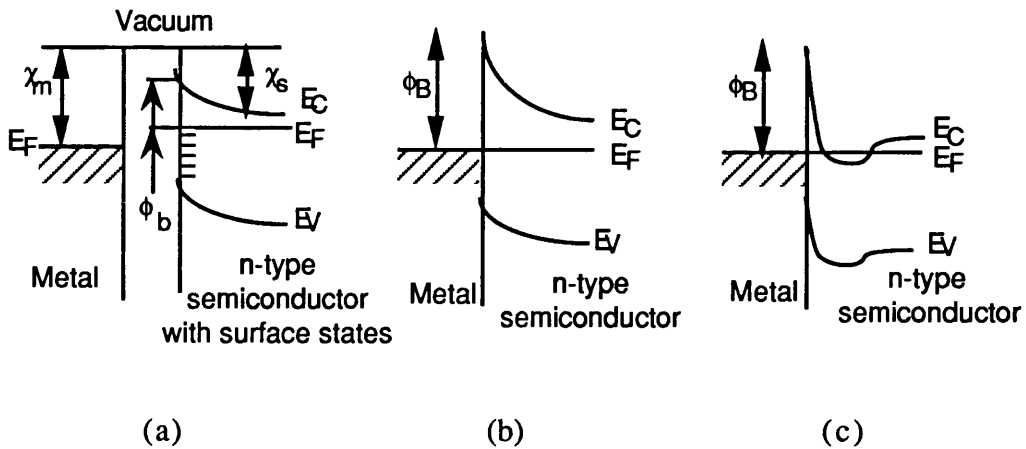
Fig. 5.6 *The energy level diagrams for a metal and an n-type semiconductor with surface states; a) before contact, the work function of the metal χ_m is greater than that of the semiconductor χ_s b) after contact, a Schottky barrier ϕ_B is formed c) thin barrier after thermal indiffusion (annealing).*

Some of the materials used in this project were p-i-n GaAS/GaAlAs quantum well structure, grown on n^+-GaAs substrate. A p-type ohmic contact was evaporated on the top of the active device and n-type ohmic contact on the bottom. The two types of contacts are described below in details.

Fabrication of Ohmic Contacts on GaAs:

Prior to evaporation, samples were cleaned with organic solvents. Oxide reduction was carried out by wet etching using 1:1 of $HCl:H_2O$, which attacks the oxide layer and not the

GaAs. In addition , RF argon plasma cleaning was performed in a vacuum system prior to metal deposition.

The metal composition and thickness for n-type ohmic contact consisted of Au($\approx$850 Å)/Ge($\approx$500 Å)/Ni($\approx$250 Å)/Au(1000-2000 Å). For the p-type ohmic contact, it consisted of Au($\approx$300 Å)/Zn($\approx$300 Å)/Au(1000-2000 Å).

The metals were thermally evaporated in the vacuum system described in section 5.3.6. Ohmic contacts were obtained by annealing the samples at 360 °C for 30 seconds on a graphite heating element in a reducing atmosphere of (5% H_2+95%Ar). During annealing, in n-type contact , Au enhances the out diffusion of Ga (of group III) from GaAs, and Ni (a fast diffuser) greatly enhances the indiffusion of Ge into GaAs [5,6]. Consequently, Ga vacancies were filled by Ge atoms (of group IV) creating a highly doped n-type layer on the GaAs surface, which was necessary for the ohmic contact. In the case of p-type ohmic contact, the Ga vacancies were filled by Zn (of group II). The top layer of Au provided a small sheet resistance and also for the purpose of bonding the optical device.

5.5 Cleaving and Mounting The Optical Waveguides:

To obtain optimum coupling into waveguides, mirror finish end facets were required. This was achieved by cleaving the sample along the crystallographic planes [110] and [1$\underline{1}$0], using a diamond stylus scriber to initialise the cleave.

Active optical devices were bonded onto specially designed p.c.b., with substrate down , using a silver epoxy (Johnson-Mattey). Top contacts of the devices were connected to the p.c.b. mount with an aluminium wires using an ultrasonic bonder. Fig. 5.7 shows a photograph of bonded devices.

5.6 Propagation Loss Mechanisms in Optical Waveguides:

The fabrication of low-loss integrated optical circuits is a necessity for practical applications of such systems. Scattering and waveguide loss can often limit device performance and directly reduces the maximum transmission length of these devices. In this section the optical waveguide propagation loss mechanisms are described and two techniques for loss measurement with experimental results are presented.
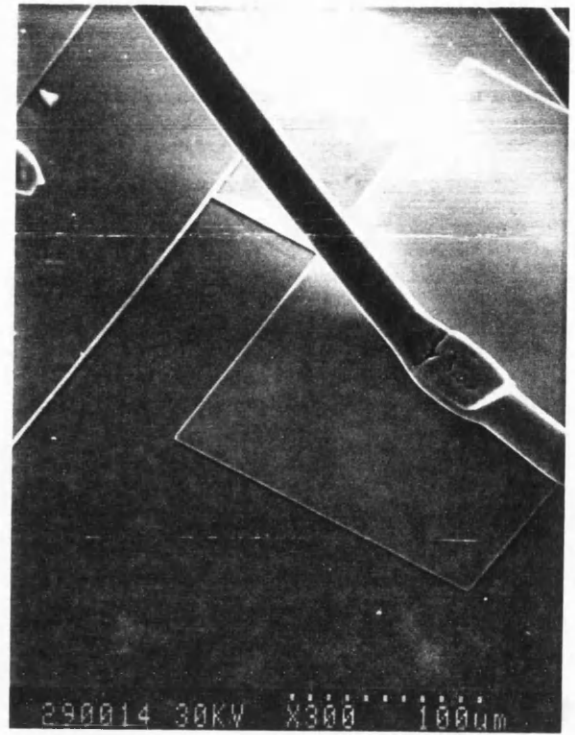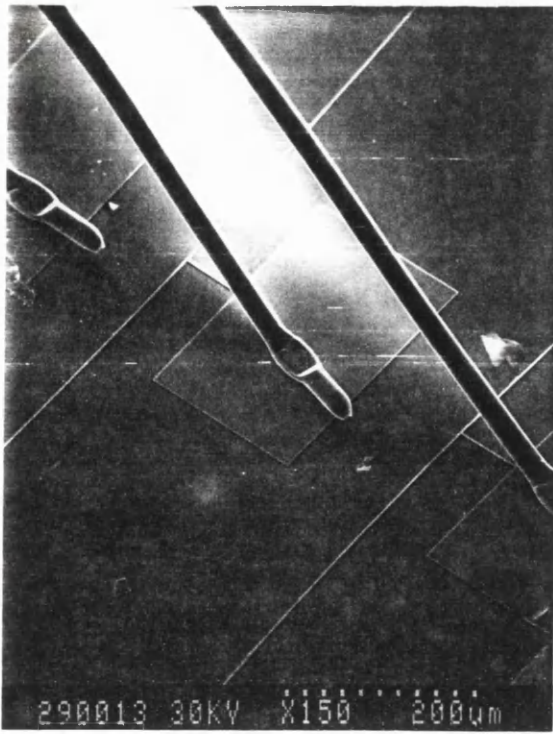
Fig. 5.7 *A photograph of a bonded active device.*

Figure 5.8 shows a schematic diagram of a typical semiconductor waveguide structure. The optical confinement is achieved in the transverse direction due to material compositional change, and in the lateral direction by the effective index difference due to etched rib into the material layers. Optical loss sources in such waveguide (as indicated in Fig. 5.8) can be classed as scattering (1, 2), leakage (3) and absorption (4).
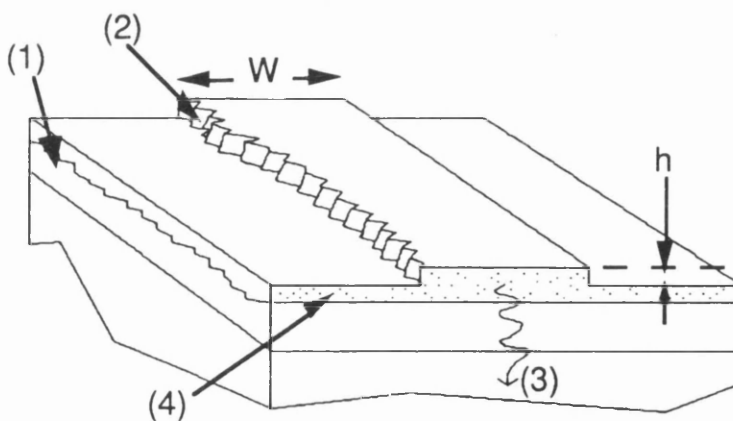
Fig. 5.8 *Schematic diagram of a GaAs/GaAlAs rib waveguide showing the possible propagation loss mechanisms; scattering loss due to roughness in the (1) epitaxial layers interfaces, (2) sidewalls roughness, (3) leaky modes into the substrate and (4) free carriers absorption.*

103

5.6.1 Scattering:

Scattering loss in semiconductor waveguides results primarily from rough interfaces (both epilayer boundaries and etched rib surfaces). Theoretical treatments are available for scattering loss in planar waveguides [7,8], which can be used to estimate the epilayer scattering loss. Scattering of light at a wavelength λ is expected from roughness with spatial period Λ in the range:

$$\frac{\lambda}{(n_1 - n_2)} > \Lambda > \frac{\lambda}{(n_1 + n_2)}$$

where n_1 and n_2 are the effective refractive indices of the guiding and cladding layers.

Tien [9] express the scattering loss α of a symmetric planar guide as:

$$\alpha = \frac{4\sigma^2 h^3}{\beta \left(t + \frac{2}{p} \right)} = \frac{\sigma^2 k_0^2 h}{\beta} \cdot \frac{E_s^2 \Delta n^2}{\int E^2 dx} \qquad (5.1)$$

where σ is the interface roughness, t is the guide thickness, k_0 is the free-space wave number, β is the modal propagation constant, Δn^2 is the difference in dielectric constants between the guiding and cladding layers, and h, p are transverse propagation constants in the guiding and cladding layers respectively.

Equation 5.1 shows that the scattering is proportional to the normalised optical intensity at the guiding-cladding interfaces, $E_s^2 / \int E^2$. In general, epilayer scattering increases with increasing index difference $\Delta n = n_2 - n_1$, decreasing the guiding layer thickness, increasing the mode number and σ^2.

5.6.2 Leakage:

Waveguide losses can also results from leakage of guided light into the substrate. This situation exists in GaAs/GaAlAs material system, where the waveguide structure is grown on GaAs substrate with equal or greater refractive index than the guiding region. To minimise the leakage loss, a thick lower cladding layer of GaAlAs with large Al mole fraction is required [10,11]. The leakage-induced propagation loss of the fundamental TE-mode in a GaAs/GaAlAs single hetrostructure is given by [10]:

$$\alpha \approx \frac{\lambda^3 h p^2 \sin^2(ht) e^{-2pT}}{\pi^3 n \nabla n^2 t} \qquad (5.2)$$

where T is the GaAlAs cladding thickness. In general the loss coefficient due to leakage decreases exponentially with increasing cladding thickness T.

5.6.3 Absorption:

Many semiconductor alloys, exhibit a direct bandgap, and absorb strongly at photon energies close to or above the corresponding band edge. Absorption is also introduced by free carriers. In general, this involves both intraband and interband transitions. The absorption loss of a given waveguide mode depends both on bulk material losses and the overlap of the modal intensity distribution with the absorbing material.

5.6.4 Facet Reflectivity:

Another important parameter in the optical losses of a waveguide is the facet reflectivity. For certain applications, such as travelling wave devices (e.g. our nonlinear Mach-Zehnder interferometer and directional coupler) and distributed feedback lasers [12], it is desirable to reduce the end facet reflectivity also to suppress the multireflections caused by the end facets. This can be achieved by coating the end facets with antireflection dielectric film or multilayer stack [13]. Multireflection in a waveguide cavity can also be reduced by arranging the waveguide such that it meets the end facet at an angle sufficiently large to permit only a small amount of the reflected light to be captured by the waveguide [14,15]. This approach was fully investigated during the course of this work.

5.7 Linear Propagation Loss Measurements:

The simplest method to evaluate the waveguide insertion loss was to measure the output transmission of the waveguide. The ratio of the output to the input optical intensities yields the overall insertion loss, which includes both coupling and waveguide propagation losses. To distinguish between the coupling and propagation losses in a waveguide it was necessary to measure the output transmission as a function of the waveguide length. This method is known as the sequential cleaving method [16]. The major difficulty with this technique was to have the same input coupling to the waveguide. A second difficulty was caused by waveguide end facet reflections, which give rise to resonator effects that significantly complicate the data analysis. As we will see later in this section, resonator attenuation does not vary linearly with guide length, and back-reflected light can cause feedback effects if the light source is not properly isolated [17].

105

In order to overcome the problems with input coupling reproducibility, the waveguide propagation loss can be measured using Fabry-Perot method [18]. This technique relies on cleaved waveguide end facets to form a Fabry-Perot waveguide resonator. The finesse of the cavity is measured by varying the waveguide phase f (i.e. optical path length). This can be achieved by heating the sample, or wavelength [19], or electro-optic modulation tuning [20].

5.7.1 Theory:

In a cavity of length L, the single-pass output transmission power is given by:

$$I = I_i A T^2 \qquad \text{where} \qquad T = (1 - R)$$

where I_i is the incident intensity, A is the material intensity attenuation, T and R are the intensity transmission and reflection respectively. The intensity attenuation factor A can be expressed in term of the waveguide propagation loss α as:

$$A = e^{-2\alpha L}$$

where α is in npr.cm^{-1}. If we assume that A is large so that multireflections are small, then the intensity of the output transmission is given by:

$$I(L) = I_i \gamma (1 - R)^2 e^{-2\alpha L} = I_0 e^{-2\alpha L} \qquad (5.3)$$

where I_0 is the effective input intensity and include terms due to input and output coupling efficiencies. Thus by measuring the output transmission for different lengths and plotting In(I) as a function of L, a straight line with gradient 2α is resulting. The propagation loss usually is expressed in dB/cm, where:

$$2\alpha(\text{npr.cm}^{-1}) = \alpha(\text{cm}^{-1})$$

$$10 \log_{10} e . \alpha(\text{cm}^{-1}) = \alpha'(\text{dB.cm}^{-1})$$

In a waveguide resonator , A is not large and multireflections inside the cavity can not be neglected. The output transmission of the Fabry-Perot cavity can be derived from the

convergent geometric series obtained by adding wave amplitudes due to successive reflections. Assuming a coherent monochromatic light, the output transmission is :

$$T = \frac{I_0 A}{1 - 2AR \cos \phi + A^2 R^2} \tag{5.4}$$

Then resonant and antiresonant output transmissions are given by:

$$T_R = \frac{I_0 A}{(1 - AR)^2} \tag{5.5}$$

$$T_R = \frac{I_0 A}{(1 + AR)^2} \tag{5.6}$$

If R is known but not I_0, then the single-pass loss Γ_k (dB) is readily obtained from the ratio of the Fabry-Perot fringes $K=T_R/T_A$, and is given by:

$$\Gamma_k (dB) = -10 \log_{10} A = -10 \log_{10} \left[\frac{1}{R} \cdot \frac{\sqrt{k} - 1}{\sqrt{k} + 1} \right] \tag{5.7}$$

Similarly, if I_0 is known but not R, the propagation loss may be derived from the single-pass transmission T_S where:

$$T_s = I_0 A = 4 \left[T_R^{-1/2} - T_A^{-1/2} \right] \tag{5.8}$$

$$\Gamma_{T_s} (dB) = 10 \log_{10} \left(\frac{T_s}{I_0} \right) \tag{5.9}$$

Equation 5.7 shows no dependence on the input coupling, and thus coupling reproducibility problems are avoided.

In order to determine I_0 and R and thus obtain absolute loss measurements, it is necessary to cleave sample 1 into two lengths (sample 2 and 3). R should be the same for all three samples so that:

$$\Gamma_1 = \Gamma_2 + \Gamma_3$$

thus

$$I_0 = \frac{T_{s2} \cdot T_{s3}}{T_{s1}} \qquad\qquad (5.10)$$

and

$$R = \frac{F(k_2) \cdot F(k_3)}{F(k_1)} \qquad\qquad (5.11)$$

where

$$F(k) = \frac{\sqrt{k} - 1}{\sqrt{k} + 1}$$

5.7.2 Experimental Arrangements:

5.7.2.1 End-Fire Coupling Technique:

Coupling of light into a waveguide can be achieved in three different ways, prism, grating and end-fire coupling techniques. Prism coupling requires that the refractive index of the prism to be higher than that of the waveguide material. For GaAs waveguides (refractive index ≈ 3.5) it is difficult to obtain a prism with a higher refractive index. The grating couplers are widely used to lunch light into slab waveguides. In both these techniques the coupling of the incident light into a guided mode is achieved by matching the propagation wave vector of the incident light to that of the slab mode. The third technique, used in this work, is the endfire coupling. In this technique, the conversion of the incident light into a guided mode is achieved by matching the field profile of the incident beam to that of the guided mode. The field match can be affected by suitably reducing the input beam so as to conform as closely as possible to the guide mode field profile. Therefore any mismatch in the field profile will lose energy into radiated modes. Also, because the waveguide cross-section area has a dimension of the order of micron, input beam position is critical and requires sensitive micro-manipulation.

5.7.2.2 Experimental Set-up:

The end-fire coupling system used to characterise waveguides is shown in Fig. 5.9. It consisted of two trinocular metalurgical microscopes were coaxially mounted on an optical
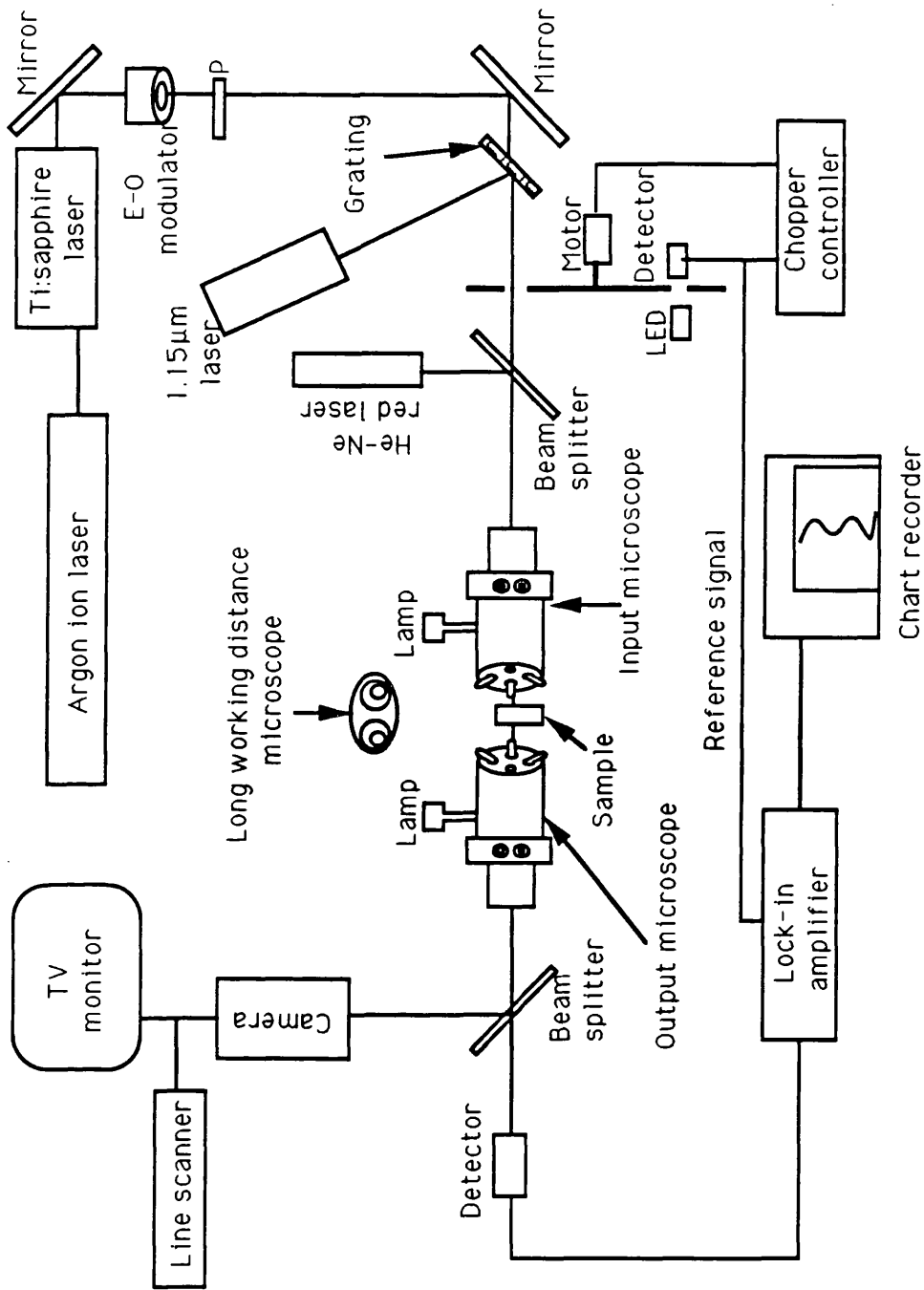
Fig. 5.9 *Schematic diagram of an end-fire coupling system* .

bench to couple the light into and out of the waveguide. A He-Ne laser (λ=0.632 μm) aligned centrally through them. The objective turrets, contain 10×, 20×, 50× and 80× objectives. This allows to change the size of the incident beam for optimum coupling to the waveguide. The sample holder was an arm attached to an x, y and rotation stage which was positioned between the microscopes. This allowed a precise positioning of the waveguide with respect to the incident laser beam. A long working distance, zoom, stereo microscope allowed the top of the sample to be observed when active devices were probed. The eyepieces of the input and output microscopes were used to ensure that the laser is incident on the desired waveguide and also to examine the quality of the input and output end facets of the waveguides.

The propagation losses of stripe waveguides were measured at λ=1.15 μm He-Ne laser. This laser was diffracted from a 600 line/mm grating and aligned with respect to the λ=0.632 μm laser. The grating was used to separate the two wavelengths λ_1=1.153 μm and λ_2=1.162 μm, of the infrared laser. The later line had an intensity of one quarter of that of the former. The intensity profile of the output coupled mode was observed by using a Hamamatsu camera with a data logging computer. This enabled us to examine the waveguide far field mode profile. The output of the waveguide was specially filtered and focused into a Ge detector. The input laser (λ=1.15 μm) was chopped at 1 kHz and the detected signal was send to a lock-in amplifier, and then to a chart recorder.

5.7.2.3 Sample Heating:

To produce the Fabry-Perot resonant/antiresonant cycles, the optical path length of the waveguide was changed. This was achieved by heating the sample, which caused a change in the refractive index as well as the length of the chip. The accuracy of the propagation loss measurement depended on the way the samples were heated. The key point of avoiding any experimental error was by keeping the coupling coefficient of the incident light into the waveguide unchanged while heating the sample. The change in the coupling coefficient was mainly caused by heating the input and/or output objective lenses. This happened when a soldering iron was used as a heat source. Later, this was replaced with a resistor (0.25 W) suspended close to the top of the sample ($\approx$1 mm) as a heat source. By heating the sample to $\approx$12 °C above room temperature, it was possible to trace 6 to 8 Fabry-Perot cycles. The rate of change of temperature on the sample after removing the heating source was measured by using a thermocouple attached to the sample. This is shown in Fig. 5.10, the drop of temperature was exponential with time.
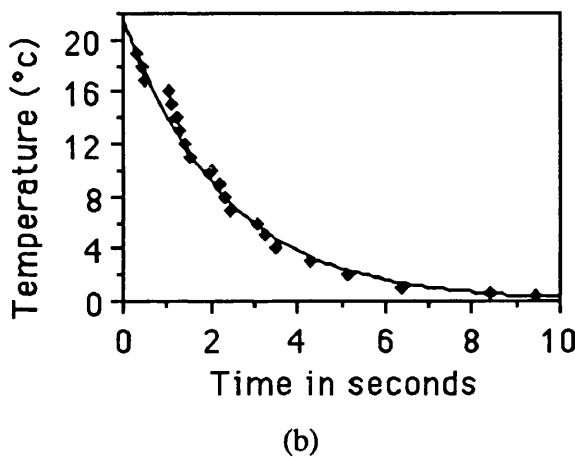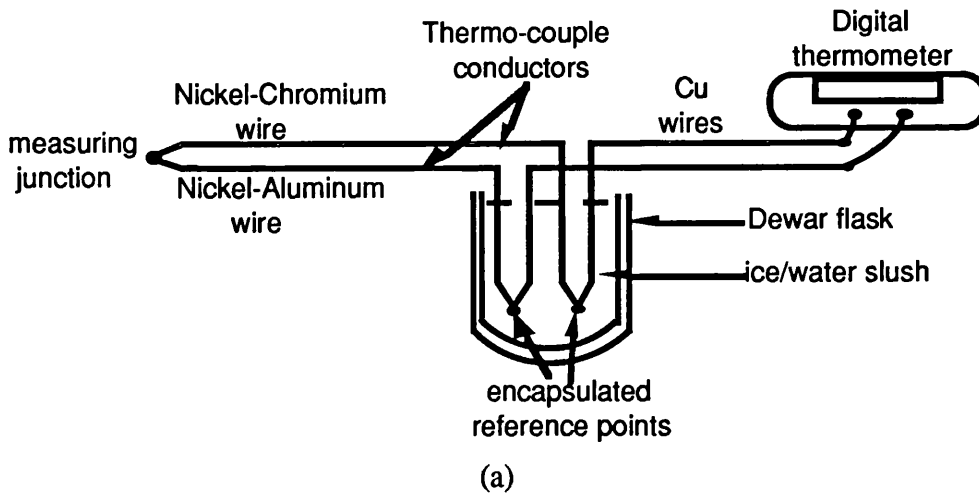
Fig. 5.10 a) *Experimental apparatus to measure the temperature of the sample,* b) *The rate of change of temperature after removing the heat source from the sample.*

Figure 5.11 shows the Fabry-Perot output transmitted resonant cycles produced by the two methods. In Fig. 5.11a, the drift of the cycles during and after heating the sample (using a soldering iron) reflects the change of coupling coefficient of the incident light to the waveguide.

5.7.3 Experimental Results:

The single-mode straight waveguide propagation losses and the end facets reflectivity were investigated as a function of the waveguide and guided mode parameters. These parameters include the waveguide rib width and height, and the tilt angle of the end facets with respect to the longitudinal axis of the waveguide. Fig. 5.12 shows a schematic diagram of a rib

111
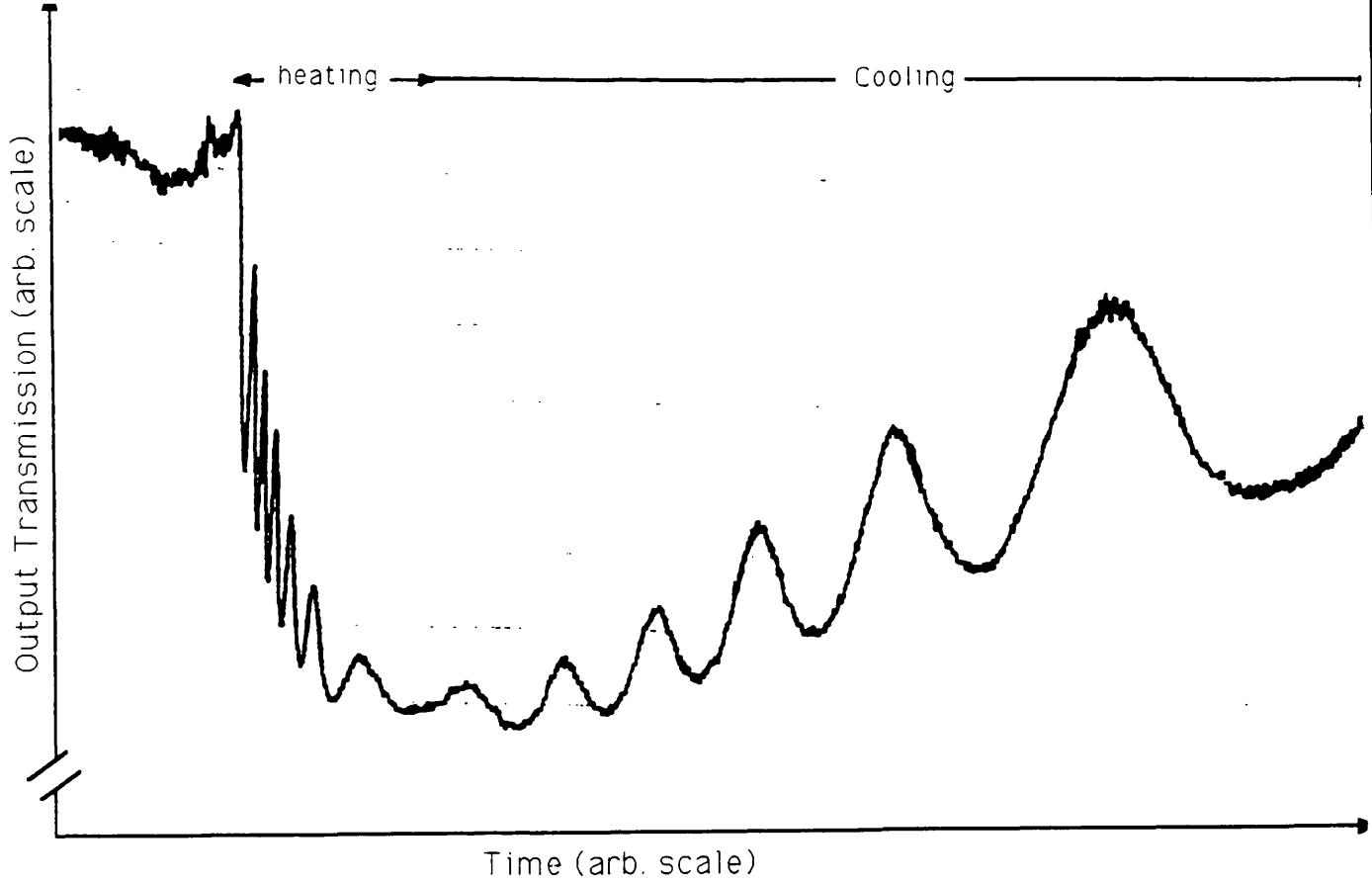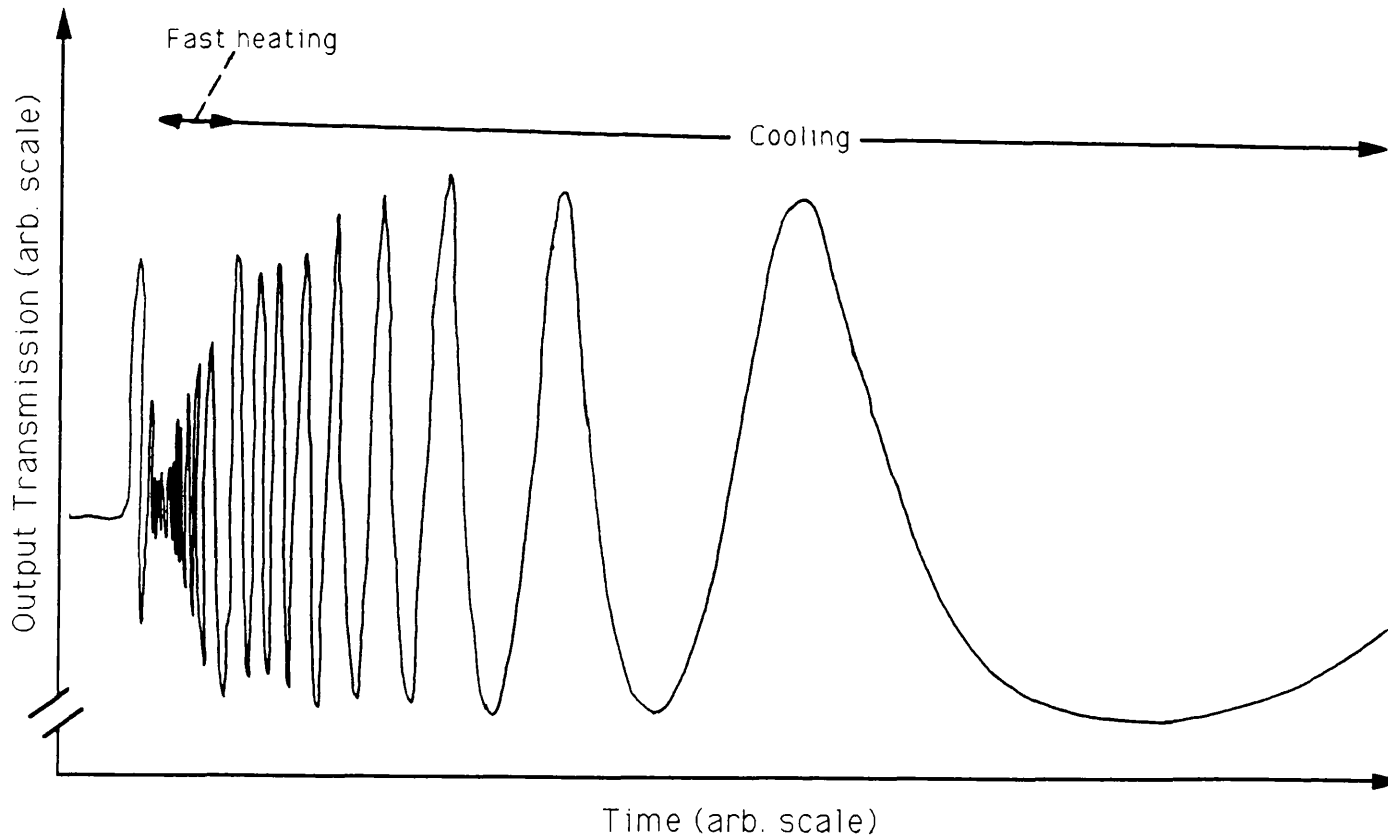
Fig. 5.11 *The Fabry-Perot resonant/antiresonant cycles of a single mode GaAs/GaAlAs*
waveguide cavity produced by heating the samples using a)soldering iron b)resistor.

waveguide with its end facets tilted at an angle θ with respect to the waveguide longitudinal axis and having a rib with W and etching depth t. The waveguide parameters (end facets and propagation losses) were investigated in two wafers, single and double hetrostructure GaAs/GaAlAs materials. Two masks were designed for this purpose.
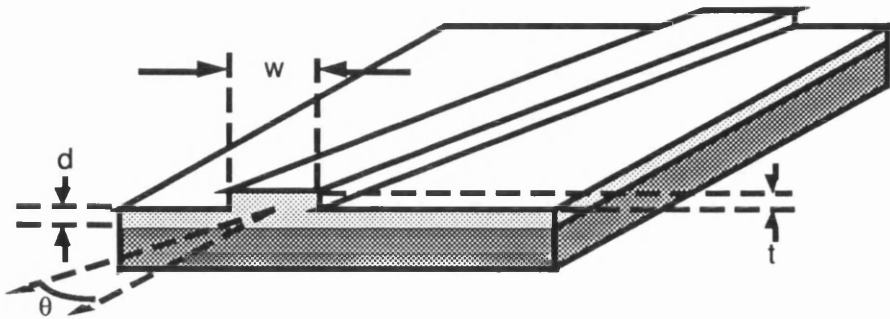
Fig. 5.12 *Schematic diagram of a rib waveguide with a tilt end facets. The longitudinal axis of the waveguide is tilted at an angle θ with respect to the normal to the end facet.*

5.7.3.1 Results in GaAs/GaAlAs Single Heterostructure Material:

A chrome mask was designed to allow studies of the change in the power reflection coefficient of a single mode rib waveguide as a function of the angle θ. The mask consisted of 36 waveguides divided into four sets with 2 μm and 3 μm linewidths. Each set consisted of two straight waveguides (θ=0), while the rest were inclined with angles θ of 0.25°, 0.5°, 1°, 1.5°, 2°, 3° and 4° with respect to the straight lines (almost as in Fig. 5.15, but only half the fan). A straight line with 10 μm linewidth was used to align the pattern with respect to the cleavage plane of the sample.

A GaAs heterostructure grown by MBE was used. It consisted of a 0.85 μm thick GaAs guiding region and a 3 μm thick $Ga_{0.9}Al_{0.1}As$ lower cladding layer. The epitaxial layers were nominally undoped and grown on a semi-insulating (SI) substrate. Optical lithography was used to produce 2 μm and 3 μm linewidth stripes of Shipley AZ1350J photoresist. A mask aligner was used to align the pattern with respect to the cleaved edge of the sample. The quality of the alignment was examined using an optical microscope with a rotation plate which enabled measurement of any offset greater than 2 minutes of arc in the pattern with respect to the cleaved edge. The patterned samples were then etched in a Plasmatech RIE80 reactive ion etcher RIE using a $SiCl_4$ gas. The photoresist mask was subsequently removed

113

with acetone in ultrasonic agitator. These waveguides were designed to be single-mode (using NWAVE program).

From Fresnel's law for plane wave reflection, the facet reflectivity R of these waveguides (at 1.15 μm wavelength) at normal incidence to the cleaved edge was 0.302. The average propagation losses of the 2 μm and 3 μm wide ridge waveguides, with an etching depth of 1 μm, were 7.89 dB.cm^{-1} and 4.86 dB.cm^{-1} respectively with standard deviations of 0.8 dB.cm^{-1} and 0.9 dB.cm^{-1}. These measurements were achieved by using Fabry-Perot method. The waveguides were etched into the cladding region. Therefore, the overlap integral between the optical guided light and the sidewall roughness was high [21], [22]. This gave substantial scattering losses which reflected the high and significant difference in the propagation losses between the 2 μm and 3 μm waveguides.

Assuming that the inclined waveguides on the same sample have the same propagation losses as that of the untilted waveguide, the facet reflectivity was deduced from measurements of the total loss in the tilted waveguide. Fig. 5.13a and Fig. 5.13b shows the reflection coefficient as a function of the angle θ for the 2 μm and 3 μm single mode waveguides respectively. Results have been plotted using the lowest, highest and mean values of attenuation observed in the untilted waveguides.

Intuitively, the oscillations in the facet reflectivity as a function of θ can be explained by interference between the incident and reflected guided fields at the facets. At the tilted end mirror facet, the reflected guided field is multiplied by a phase factor [23] exp(i2$\theta\beta$x), where β is the propagation constant of the guided TE-mode and x is the transverse coordinate of the mode. This difference in phase between the incident and reflected guided waves caused either a constructive or destructive interference depending on the relative phase of the two fields. Thus when a$\theta=\lambda_g/2$, where a is the " half-width " of the mode and λ_g is the guiding region wavelength, one would expect a dip in the reflectivity.

While this explanation seems reasonable, it is difficult to reconcile the observed spacing of the dips in the reflectivity with this explanation. Taking the largest possible value of a=1 μm, θ is 5°; this is much greater than the observed spacing. These anomalous results led us to carry out further investigations of the facet reflectivity as a function of the facet tilting angle for different degrees of confinement of the lateral optical field.

114
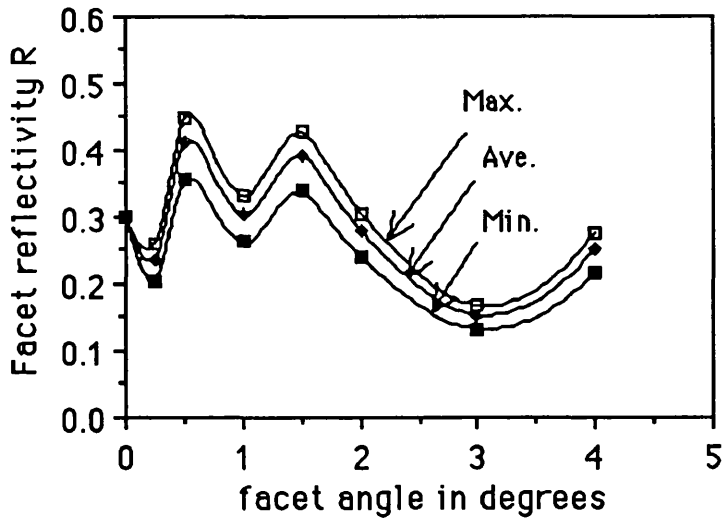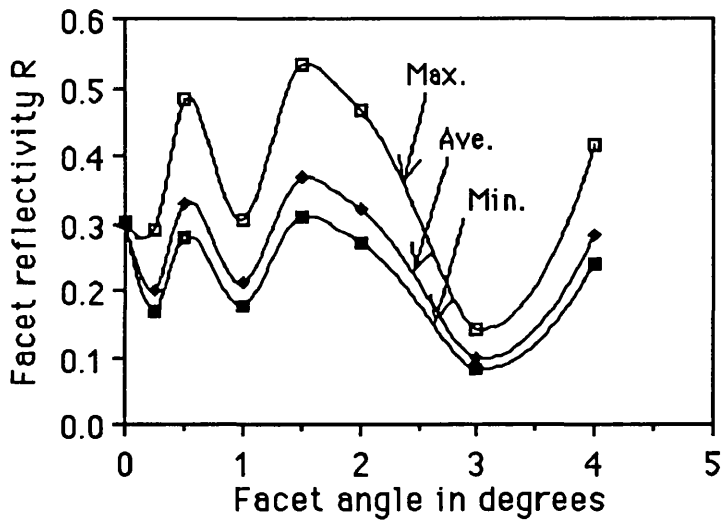
Fig. 5.13 *The end facet power reflection coefficient of a GaAs/GaAlAs heterosture waveguide as a function of the facet tilting angle θ. The waveguide etching depth was 1 μm and the rib width was;* a) *2 μm and* b) *3 μm.*

5.7.3.2 Results in GaAs/GaAlAs Double Heterostructure Material:

The previous chrome mask was slightly modified. The new mask consisted of a set of 2 μm lines in the form of a fan, with inclination angles, θ, of 0.25°, 0.5°, 1°, 1.5°, 2°, 2.5°, 3°, 3.5° and 4°, as shown in Fig. 5.14.

115

10 µm reference line
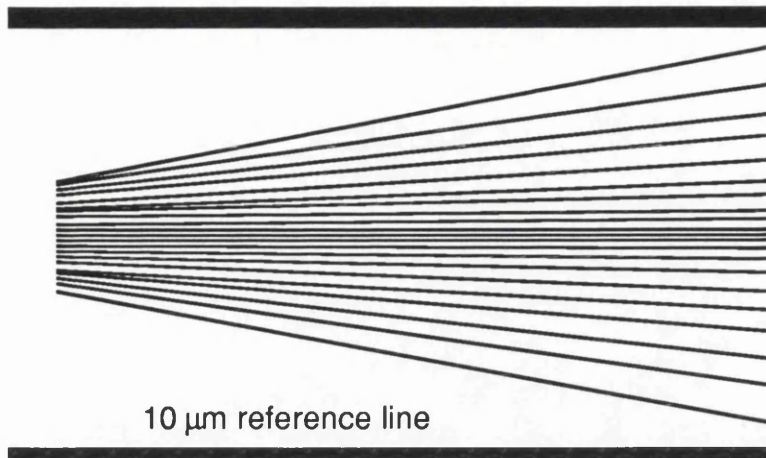
Fig. 5.14 *Schematic diagram of a chrome mask consisted of a set of 2 µm lines in the form of a fan, with inclination angles, θ, of 0.25°, 0.5°, 1°, 1.5°, 2°, 2.5°, 3°, 3.5° and 4°. The 10 µm is used to align the pattern with respect to the cleaved edge of the sample.*

Waveguides were fabricated using the new mask in GaAs/GaAlAs wafer grown by MOCVD at plessey Research (Caswell) Limited (OC396). A schematic diagram of (OC396) wafer is shown in Fig. 5.15. It consisted of 0.8 µm thick GaAs sandwiched between two layers of 0.2 µm thick of GaAlAs. The Al dopant was graded from zero, at the GaAs/GaAlAs interfaces, to 10%. In this structure the effective thickness of the nominally undoped guiding region was 1 µm.
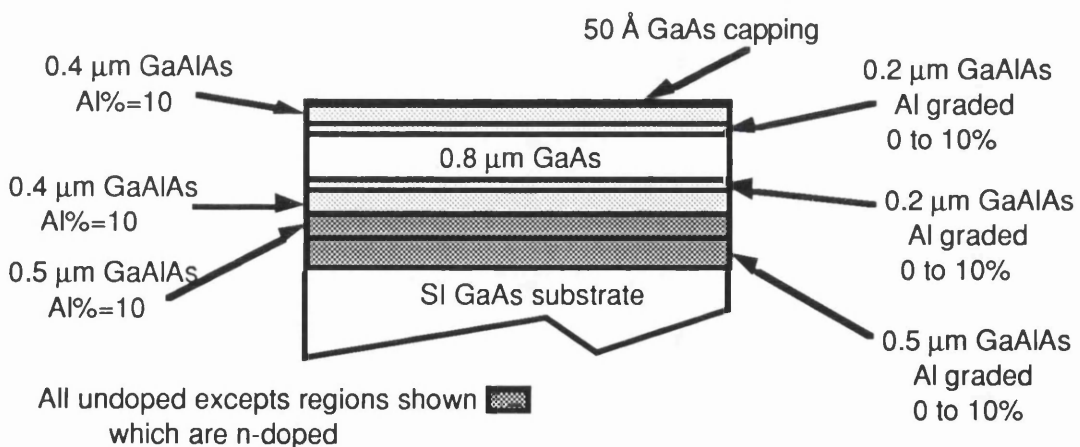
Fig.5.15 *Schematic diagram of a GaAs/GaAlAs waveguide structure, the guiding region effective thickness is 1 µm.*

The lateral optical confinement was varied by changing the etching depth t, as indicated in Fig. 5.12, of the rib waveguide. Three sets of single mode waveguides were fabricated.

In the first set of rib waveguides, the etch depth was 1.13 μm and the adjacent slab thickness was well below cutoff. Sequential cleaving was used to determine the facet reflectivity, using Eq. (5.11), R=0.28. The propagation loss of the untilted 2 μm rib waveguide was 7.15 dB.cm^{-1} with a standard deviation of 0.9 dB.cm^{-1}. The facet reflectivity of the inclined waveguides of this set was measured in the same manner as before. Fig. 5.16 shows the oscillation in facet reflectivity R of the inclined waveguides as a function of the tilt angle θ. The poor facet reflectivity R of waveguides with facet angles θ less than -2.5° was investigated by examining these waveguides using the Scanning Electron Microscope (SEM) and major overgrowth defects were noticed at several points along these waveguides, as shown in Fig. 5.17.
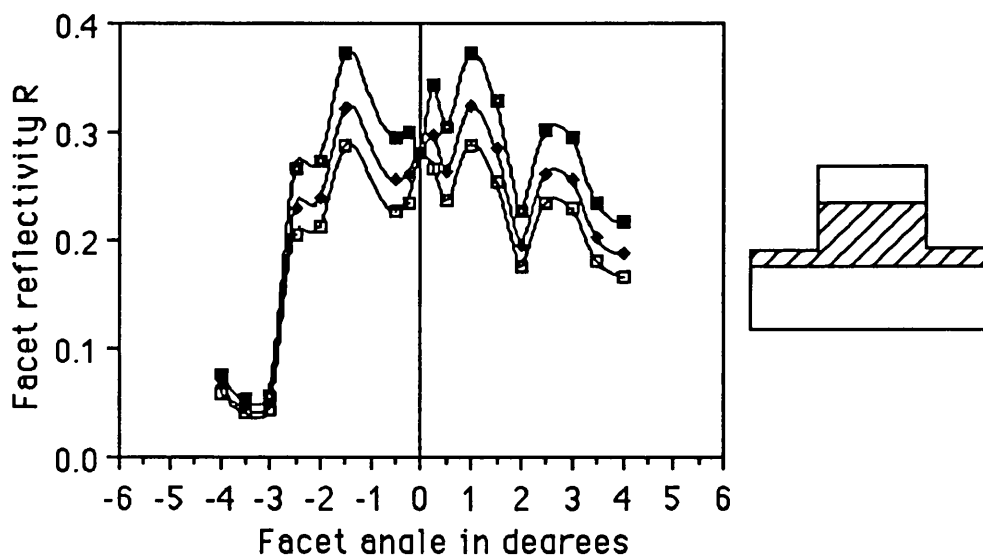
Fig. 5.16 *The end facet power reflection coefficient of a GaAs/GaAlAs waveguide as a function of the facet tilting angle θ. The waveguide rib width and etching depth were 2 μm and 1.13 μm, respectively. The etched slabs thickness is well below the cut-off thickness of the fundamental mode. Results have been plotted using the lowest, highest and mean values of attenuation observed in the untilted waveguides.*

In the second set, the etch depth was 0.35 μm and the slab waveguide sections adjacent to the rib were well above the cutoff thickness. The alignment of this sample was examined under the microscope and it was found that the waveguide pattern was offset by 12 minutes

117

±2 with respect to the cleaved edge. The propagation loss of the nominally untilted 2 μm strip loaded waveguide was 3.4 dB.cm^{-1} with a standard deviation of 0.3 dB.cm^{-1}. The lower propagation losses in these shallow etched waveguides confirm that scattering loss dominated the propagation losses in the more deeply etched waveguides.
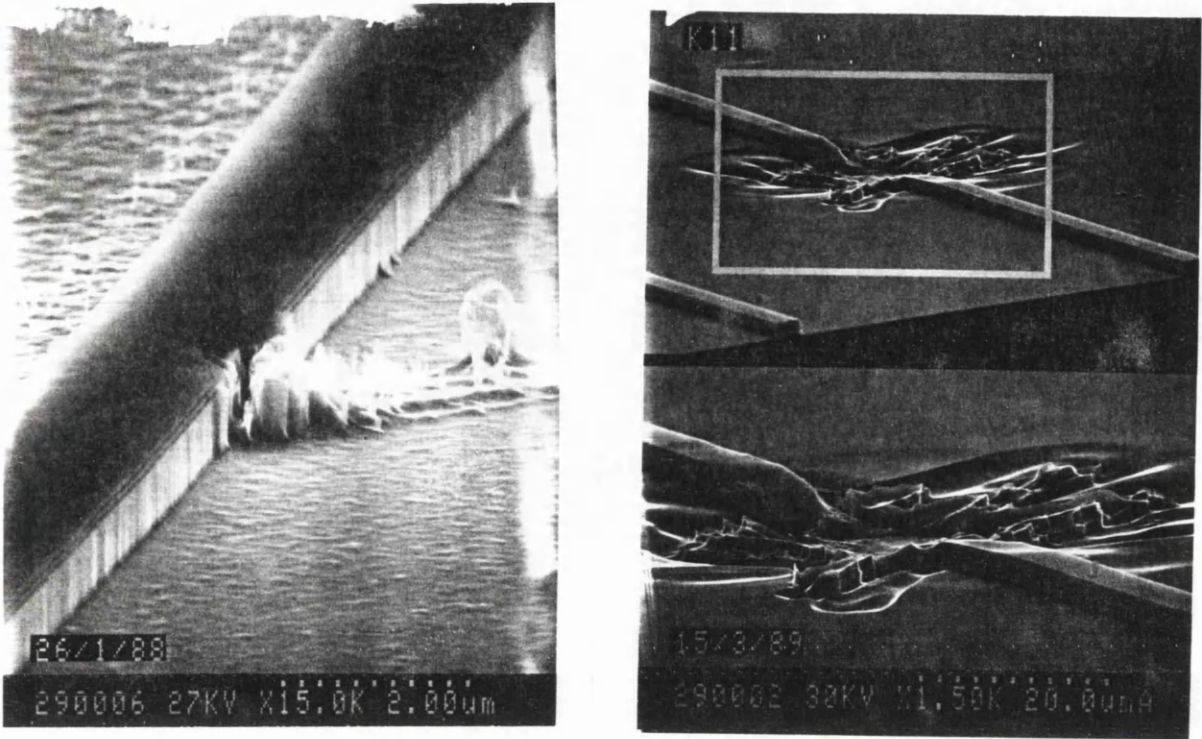
Fig. 5.17 *SEM micrographs showing overgrowth defects.*

The value of R for the inclined waveguides was measured and is shown in Fig. 5.18. The disappearance of oscillations in the facet reflectivity of the inclined waveguides as a function of angle θ was expected. For such shallow rib waveguides a significant part of the light reflected at the tilted facet mirror goes from the rib waveguide into the adjacent slab as a radiated mode and does not contribute to the waveguide Fabry-Perot interference. In other words, The Fabry-Perot finesse of these inclined waveguides becomes monotonically smaller as the facet tilted angle increases.

Marcuse [23] presented a simple theoretical model to calculate the reflection coefficient at a tilted end facet of the lowest order TE-mode of a slab waveguide:

$$R = R_f(\theta) \times \left[\frac{MU^2 \left\{ \left[M^2 - \left(\frac{1}{2}\beta\theta W \right)^2 \right] \frac{\sin(\beta\theta W)}{\beta\theta W} + M\cos(\beta\theta W) \right\}}{(1 + M)\left[U^2 - \left(\frac{1}{2}\beta\theta W \right)^2 \right]\left[M^2 + \left(\frac{1}{2}\beta\theta W \right)^2 \right]} \right]^2 \quad (5.12)$$

where $R_f(\theta)$ is the Fresnel reflection coefficient of a Plane wave that is reflected from the tilted interface of the semiconductor and air. M and U are the normalised transverse propagation constants of the wave in the core and the slab of the waveguide, respectively.

$$M = \tfrac{1}{2} W \left(\beta^2 - n_2^2 k_0^2 \right)^{\frac{1}{2}}$$

$$U = \tfrac{1}{2} W \left(n_1^2 k_0^2 - \beta^2 \right)^{\frac{1}{2}}$$

k_0 is the free space wave number, n_1 and n_2 are the effective refractive indices of the slab and core of the waveguide. In rib waveguides, the EIM was used to calculate the effective refractive indices.

This theory is applicable to waveguides with shallow rib height, where the EIM gives approximate results of the effective indices. As the rib height increases (i.e. larger etch depth), Marcuse model was not applicable and did not explain the experimental results of the tilted facet reflectivity. Fig. 5.18 shows the theoretical data plotted along side with the experimental results of the facet reflectivity, of the shallow etched tilted waveguides, as a function of θ.
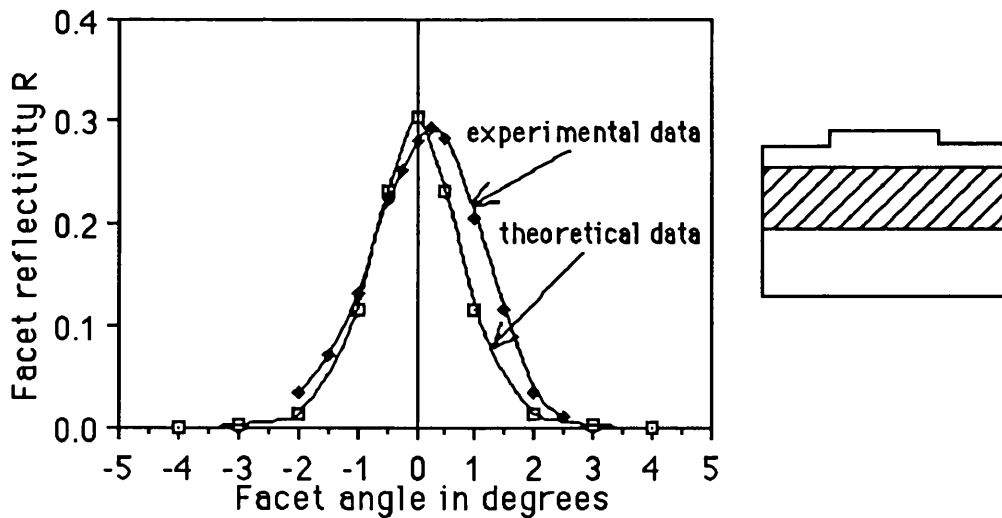
Fig. 5.18 *The end facet power reflection coefficient of a GaAs/GaAlAs waveguide as a function of the facet tilting angle* θ. *The waveguide rib width and etching depth were 2 μm and 0.35 μm, respectively. The etched slabs thickness is well above the cut-off thickness of the fundamental mode.*

The last set of rib waveguides was intermediate between the first two sets, with an etch depth of 0.65 μm. In this set the adjacent waveguide slabs were just above the cutoff thickness. The propagation losses of the untilted 2 μm single mode waveguides were measured to be 3.46 dB.cm^{-1} with a standard deviation of 0.5 dB.cm^{-1}. Fig. 5.19 shows the power reflection coefficient as a function of θ. The decaying oscillation in the facet reflectivity is thought to be due to the combination of the two effects seen in the first two sets of waveguides. In Fig. 5.19, resonant cavity effects are clearly suppressed at a facet angle greater than 3°.
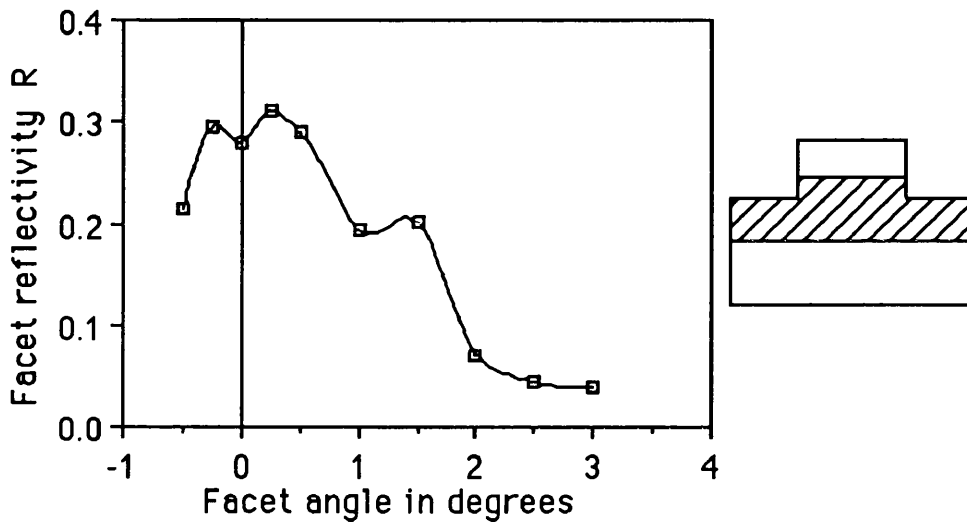
Fig. 5.19 *The end facet power reflection coefficient of a GaAs/GaAlAs waveguide as a function of the facet tilting angle θ. The waveguide rib width and etching depth were 2 mm and 1.13 mm, respectively. The etched slabs thickness is close to the cut-off thickness of the fundamental mode.*

5.7.4 Conclusions:

We have found that the propagation loss was larger for deeply etched waveguides. This was due to the increase in scattering loss from the roughness in the sidewalls of the waveguide, where the overlap integral between the optical guided light and the sidewall roughness was greater.

The facet reflectivity of GaAs/GaAlAs single mode rib waveguides was measured as a function of the tilting angle θ between the longitudinal axis of the waveguide and the normal to the facets and also as a function of the lateral optical field confinement. The lateral

optical confinement was controlled by changing the etching depth of the waveguide adjacent slabs (i.e. rib height).

We have seen from the experimental results, that the facet reflectivity of the single mode waveguide changes dramatically with the facet tilting angle as well as the lateral optical confinement of the waveguide. In other words, the mirror reflectivity of the waveguide end facets was a strong function of the waveguide parameters and the consequent modal parameters.

5.8 Tunable Laser Systems:

A laser usually consists of a gain medium enclosed within an optical resonator. The optical radiation circulating inside the resonator is confined to well defined modes, characterised by the field distribution transverse to the laser beam propagation direction. The laser output can be confined to operate in the most fundamental transverse mode (TEM$_{00}$ mode) by inserting an aperture or careful alignment of the resonator.

The laser resonator is a closed optical loop and a standing wave is established where an integral number of half wavelengths fit into the cavity, ensuring a node at each mirror. Considering the cavity by itself for the moment, an infinite number of discrete longitudinal modes may exist for this single TEM$_{00}$ transverse mode. The longitudinal resonance condition for any optical cavity is:

$$L = n\frac{\lambda}{2} \qquad n = 1, 2, 3, \ldots$$

or equivalently

$$\upsilon = \frac{c}{\lambda} = \frac{nc}{2L}$$

where L is the optical cavity length, λ is the optical wavelength v is the optical frequency, c is the speed of light and n is an integer.

Hence, the frequency separation between two adjacent output frequencies is $\Delta v = c/2L$. Thus the optical cavity support laser action at every wavelength for which the optical path is an integral number of wavelengths in length. The actual oscillating frequencies are those for which the unsaturated gain is larger than the intracavity losses. Fig. 5.20 shows the axial modes with a gaussian distribution of the mode amplitude.

121
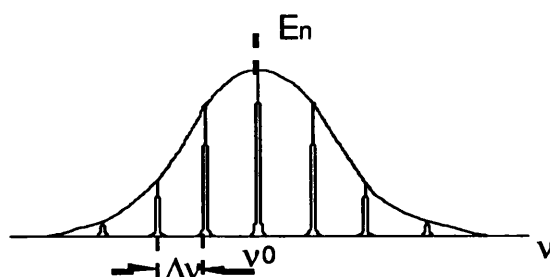
Fig. 5.20 *Gaussian spectral amplitude distribution imposed on the longitudinal modes of a resonator.*

Single frequency operation can be obtained, generally by using intracavity optical elements, when all the axial modes but one have been suppressed.

In the early stage of this project a CW tuneable dye laser was used, this was replaced later by a Ti:sapphire laser. The later laser system was mode-locked and used in the nonlinear resonant experiments. The nonlinear nonresonant experiments were performed by using a colour-centre laser (KCl:Tl), at St. Andrews University. In the following sections, the dye and Ti:sapphire laser systems are described.

5.8.1 Dye Laser System:

The dye laser resonator (Spectra-Physics Model 375B) consisted of three mirror-folded cavity. A fourth mirror focuses the incoming pump laser beam (Ar^+-ion laser) into a high velocity horizontal dye jet, as shown in Fig. 5.21. The dye is in liquid solution form and pumped through a nozzle so as to form a thin and flat jet oriented at Brewster's angle with respect to the intracavity beam to minimise intracavity reflection losses. Upon excitation with the intense pump beam, a population inversion between ground and first excited state of the complex organic dye molecules is achieved. The dye solution then act as a gain medium for amplification of the spontaneous emission (fluorescence) of the dye molecules returning to the ground state. Since this relaxation occurs into the quasi continuum of ground state vibrational levels, the fluorescence has a continuous character and laser action can be obtained over a broad wavelength range. A tuning element was inserted in the intracavity space near the output coupler. It consisted of three birefringent plates of crystalline quartz tilted at Brewster angle. The dye laser linewidth was ~60 GHz. The

output beam depends greatly on the characteristics of the pump beam, which should be TEM$_{00}$ and vertically polarised.
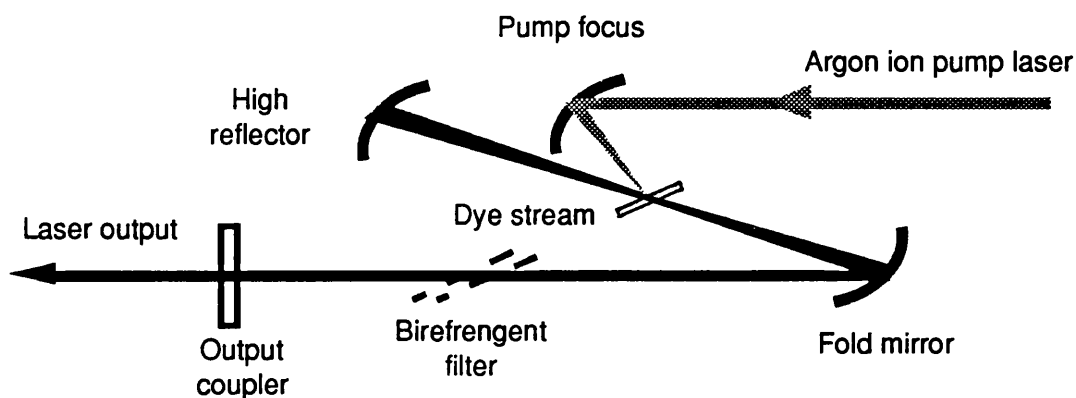
Fig. 5.21 *Three mirror-folded cavity of a dye laser.*

The dye used in this work was styryl 9, and pumped with a 5 watt all-lines Ar$^+$-ion laser. The spectrum range of the laser was from 824 nm to 865 nm, and scaned by a motorised driver unit attached to the micrometer control of the birefringent filter. The laser output intensity was checked over the spectrum and was found to be flat ~50 mwatt.

5.8.2 Ti:sapphire Laser System:

The Ti:sapphire laser resonator (Spectra-Physics model 3900) consisted of a four mirror folded cavity, as shown in Fig. 5.22. The gain is obtained by having a high inversion density and sufficient length of Ti:sapphire material. A high inversion density comes from having a high pump intensity and a high Ti^{3+} ion concentration.

A high inversion density over the entire volume of the Ti:sapphire rod (several millimetres in diameter) is difficult. Therefore, the pump light was focused to a narrow line within the rod and the oscillating laser mode was similarly focused and overlapped within the same volume.

However, unlike the typical dye laser, in which the pump light illuminates a thin dye stream at a small angle of incidence, the pump illumination in the Ti:sapphire laser must be collinear to the cavity mode over a relatively long length of the laser rod. If the typical three-mirror cavity of the dye laser, Fig. 5.21, was used with the Ti:sapphire laser, the pump and

cavity modes would overlap at one of the fold mirrors, making laser alignment difficult. Therefore an additional collimated leg was used in the model 3900 laser and the remaining pump beam was dumped through one of the fold mirrors.
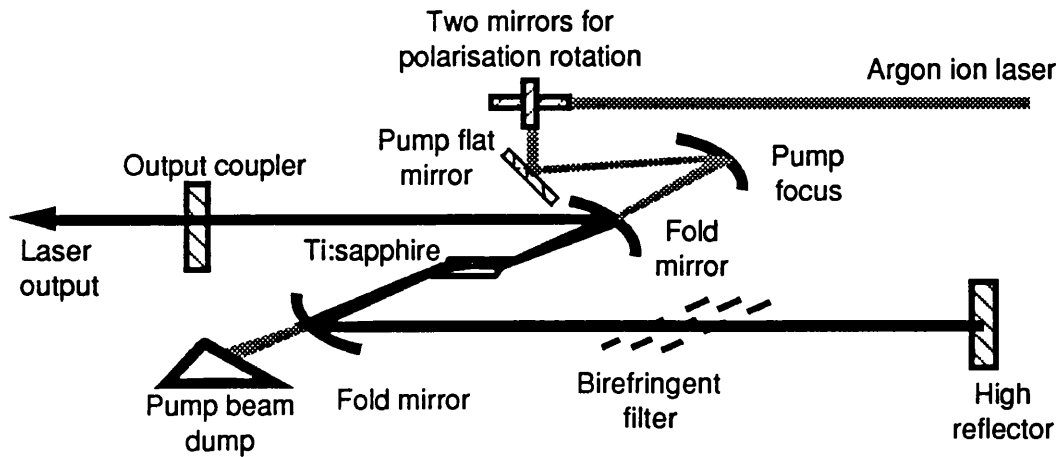
Fig. 5.22 *A four mirror-folded cavity of a Ti:sapphire laser.*

The Ti:sapphire laser was pumped with a 5 watt all-lines Ar^+-ion laser (Spectra-Physics model 2016). The emission spectrum of the laser was from 660 nm to 1100 nm, five sets of mirrors can be used to cover the whole spectrum. In our experiments, the middle set of mirrors was used which cover the range from 800 nm to 900 nm. A three birefringent plates were placed close to the high reflecting mirror, at Brewster angle. The output power of the laser was ~800 mwatt, this was deteriorate with time to ~250 mwatt due to the contamination of the mirrors and rod surfaces. Therefore a regular cleaning of these surfaces, with a microscopic grade methanol, was required.

5.9 Ultrashort Pulse Laser System:

In the previous section, we have seen that lasing action takes place at discrete longitudinal modes separated in frequency by:

$$\Delta \upsilon = \frac{c}{2L}$$

Each oscillating mode is independent of any other and the output of the laser fluctuates in time as the modes interfere in a random manner due to perturbations within the gain medium. By forcing the modes to maintain a fixed phase relationship, the output becomes

periodically modulated as a train of short pulses, each separated by the round trip time of the cavity (2L/c). The laser is then said to be phase locked or more commonly, mode-locked [24,25]. Mode-locking may be accomplished by periodically modulating the cavity losses or the gain, which creates sidebands on each of the cavity modes. If the modulation period concides with the cavity round trip time, the sidebands will overlap with the adjacent cavity modes and injection locking effects lead to strong mode coupling and cause phase-locking of the longitudinal modes. The duration of each pulse and peak intensity, depends on the number of modes N that are phase-locked.

From simple fourier theory, the duration of mode-locked pulses, τ_p, is inversely proportional to the oscillating bandwidth δv:

$$\tau_p = \frac{B}{\delta_v}$$

where B is a constant and depends on the exact shape of the pulse.

The production of short optical pulses by means of laser mode-locking, requires the insertion of an external element into the laser resonator. The external element initiate and maintains the proper coupling between the axial modes. If the mode-locking device must be driven by a source of energy external to the laser, the method is called active mode-locking. If no other energy than the energy available in the laser oscillator is required, then the method is called passive mode-locking.

5.9.1 Active Mode-Locking:

Active mode-locking can be obtained by intracavity loss or gain modulation or frequency modulation [24,26]. These techniques are briefly outlined below.

5.9.1.1 Acousto-Optic Loss Modulation:

The acousto-optic AO modulator is the most widely used intracavity loss modulator, and based on the diffraction of light by ultrasound wave [27]. Fig. 5.23 shows a schematic diagram of an AO modulator, a radio frequency RF signal is applied to the transducer attached to a crystal of quartz. An ultrasonic standing wave is set-up in the crystal modulator due to the refractive index variations, which cause a diffraction of the incident

125

light. Twice every RF period, the standing wave collapses and the modulator then appears as a low loss element within the cavity. Thus the AO modulator acts as an optical shutter.
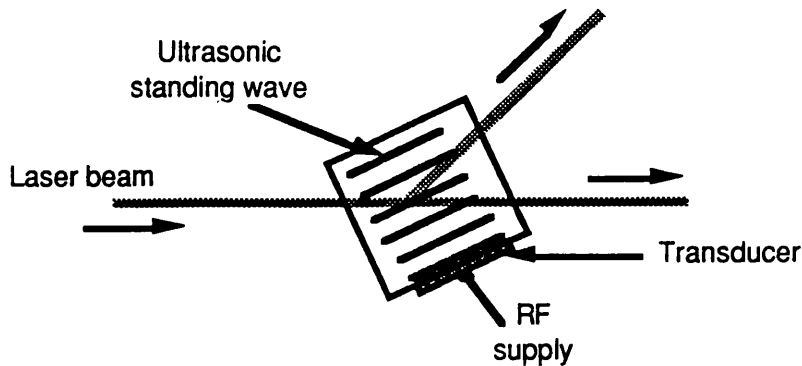
Fig. 5.23 *Schematic diagram of an AO modulator, a RF signal is applied to the transducer attached to the quartz crystal.*

By setting the RF frequency to half the inter-mode spacing Δv of the resonator, mode-locking of the laser can be thought to arise due to the shutting action (in time domain) or due to generation of the sidebands at the cavity mode spacing (in frequency domain). The degree of mode-locking is a function of the diffraction efficiency and can be enhanced by increasing the RF power.

5.9.1.2 FM Mode-Locking:

Frequency modulation FM of a laser may also be used to produce mode-locked pulses [28]. An FM modulator, such as an electro-optic phase modulator, will generally cause the circulating radiation to receive a doppler shift proportional to $d\phi/dt$ where $\phi(t)$ is the intracavity phase modulation. Successive passes through the modulator eventually push the energy outside of the gain bandwidth. If the laser pulse passes through the modulator at a stationary point in phase, then no doppler shift is imparted and the modulator appears transparent,as shown in Fig. 5.24. Note there are two stationary points which cause an uncertainty in the mode-locked pulse position and may result in double pulsing and instability.

126
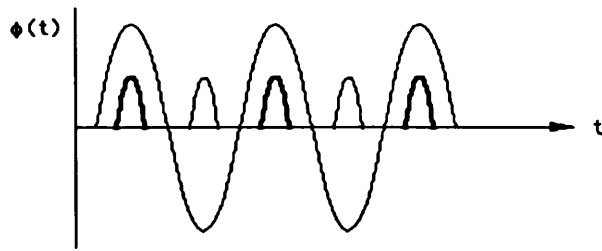
Fig. 5.24 *FM mode-locking, the intracavity phase modulation achieved by the use of an electro-optic modulator.*

Since the mode-locking is achieved by external means, the above methods enable the central wavelength of the laser output to be tuned over most of the gain bandwidth whilst still retaining mode-locking. However, a laser actively mode-locked by either of these techniques, is very sensitive to cavity length fluctuations.

5.9.1.3 Mode-Locking by Synchronous Pumping:

Synchronous pumping is a method of gain modulation where a mode-locked pump laser is used to mode-lock another laser at the same repetition rate [29,30]. This modulation technique requires precise matching of the laser and pump optical cavities length such that the laser and pump pulses overlap both temporally and spatially inside the gain medium.

5.9.2 Passive Mode-Locking:

Passive mode-locking can be obtained by including a saturable absorber in the laser resonator [25,31]. With sufficient pumping, a relatively intense burst of spontaneous emission from the CW pumped gain medium causes the absorber to saturate or bleach and so is able to experience a net gain. This noise burst rapidly becomes shorter in duration and higher in intensity, forming a well defined shape and becomes a mode-locked pulse.

The cavity length of a laser mode-locked in this way is relatively of minor importance (mode-locking is independent of the cavity period) and so length fluctuations are much less critical. A disadvantage with this method is that the output wavelength is fixed, and is determined by the absorption peak of the saturable absorber.

5.9.2.1 Coupled Cavity Mode-Locking:

This technique involves the use of an intensity dependent nonlinear medium inside a second external coupled-cavity. By optically coupling the two cavities, a pulse initiated inside the laser cavity will pass into the coupled-cavity and undergo an intensity-dependent phase shift. When it is fed back into the laser the pulse interferes with the residual pulse resonating in the cavity. By appropriate matching of the phase delay between the laser and coupled-cavity pulses, pulse shortening in the main laser may be realised [32].

5.9.3 Ultrashort Pulse Measurement Techniques:

The most direct and simple way of measuring ultrashort pulses is to use a photodiode and a sampling oscilloscope. This method is generally limited by the rise time of the detector head. The other technique with the best temporal resolution is by using a nonlinear second harmonic autocorrelator, which has enabled the measurement of compressed pulses ~6 fsec in duration [33]. This technique is described in the following section.

5.9.3.1 Second Harmonic Autocorrelation Technique:

The autocorrelation technique is the most common method used for determining pulse width characteristics on a femtosecond time scale. The technique effectively translates differences in optical path length into time, by taking advantage of the fact that the speed of light within a given medium is constant.

The basic optical configuration is similar to that of a Michelson interferometer. An incoming pulse train is split into two beams of equal intensities. An adjustable optical delay is imparted to one of the beams and the two beams are then recombined within a nonlinear crystal for second harmonic generation. The efficiency of the second harmonic generation is proportional to the degree of pulse overlap within the crystal. Monitoring the intensity of the SHG as a function of delay between the recombining pulses produces a correlation function directly related to the pulse width.

Two types of autocorrelation configurations are possible. In the first type, as shown in Fig. 5.25a, the two beams are recombined in a collinear fashion. This configuration results in an autocorrelation signal on top of a constant DC background. The background is produced by the SHG light result from the portions of the scan during which the pulses are not

128

overlaped. In the second type, as shown in Fig. 5.25b, the two beams are displaced from a common optical axis and recombined in a noncollinear fashion [34]. In this configuration, the background is eliminated because the SHG is generated only at the point where the two beams intersect (correct phase matching conditions).
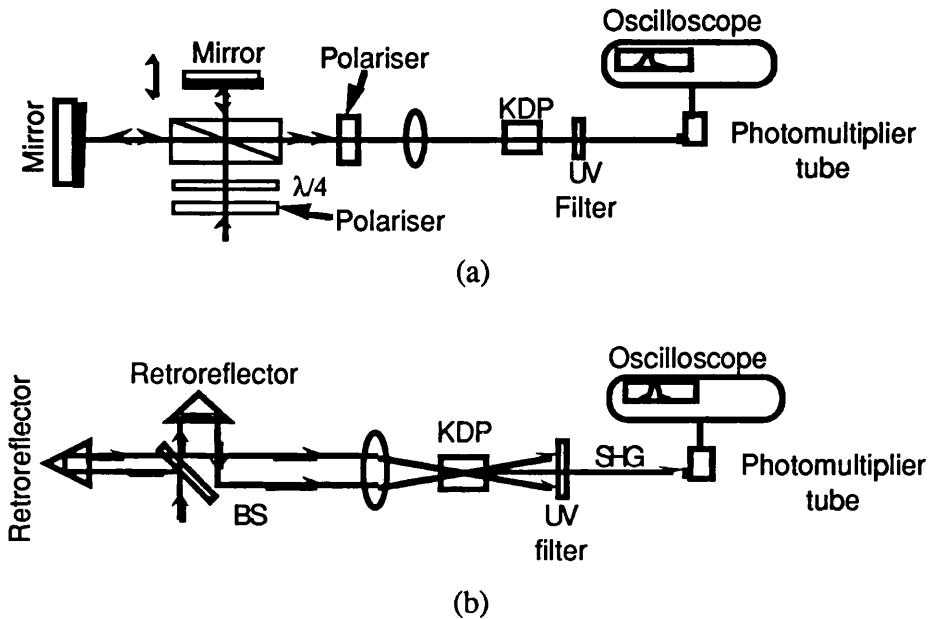
Fig. 5.25 *Schematic diagram of a second harmonic autocorrelation; a) collinear b) collinear.*

The path length of the two beams were approximately equal, and one of the arms comprises of a retroreflecting corner cube (or flat mirror) mounted on a vibrator driven by a sine waveform. The other reflector was mounted on a translation stage. The two beams were then focused into a crystal, "pohtassium dihydrogen phosphate (KDP)" and the SHG signal was detected using a photomultiplier tube with an optical filter to prevent any of the fundamental signal from being detected.

The relation between the correlation width Δt and the full width at half maximum FWHM of the laser pulse τ_p is:

$$\tau_p = \frac{\Delta t}{k}$$

where k is a constant depending on the actual shape of the pulse. Table 1 gives values of k for some standard pulse shapes.

Pulse shape	Intensity profile	k parameter
Square	$1 \quad `t`\leq t_p/2$ $0 \quad `t`>t_p/2$	1
Gaussian	$\exp-\left(\dfrac{4\ln2\,t^2}{\tau_p^2}\right)$	$\sqrt{2}$
Hyperbolic(sech^2)	$\mathrm{sech}^2(1.76t/t_p)$	1.55

5.10 Mode-Locking of the Ti:Sapphire Laser:

Two techniques were employed to mode-lock the tuneable Ti:sapphire laser available in the Department, firstly by using the nonlinear coupled cavity mode-locking and secondly by using FM mode-locking.

5.10.1 Nonlinear Coupled-Cavity Mode-Locking:

A schematic diagram of the set-up used to mode-lock the Ti:sapphire laser is shown in Fig. 5.26. It consisted of two cavities, the Ti:sapphire laser main cavity and an external cavity with an optical fibre called the control cavity. The control cavity consisted of a beam splitter that reflected a portion of the main cavity laser output power into the nonlinear external cavity. The reflected beam was coupled into a single-mode (4.5 μm core diameter) non-polarization maintaining optical fibre using an antireflection-coated lens. The output optical beam was coupled back to the fibre using a peizoelectric mirror mounted on a translation stage.

The operation of the external-cavity mode-locked laser can be understood either in the time domain [35,36] or in frequency domain [37,38]. When a pulse from the main laser is coupled into the external optical fibre, it experiences an intensity-dependent phase shift and will interferometrically recombine with the pulse in the main laser cavity. When the relative phases are set appropriately, the peak of the pulse constructively interfere, while the wings of the pulse destructively interfere.

This model for the pulse shaping has been termed as additive-pulse mode-locking [35,36]. Alternatively in the frequency domain, self-phase modulation in the external fibre feeds

130

back a spectrally broadened pulse, which couples to the longitudinal modes of the laser. This model has been termed as coupled-cavity mode-locking [38].
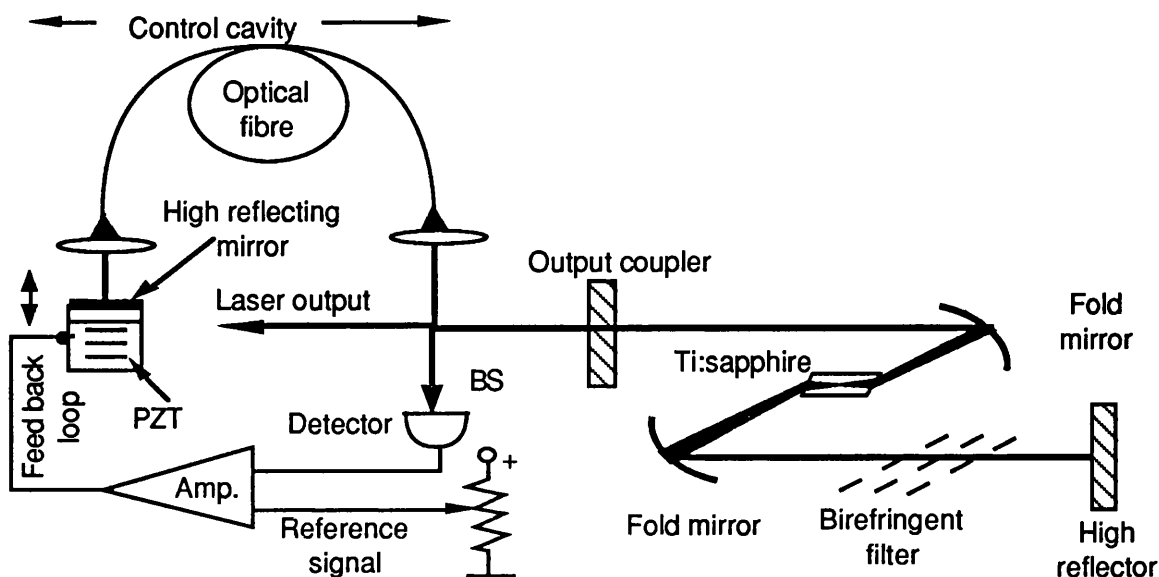
Fig. 5.26 *Schematic diagram of the coupled-cavity mode-locked Ti:sapphire laser, the main laser cavit is formed of the four-folded mirrors and the nonlinear cavity is formed of the output coupler-BS-optical fibre-PZT mirror. The two cavities are interferometrically matched.*

Pulse formation is possible if the laser is seeded with sufficient intensity to induce the nonlinear pulse shortening process. Possible mechanisms for self-starting in the Ti:sapphire laser are the longitudinal mode beating and the self Q switching induced by the external cavity. In a standing-wave cavity, spatial hole burning causes several longitudinal modes to lase and full amplitude intensity oscillations can be observed. Theoretical studies have shown that an external cavity can produce Q switching [39] and thus yield high intensities.

Since feedback from the nonlinear external cavity is interferometric, the relative lengths of the main cavity and the external cavity must be stabilized to within a fraction of a wavelength. This can be obtained by using an electronic circuit that monitor the laser output power and control the piezoelectric translator on the control cavity. The circuit was similar to that employed for stabilizing the soliton laser [40]. The relative phase of the two cavities can be adjusted by changing the set point for the feedback circuit.

Results:

The Ti:sapphire laser was pumped with a 5 watt Ar⁺-ion laser (all-lines), the cavity length was 67 cm and the output coupler transmission was 8%. In the control cavity, the length of the fibre was 30 cm and the coupling efficiency to the fibre, using endfire coupling, was around ~40%. The two cavities were roughly phase matched by moving the translation stage of the control cavity end mirror.

A great efforts were spent to mode-lock the Ti:sapphire laser with this method, but without success. Later it was found that the output of the laser (without the control cavity) was highly multi-mode. This was due to the pump laser intensity profile was TEM_{01}, which caused by the low pressure of the Ar⁺-ion laser tube. Therefore, the interferometeric interference between the beam coming from the control cavity (TEM_{00}) and the main cavity (multi-mode) was very poor.

5.10.2 FM Mode-Locking Technique:

A phase modulator made of a MgO:LiNbO₃ crystal was used. The crystal was 12 mm long and the facets were cut and polished at Brewster angle (Isle Optics). At Megahertz operating frequencies, the crystal can be used as a capacitive element in resonant LC circuit, as shown in Fig. 5.27. The resonance frequency of the circuit can be adjusted by the appropriate choice of the inductance L, ($\omega=1/LC$). The RF power supply was (Isle Optics) oscillated at a fixed frequency of 76 MHz and was coupled into the LC circuit through a second inductive coil. The electric field was applied along the crystal axis to produce a time-varying refractive index by exploiting the r_{13}, and r_{33} electro-optic coefficients [41].
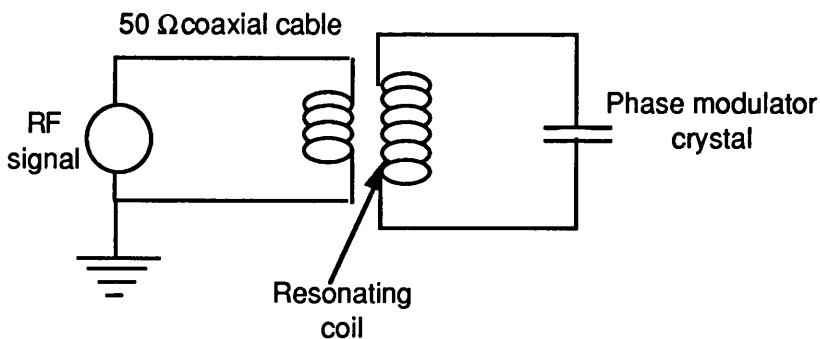
Fig. 5.27 *Equavlent circuit diagram of a phase modulator.*

The modulation efficiency of the crystal was tested , at Strathclyde University, by passing a He-Ne laser beam (λ=0.633 µm) through the modulator and observe the carrier and generated FM sidebands. This was achieved by using a scanning confocal interferometer driven by a ramp signal, as shown in Fig. 5.28.
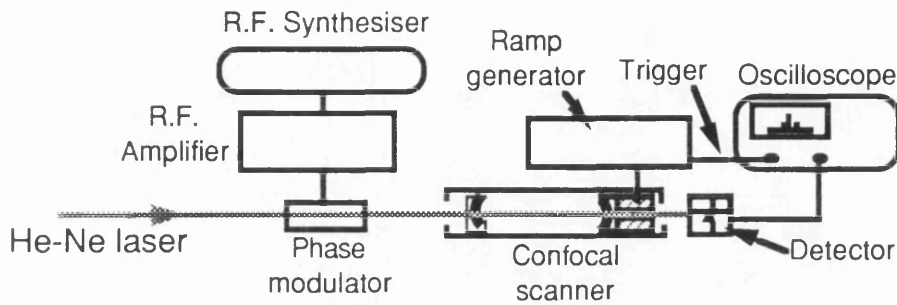
Fig. 5.28 *Phase modulator characterisation using a scanning confocal interferometer.*

The generated sidebands and the drive ramp signals of the interferometer are shown in Fig. 5.29.
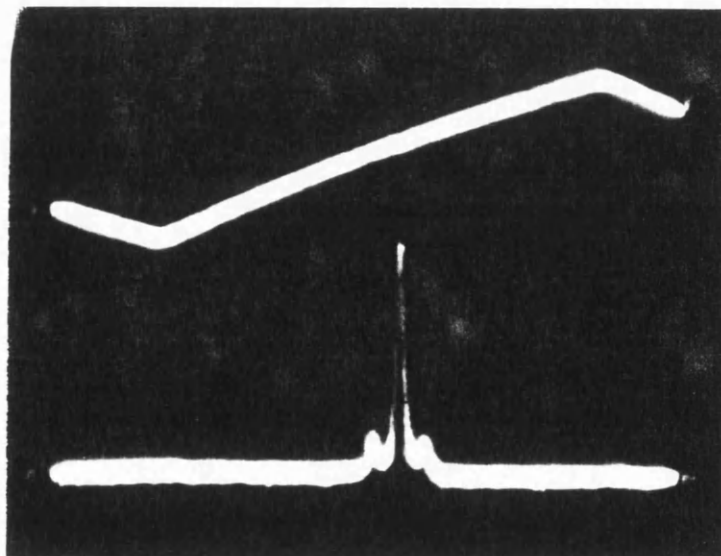
Fig. 5.29 *Generated FM sidebands (lower trace) induced by the phase modulator and the ramp signal (upper trace) which drive the confocal interferometer in Fig. 5.28.*

The modulator was placed inside the Ti:sapphire laser cavity, close to the high reflecting mirror, at Brewster angle. The alignment of the crystal was obtained by using an x, y and rotation axis mount. Because the RF frequency of the power supply was fixed at 76 MHz, mode-locking was made possible by tuning the laser cavity length. This was achieved by mounting the high reflecting mirror on a translation stage with a micrometer controller. The Ti:sapphire laser cavity extended to 1.97 m.

Fig. 5.30a shows a train of pulses of the mode-locked output of the laser observed by using a fast detector and a 2 GHz sampling oscilloscope. The repetition time of these pulses was 13 nsec, 76 MHz. We were not able to measure the pulse width using the SHG autocorrelator, due to the limited scanning displacement of the vibrating mirror of the interferometer. But from autocorrelation measurements in an integrated waveguide, the pulse width was estimated to be ~50 psec, as described in section 6.3.1. Using the fast detector, the pulse width was around 200 psec, as shown in Fig 30b. This was due to the limited rise and fallen time of the detector.

(a)   (b)
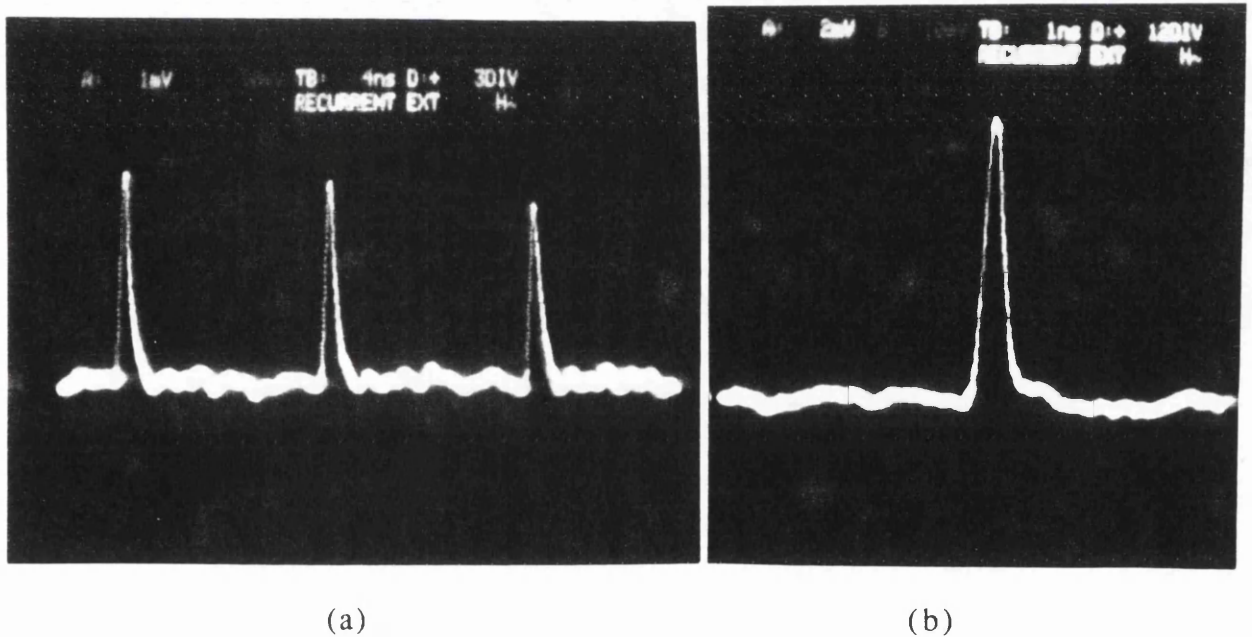
5.30 *The output pulses of the actively mode-locked Ti:sapphire laser traced using a fast detector and 2 GHz sampling oscilloscope;* a) *Train of pulses with a repetion rate of 13 ns.* b) *Intensity profile of individual pulse.*

5.11 Coupled-Cavity Mode-Locked Colour Centre Laser:

A coupled-cavity mode-locking was used to produce ultrashort pulses [42,43]. This technique is similar to that described in section 5.9.2 for mode-locking the Ti:Al$_2$O$_3$ laser. An optical feedback from a control cavity appended directly onto the main cavity, the

control cavity incorporated an optical fibre which provided pulse compression through the effect of SPM in the fibre. Two different configurations for the coupled-cavity can be used, either a Michelson cavity configuration or the more common Fabry-Perot arrangement [43]. A CCML colour centre laser was available at St. Andrews University, Department of Physics. This system was used for all our nonresonant nonlinear experiments, below half the band gap of GaAs/GaAlAs waveguide structures.

Fig. 5.31 shows a schematic diagram of the laser system, it consisted of a KCl:Tl colour-centre laser excited in a noncollinear geometry by a CW mode-locked Nd:YAG laser. the pump laser operated at 1.06 μm and was actively mode-locked by an intracavity acousto-optic loss modulator at 82 MHz. This frequency corresponds to a cavity round trip time of $\approx$12 ns and a cavity length of $\approx$1.83 m. The pump intensity was $\approx$2 W and the laser was vertically polarised, using a Brewster loss plate which selected vertically polarised modes.
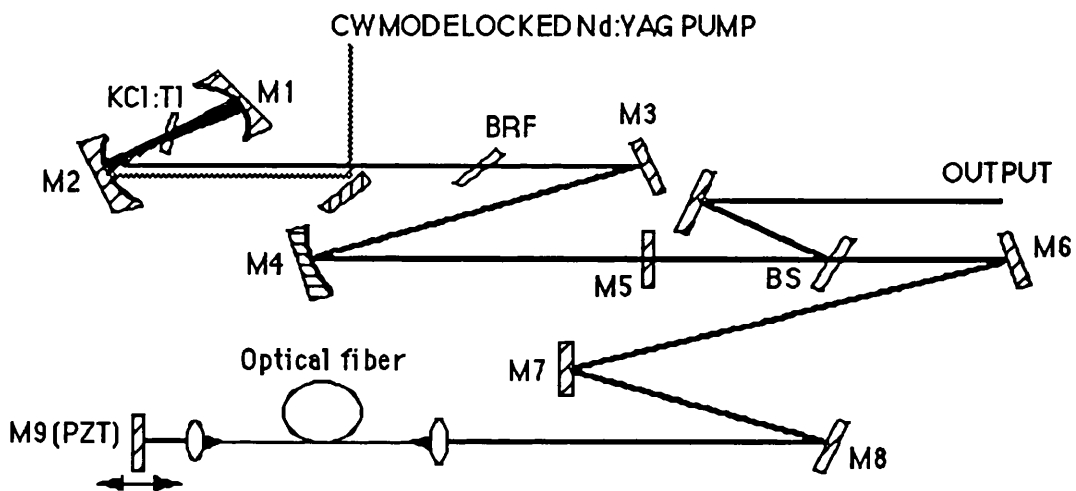
Fig. 5.31 *Schematic diagram of a coupled-cavity mode-locked KCl:Tl coulor centre laser in a nonlinear Fabry-Perot configuration; M's: mirrors, BS: beamsplitter, BRF: birefringent filter.*

The optical path lengths of the nonlinear external cavity, M5-BS-M6-M7-M8-M9, and the linear main laser cavity, M1-M2-M3-M4-M5, were the same. The interferometeric matching of the two cavities was achieved by mounting the back mirror, M9, on a peizoelectric mount and a translation stage. An electronic feed back loop, circuit was used to maintain the phase matching of the two cavities. M5 was a 12% output coupler and the beamsplitter BS was 63% reflecting, i.e 37% was transmitted into the nonlinear cavity. The fibre length was 33.5 cm, and the coupling efficiency to the fibre was $\approx$60%. The laser was tunable from 1.51 μm to 1.54 μm.

135

Ultrashort pulses were generated at wavelength $\lambda=1.52$ μm with pulse width $\tau_p \approx 330$ fsec at a repetition rate of 82 MHz. The average power from the laser was ≈ 65 mW (i.e. ≈ 2.33 KW peak power). The pulse width was measured using a SHG autocorrelator, described in section 5.9.3. The linewidth of the laser was scanned by using a monochrometer, $\Delta\lambda \approx 8$ nm at FWHM. Fig. 5.32 shows the pulse width and linewidth of the KCl:Tl coupled-cavity mode-locked laser. The laser pulse width without the nonlinear coupled cavity was 30 ps with the same average power as that of the coupled cavity.
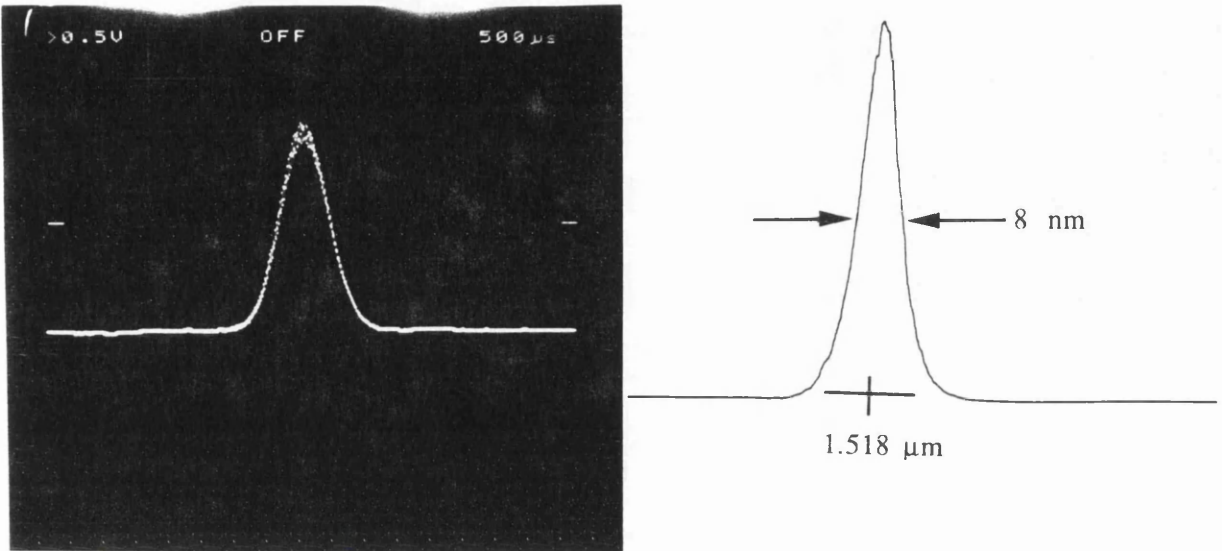
Fig. 5.32 *Intensity autocorrelation (left) and corresponding spectrum (right) for the coupled-cavity mode-locked KCl:Tl coulor centre laser operated at a wavelength of 1.52 μm.*

5.12 Conclusions:

In this chapter the fabrication details of GaAs/GaAlAs active and passive optical devices were described, this included photolithography, ohmic contacts and dry etching techniques. The linear propagation losses in straight waveguideswere measured using the Fabry-Perot method. These studies showed that the propagation loss is sensitive to the waveguide rib width and etching depth and is dominated by the scattering loss due to the sidewalls roughness of the rib waveguide. Also the end facet reflectivity of these waveguides was fully characterised as a function of the waveguide and the guided mode parameters. The facet reflectivity was a strong function of the waveguide tilting angle with respect to the waveguide longitudinal axis. In the last sections of this chapter we discussed the active and passive mode locking techniques of high power lasers. The laser systems used during the course of this project were described, these were: a CW dye laser, CW and mode locked Ti:Al$_2$O$_3$ laser and the coupled-cavity mode-locked KCl:Tl colour centre laser.

References:

[1] O. Auchiello and R. Kelly, *"Beam modifications of materials"*, Vol. 1: Ion bombardment modification of surfaces, Elsevier, Oxford (1984).

[2] B. Chapman, *"Glow discharge processes, sputtering and plasma etching"*, John Wiley and sons, New York (1980).

[3] W. Kern and C.A. Deckert, *"Thin film processes"*, Academic Press, Inc (1978).

[4] E.H. Rhoderick, *"Monographs in electrical and electronic engineering: Metal-semiconductor contacts"*, Clarendon Press, Oxford (1980).

[5] A. Piotrowska, A. Guivarch and G. Pelous, *"Ohmic contacts to III-V compound semiconductors: a review of fabrication techniques"*, Solid State Electron., Vol. 26, p. 179 (1983).

[6] G.S. Marlow, M.B. Das, L. Tongson, *"The characterisation of Au-Ge based ohmic contacts to n-GaAs including the effect of aging"*, Solid State Electron., Vol. 26, p. 259 (1983).

[7] D. Marcuse, *"Mode conversion caused by surface imperfactions of a dielectric slab waveguide"*, Bell Syst. Tech. J., Vol. 48, p. 3187 (1969).

[8] G.H. Ames and D.G. Hall, *"Attenuation in planar optical waveguides: Comparison of theory and experiment"*, IEEE J. Quantum Electron., Vol. QE-19, p. 845 (1983).

[9] P.K. Tien, *"Light waves in thin films and integrated optics"*, Appl. Opt., Vol. 10, p. 2395 (1971).

[10] E. Garmie, *"Semiconductor components for monolithic applications"*, Integrated Optics, Ed. T. Tamir, New York, Springer-Verlag, p. 243 (1985).

[11] E. Kapon and R. Bhat, *"Low-loss single-mode GaAs/GaAlAs optical waveguides grown by organometallic vapor phase epitaxy"*, Appl. Phys. Lett., Vol. 50, p. 1628 (1987).

[12] T. Mukai, Y. Yamamoto and T. Kimura, *"Optical amplification by semiconductor lasers"*, Semiconductor and Semimetals, Vol. 22, New York, Academic, p. 265 (1985).

[13] H.A. Macleod, *"thin-film optical filters"*, Adam Hilger LTD, London (1969).

[14] D.R. Scifres, W. Strecfer and R.D. Burnham, *"GaAs/GaAlAs diode lasers with angled pumping stripes"*, IEEE J. Quantum Electron., Vol. QE-14, p. 223 (1978).

[15] T. Ikegami, *"Reflectivity of mode at facet and oscillation mode in double-heterostructure injection lasers"*, IEEE J. Quantum Electron., Vol. QE-8, p. 470 (1972).

[16] A.J.N. Houghton, D.A. Andrews, G.J. Davies and S. Ritchie, *"Low-loss optical waveguides in MBE-grown GaAs/GaAlAs heterostructures"*, Opt. Comm., Vol. 46, p. 164 (1983).

[17] R.G. Walker and R.C. Goodfellow, *"Attenuation measurements on MOCVD-grown GaAs/GaAlAs optical waveguides"*, Electron. Lett., Vol. 19, p. 590 (1983).

[18] R.G. Walker, *"Simple and accurate loss measurement techniques for semiconductor optical waveguides"*, Electron. Lett., Vol. 21, p. 581 (1985).

[19] H. Takeuchi and K. Oe., *"Low-loss single-mode GaAs/GaAlAs miniture optical waveguides with straight and bending structures"*, J. Lightwave Tech., Vol. 7, p. 1044 (1989).

[20] R.J. Deri, E. Kapon, J.P. Harbison, M. Seto, C.P. Yun and L.T. Florez, *"Low-loss GaAs/GaAlAs waveguide phase modulator using a W-shaped index profile"*, Appl. Phys. Lett., Vol. 53, p. 1803 (1988).

[21] R.J. Deri, R.J. Hawkins and E. Kapon, *"Rib profile effects on scattering in semiconductor optical waveguides"*, Appl. Phys. Lett., Vol. 53, p. 1483 (1988).

[22] R.J. Deri, E. Kapon and L.M. Schiavone, *"Scattering in low-loss GaAs/GaAlAs rib waveguides"*, Appl. Phys. Lett., Vol. 51, p. 789 (1987).

[23] D. Marcuse, *"Reflection loss of laser mode from tilted end mirror"*, J. Lightwave Tech., Vol. 7, p. 336 (1989).

[24] A.E. Siegman, D.J. Kuizenga, "*Active mode-coupling phenomena in pulsed and continuous lasers*", Opto-Electronics, Vol. 6, p. 43 (1974).

[25] D.J. Bradley, G.H.C. New, "*Ultrashort pulse measurments*", Proc. IEEE, Vol. 62, p. 313 (1974).

[26] G.H.C. New, L.A. Zenteno, "*New techniques in the theory of active mode-locking*", Opt. Comm., Vol., p. 149 (1983).

[27] A.J. DeMaria, "*Ultrasonic-diffraction shutters for optical maser oscillators*", J. Appl. Phys., Vol. 34, p. 2984 (1963).

[28] D.J. Kuizenga, A.E. Siegman, "*FM and AM mode-locking of the homogeneous laser-part I: theory*", IEEE J. Quantum Electron., Vol. QE-6, p. 694 (1970).

[29] C.P. Ausschnitt, R.K. Jain, J.P. Heritage, "*Cavity length detuning characteristics of the synchronously mode-locked CW dye laser*", IEEE J. Quantum Electron., Vol. QE-15, p. 912 (1979).

[30] U. Stamm, F. Weidner, "*Pulse formation in synchronously pumped infrared dye lasers*", Appl. Phys. B, Vol. 48, p. 149 (1989).

[31] H.A. Haus, "*Theory of mode locking with a fast saturable absorber*", J. Appl. Phys., Vol. 46, p. 3049 (1975).

[32] L.F. Mollenauer, R.H. Stolen, "*The soliton laser*", Opt. Lett., Vol. 9, p. 13 (1984).

[33] R.L. Fork, C.H. Brito Cruz, P.C. Becker and C.V. Shank, "*Compression of optical pulses to six femtoseconds by using cubic phase compensation*", Opt. Lett., Vol. 12, p. 483 (1987).

[34] E.P. Ippen, C.V. Shank, "*Ultrashort Light Pulses*", Chapter 2, Ed. S.L. Shapiro, Springer Verlag (1977).

[35] J. Mark, L.Y. Liu, K.L. Hall, H.A. Haus and E.P. Ippen, "*Femtosecond pulse generation in a laser with a nonlinear external resonator*", Opt. Lett., Vol. 14, p. 48 (1989).

[36] E.P. Ippen, H.A. Haus and L.Y. Liu, "*Additive pulse mode locking*", J. Opt. Soc. Am. B, Vol. 6, p.1736 (1989).

[37] K.J. Blow and D. Wood, "*Mode-locked lasers with nonlinear external cavity*", J. Opt. Soc. Am. B, Vol. 5, p. 629 (1988).

[38] X. Zhu, P.N. Kean and W. Sibbett, "*Spectral and temporal characterisations of coupled cavity mode locking in a KCl:Tl color center laser*", IEEE J. Quantum Electron., Vol. 70, p. 2445 (1989).

[39] S.M.J. Kelly, "*Mode-locking dynamics of a laser coupled to an empty external cavity*", Opt. Commun., Vol. 70, p. 495 (1989).

[40] F.M. Mitschke and L.F. Mollenauer, "*Stabilisating the soliton laser*", IEEE J. Quantum Electron., Vol. QE-22, p. 2242 (1986).
[
41] B.E.A. Saleh, M.C. Teich, "*Fundamentals of photonics*", Wiley-Interscience, John-Wiley and sons (1991).

[42] R.S. Grant, P.N. Kean and W. Sibbett, paper 147, 9th National Quantum Electronics Conference, Oxford, U.K. (1989).

[43] R.S. Grant and W. Sibbett, "*Cavity configurations for coupled-cavity mode locking*", Optics Communication, vol. 86, p. 177 (1991).

Chapter 6

Nonlinear Characterisation of GaAs/GaAlAs Waveguides

6.1 Introduction:

The nonlinear optical properties of semiconductor materials are highly dependent on the regime into which the operating wavelength falls. Operation at photon energies well below the material band gap is often desirable because the linear absorption loss is quite small. The contributions of the lattice and free carriers to the nonlinear index change of the material have a fast recovery time well below the femtosecond regime. These nonresonant nonlinearities are weak and relatively high power density is required even over a long interaction length. Therefore, the use of the nonresonant nonlinear effects in all-optical switching devices with fast recovery time may require a relatively high intensity to achieve the required phase change within a workable interaction length of the device.

If the operation wavelength is allowed to reach or exceed the absorption threshold, the optical nonlinear effects in semiconductors (known as the resonant nonlinearity) can be enhanced through a variety of mechanisms arising from the optically induced changes in the free-carrier population. These mechanisms, as discussed in section 2.3, include band filling, plasma screening and band gap renormalisation [1-3]. The relatively large optical nonlinearities near a semiconductor band gap are attractive for producing lower power or more compact optical switching devices with the capability of integration or packaging with other optoelectronic components.

Studies of the resonant and nonresonant optical nonlinearities provide essential information for the development of optical switching devices. In particular, measurement of the nonlinear index n_2 is critical for assessing potential applications of all-optical switching devices.

The refractive index and absorption of a semiconductor can be perturbed through other mechanisms, e.g. applying an electric field perpendicular to the semiconductor epitaxial layers [4]. The electric field induced changes in the optical properties of semiconductors are described in section 2.4. The idea of studying the electro-refractive and absorptive effects, in GaAs/GaAlAs QW waveguides, was to combine these effects with the resonant nonlinear effects in QWs for designing fast all-optical switching devices with a larger

switching depth. These devices are based on the nonlinear integrated Mach-Zehnder interferometer and directional coupler.

In the previous chapter the linear optical properties of GaAs/GaAlAs heterostructure stripe waveguides were examined at photon energies below the material band edge. These measurements were vital in designing stripe waveguides with low linear propagation losses. This chapter is divided into two main sections. Firstly, the nonlinear optical properties of GaAs/GaAlAs single and multiple quantum well stripe waveguides were investigated at photon energies close to and above the material band edge. This involved the measurements of the saturation of the photo-absorption and -refraction nonlinear effects in single and multiple quantum well waveguides. Also the relaxation time of the resonant nonlinearity has been studied. The electro-refractive and -absorptive effects in p-i-n quantum well waveguides were investigated.

Secondly, the nonresonant nonlinear effect in GaAlAs stripe waveguides was investigated at photon energies below half the material band gap. This involved the measurement of the nonlinear refractive index coefficient n_2, using self-phase-modulation SPM effect in GaAlAs stripe waveguides, and the two-photon absorption TPA coefficient β.

6.2 Design Considerations of GaAs/GaAlAs QW Waveguides:

The engineering design of GaAs/GaAlAs quantum well materials play an essential rule in determining the size and the speed of the recovery time of the resonant nonlinearity. The materials used in this project were, GaAs/GaAlAs single and multiple quantum wells, described in section 4.3.

The resonant optical nonlinearity in GaAs/GaAlAs waveguides can be enhanced by using the advantage of the excitonic effects in quantum wells, as described in section 2.3.2. This was achieved by placing the single or multiple quantum wells in the guiding region. The size of the resonant nonlinearity depends on the number and the place of these QWs in the guiding region.

The absorption coefficient of the quantum well waveguides, close to the band edge, increases dramatically with the increase in the number of the QWs. Therefore in considering the required length of the all-optical switching devices there is a trade-off between the size of the nonlinearity and the number of the quantum wells in designing GaAs/GaAlAs quantum well structures.

In single quantum well SQW waveguides, the absorption coefficient, close to or even above the excitonic resonant peaks, is small compared to that of the multiple quantum well MQW waveguides. This allows us to design longer all-optical switching devices, like the integrated Mach-Zehnder interferometer and directional coupler. Also the SQW materials may show a strong excitonic resonance with narrow linewidth, in contrast with the MQW materials which may possibly show a broader excitonic peak due to the fluctuation in the thicknesses from one well to another.

The recovery time of the resonant nonlinearity is a focal point in the engineering design of quantum well waveguides for resonant all optical switching devices. Therefore it is vital to do a quick survey of the techniques used, in literature, to improve the recovery time of the resonant nonlinearity.

6.2.1 Relaxation Time Of Resonant Nonlinearity:

The response times of all-optical switching devices employing resonant optical nonlinearities in semiconductors are governed by the temporal and spatial dynamics of the photogenerated carriers. The switch-up time is inherently governed by the temporal shape of the excitation pulse, however the recovery time depends on the speed at which the carriers are removed. Normally the recovery time is limited by the recombination rates (both radiative and non-radiative) or the rate at which carriers leave the waveguide through transport (drift and diffusion). The nonradiative recombination involves the annihilation of e-h pair and generation of phonons which go to the lattice in the form of heat. The non-radiative recombination lifetime in a thin semiconductor layer (e.g. QWs) may not only be determined by the recombination parameters of the material in the layer itself, but also dominated by surface recombination.

For a semiconductor layer of thickness d sandwiched between two surfaces labelled 1 and 2, the effective recombination lifetime is [5];

$$\frac{1}{\tau} = \frac{1}{\tau_{NR}} + \frac{s_1 + s_2}{d} \qquad (6.1)$$

where s_1 and s_2 are the property of each of the surfaces known as the recombination velocity. The recombination velocity of GaAs-air interface is typically very high (5×10^5 cm/sec) [6], therefore any carriers which diffuse to such a surface will rapidly recombine. In GaAs/GaAlAs interface the recombination velocity is much smaller, 53 cm/sec measured for a GaAs/Ga$_{0.65}$Al$_{0.35}$As interface [5]. From Eq. (6.1), the effective recombination

143

lifetime of the photogenerated carriers depends on the layer thickness, therefore τ is shorter in quantum wells than in thick layers produced by the same epitaxial growth system.

In GaAs, the time for carriers to recombine is typically 10 ns and of the order 5 ns in GaAs/GaAlAs MQWs [7]. In devices with a waveguide geometry, the carriers can diffuse sideways due to the high concentration gradient with a time constant around 1 ns [8] depending on the waveguide geometry. Proton bombardment of the MQW material speed the material recovery time into the 100 ps range without destroying the exciton line and hence the nonlinearity [9]. With the proton bombardment, the fast recovery time was due to the creation of traps caused by dislocations in the crystal structure. The application of an electric field perpendicular to the quantum wells is another way to reduce the relaxation time of resonant nonlinearity. This was due to the rapid sweeping of the photogenerated carriers out of the wells and the guiding region such that the recovery time reduced to 100 ps [10]. This is due to the tunnelling transport of the photogenerated carriers through the barriers of the QWs caused by the electric field strength across the depletion region.

In this project, GaAs/GaAlAs QW structures were designed using two approaches (for fast resonant nonlinearity), surface recombination and electric field effects.

An important distinction should be made regarding the relaxation time of the resonant nonlinearity and the nature of the laser excitation. This is a vital role in determining the character of the nonlinear effect. When the pulse length of the laser is shorter than the recovery time of the nonlinear effect, then the effect is integrated over the duration of the pulse so that the size of the net effect depends on the energy of the pulse. If the laser pulse is longer than the relaxation time of the nonlinearity, then the effect is proportional to the instantaneous intensity of the pulse. Therefore it is possible to distinguish between energy dependant and intensity dependant nonlinear effects.

6.3 GaAs/GaAlAs Single Quantum Well Materials:

Two GaAs/GaAlAs SQW materials were used during the course of this project, these were undoped A187 grown by MBE and p-i-n QT147 grown by MOCVD. The first wafer was designed to investigate the fast recombination lifetime of the photo-generated carriers via the semiconductor-air interface surface recombination process. In the second wafer, the electric field induced changes in the optical properties of the QW semiconductor material were studied to be used alongside the resonant nonlinear optical properties of QWs.

144

6.3.1 Undoped GaAs/GaAlAs Single Quantum Well Waveguides:

A187 GaAs/GaAlAs SQW material grown by MBE was used. The epitaxial layers are described in section 4.3, all the layers were undoped. The SQW was a 100 Å thick of GaAs embedded in a 0.65 μm thick of $Ga_{0.75}Al_{0.25}As$ guiding region. The SQW was placed only 400 Å below the top surface of the wafer. As the top surface was within the diffusion length of the photo-generated carriers, this enhanced the recombination time of these carriers via the surface recombination [11].

Single mode waveguides of A187 SQW were designed using the NWAVE and FWAVE programs, described in section 3.3. Fig. 6.1 shows the contour plot of the optical field of the fundamental TE- and TM-modes (using the later program) at a wavelength of 830 nm. The waveguide rib width was 3 μm and etching depth 1.2 μm. The price paid for placing the SQW close to the top surface, to reduce the recovery time of the resonant nonlinearity via the semiconductor-air interface recombination, was the requirement of higher power density to saturate the photo-refractive and -absorptive nonlinearity. This was due to the smaller overlap integral between the SQW and the optical field. The SQW is very close to the top surface and is not shown in Fig. 6.1.
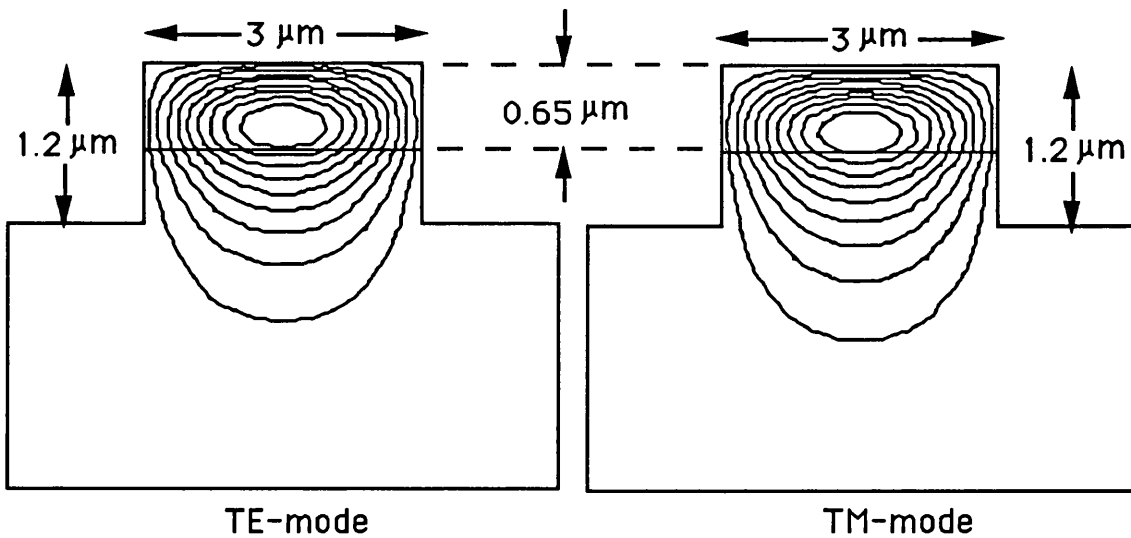
TE-mode　　　　TM-mode

Fig. 6.1 *The modal field distributions for the TE-mode in* (a) *and TM-modes in* (b) *of the A187 SQW waveguide, calculated using the* FWAVE *program at a wavelength of 830 nm. The waveguide rib width and height are 3 μm and 1.2 μm, respectively.*

The Fabry-Perot method, described in section 5.7, was used to measure the linear propagation loss in these waveguides at wavelength $\lambda=1.15\,\mu m$. Assuming the waveguide end facet reflectivity R=32%, the propagation loss was ≈ 17 dB/cm with a standard deviation of 2.5 dB/cm. The high linear loss was due to the scattering loss from the sidewalls roughness caused by the deep etching through the guiding region and over growth defects.

6.3.1.1 Photo-Absorptive Nonlinear Effect Measurements:

At a photon energy close to or above the material absorption edge, the waveguide propagation loss is dominated by the band gap absorption and exciton resonant transitions of the quantum well.

The absorption spectrum of the single mode A187 SQW was measured for the TE- and TM-modes. An end fire coupling technique was used to couple the light in and out of the waveguide. The CW dye laser, described in section 5.8.1, was used. The output intensity of the laser was checked over the spectrum (824 nm - 865 nm) and it was found to be flat ≈ 65 mW. The wavelength of the laser was changed continuously by a motorised driver unit attached to the micrometer control of the birefringent filter.

The laser was chopped at 1 KHz and the output transmission of the waveguide was specially filtered, using a pinhole to eliminate the radiated modes and the scattered light from reaching the detector, and focused onto a Si detector. A lock-in amplifier was used to enhance the signal to noise ratio. The output signal was recorded in a chart recorder.

Linear Absorption Results:

Fig. 6.2 shows the output transmission of the TE-mode of a 3 μm rib width waveguide with etching depth 1.2 μm. The sample length was $l=2.55$ mm. The input light intensity was kept $\leq 20\,\mu W$ to avoid the saturation of the excitonic resonant peaks due to the screening effect [12]. The transmission spectrum of the single mode waveguide shows two troughs at photon energies 1.451 eV and 1.458 eV, these are referred to as the hh- and lh-exciton peaks of the SQW at room temperature.
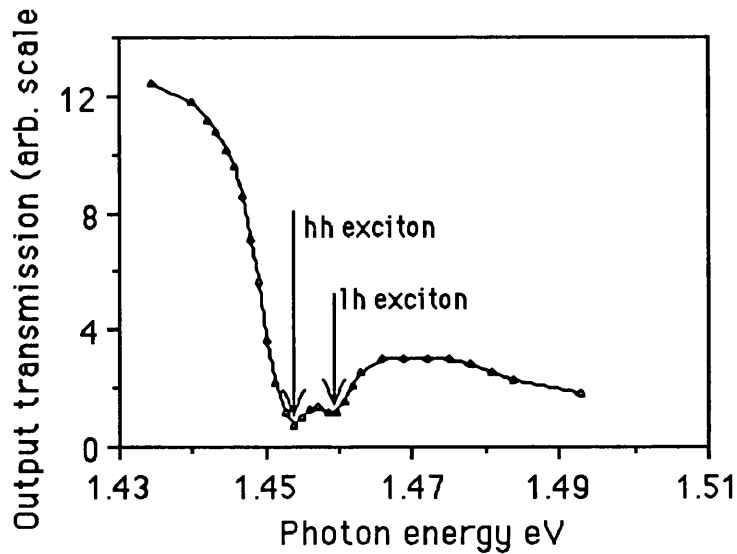
Fig. 6.2 *Output transmission spectrum of the TE-mode of a 2.55 mm long SQW rib waveguide with rib width and height of 3 µm and 1.2 µm, respectively. The two troughs at photon energies 1.451 eV and 1.458 eV referred to the large absorption of the hh and lh excitons of the SQW, respectively.*

The same measurement was repeated for the TM-mode, Fig. 6.3 shows the TM-mode output transmission spectrum of the same waveguide. There is only one trough at a photon energy 1.458 eV. This is attributed to the lh-exciton of the SQW, where the transition strength of the hh-exciton is zero for the TM-mode [2].
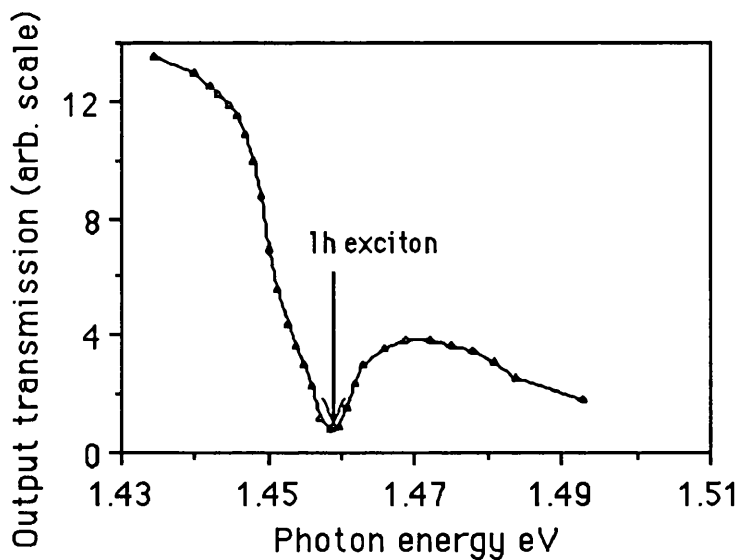
Fig. 6.3 *Output transmission spectrum of the TM-mode of a 2.55 mm long SQW rib waveguide with rib width and height of 3 µm and 1.2 µm, respectively. There is only one trough at photon energy 1.458 eV due to the large absorption of the lh exciton of the SQW.*

147

Before we discuss these results, the output transmission arbitrary scale was calibrated to give the absorption coefficient α(cm^{-1}) spectrum. This was achieved by recalling the expression of the waveguide output transmission in Eq. (5.3) section 5.7. Ignoring the multiple cavity reflections, the relationship between the transmitted intensity and the waveguide propagation loss α (nepers per unit length) is given by;

$$I(L, \lambda) = I_i \gamma (1 - R)^2 e^{-2\alpha L} = I_0 e^{-2\alpha L} \qquad (6.2)$$

Taking into account the wavelength dependence of the Si detector and the end fire system transmission, the detected signal I_D can be written as;

$$I_D(L, \lambda) = I(L, \lambda) . T_s . D \qquad (6.3)$$

where T_S is the transmission of the end fire coupling system and D is the detector sensitivity.

A waveguide with a given length L_0 was placed on the end fire coupling system, and $I_D(L_0, \lambda)$ was measured over the whole spectrum for the TE- and TM-modes. The same measurement was then repeated without the sample.

$$I_s(\lambda) = I_i . T_s . D \qquad (6.4)$$

clearly I_S and D can not be measured absolutely, but by dividing $I_D(L_0, \lambda)$ by $I_S(\lambda)$ it is possible to remove the system's wavelength dependence. Relative to some constant $\alpha(\lambda_0)$, the absorption coefficient α (cm^{-1}) can be calculated for both polarisations, thus;

$$\alpha(\lambda) = \Delta\alpha(\lambda) + \alpha(\lambda_0) \qquad (6.5)$$

$$\Delta\alpha(\lambda) = \left(-\frac{10}{L_0}\right) . \left(\log\left[\frac{I_D(L_0, \lambda)}{I_s(\lambda)}\right] - \log\left[\frac{I_D(L_0, \lambda_0)}{I_s(\lambda_0)}\right]\right) \qquad (6.6)$$

The sequential cleaving technique, described in section 5.7.1, was used to measure $\alpha(\lambda_0)$. The output transmission of a number of waveguides was measured in a sample with length l_1=2.55 mm, then it was cleaved into two different lengths l_2=1.1 mm and l_3=1.45 mm The output transmission of the waveguides in the respective samples was measured at λ_0. These measurements were repeated at discrete number of wavelengths. Fig. 6.4 shows ln(I) versus waveguide length at four different wavelengths. The gradient of the best fit line is equal to α.
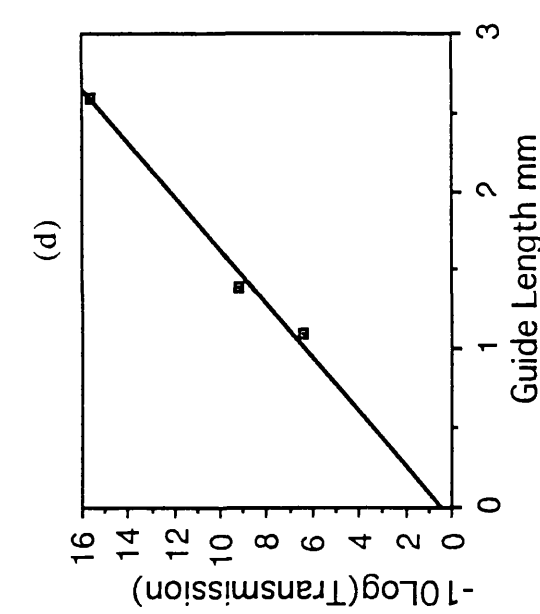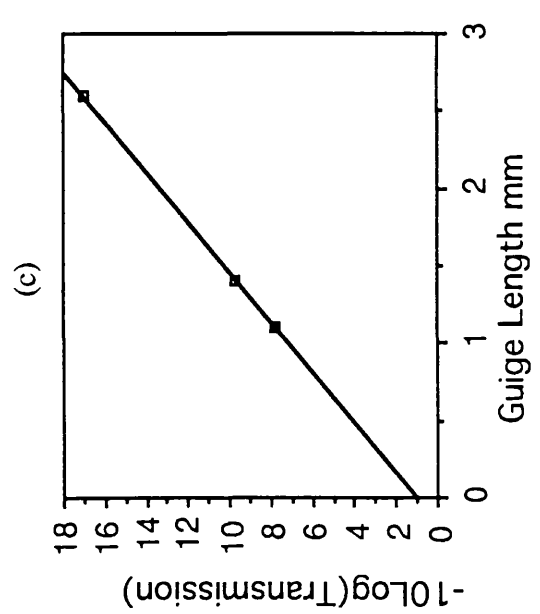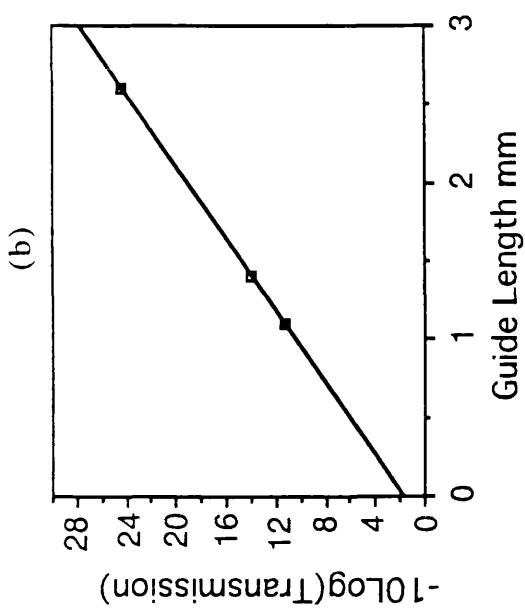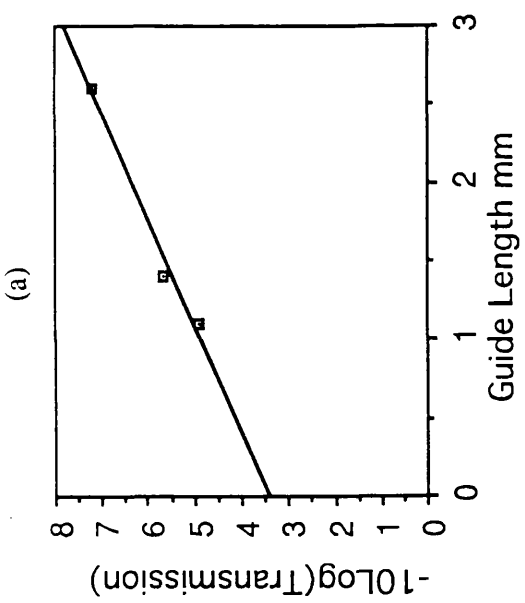
Fig. 6.4 *The results of sequential cleaving loss measurements on A187 SQW waveguide with rib width and height of 3 μm and 1.2 μm, respectively. These measurements were at photon energies: a) 1.436 eV, b) 1.457 eV, c) 1.473 eV and d)1.505 eV.*

Fig. 6.5 shows the absorption spectrum of the TE-mode of the single mode GaAs/GaAlAs SQW waveguide. The absorption coefficient α is in (cm^{-1}). The solid line is a trace of the calibrated results of the transmission spectrum, the open circles are the measured absorption coefficients (cm^{-1}) using the sequential cleaving technique at discrete photon energies. It shows a good agreement between the calibrated and measured results. The same procedure was used to calibrate the transmission spectrum for the TM-mode. Fig. 6.6 shows the TE- and TM-modes absorption spectra, α(cm^{-1}).

From the results of the absorption spectra of the TE- and TM-modes, it shows clearly the highly polarisation dependent absorption of the SQW. The selection rule [2], explained in section 2.3.2, predicted that the oscillation strengths of the hh- and lh-excitons of the TE-mode are 3/4 and 1/4, and for the TM-mode are 0 and 1 respectively, our results agrees with these predictions. Similar results were seen experimentally by Weiner et al [17].
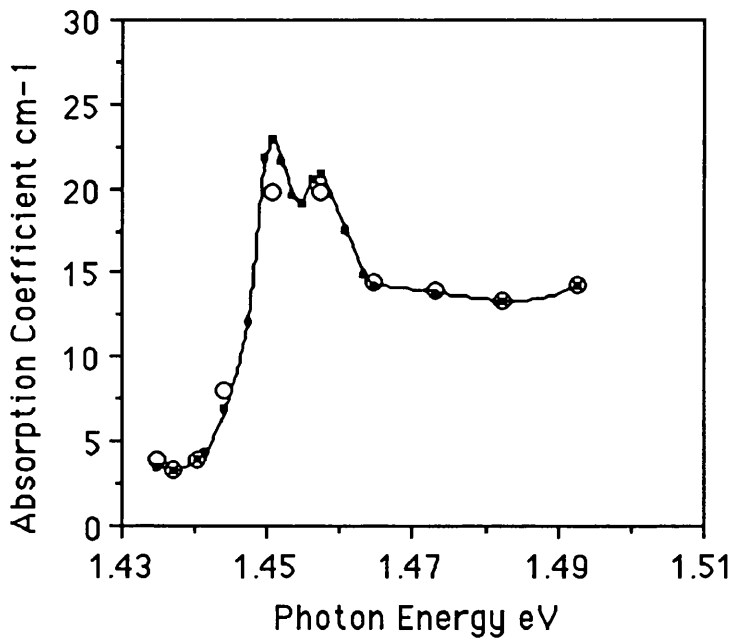
Fig. 6.5 *Room temperature absorption spectrum for the TE-mode of A187 SQW waveguide. The small squares are the calibrated absorption coefficient (cm^{-1}) derived from the transmission spectrum results. The solid line is a trace for these data points. The open circles are the measured absorption coefficient (cm^{-1}) using the sequential cleaving method. The two results of absorption coefficient agree well.*
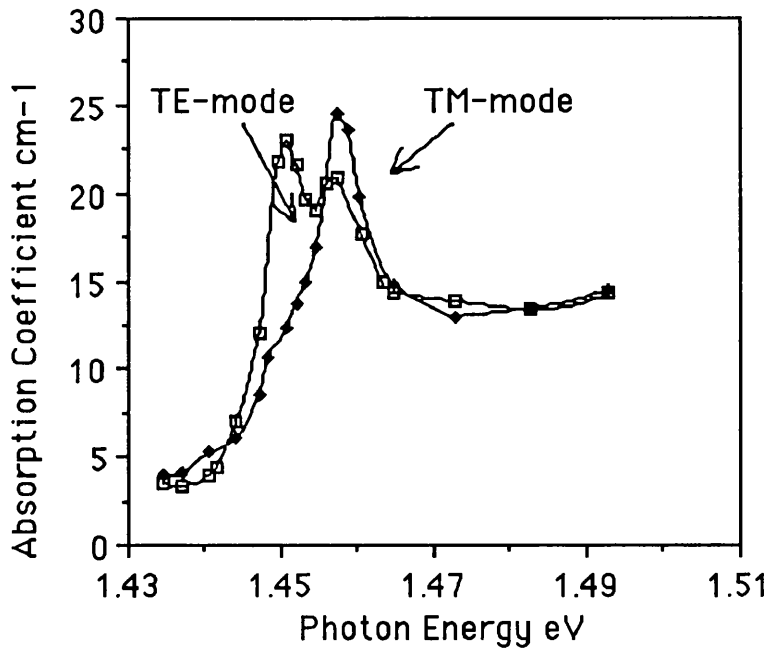
Fig. 6.6 *Room temperature absorption spectra for the TE and TM modes of A187 SQW waveguide..*

Nonlinear Absorption Saturation Results:

The intensity dependence of the absorption spectra for the TE- and TM-modes in the single mode GaAs/GaAlAs SQW waveguides were investigated. The absorption spectrum measurements were repeated, but this time at a high input optical excitation. The maximum input power in the waveguide was ≈ 10 mW, taking into account the end facets reflectivity ($R \approx 32\%$), coupling efficiency to the waveguide ($\gamma \approx 50\%$) and the end fire objective lenses transmission ($T \approx 90\%$).

Fig. 6.7 shows the absorption spectrum at low power (≤ 20 μW) and high power (≈ 10 mW) for the TE-mode of the A187 SQW waveguide. The length of the sample was $l=2.55$ mm.

It is clear that the hh- and lh-excitonic peaks were not fully saturated. This was due to the limited dye laser output power, the alternative way of saturating the absorption was to cleave the sample to a shorter length $l=1.1$ mm. Fig. 6.8 shows the full saturation of the absorption spectrum of the TE-mode. The same results were achieved for the TM-mode, as shown in Fig. 6.9.
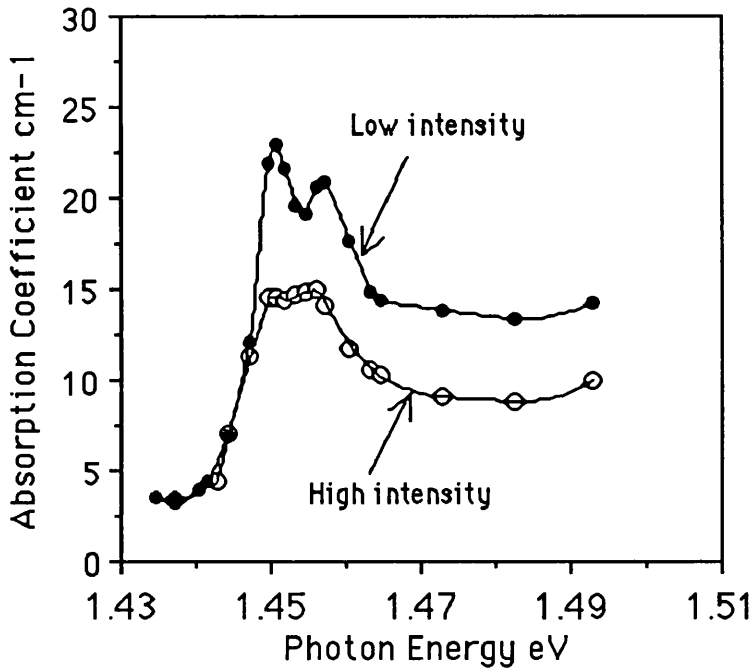
Fig. 6.7 *Room temperature absorption spectra for the TE-mode of A187 SQW waveguide, at low (>200 W/cm²) and high (160 kW/cm²) excitation intensities. The length of the sample was 2.55 mm. A partial saturation of the hh and lh excitons, at high intensity, due to the photogenerated carriers*
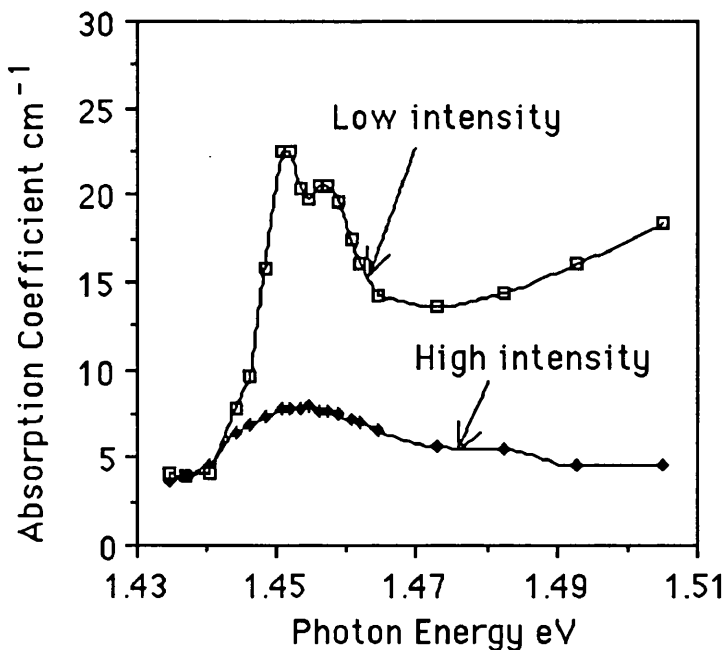
Fig. 6.8 *Room temperature absorption spectra for the TE-mode of A187 SQW waveguide, at low (>200 W/cm²) and high (160 kW/cm²) excitation intensities. The length of the sample was 1.1 mm. A complete saturation of the hh and lh excitons, at high intensity, due to the photogenerated carriers.*

152
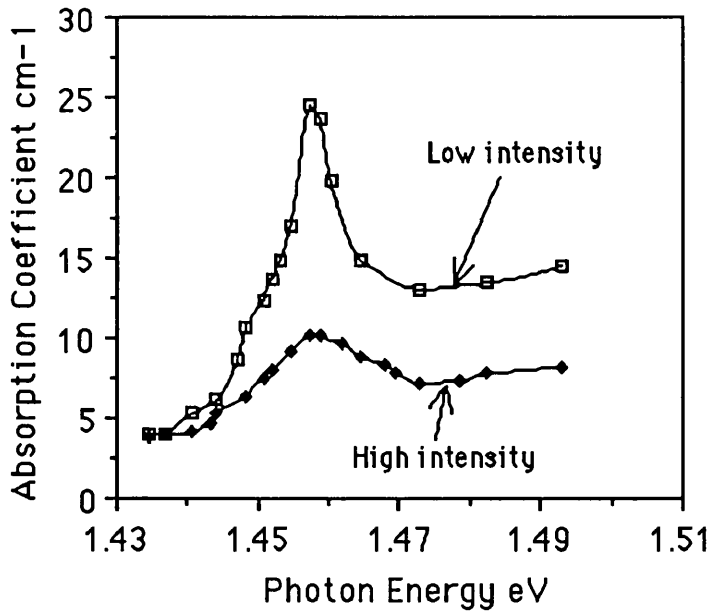
Fig. 6.9 *Room temperature absorption spectra for the TM-mode of A187 SQW waveguide, at low (>200 W/cm²) and high (160 kW/cm²) excitation intensities. The length of the sample was 1.1 mm. The saturation of the lh exciton, at high intensity, was due to the photogenerated carrier*

The change in the absorption spectrum due to the increase in the input light intensity for the TE- and TM-modes are shown in Fig. 6.10 and Fig. 6.11 respectively.
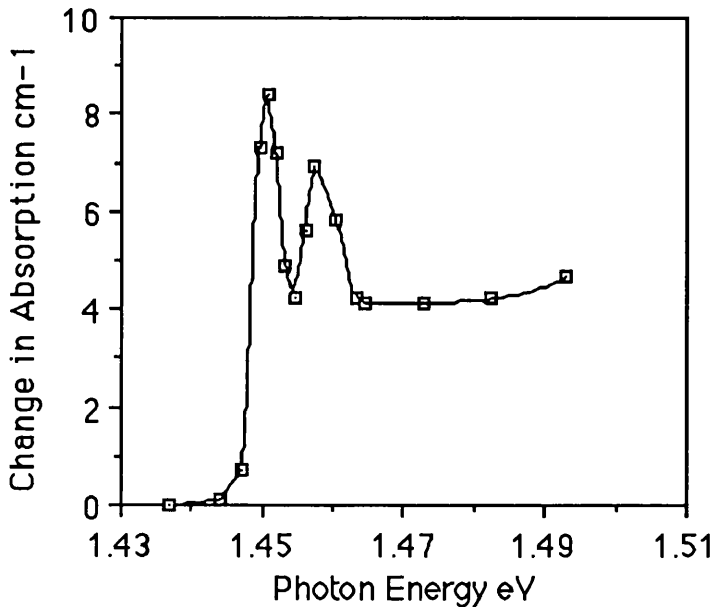
Fig. 6.10 *Absorption coefficient change (cm⁻¹) for the TE mode of the A187 SQW waveguide,derived from the results of Fig. 6.8. The maxima are at the hh and lh excitonic peaks.*

153
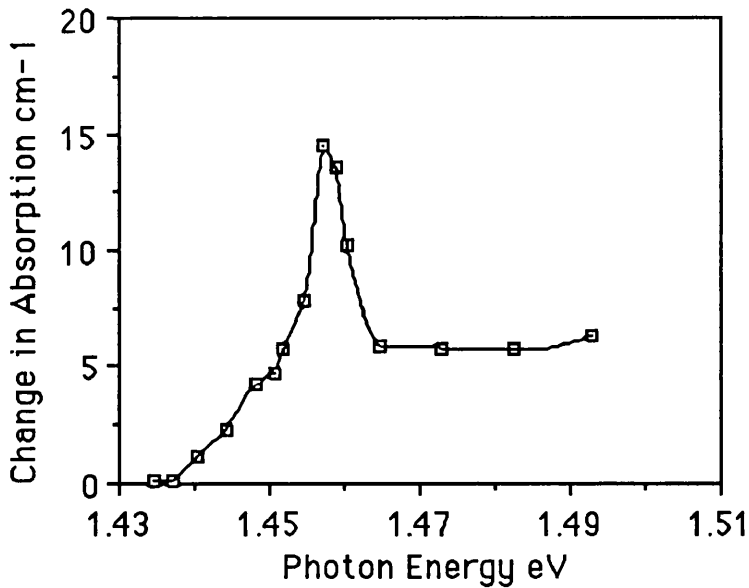
Fig. 6.11 *Absorption coefficient change (cm⁻¹) for the TM mode of the A187 SQW waveguide,derived from the results of Fig. 6.9. The maximum change is at the lh excitonic peak.*

These results were derived from the absorption saturation measurements. A maximum change in the intensity dependent absorption were at the SQW exciton transitions. For the TE-mode, it was ($\Delta\alpha \approx 8.4$ cm⁻¹) at the hh-exciton and ($\Delta\alpha \approx 7$ cm⁻¹) at the lh-exciton of the SQW. For the TM-mode, it was ($\Delta\alpha \approx 14.4$ cm⁻¹) at the lh-exciton of the SQW. This was due to the screening effect of the excitons caused by the photo-generated carriers. At photon energies above the excitonic peaks, the change in absorption was nearly constant and it was due to the band filling effect.

6.3.1.2 Photo-Refractive Nonlinear Effect Measurement:

The intensity dependent refractive index change in GaAs/GaAlAs SQW waveguides was measured, using the external Mach-Zehnder interferometric set-up. This technique was previously used to characterise semiconductor-doped glass [13] and demonstrated by Li-Kam-Wa et al [14] who measured the nonlinear phase shift in MQW strain induced waveguides.

154

External Mach-Zehnder Interferometric Set-up:

Fig. 6.12 shows the experimental set-up used in these measurements. The laser source was a CW Ti:sapphire laser, pumped by an Ar$^+$-ion laser, described in section 5.8.2. The light was linearly polarised and split into two beams by partial reflection off a beam splitter with about 10% of the energy carried in the reflected wave. The transmitted beam was focussed onto the cleaved input facet of the waveguides using a ×40, 0.65 N.A. microscope objective lens. An identical lens was used to image the output of the device onto an infrared C1000 Hamamatsu videcon camera. On the reference side, the beam reflected off the beam splitter was also focussed onto the camera using a pair of microscope objectives, a mirror and a 50/50 beam splitter. The microscope objectives in the reference beam allowed to adjustment of the size and intensity of the reference beam to be comparable with that of the waveguide output transmitted beam, by focusing and defocusing the laser beam spot. The recombination of the two beams produced interference fringes which were observed on the Hamamatsu camera. The angle at which the two beams met determined the fringe separation and this was controlled by the position and angle of the beam splitter. This layout was chosen to allow most of the power to be coupled into the sample. For a clear and stable fringe pattern, mechanical stability in the interferometer was required. Therefore, all the optical components were mounted on rigid mounts with the optical axis as close to the bench top as possible ≈75 mm. Also the path difference of the two beams of the interferometer should be kept within the coherence length of the light source ($\lambda^2/2\Delta\lambda$).
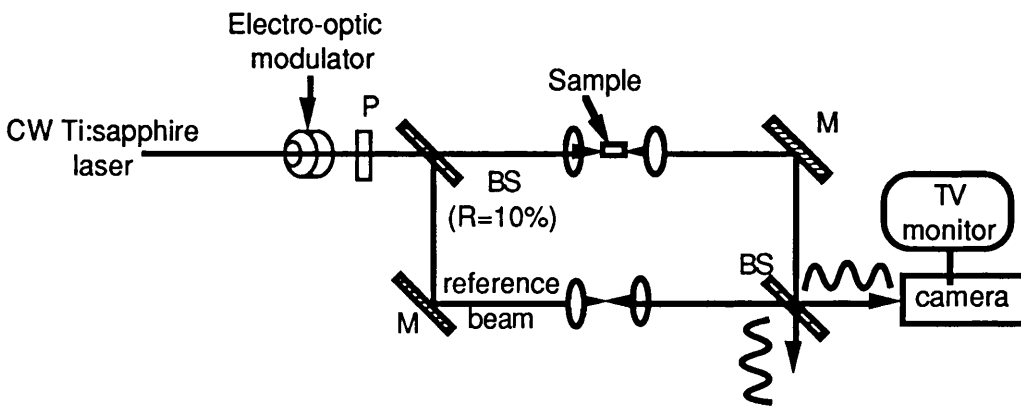
Fig. 6.12 *External Mach-Zehnder interferometric experimental set-up for refractive index and absorption change measurements. M: mirror, BS: beam splitter, P: polariser and R: reflectivity of the BS.*

The intensity distribution of the fringes pattern at the output beam splitter can be expressed as;

$$I = I_1 + I_2(\alpha) + 2\sqrt{I_1} \cdot \sqrt{I_2(\alpha)} \, \cos(\phi(n)) \qquad (6.7)$$

where I_1 is the intensity of the reference beam and I_2 is the intensity of the transmitted beam through the sample, which in general can be a function of absorption coefficient in the sample. $\phi(n)$ is the relative phase difference between the two beams which is a function of the refractive index of the sample. Therefore, changes in the refractive index cause the fringes pattern to move in position and changes in absorption cause the visibility of the fringes to change. This means that the absorption and refractive index changes in the sample can be measured.

Fig 6.13 shows a photograph of the interference fringes of the two recombined beams with a scan of the intensity distribution of the fringes.
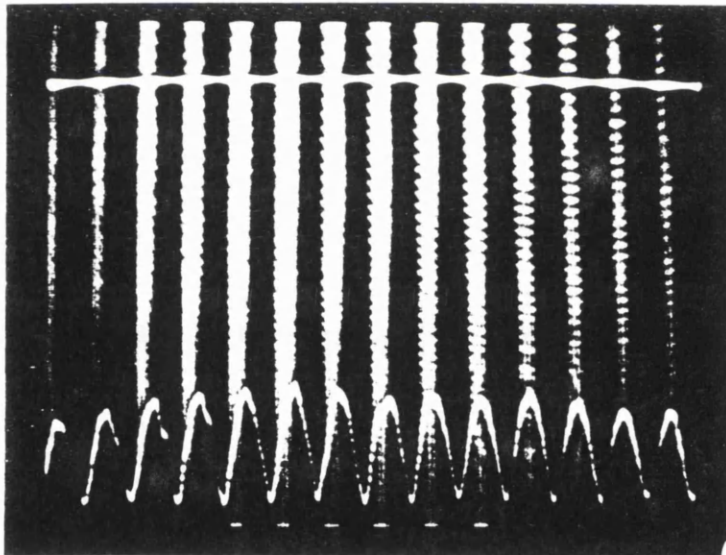
Fig. 6.13 *A photograph of the interference fringes of the external Mach-Zehnder interferometer and a line scan of their intensity profile, obtained by an infrard camera.*

Having obtained the interference fringes, the amount of power being coupled into the waveguide was varied by using an electro-optic modulator and polariser. The modulator was a commercially available mounted lithium niobate crystal which was driven by a high voltage amplifier. Both components were produced by Electro-Optic Developments. This enabled both D.C. and A.C. control of the polarisation of the light transmitted through the crystal. By using this in conjunction with the polariser placed after the modulator, control of the light intensity could be achieved without the need for any physical adjustment of optical components thus eliminating beam misalignment problems.

The intensity dependent refractive index change in the waveguide produces a relative phase difference between the two arms of the external Mach-Zehnder interferometer. This intensity dependent phase change results in a shift in the position of the fringes pattern. The relation between the phase shift and the nonlinear refractive index n_2 can be derived as follows;

Light travelling in a waveguide of length L with a phase propagation constant β experience a net phase shift ϕ given by;

$$\phi = \int_0^L \beta \, dz \qquad\qquad (6.8)$$

$$\beta = k_0 n_e = \frac{2\pi}{\lambda_0} n_e \qquad\qquad (6.9)$$

where λ_0 is the free space wavelength and n_e is the effective refractive index.

The intensity induced change of phase at the output of the waveguide is;

$$\phi = k_0 \int_0^L n_2 \, I \, dz \qquad\qquad (6.10)$$

In a lossy waveguide the intensity of the light propagating in the Z-direction decays as;

$$I = I_i e^{-\alpha z} \qquad\qquad (6.11)$$

where I_i is the incident intensity, which includes the coupling efficiency and the waveguide facet reflectivity, and α is the intensity attenuation coefficient. Therefore, integrating over the length of the sample, the total change in phase is;

$$\phi = \frac{2\pi}{\lambda_0} n_2 I_i L_{\text{eff}}$$

(6.12)

where

$$L_{\text{eff}} = \frac{1 - e^{-\alpha L}}{\alpha}$$

Relative Phase Change Measurement Techniques:

There are two different methods of measuring the phase change (i.e. fringe pattern shift). The simple, less accurate, method is by measuring the fringe shift through the Hamamatsu camera. The method becomes less accurate when the relative phase change between the two arms is small.

The more accurate method is to incorporate an electronic feedback loop into the interferometer, to stabilise the fringes and also provides a more accurate way of measuring a small fringe shift. The fringe pattern is expanded by a ×40 microscope objective and focused onto a bicell detector. It consists of two elements A and B which are initially positioned as shown in Fig. 6.14(a). Firstly, processing the two signals in the form (A-B)/(A+B) provides the fringe position signal. This signal is employed as an error signal which is fed via a high voltage amplifier to a piezo-electric translation PZT mirror in the reference beam. Any shift in the fringe position, due to the waveguide refractive index change, cause a change in the error signal which drives the PZT mirror back or forth until the error signal is zero. Secondly, processing the two signals in the form (A+B) provides the change in absorption. The block diagram of this stabilisation circuit is shown in Fig. 6.14(b).

A calibration of the phase compensation of the PZT mirror was necessary at the end of each experiment as a consequence of the hysteretic loop of the PZT with the change of the polarity of applied voltage. Therefore an external voltage was applied directly to the PZT amplifier, exactly the same as that provided by the feedback circuit (A-B)/(A+B). As the external signal is applied, the fringe shift is monitored by one element A of the bicell detector. The measured signal was sinusoidal and normalised between ±1, the arc sine of the measured signal gives the phase change $\Delta\phi$ as a function of the applied voltage.

158
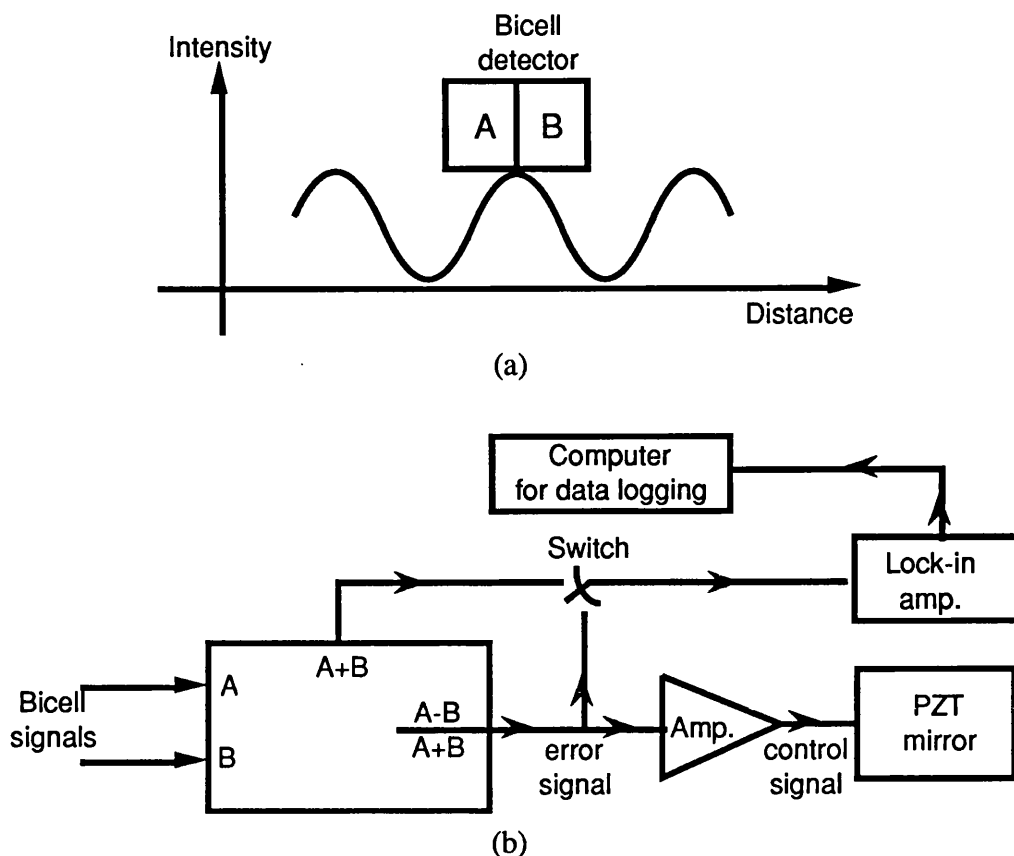
Fig. 6.14 a) *The alignment of the bicell detector with respect to the interferometer fringe pattern. b) A block diagram of the electronic feed-back loop circuit, the (A+B) signal provides a measure of the fringe intensity change via the absorption change in the sample in request and the (A-B)/(A+B) signal provides a measure of the fringe position change via the refractive index change in the sample in request.*

Experimental Results:

Fig. 6.15 shows the change in the refractive index for the TE-mode as a function of the input light intensity at three different photon energies. The refractive index change Δn was calculated from the measured fringe shift $\Delta\phi$;

$$\Delta n = \Delta\phi\frac{\lambda}{2\pi}L_{eff} \qquad (6.13)$$

These measurements were achieved by using the Hamamatsu videcon camera. For photon energies below or near to the excitonic peak (1.43 and 1.45 eV) , the intensity dependent refractive index change exhibits a negative change in refractive index (electronic effect), passes through a minimum, and then rises linearly (positive thermal effect) with the

increase in the input light intensity. The refractive index dependence on the input intensity is attributed to the influence of competing thermal and electronic nonlinearities. Because the electronic nonlinearity saturates, at the high input intensities, the dominant mechanism underlying the refractive index change is thermal. At the zero change in the refractive index the electronic effect equals the thermal effect. This is similar to behaviour which was observed before in semiconductor-doped glass waveguides [13]. The value of the unsaturated electronic refractive nonlinearity, n_2, was 1.4×10^{-8} cm^2/W calculated from the negative part of Fig. 6.15. This value is nearly an order of magnitude smaller than that measured in MQW elastic waveguides, $n_2 \approx 10^{-7}$ cm^2/W, at photon energy close to the exciton resonance [14]. The large value of n_2 in these elastic waveguides is due to the large number of QWs, 25 wells.

For photon energies above the exciton peak (the 1.50 eV curve in Fig. 6.15) it is predicted in [43] that the electronic part is positive at this photon energy and we did not observe a negative refractive index change.
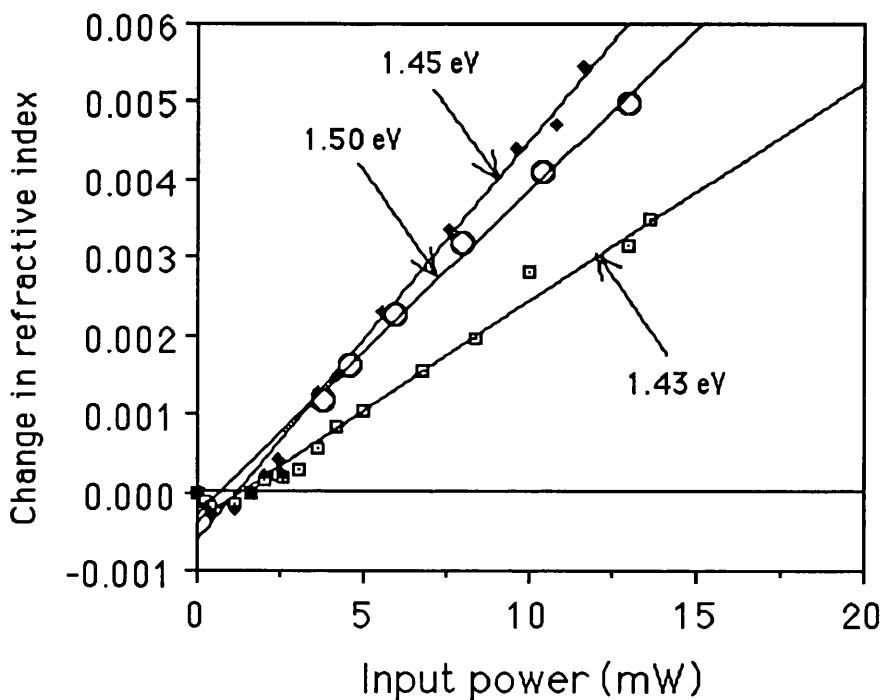
Fig. 6.15 *The change in the refractive index for the TE-mode in the A187 SQW waveguide as a function of the CW input light intensity at different photon energies. These measurements were obtained by using the external Mach-Zehnder interferometric set-up.*

At larger power levels with significant CW changes in refractive index the effect is dominated by the thermal mechanism. From previous observations [13] it is known that the thermally induced refractive index effect tended to be equalised in the guides by thermal diffusion thereby removing any differential phase shift; this is a relatively slow effect and takes place on a several tens of nanosecond timescale (depends upon the device configuration). Furthermore thermal effects are intrinsically slow to switch off.

The direction of movement of the fringe pattern due to the electronic and/or thermal effects was investigated by monitoring the fringes shift direction while heating the sample with a resistor (0.25 W) suspended above the sample (≤1 mm).

6.3.1.3 Time Resolved Resonant Nonlinear Effects:

The recovery time of the resonant nonlinearity is limited by the recombination rate of the photo-generated carriers. For usable application of the resonant nonlinearity for all optical switching devices, the recovery time of the photo-generated carriers should be in the picosecond or even femtosecond region. In this section the recovery time of the photo-absorption nonlinear effect was investigated by using the pump-probe experimental set-up.

In this method two orthogonally polarised pulsed beams were used; one was the pump beam (with high intensity) which causes the nonlinear effect and the other was the probe beam (with low intensity) which measures the nonlinear effect.

The experimental arrangement is shown in Fig. 6.16, the laser source was an actively mode-locked tunable Ti:sapphire laser, described in section 5.10.2. The laser output consisted of a train of ≈50 ps pulses spaced by 13 ns with an average power ≈350 mW. Therefore the pulse energy was approximately 5 nJ and a peak power ≈100 W.

Polariser beam splitters were used to split the laser beam into two beams pump and probe, the split ratio of the two beams can be adjusted by rotating the polarisation of the laser using a λ/4 waveplate. A variable delay was introduced in the probe beam by use of a retro-reflecting corner cube mounted on a linear translation stage. By adjusting the relative delay between the pump and probe pulses, it was possible to measure the relaxation time of the nonlinear effect to time scales as short as the pulse width but not to times greater than the pulse repetition time. The probe beam was chopped at 1 KHz. Another polariser-beam splitter was used to recombine the pump and probe beams, with orthogonal polarisations. The probe beam was TE polarised and the pump beam was TM polarised. The two beams were coupled through the waveguide using an end fire coupling rig. In the output side of

161

the rig, the pump beam was separated (blocked) from the probe beam by using a polariser. The transmitted probe beam was specially filtered (to eliminate scattered light and radiated modes) and focused onto a Si photodiode which was connected to a lock-in amplifier. An optimum input laser intensity was required to reduce optothermal nonlinear effects. This was achieved by A.C. modulation of the laser light using a combination of an electro-optic modulator and polariser, described in section 6.3.2.
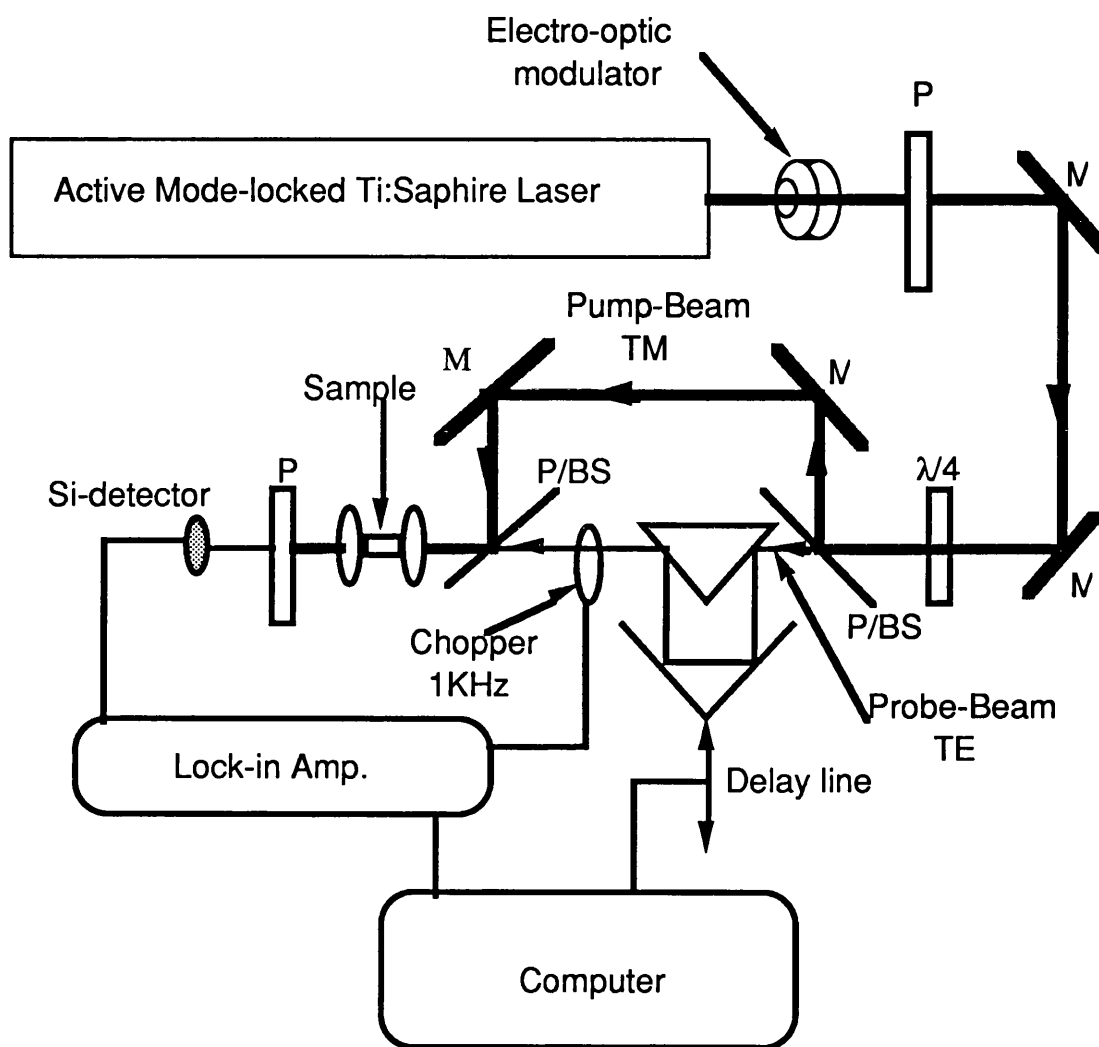
Fig. 6.16 *The pump-probe experimental apparatus, M's: mirrors, P/BS's: polariser beam splitters, P's: polarisers, $\lambda/4$: quarter-wave plate.*

Experimental Results:

The change in the probe beam output transmission as a function of the delay between the pump and probe pulses was measured at photon energies ranging from 1.431 eV to 1.468

eV. This range of energies covered the resonant excitonic transitions of the A187 SQW material. A maximum change in the probe output transmission was achieved at the lh-exciton resonance energy 1.458 eV. This is shown in Fig. 6.17, the change in the output transmission of the probe was due to the saturation of the absorption of the SQW caused by the pump beam.
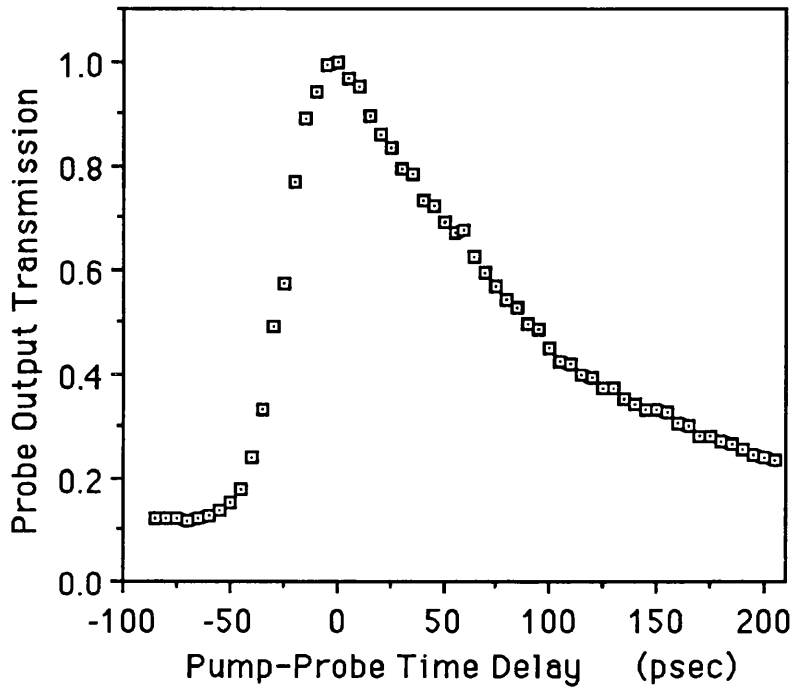
Fig. 6.17 *The normalised probe-beam output transmission of the A187 SQW waveguide as a function of the delay time between the pump and probe pulses. The probe beam is TE polarised and is orthogonal to the TM pump beam. The photon energy employed is 1.458 eV, the lh excitonic peak.*

From these measurements, the recovery time (1/e) of the nonlinear absorption was 125 ps. We believe the short recovery time is due to the reduction of the recombination time of the photogenerated carriers caused by surface recombination, where the quantum well is only 40 nm from the surface of the material. The process may well be assisted by a built-in electric field due to the depletion layer associated with the proximity of the surface. A similar reduction in recovery time has been observed by other authors [10] by the application of an electric field.

6.3.2 p-i-n GaAs/GaAlAs Single Quantum Well Waveguides:

The second generation of SQW waveguides were p-i-n GaAs/GaAlAs heterostructure. The design structure of QT147 SQW is shown in Fig. 4.4 in section 4.3. The SQW was 100 Å thick of GaAs embedded in a 0.6 μm thick of $Ga_{0.75}Al_{0.25}As$ guiding region. The intrinsic region was 1 μm thick and sandwiched between the top (p-type) and bottom (n-type) of $Ga_{0.71}Al_{0.29}As$ cladding layers. The epitaxial layers were symmetrical around the SQW which was placed in the centre of the guiding region.

Single-mode waveguides were designed in QT147 SQW material, the waveguide rib width and height were 3 μm and 2 μm respectively. This time the SQW overlap with the confined optical field is at its peak, therefore less power may required to saturate the resonant nonlinearity.

Passive waveguides were fabricated on QT147 SQW wafer. The rib widths W of these waveguides were 2 μm, 3 μm and 4 μm and the etching depth was 2.2 μm. The length of the sample was L=3.46 mm. The linear propagation loss in these waveguides was measured at λ=1.15 μm using Fabry-Perot technique. The facet reflectivity was assumed to be equal in all the waveguides R=30%. The propagation loss for the W=2 μm waveguides was 18 dB/cm with standard deviation of 2.5 dB/cm, for W=3 μm it was 15 dB/cm with standard deviation 1.8 dB/cm and for W=4 μm the loss was 14 dB/cm with 1.5 dB/cm standard deviation. This clearly shows the increase in the scattering loss due to the roughness in the waveguide sidewalls. As the rib width decreases, the overlap integral of the confined optical field and the sidewall roughness increases and therefore the scattering loss increases [15, 16].

Single-mode rib waveguides were fabricated with ohmic contacts on the top p-type and bottom n-type faces. The etching depth was 2.2 μm, this provided an electrical isolation between the neighbouring waveguides and enhanced the lateral optical confinement.

In the following sections, the linear and nonlinear characteristics of QT147 SQW waveguides were studied. This involved measurements of the electrical and optical fields induced effects on the waveguide absorption and refraction for the TE- and TM-modes.

6.3.2.1 Transmission Spectrum Measurements of QT147 SQW Waveguides:

The transmission spectrum of the QT147 SQW waveguides was measured using the end fire coupling system described in section 5.7.2. A CW tunable Ti:sapphire laser was used.

Fig. 6.18 shows the transmission spectra of the waveguide for the TE- and TM-modes. The waveguide length was 1 mm.
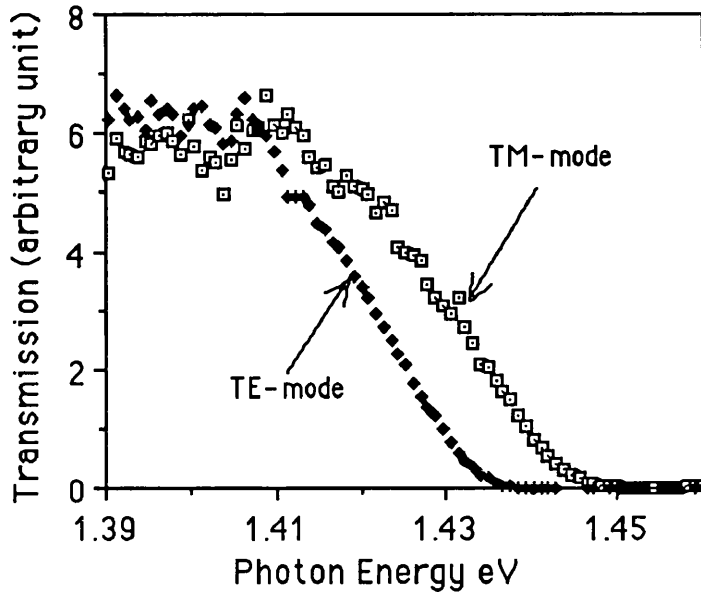
Fig. 6.18 *The transmission spectra of the TE- and TM-modes of the QT147 SQW waveguide with a rib width and height of 3 μm and 2.2 μm, respectively. The waveguide length was 1 mm.*

The incident light was fully absorbed at photon energies ≥1.434 eV and ≥1.447 eV for the TE- and TM-modes respectively. Recalling the results of the photo-current measurements, presented in section 4.5.4, the hh- and lh-exciton resonances of the QT147 SQW were at photon energies 1.562 eV and 1.566 eV respectively. Therefore, the incident light was completely absorbed at photon energies 128 meV and 119 meV below the SQW band edge for the TE- and TM-modes, respectively. Comparing the two results of Fig. 6.18 and Fig. 4.13 showed a clear discrepancy in the SQW absorption edge, the results in Fig. 6.18 indicated an absorption edge at ≈1.41 eV which is close to the band gap of the bulk GaAs.

6.3.2.2 Electric Field Induced Effects in QT147 SQW Waveguides:

The large electro-absorptive and -refraction effects in semiconductor quantum wells, close to the absorption band edge, has shown a great potential in using QW waveguides in electro-optic devices [18]. The large electric field induced changes in the optical properties of QWs was due to the QCSE [19], this was discussed in section 2.4. This effect was

demonstrated in the transmission measurements through the QW layers [20] and transmission along the QW layers in a waveguide configuration, for the TE- and TM-modes [21].

Our interest in the electro-absorption effect in GaAs/GaAlAs quantum well materials is to implement this effect along side the resonant nonlinear effects for designing all-optical switching devices with high throughput and larger switching modulation depths. These devices are proposed in section 7.4.

In considering the electro-refractive effect in relation to the Franz-Keldysh effect in bulk III-V semiconductors, it has been shown theoretically [22] that, at photon energies close to the band edge, the electric field induced refractive index change is quadratic with the electric field strength. In MQWs, the quadratic nature of the electro-refractive effect, close to the band edge, is due to the QCSE. This has been demonstrated experimentally in GaAs/GaAlAs MQWs [23, 24]. Following the work by A. Jennings [25] and Faist [26], the linear and quadratic effects were isolated by using the directional dependence of the linear electro-optic effect in the crystal. The electric field index change in a waveguide can be expressed as;

$$\Delta n(E) = \tfrac{1}{2}n_0^3 \left[\pm \Gamma_1 r_{63} E_z + \Gamma_2 s E_z^2 \right] \qquad (6.14)$$

where $\Delta n(E)$ is the change in the effective index of the waveguide in an electric field E_z which is in the direction perpendicular to the plane of the quantum well layers, Γ_1 and Γ_2 are the optical field confinement factors in the active region of the waveguide for the linear and quadratic electro-optic effects respectively and r_{63} and s are the linear and quadratic coefficients of the electro-optic effects respectively.

The sign of the linear electro-optic is positive for light propagating along [1$\bar{1}$0] and negative for light propagating along [110]. Therefore to enhance the electric field induced refractive index change in quantum well waveguides, they were fabricated along [1$\bar{1}$0]. In the nonlinear directional coupler, the applied electric field across one guide was to tune the initial state of the outputs as well as to enhance the recovery time of the nonlinearity. Therefore a large electro-refractive change in the directional coupler was required, and it was fabricated along [1$\bar{1}$0]. In the nonlinear AM-ZI devices, the applied electric field across one arm was to change the electro-absorption, therefore these devices were fabricated along [110].

The electric field was applied across the SQW by probing the top (p-type) and bottom (n-type) ohmic contacts and reverse biasing the double-heterostructure. The waveguide I-V characteristic is shown in Fig. 6.19, the reverse bias break down voltage was $V_b > 40$ V.
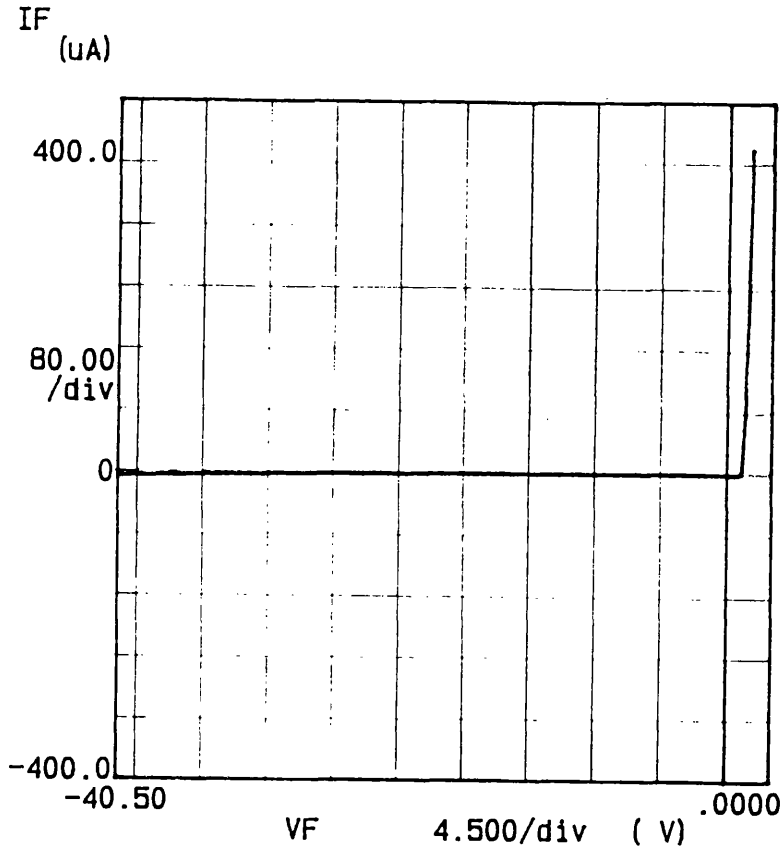
Fig. 6.19 *The diode I-V characteristics of a QT147 SQW p-i-n structure.*

In the following sections, the electro-absorption and -refraction effects in QT147 SQW waveguides were investigated.

Electro-Absorption Results:

Fig. 6.20 shows the transmission spectra of the QT147 SQW waveguide at different reverse bias voltages V_b, for the TM-modes. As expected, a red shift in the spectrum, as the bias voltage V_b increases, a shift of 35 meV in the absorption band edge was achieved at a bias voltage V_b=24 V.

The absorption change $\Delta\alpha(cm^{-1})$ as a function of the reverse bias voltage V_b was measured at a discrete photon energies. This is shown in Fig. 6.21, it shows a sharp increase in the absorption coefficient at photon energies closer to the band edge.
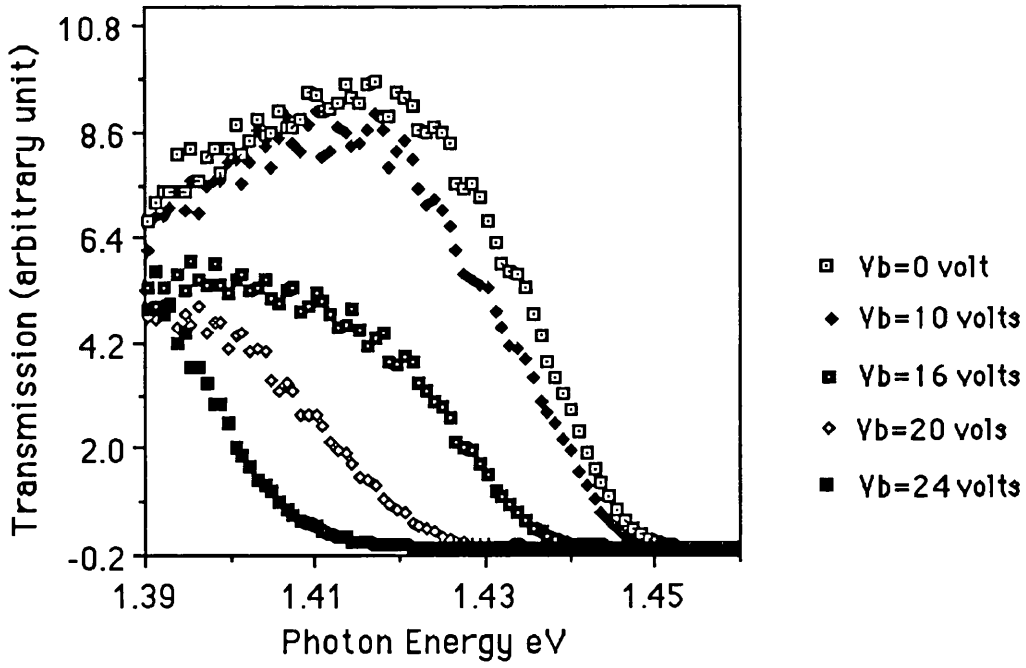
Fig. 6.20 *The transmission spectra of QT147 SQW waveguide as a function of the reverse bias voltage V_b.*
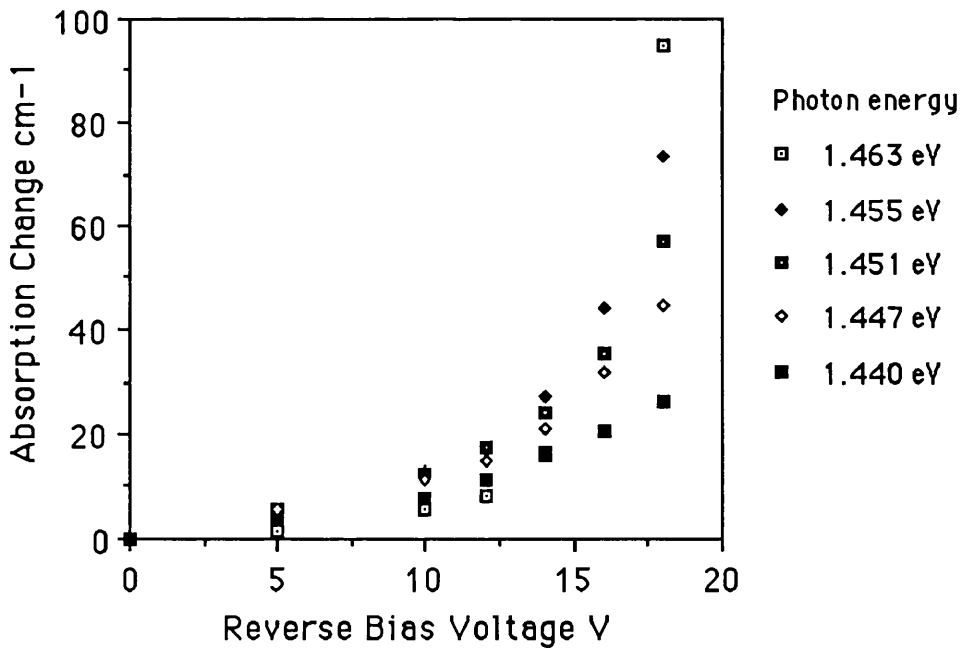
Fig. 6.21 *The change in the absorption coefficient (cm^{-1}) of the QT147 SQW waveguide as a function of the reverse bias voltage V_b, at different photon energies close to the SQW absorption edge.*

Fig. 6.22 shows the change in the absorption spectrum at different applied reverse bias voltages. At a bias voltage V_b= 18 V, an increase of 95 cm^{-1} in the absorption coefficient was obtained at a photon energy 1.463 eV. This is $\approx$4 times larger than that at 1.44 eV.
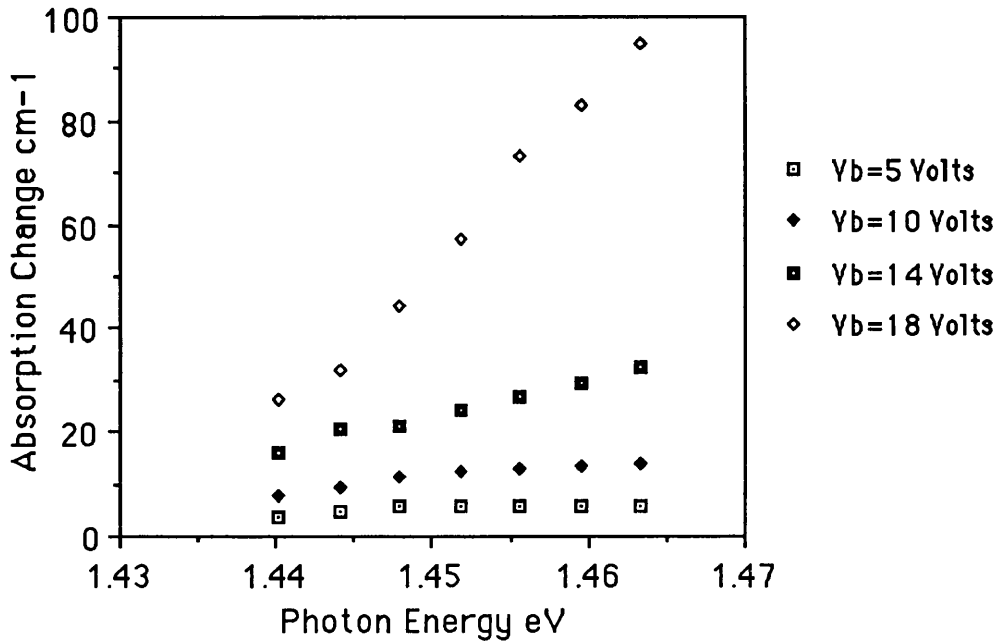
Fig. 6.22 *The change in the absorption spectra (cm^{-1}) of the QT147 SQW waveguide at different reverse bias voltages V_b, derived from the data in Fig. 6.21.*

Electro-Refractive Results:

The external Mach-Zehnder interferometric experimental set-up, described in section 6.3.1.2, was used to measure the electric field induced refractive index change in QT147 SQW waveguides. A CW tunable Ti:sapphire laser system was used.

The change in the SQW waveguide refractive index induced by applying an electric field perpendicular to the SQW was studied at photon energies away from and close to the material band edge. At a photon energy well below the band edge, λ=1.15 μm (1.079 eV), there was no shift in the external Mach-Zehnder interferometric fringes with applied reverse bias voltage. This means that there was no change in the SQW waveguide refractive index with applied electric field, via the linear electro-optic effect. This was the same for both polarisations, TE and TM. At photon energies close to the material band edge, the change in refractive index with applied reverse bias voltage V_b was small. For an applied voltage V_b=19 V, an index change of 1.2×10^{-4} at a photon energy 1.448 eV (118 meV below the

169

TM-mode lh-exciton) and increased by a factor of 2 to 2.39×10^{-4} at a photon energy 1.453 eV. These values of Δn are an order of magnitude smaller than measurements reported by A. Jennings[25] for GaAs/GaAlAs MQW and Yariv [27] for bulk GaAs.

6.3.2.3 Intensity Dependent Refractive Index Measurements in QT147 SQW Waveguides:

The intensity dependent refractive index change of waveguides fabricated on QT147 SQW were investigated, using the external M-Z interferometric set-up. The intensity of the CW Ti:sapphire laser was changed using the combination of the electro-optic modulator and polariser, described in section 6.3.1.2. The possible photon energy of the incident light used in the experiment was 1.453 eV (150 meV below the lh-exciton) before the fringes pattern disappear. There was no significant shift in the fringe pattern position, for the TE and TM polarisations, even at maximum input light intensity ($\approx$300 mW).

6.4 p-i-n GaAs/GaAlAs Multiple Quantum Well Waveguides:

A large intensity dependent refractive index variation is desirable for small size optical switches. The size of resonant nonlinear effects can be enhanced by increasing the number of the quantum wells in the guiding region. Sample A163 GaAs/GaAlAs MQW material was used in this work. The layer structure is shown in Fig. 4.5 in section 4.3, it was grown by MBE. It consisted of a 0.51 μm thick MQW intrinsic guiding region sandwiched between p-type (top) and n-type (bottom) cladding layers of $Ga_{0.75}Al_{0.25}As$ for transverse optical confinement. The quantum wells were designed with a well width of 100 Å and a barrier Al concentration of 30%. This wafer was designed by Dr. Andrew Jennings to investigate the electro-optic effects in MQW waveguides.

Stripe waveguides were designed to sustain a single mode for wavelengths close to the MQW absorption edge. Waveguides were fabricated, on A163 MQW material, with p-type and n-type ohmic contacts on the top and bottom faces of the waveguide. The waveguide rib width and etching depth were 3 μm and 1.9 μm respectively. The I-V characteristics of the waveguide gave a reverse bias break down voltage of 38 V.

6.4.1 Electro-Absorption Effect in A163 GaAs/GaAlAs MQW Waveguides:

The output transmission spectra of A163 MQW single mode waveguides were measured using the end fire coupling system, described in previous sections. Fig. 6.23 shows the transmission spectra for the TE- and TM-modes, the waveguide length was 1.8 mm.

It shows that the incident light was completely absorbed at photon energies 1.462 eV and 1.474 eV for the TE- and TM-modes respectively. From the photocurrent measurements, presented in section 4.5.4, the hh- and lh-excitonic resonant transitions were at photon energies 1.508 eV and 1.515 eV respectively. Therefore at photon energies 46 meV (for the TE-mode) and 41 meV (for the TM-mode) below the band edge, the incident light was fully absorbed. Comparing the two results of Fig. 6.23 and Fig. 4.15 showed a clear discrepancy in the MQW absorption edge, the results in Fig. 6.18 shows an absorption edge at $\approx$1.45 eV which is about 60 meV lower than the detected hh-exciton absorption in the photocurrent results.
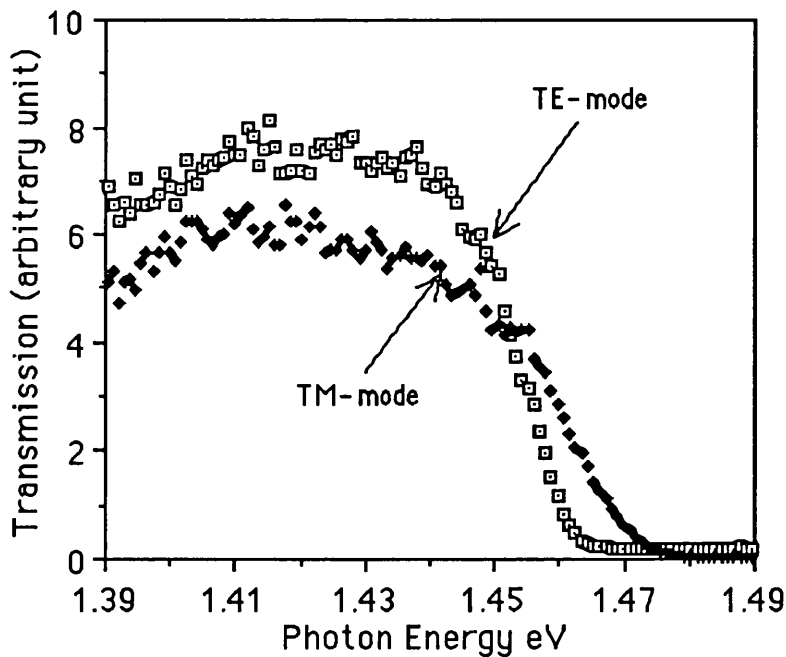
Fig. 6.23 *The transmission spectra of the TE- and TM-modes of the A163 MQW waveguide with a rib width and height of 3 μm and 1.9 μm, respectively. The waveguide length was 1.8 mm.*

In the next stage, the red shift in the absorption band edge in the MQW was measured. Fig. 6.24 shows the transmission spectra at different reverse bias voltages. A red shift of 34 meV in the band edge was achieved when the reverse bias voltage applied across the MQW region increased from zero to 14 volts.
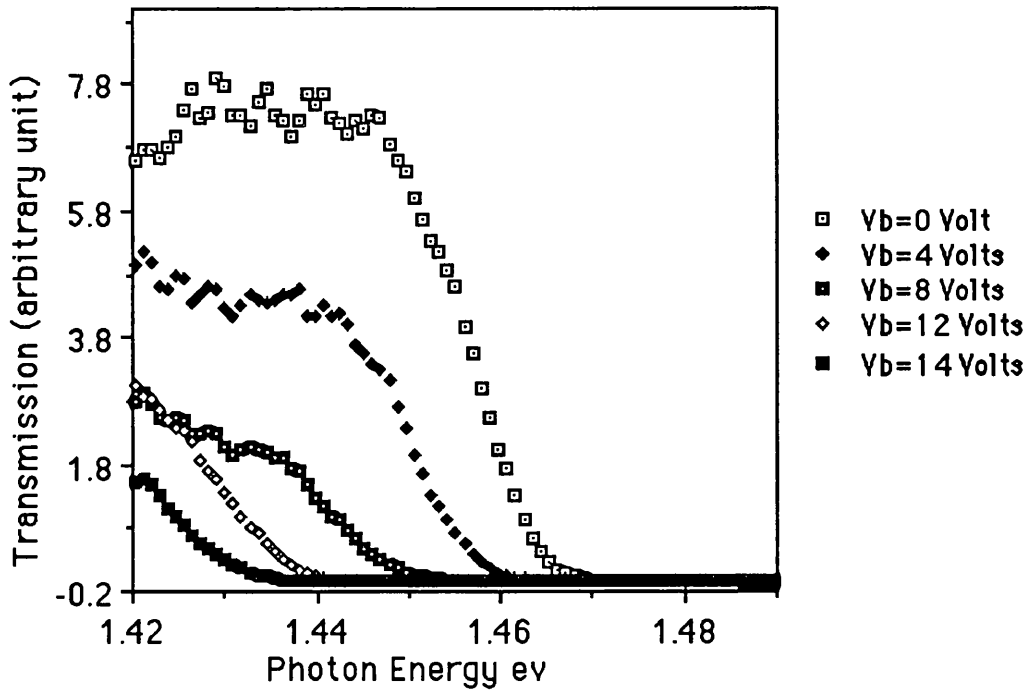
Fig. 6.24 *The transmission spectra of A163 MQW waveguide as a function of the reverse bias voltage* V_b.

6.4.2 Electro-Refractive Effect in A163 GaAs/GaAlAs MQW Waveguides:

The external Mach-Zehnder interferometer described in section 6.3.1.2 was used to measure the change in refractive index Δn as a function of the applied electric field across the A163 MQW waveguides. The measurements were achieved at discrete photon energies approaching the material band edge. These measurements were carried out on stripe waveguides with nominal width of 3 μm and etching depth 1.9 μm. The incident light was TM polarised.

Fig. 6.25 shows the change in refractive index Δn, for the TE-mode, as a function of the reverse bias voltage at four different photon energies. At photon energies greater than 1.444 eV, the maximum possible voltage can be applied across the waveguide, before the fringes pattern disappear, was 8 V. This was due to the increase in absorption of the waveguide via the QCSE which reduces the output transmission of the waveguide and causing a poor contrast in the interference fringes of Mach-Zehnder interferometer.

From the results in Fig. 6.25, there are two prominent features. Firstly, there is a large spectral variation in the electro-optic effect, Δn increases dramatically at photon energies closer to the excitonic resonance peak. Secondly, the refractive index change Δn is

nonlinear with the applied electric field. These indications suggest that there is a significant contribution from the quadratic electro-refractive effect unlike that of bulk GaAs and GaAs/GaAlAs MQW away from the material band edge [28]. In both cases, the linear electro-optic effect dominates the refractive index change.
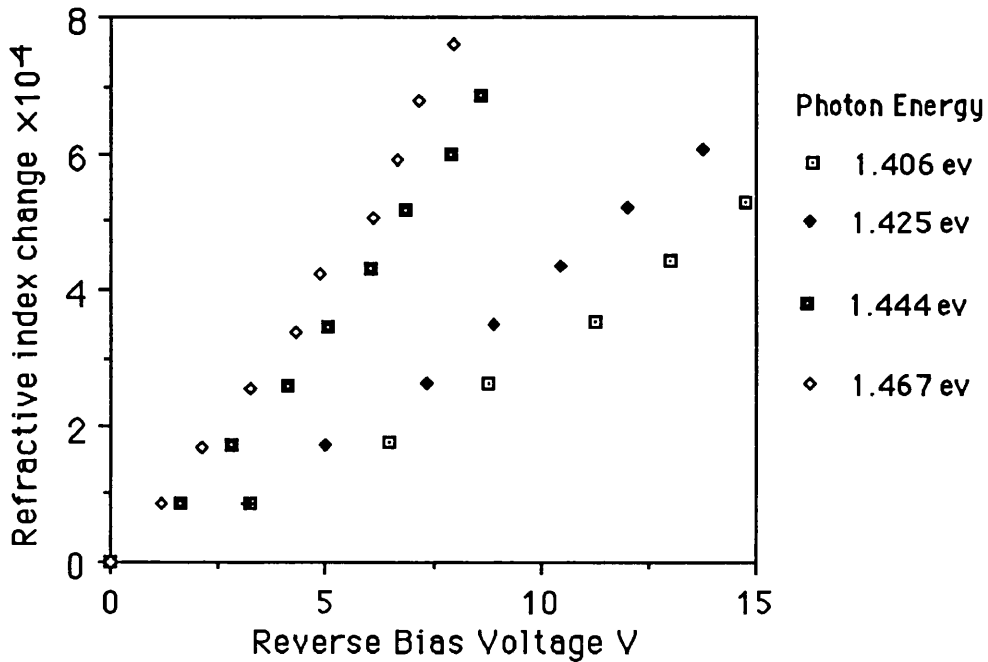
Fig. 6.25 *The change in refractive index for the TE-mode of A163 MQW waveguide as a function of the reverse bias voltage V_b, at different photon energies close to the MQW absorption edge.*

6.5 Nonresonant Nonlinearity in GaAlAs Stripe Waveguides:

There has been a considerable interest in all-optical switching devices which utilises the nonresonant contribution to the nonlinear refractive index n_2. These devices are desirable because they operate at photon energies well below the material absorption edge, i.e. low loss devices. Although the nonresonant nonlinearity has a fast recovery time (in the femtosecond region), the effect is small compared to the resonant nonlinearity and a high power density is required over a longer interaction length to achieve the necessary phase change. At these high power densities, the two-photon absorption TPA effect can become important. TPA effect can reduce the intensity of the input power before the required nonlinear phase shift is reached. Also the photo-generated carriers by the TPA induce a negative index change which washes out the small positive contribution from the nonresonant term [29-31].

173

6.5.1 Two-Photon Absorption TPA:

The effects of the TPA have been observed for photon energies below the material band gap [32-34]. It involves a two photon absorption at high intensity, and is allowed if twice the photon energy is greater than the semiconductor band gap. In this process an electron is promoted from the valence band to the conduction band via an intermediate state. The promoted electron reaches a final state such that $E_f-E_i=2\hbar\omega$.

The TPA coefficient β can be defined from the equation of attenuation of a propagating light through the material [43]:

$$\frac{dI}{dz} = -\alpha I - \beta I^2 \tag{6.15}$$

where α is the linear propagation losses coefficient (which includes both linear absorption loss and waveguide scattering loss), β is the two photon absorption coefficient and I is the effective laser intensity as a function of z. Integration of Eq. (6.15) yields:

$$I(z) = \frac{I(0)\,\alpha\,e^{-\alpha z}}{\alpha + \beta I(0)\,(1 - e^{-\alpha z})} \tag{6.16}$$

The output transmission of a waveguide with a length L is given by:

$$I(L) = I(0)\,\frac{e^{-\alpha L}}{1 + \beta L_{eff}\,I(0)} \tag{6.17}$$

where $L_{eff}=(1-e^{-\alpha L})/\alpha$, $I(0)=P_{in}/A_{eff}$ is the effective peak power density in the waveguide. This included the effective area of the guided mode, the coupling efficiency to the waveguide and the facet reflectivity of the waveguide. Eq. (6.17) can be rewritten as [44]:

$$T^{-1} = T_0^{-1} + \frac{\beta L_{eff}\,I(0)}{e^{-\alpha L}} \tag{6.18}$$

where $T=I(L)/I(0)$ is the measured waveguide transmission and T_0 is the linear transmission. By plotting T^{-1} as a function of the input peak power density $I(0)$, it is possible to deduce the TPA coefficient β from the slope of the best straight line fit to the points.

From Eq. (6.16), the TPA reduce the throughput of the waveguide. A general criterion for avoiding large TPA-induced loss can be introduced [29]:

$$\beta I(0) L_{eff} \langle 1 \qquad\qquad (6.19)$$

All-optical switching devices are based on generation of a phase shift ϕ, via the intensity dependent refractive index change n_2, of the order $p\pi$. Recalling Eq. (6.12):

$$p\pi = \frac{2\pi n_2 I_{in} L_{eff}}{\lambda} \qquad\qquad (6.20)$$

Combining Eq. (6.20) and relation (6.19), we can obtain the following relation

$$\frac{p\lambda\beta}{2 n_2} \langle 1 \qquad\qquad (6.21)$$

The TPA can be a sever limitation for all-optical switching devices, and can be quantified by a parameter derived from the relation (6.21) [35]:

$$\eta = \frac{p\beta\lambda}{n_2} \qquad\qquad (6.22)$$

For a given waveguide device, p varies from 0.5 to 3.5 [36], e.g. for a nonlinear directional coupler p=2 and for a nonlinear asymmetric Mach-Zehnder interferometer p=1. When η increases to values lager than unity, the power required for switching rises, the switching becomes incomplete, and the throughput drops dramatically [37]. Delong et. al. [35] have evaluated theoretically the parameter η which quantifies the effects of TPA on all-optical switching waveguide devices, utilizing nonresonant nonlinearities. Fig. 6.26 shows a plot of TPA parameter $\eta = p\beta\lambda/n_2$ as a function of a semiconductor photon energy (after reference 35). For efficient operation of an all-optical switch, η required to be less than 1. The divergence near $\hbar\omega=0.74E_g$ is due to the fact that n_2 vanishes at that point. For photon energies less than half the band gap energy, β (and thus η) is equal to zero. Realistically, β does not go to zero at photon energies $\hbar\omega<E_g/2$ due to defect and trap states and band gap tail states. From that model, it is clear that as soon as the photon energy reaches half the band gap energy (where TPA is allowed), the TPA parameter η becomes greater than unity and the condition for viable switching is violated. This suggest that in order to use the nonresonant nonlinearity in semiconductor, the photon energy must be kept out of the region where TPA is allowed (i.e. $\hbar\omega<E_g/2$). Therefore the nonresonant nonlinearity in

GaAlAs semiconductor waveguides was investigated at photon energies below half the band gap.
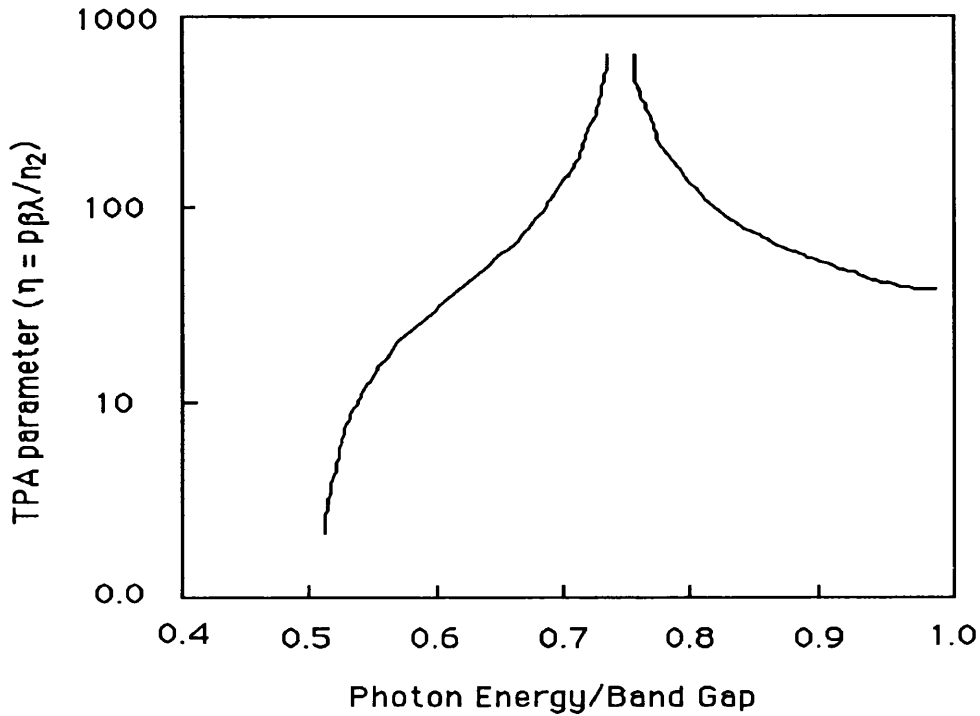
Fig. 6.26 *Two-photon parameter $\eta=p\beta\lambda/n_2$ as a function of a semiconductor photon energy, η is required to be less than 1. The divergence near $h\omega=0.74E_g$ is due to the fact that n_2 vanishes at that point. For photon energies less than half the band gap energy, β (and thus η) is equal to zero.(after ref. 37).*

In the following section the SPM technique is described. This includes firstly the theory, and secondly presenting the experimental arrangement and results of SPM. The nonlinear Kerr coefficient n_2 in GaAlAs waveguides is measured using self-phase modulation SPM technique.

6.5.2 Self-Phase Modulation SPM:

The intensity dependent refractive index change of a dielectric material is expressed as;

$$n = n_0 + n_2 I \qquad (6.23)$$

where all symbols have their usual meaning, see chapter 1. If a dielectric material is subject to an intense pulse then a refractive index change will be induced. When the relaxation time of this effect is shorter than the pulse width (a few femtoseconds), then the index change will vary with the shape of the pulse. This means that the more intense part of the pulse experience a higher refractive index. The central portion of the pulse is therefore delayed with respect to the less intense leading and trailing parts of the pulse. This lead to a frequency chirping. Self-phase modulation is a nonlinear effect in which the phase relation between different parts of the pulse are modified. It is an accumulative effect and over long enough propagation distances, the induced chirp may become large enough so that dispersion effects lead to changes in the pulse shape.

6.5.2.1 Theory:

Consider an optical pulse with a gaussian temporal profile propagating along a length L. It is clear that each part of the pulse, having a different intensity, will experience a different refractive index and hence a change in phase occur across the pulse given by;

$$\Delta\phi(t) = -kn_2I(t)L_{eff} \tag{6.24}$$

where k is the wavenumber of the pulse and L_{eff} is the effective length of the waveguide $L_{eff}=(1-e^{-\alpha L})/\alpha$. Since the intensity and hence the phase shift is a function of time, the pulse develops a frequency shift $\Delta\omega$ from the carrier frequency ω_0. The frequency shift $\Delta\omega$ is proportional to the time derivative of the intensity;

$$\Delta\omega(t) = \frac{\partial\Delta\phi(t)}{\partial t} = -kn_2L_{eff}\frac{\partial I(t)}{\partial t} \tag{6.25}$$

From this, it can be seen that the instantaneous frequency of the carrier in the leading part of the pulse (t<0) is down-shifted and the trailing part (t>0) is up-shifted.

A gaussian input pulse of duration τ_p at full width half maximum FWHM has the form;

$$I(t) = I_0 e^{-\left(\frac{t}{\tau}\right)^2} \tag{6.26}$$

where

$$\tau_p = 2\sqrt{\ln 2}\,\tau$$

Fig. 6.27 shows the pulse shape and the instantaneous frequency shift as a function of time. The maximum phase shift occurs at the peak of the pulse, $\Delta\phi_{max} = -kn_2L_{eff}I_0$, and the maximum frequency shift at the points of inflection, where $\partial I/\partial t$ is a maximum. Setting $\partial^2 I/\partial t^2 = 0$ we obtain;

$$t = \tau / \sqrt{2}$$

and

$$\Delta\omega_{max} = \pm \sqrt{\frac{2}{e}} kL_{eff} n_2 I_0 \frac{2\sqrt{\ln 2}}{\tau_p} \qquad (6.27)$$
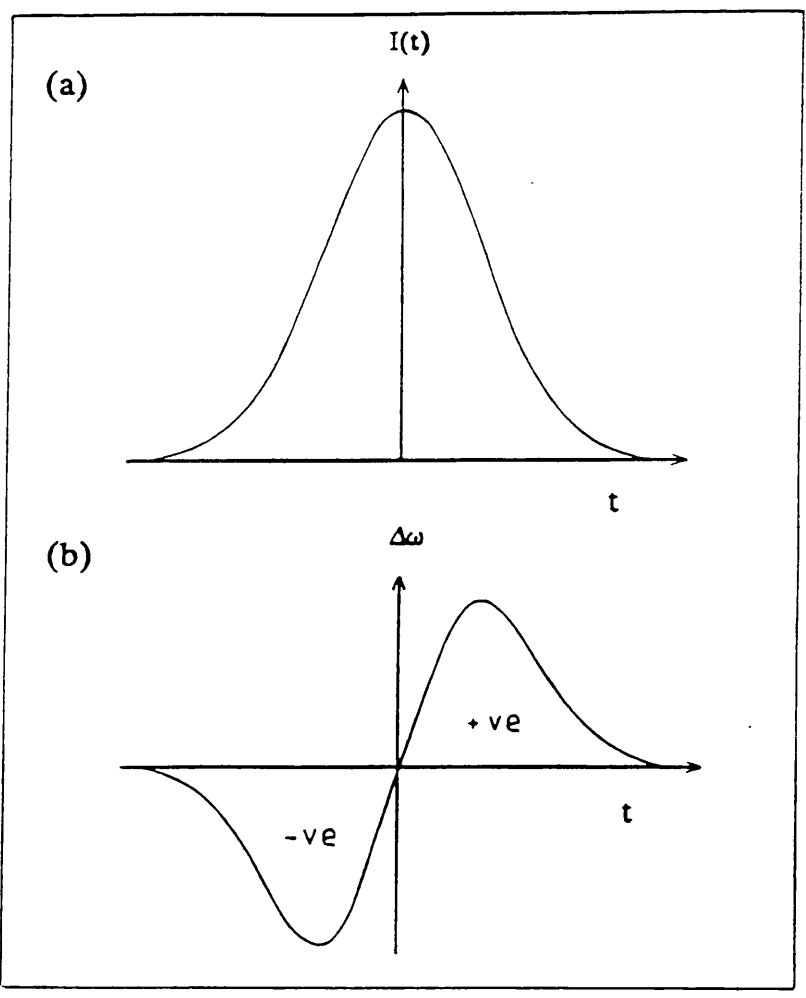
Fig. 6.27 a) *Input gaussian pulse* b) *Instantaneous frequency shift due to SPM.*

From Fig. 6.27b, the linear portion of the frequency chirp of the pulse is refereed to as an up-chirp since the frequency increases with time. It should be noted that the time-dependent phase modulation does not affect the temporal intensity distribution of the pulse. In the absence of any group velocity dispersion GVD, the pulse envelope should be exactly the same as the input pulse after propagating through the length L of the sample. The frequency spectrum of the pulse can be obtained from the Furrier transform of the electric field of the pulse. The electric field amplitude for a gaussian pulse is;

same as the input pulse after propagating through the length L of the sample. The frequency spectrum of the pulse can be obtained from the Furrier transform of the electric field of the pulse. The electric field amplitude for a gaussian pulse is;

$$E_{in}(t) = \sqrt{I_0}\, e^{-\frac{1}{2}\left(\frac{t}{\tau}\right)^2} e^{j\omega_0 t} \qquad (6.28)$$

After passing through the length L of the sample;

$$E_{out}(t) = \sqrt{I_0}\, e^{-\frac{1}{2}\left(\frac{t}{\tau}\right)^2} e^{j(\omega_0 t - \Delta\phi(t))} \qquad (6.29)$$

The Fourier transform of Eq. (6.29) gives the frequency spectrum $\vert E(\omega)\vert^2$ where;

$$E(\omega) = \sqrt{I_0}\, \int_{-\infty}^{\infty} e^{-\frac{1}{2}\left(\frac{t}{\tau}\right)^2} e^{-j\Delta\phi(t)} e^{-j(\omega-\omega_0)t} dt \qquad (6.30)$$

This function can be solved numerically. R.H. Stolen [38] calculated the frequency spectrum for a gaussian pulse at different intensities, as shown in Fig. 6.28. From Fig. 6.27 it can be seen that there are in general two points in time which give the same frequency shift. The SPM spectrum can be thought to arise from a constructive and destructive interference of the pairs of frequency components generated from the two points in time.

In experimental measurements of the SPM, the total band width of the pulse in term of wavelength is measured. Therefore Eq.(6.27) can be converted to give the maximum spectral width of the pulse [39];

$$\Delta\lambda = \Delta\lambda_i + \frac{\lambda L_{eff} n_2 P_0}{CA_{eff} T_p} 4\sqrt{2\ln 2\, /\, e} \qquad (6.31)$$

where $\Delta\lambda_i$ is the initial bandwidth of the pulse, P_0 the pulse peak power and A_{eff} is the effective cross section area of the waveguide.

In the above analysis, the refractive index of the medium has been assumed to be independent of the optical frequency. If there is no nonlinear effect present in the material, then dispersion in the material will lead to pulse broadening. This is true regardless of whether the group velocity dispersion GVD of the material $(\partial v_g/\partial\lambda)$ is negative or positive.

6.5.3 Experimental Measurements:

The nonresonant nonlinear effects in GaAlAs waveguides have been investigated at wavelength λ=1.55 μm (below half the band gap) to eliminate the problem of TPA. Furthermore, for devices operates in this spectral region are attractive because this is one of the low loss telecommunication windows (i.e. 1.3 μm and 1.55 μm). All the nonresonant nonlinear experiments were carried out at St. Andrews University/Department of Physics.
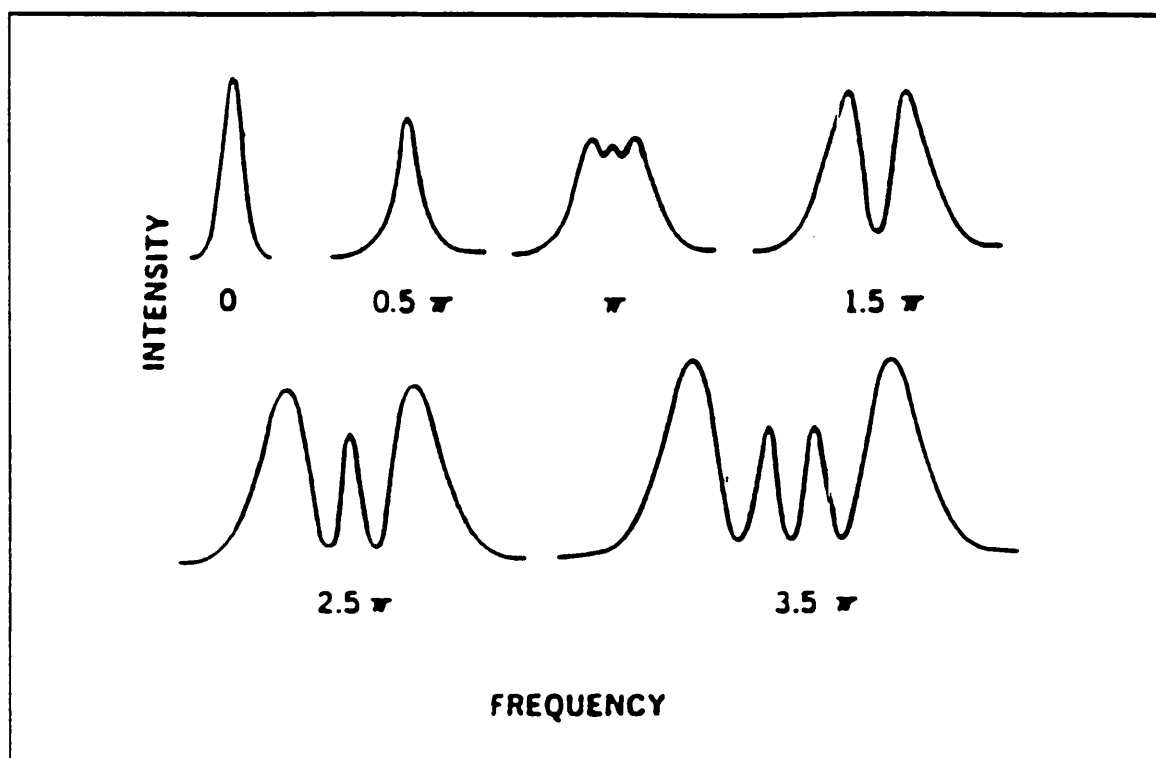
Fig. 6.28 *The calculated spectra broadening due to SPM for a gaussian pulse of varying intensity (after ref. 38).*

6.5.3.1 Experimental Set-up:

Fig. 6.29 shows a schematic diagram of the experimental set-up, the laser source was the coupled-cavity mode-locked KCl:Tl colour centre laser describe in section 5.11. Ultrashort pulses were generated at a wavelength λ=1.52 μm with pulse width $\tau_p \approx$330 fsec at a repetition rate of 82 MHz. The average power from the laser was $\approx$65 mW (i.e. $\approx$2.33 KW peak power). The pulses of the laser were coupled into the waveguide by using an antireflection coated ×20 objective lens and coupled out using a ×40 objective lens. A Faraday optical isolator was placed between the KCl:Tl coupled-cavity laser and the end fire rig to prevent any optical feedback from the waveguide facet to the laser cavity, which

180

degrades the mode-locking. The peak power of the input pulses was varied by using a motor controlled attenuating wheel. A halfwave plate and polariser were used to set the polarisation of the laser to either a TE or TM.
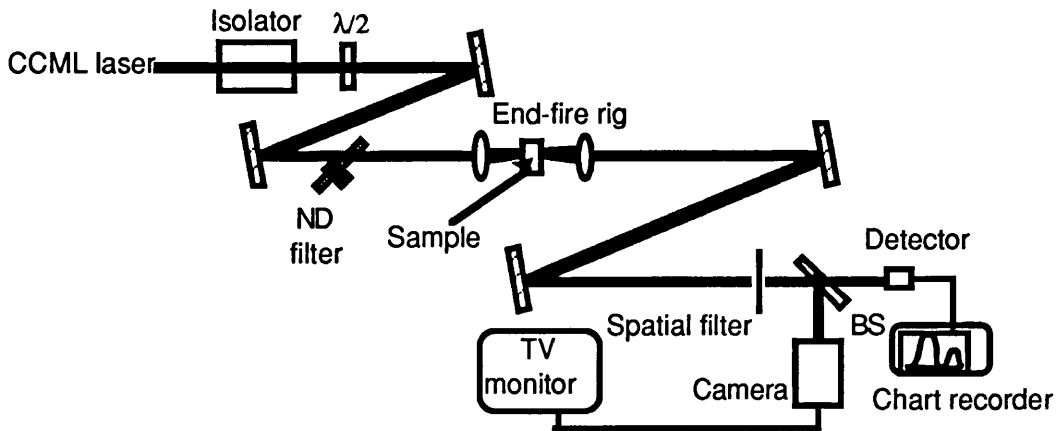
Fig. 6.29 *Schematic diagram of the experimental set-up using an ultrashort pulses from a CCML colour centre laser. BS: beamsplittor, ND filter: nutral density filter.*

The incident and transmitted lights were measured using a calibrated Ge detector. The output of the waveguide was specially filtered to eliminate any stray and scattering lights from reaching the detector. This was achieved by focusing the output of the waveguide through a <0.5 mm in diameter aperture placed at a distance around 1.5 m from the output objective lens.

6.5.3.2 Self-Phase Modulation SPM Results:

Waveguides were fabricated in GaAlAs A293 material, described in section 4.3, using the standard optical lithography and lift-off processes. Measurements were performed on waveguides with rib width and height 3 μm and 1.6 μm respectively. The length of these waveguides was 7.4 mm. The far field mode profile of the output was examined using a C1000 Hamamatsu camera which confirmed that these waveguides were single moded. The linear propagation losses was measured using Fabry-Perot technique, $\alpha=1.7\pm0.15$ cm^{-1}.

The optical spectral broadening of the input pulse propagating in the waveguide, via the SPM was scanned by using a monochrometer. Fig. 6.30 shows the output spectra for the TE-mode of the transmitted pulses through the waveguide at different input peak intensities. Comparing these results with ref. [38], a phase shift of $3\pi/2$ and $5\pi/2$ were obtained at 3 GW/cm^2 and 6.25 GW/cm^2 respectively.

181

The spectra exhibited broadening on both sides, indicating that the rise and recovery times of the nonlinearity were much faster than the pulse width (<<100 fsec). The spectral broadening due to the SPM was measured for the TM-mode in these waveguides, this showed that the SPM was polarisation independent for the GaAlAs waveguides.
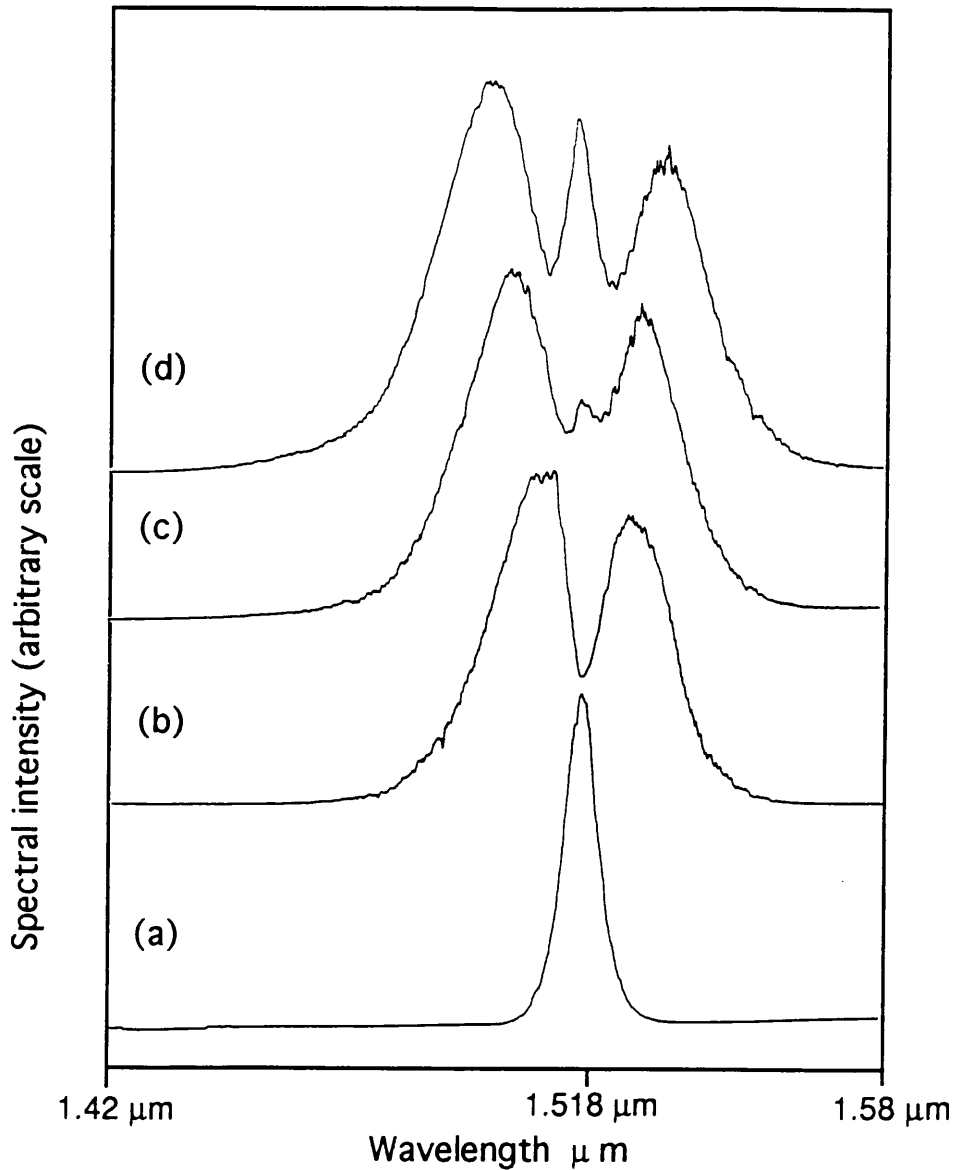
Fig. 6.30 *Observed self-phase modulated spectra of the output pulses from GaAlAs waveguide at peak power densities;* a) *low power* b) *3 GW.cm^{-2}* c) *4 GW.cm^{-2}* d) *6.25 GW.cm^{-2}.*

The nonresonant intensity dependent refractive index coefficient n_2 of GaAlAs rib waveguide was obtained from the SPM measurements using Eq. (6.31), $n_2 \approx +(5.405 \pm 0.5) \times 10^{-14}$ cm^2/W. This was smaller than the calculated $n_2 \approx +1.1 \times 10^{-13}$ cm^2/W for the same material in ref. [41]. Their value was estimated by fitting the experimental results of the ultrafast switching of the directional coupler, at a wavelength

182

λ=1.54 μm. As we will see later in section 7.8.2, that our value of n_2 was confirmed by the experimental results of the demonstrated ultrafast asymmetric Mach-Zehnder interferometer. Ho et al [40] calculated n_2 coefficient, from SPM measurements, in $Ga_{0.8}Al_{0.2}As$ waveguides at wavelength λ=1.6 μm (below half the band gap), $n_2 \approx +(3.6 \pm 0.5) \times 10^{-14}$ cm^2/W. Their results are in good agreement with our results.

6.5.3.3 Two-Photon Absorption Results:

The two-photon absorption TPA coefficient in A293 GaAlAs waveguides, described in the previous section, was investigated at photon energy below half the band gap of the $Ga_{0.82}Al_{0.18}As$ guiding region, λ=1.52 μm. The experimental set-up shown in Fig. 6.29 was used. The output transmission of the 3 μm single mode waveguide was measured as a function of the input light intensity. Fig. 6.31 shows the output transmission (mW) as a function of the average input power for two different input pulse widths, 30 ps and 330 fsec, (i.e. two different peak powers). The broad pulses were generated by excluding the nonlinear coupled cavity from the main laser cavity. Therefore the average power and coupling efficiency to the waveguide did not change for the two different peak powers.
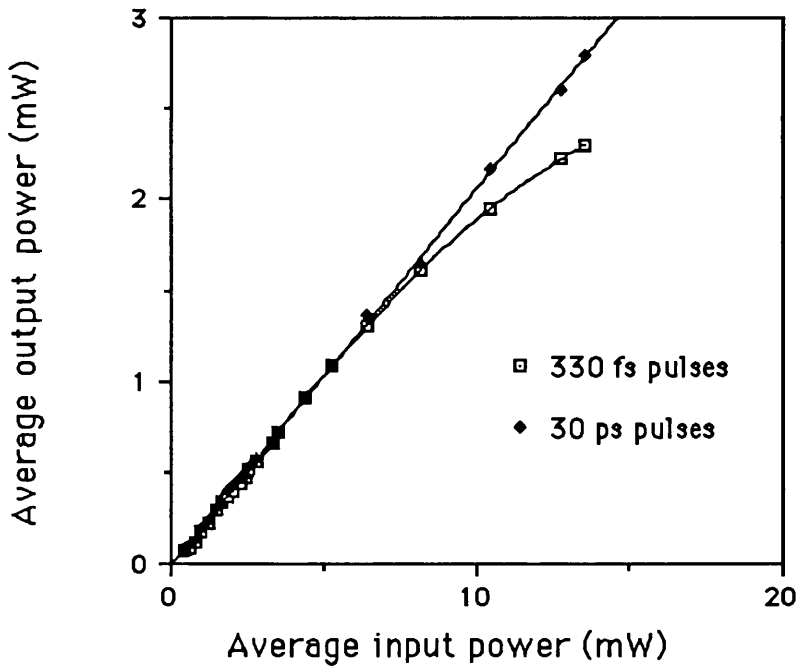
Fig. 6.31 *Comparison of transmission of high intensity (330 fs) pulses and relatively low intensity (30 ps) pulses in straight GaAlAs waveguide as a function of the input light intensity, at photon energy below half the band gap of the guiding region (λ=1.52 μm). The average power is referred to the estimated power in the waveguide after taking account of coupling and reflection losses.*

For $\tau_p\approx30$ ps, the output transmission varied linearly with the input power, there was no nonlinear absorption (i.e. $\beta=0$). As the input power was increased by a factor of 100 ($\tau_p\approx330$ fsec) the output transmission tend to saturate at high input powers ≥10 mW (≥370 W peak power). The input and output powers in Fig. 6.31 included the coupling efficiency as well as the waveguide facets reflectivity. These results indicated that at high powers, the TPA coefficient $\beta\neq0$ even at photon energies below the TPA region. This can be due to the overgrowth defects and band tail states in the $Ga_{0.82}Al_{0.18}As$ material. From Fig. 6.31 the throughput of the straight waveguide was estimated, with no TPA (i.e $\tau_p\approx30$ ps), $\approx25\%$ where the coupling and facets losses are included.

The TPA coefficient β was calculated by plotting the reciprocal of the output transmission T^{-1} as a function of the input peak power density (GW/cm^2). Fig. 6.32 shows T^{-1} verses input average power, at $\tau_p\approx30$ ps, $\beta=0$. At $\tau_p\approx330$ fsec, the obtained β value from the slop of the straight line ($slop=\beta L_{eff}/\exp(-\alpha z)$) was 0.14 cm/GW. This TPA coefficient β may increases by a factor of 100 as the photon energy enter the TPA region, $\hbar\omega\geq E_g/2$, [44].
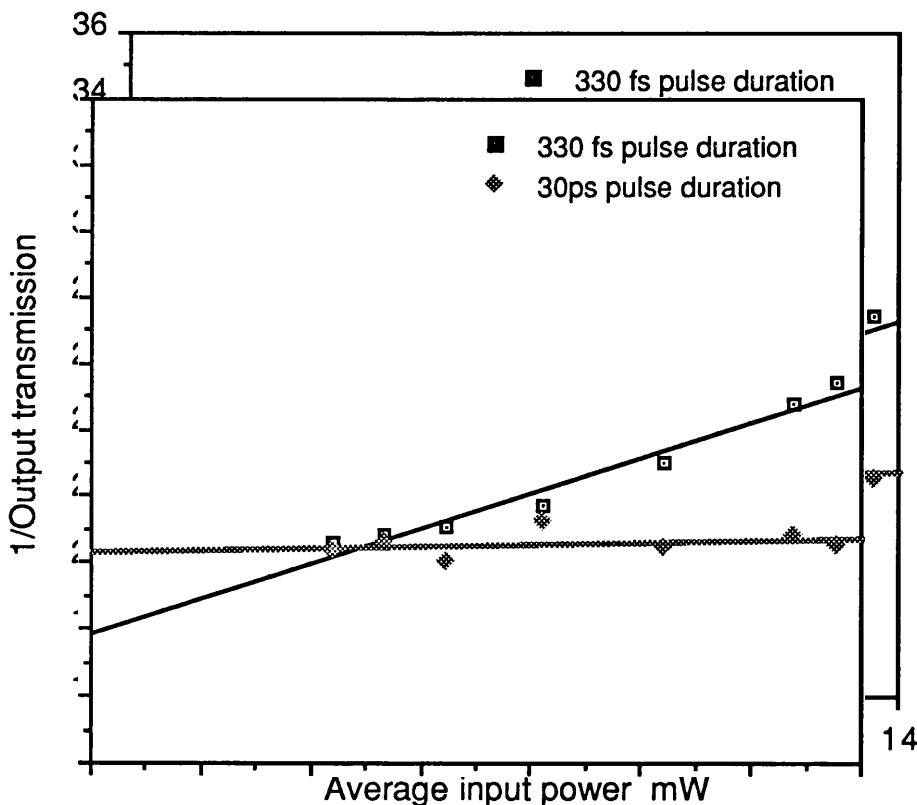
Fig. 6.32 *The reciprocal of the transmission of the GaAlAs rib waveguide as a function of the input light intensity. The gradient of the best fit straight lines are proportional to the TPA coefficient.*

TPA Parameter η:

The TPA parameter was obtained from the measured parameters of n_2 and β values for the $Ga_{0.82}Al_{0.18}As$ waveguides, $\eta \approx 0.38$ at wavelength $\lambda=1.52$ μm. From the suggested theory of DeLong and Stegeman [35], GaAlAs material was suitable to be used for all-optical switching devices, as $\eta<1$.

A very successful all-optical switching device, based on the nonresonant nonlinear directional coupler [41] and asymmetric Mach-Zehnder interferometer [described in section 7.8.2] were demonstrated with this material.

6.6 Conclusion:

In this chapter we investigated the nonlinear optical properties of GaAs/GaAlAs single and multiple QW waveguides. These investigations included, firstly: the resonant nonlinear effects, photo-absorption and refraction effects, at photon energies close to and above the material band gap. The external Mach-Zehnder interferometer was used to measure the magnitude and the type, thermal and/or electronic, of the resonant nonlinearity. A large electronic nonlinear coefficient $n_2=1.4\times10^{-8}$ cm^2/W was measured in the GaAs/GaAlAs SQW rib waveguides. The recovery time of the resonant nonlinearity in these passive waveguides was measured using the pump-probe experiment, a short recovery time of ≈125 ps was achieved. This short recovery time was due to the enhanced surface recombination of the photogenerated carrier, where the SQW was only 400 Å below the top surface of the material.

Secondly, the nonresonant nonlinear effects in $Ga_{0.82}Al_{0.18}As$ waveguides were investigated, at photon energies below half the band gap, these included the SPM and TPA measurements. The nonresonant nonlinear refractive index coefficient below half the band gap was measured, $n_2=(5.4\pm0.5)\times10^{-14}$ cm^2/W. The figure of merit, $\eta=p\beta\lambda/n_2$, showed that this material is suitable to demonstrate ultrafast all-optical switching devices.

GaAs/GaAlAs SQW and MQW p-i-n structures were used to investigate the enhancement of the relaxation time of the resonant nonlinearity with applied electric field in active rib waveguides. These studies included the investigation of the electro-refractive and absorptive effects in QW waveguides.

References:

[1] H.Haug and S. Schmitt-Rink, *"Optical nonlinearities and instabilities in semiconductors"*, Prog. Quantum Electron,. vol. 9, p. 3 (1984).

[2] D.S. Chemla and D.A.B. Miller, *"Room-temperature excitonic nonlinear-optical effects in semiconductor quantum well structures"*, J. Opt. Soc. Am. B2, p. 1155 (1985).

[3] D.S. Chemla, D.A.B. Miller, P.W. Smith, A.C. Gossord and W. Wiegmann, *"Room temperature excitonic nonlinear absorption and refraction in GaAs/GaAlAs multiple quantum well structures"*, IEEE J. Quantum Electron. QE-20, p. 265 (1984).

[4] T.E. Van Eck, L.M. Walpita, W.S.C. Chang and H.H. Wieder, *"Franz-Keldysh electro-refractive and electro-absorption in bulk InP and GaAs"*, Appl. Phys. Lett, vol. 48, p. 451 (1986).

[5] G.W. t'Hooft, M.R. Leys and F. Roozeboom, *"Low interface recombination velocity in GaAs/GaAlAs double heterostructures grown by metal organic vapour phase epitaxy"*, Jap. J. Appl. Phys., vol. 24, L761 (1985).

[6] G. Duggan, G.B. Scott, C.T. Foxon and J.J. Harris, *"Photoluminescence technique for the determination of minority-carrier diffusion length in GaAs grown by molecular beam epitaxy"*, Appl. Phys. Lett., vol. 38, p. 246 (1981).

[7] D.A.B. Miller, D.S. Chemla, D.J. Eilenberger, P.W. Smith, A.C. Gossard and W.T. Tsang, *"Large room-temperature optical nonlinearity in GaAs/GaAlAs multiple quantum well structures"*, Appl. Phys. Lett., vol. 41, p. 679 (1982).

[8] P. LiKamWa, A. Miller, C.B. Park, J.S. Roberts and P.N. Robson, *"All-optical switching of picosecond pulses in a GaAs quantum well waveguide coupler"*, Appl. Phys. Lett., vol. 57, p. 1846 (1990).

[9] Y. Silberberg, P.W. Smith, D.A.B. Miller, A.C. Gossard and W. Wiegmann, *"Fast nonlinear optical response from proton-bombarded multiple quantum well structures"*, Appl. Phys. Lett., vol. 46, p. 701 (1985).

[10] P. LiKamWa, A. Miller, J.S. Roberts and P.N. Robson, "*130 ps recovery of all-optical switching in a GaAs multiquantum well directional coupler*", Appl. Phys. Lett., vol. 58, p. 2055 (1991).

[11] J.I. Pankove, "*Optical processes in semiconductors*", Dover publications Inc., New York (1971).

[12] H. Haug, S. Schmitt-Rink, "*Basic mechanisms of the optical nonlinearities of semiconductors near the band edge*", J. Opt. Soc. Am. B, vol. 2, p. 1135 (1985).

[13] N. Finlayson, W.C. Banyai, C.T. Seaton, G.I. Stegeman, M. O'Neill, T.J. Cullen and C.N. Ironside, "*Optical nonlinearities in CdS_xSe_{1-x} doped glass waveguides*", J. Opt. Soc. Am. B6, p. 675 (1989).

[14] P. LiKamWa, J.H. Marsh, P.N. Robson, J.S. Roberts and N.J. Mason, "*Nonlinear propagation in GaAs/GaAlAs MQW waveguides*", SPIE Proc., vol. 578, p. 110 (1985).

[15] R.J. Deri, E. Kapon and L.M. Schiavone, "*Scattering in low-loss GaAs/GaAlAs rib waveguides*", Appl. Phys. Lett., vol. 51, p. 789 (1987).

[16] R.J. Deri, R.J. Hawkins and E. Kapon, "*Rib profile effects on scattering in semiconductor optical waveguides*", Appl. Phys. Lett., vol. 53, p. 1483 (1988).

[17] J.S. Weiner, D.S. Chemla, D.A.B. Miller, H.A. Haus, A.C. Gossard, W. Wiegmann and C.A. Burrus, "*Highly anisotropic optical properties of single quantum well waveguides*", Appl. Phys. Lett., vol. 47, p. 664 (1985).

[18] J.E. Zucker, K.L. Jones, M.G. Young, B.I. Miller and U. Koren, "*Compact directional coupler switches using quantum well electrorefraction*", Appl. Phys. Lett., vol. 55, p. 2280 (1989).

[19] D.A.B. Miller, D.S. Chemla, T.C. Damen, A.C. Gossard, W. Wiegman, T.H. Wood and C.A. Burrus, "*Band-edge electroabsorption in quantum well structures: The quantum confined stark effect*", Phys. Rev. Lett., vol. 53, p. 2173 (1984).

[20] D.S. Chemla, T.C. Damen, D.A.B. Miller, A.C. Gossard and W. Wiegmann, "*Electroabsorption by stark effect on room temperature excitons in GaAs/GaAlAs multiple quantum well structures*", Appl. Phys. Lett., vol. 42, p. 864 (1983).

[21] J.S. Weiner, D.A.B. Miller, D.S. Chemla, T.C. Damen, C.A. burrus, T.H. Wood, A.C. Gossard and W. Wiegman, *"Strong polarisation-sensitive electroabsorption in GaAs/GaAlAs quantum well waveguides"*, Appl. Phys. Lett., vol. 47, p. 1148 (1985).

[22] B.R. Bennett and R.A. Soref, *"electrorefraction and electroabsorption in InP, GaAs, GaSb, InAs and InSb"*, IEEE J. Quantum Electron, vol. 23, p. 2159 (1987).

[23] M. Glick, F.K. Reinhart, G. Weimann and W. Schlapp, *"Quadratic electro-optic light modulation in a GaAs/GaAlAs multiquantum well heterostructure near the excitonic gap"*, Appl. Phys. Lett., vol. 48, p. 989 (1986).

[24] M. Glick, D. Pavuna and F.K. Reinhart, *"Electro-optic effects and electroabsorption in GaAs/GaAlAs multiquantum well heterostructures near the band gap"*, Electron. Lett., vol. 23, p. 1235 (1987).

[25] J.A. Jennings, *"Electro-optic effects in multiple quantum well GaAs/GaAlAs stripe waveguides"*, Ph.D. thesis, University of Glasgow (1990).

[26] J. Faist, F.K. Reinhart, D. Martin and E. Runcel, *"Orientation dependence of the phase modulation in a p-n junction GaAs/GaAlAs waveguide"*, Appl. Phys. Lett., vol. 50, p. 68 (1987).

[27] A. Yariv, *"Optical electronics"*, Holt Reinhart and Wilson, 3rd Ed. (1985).

[28] M. Glick and F.K. Reinhart, *"electro-optical light modulation in GaAs/GaAlAs multiquantum well heterostructures"*, Helvetica Physica Acta, vol. 58, p. 403 (1985).

[29] V. Mizrahi, K.W. DeLong, G.I. Stegeman, M.A. Saifi and M.J. Andrejco, *"Two-photon absorption as a limitation to all-optical switching"*, Opt. Lett., vol. 14, p. 1140 (1989).

[30] J.S. Aitchison, M.K. Oliver, E. Kapon, E. Colas and P.W.E. Smith, *"Role of two-photon absorption in ultrafast semiconductor optical switching devices"*, Appl. Phys. Lett., vol. 56, p. 1305 (1990).

[31] A. Villeneuve, M. Sundheimer, N. Finlayson, G.I. Stegeman, S. Morasca, C. Rigo, R. Calvani and C. DeBernardi, *"Two-photon absorption in $In_{1-x-y}Ga_xAl_yAs/InP$ waveguides at communications wavelengths"*, Appl. Phys. Lett., vol. 56, p. 1865 (1990).

[32] M.J. LaGasse, K.K. Anderson, H.A. Haug, J.G. Fujimoto, *"Femtosecond all-optical switching in AlGaAs waveguides using a time division interferometer"*, Appl. Phys. Lett., vol. 54, p. 2068 (1989).

[33] R. Jin, J.P. Sokoloff, P.A. Harten, C.L. Chuang, S.G. Lee, M. Warren, H.M. Gibbs, N. Peyghamberian, J.N. Polky and G.A. Pubanz, *"Ultrafast modulation with subpicosecond recovery time in a GaAs/GaAlAs nonlinear directional coupler"*, Appl. Phys. Lett., vol. 56, p. 993 (1990).

[34] M.J. LaGasse, K.K. Anderson, C.A. Wang, H.A. Haus and J.G. Fujimoto, *"Femtosecond measurements of the nonresonant nonlinear index in AlGaAs"*, Appl. Phys. Lett., vol. 56, p. 417 (1990).

[35] K.W. DeLong and G.I. Stegeman, *"Two-photone absorption as a limitation to all-optical waveguide switching in semiconductors"*, Appl. Phys. Lett., vol. 57, p. 2063 (1990).

[36] G.I. Stegeman and E.M. Wright, *"All-optical waveguide switching"*, J. Opt. Quantum Electron, vol. 22, p. 95 (1989).

[37] K.W. DeLong, K.B. Rochford and G.I. Stegeman, *"Effect of two-photon absorption on all-optical guided-wave devices"*, Appl. Phys. Lett., vol. 55, p. 1823 (1989).

[38] R.H. Stolen, C. Lin, *"Self phase modulation in silica fibres"*, Phys. Rev. A., vol. 17, p. 1448 (1978).

[39] P.N. Kean, *"Generation and nonlinear propagation of ultrashort near infrared laser pulses"*, Ph.D. thesis, University of St. Andrews (1989).

[40] S.T. Ho, C.E. Slusher, *"Large nonlinear phase shifts in low-loss GaAlAs waveguides near half-gap"*, Appl. Phys. Lett., vol. 59, p. 2558 (1991).

[41] J.S. Aitchison, A.H. Kean, C.N. Ironside, A. Villeneuve and G.I. Stegeman, *"Ultrafast all-optical switching in $Al_{0.18}Ga_{0.82}As$ directional coupler in 1.55 μm spectral region"*, Electronics Lett., vol. 27, p. 1709 (1991).

[42] F.R. Laughton, *"Nonresonant optical nonlinearities in GaAs/GaAlAs multiquantum well waveguides"*, Ph.D. thesis, University of Glasgow (1991).

[43] S. H. Park, J. F. Morhange, A. D. Jeffery, R. A. Morgan, A. Chavez-Pirson, H. M. Gibbs, S. W. Koch and N. Peyghambrian, M. Derstine, A. C. Gossard, J. H. English and W. Weigman. *"Measurements of room-temperature band-gap-resonant optical nonlinearities of GaAs/AlGaAs multiple quantum wells and bulk GaAs"* Appl. Phys. Lett 52 1201-1203 1988.

[44] W.L. Smith, *"CRC Handbook of Laser Science and Technology"*, M.J. Wever, Ed. (CRC press, Cleveland, Ohio, 1986), vol. 3, Pt 1.

Chapter 7

Nonlinear Integrated Asymmetric Mach-Zehnder Interferometer

7.1 Introduction:

One of our target devices for all-optical switching is the nonlinear integrated Asymmetric Mach-Zehnder Interferometer AM-ZI. The interferometer as originally proposed [1], modulates an optical beam with an applied voltage, and has been used extensively in electro-optic devices such as high-speed analog-digital converters [2] and modulators [3].

In this chapter, the operation mechanism and theoretical modelling of the single-mode, AM-ZI are described, using the local normal-mode description [4] and scattering matrix model [5,6], respectively. The linear characterisation of the AM-ZI is also investigated, this includes the propagation loss measurements of the Y-junction and bend waveguides. Finally, the switching action of the AM-ZI is examined using the electro-optic effects and intensity dependent refractive index change in GaAs/GaAlAs materials.

7.2 Operational Mechanism of the Nonlinear Integrated M-ZI Device:

Figure 7.1 shows a schematic diagram of a AM-ZI, it consists of a single-mode input and output asymmetric Y-junctions. The two Y-junctions are joined back-to-back to form the two arms 1 and 2 of the AM-ZI. An input optical signal will split between the two arms of the AM-ZI at the input Y-junction and recombine at the output Y-junction. The split ratio between the two arms depends on the Y-junction angle. The output response function of the AM-ZI depends on the relative phase and amplitude of the recombined fields at the output Y-junction.

To understand the operational mechanism of the integrated M-ZI as an all-optical switch device, it is vital to underline how the Y-junction acts as a power divider. The local normal-mode description [4] will be used to explain this operation. In the general case, a symmetric Y-junction is used. When the Y-junction operates as a power divider, the guided mode in the input section splits between the two arms of the Y-junction, as shown in Fig. 7.2. The split ratio depends on the Y-junction configuration [7,8]. In the case shown, it is a 3 dB divider.

191
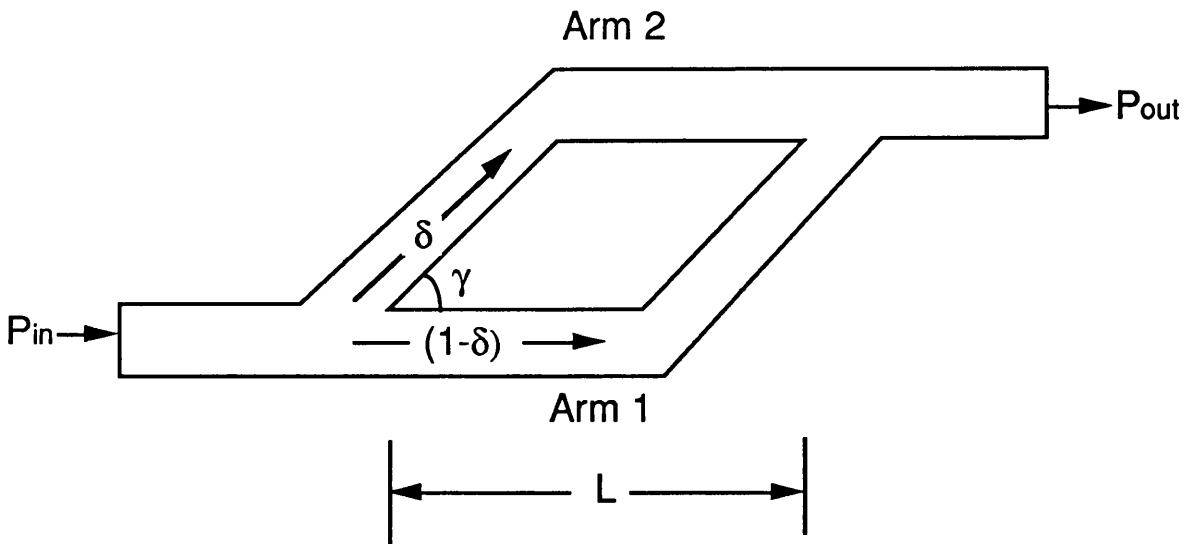
Fig. 7.1 *Schematic diagram of a single mode asymmetric Mach-Zehnder interferometer. The Y-junction full angle is γ and the power splitting in arm 1 and arm 2 are (1-δ) and δ respectively.*
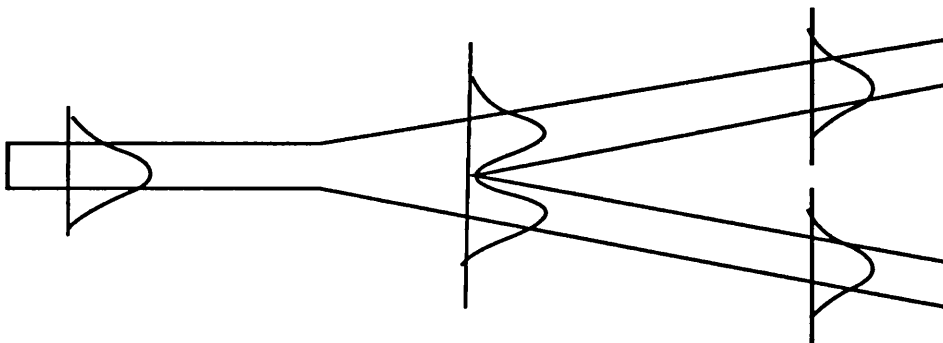
Fig. 7.2 *Schematic diagram of the basic operation of a single-mode symmetrical Y-junction as a power divider.*

When the Y-junction is used as a power combiner, the output of the Y-junction depends on the phase and amplitude of the guided modes in the two input arms. When they are in phase, the output power is the sum of the powers in the two input arms. As shown in Fig. 7.3a, the even mode is excited at the junction which will be transformed into the fundamental mode at the output waveguide. When the guided modes of the two input arms are out of phase, the odd mode is excited at the junction of the Y and because the output waveguide supports only the fundamental (even) mode, the odd mode will be coupled into the substrate as a radiation mode, as shown in Fig. 7.3b. When the input is only from one arm, the guided mode will excites the symmetric and anti-symmetric modes at the Y-

192

junction (due to the coupling between the two arms). Therefore, the output waveguide will support only the symmetric mode, as shown in Fig. 7.3c and the Y-junction insertion loss will be 3 dB.

(a)

(b)

(c)
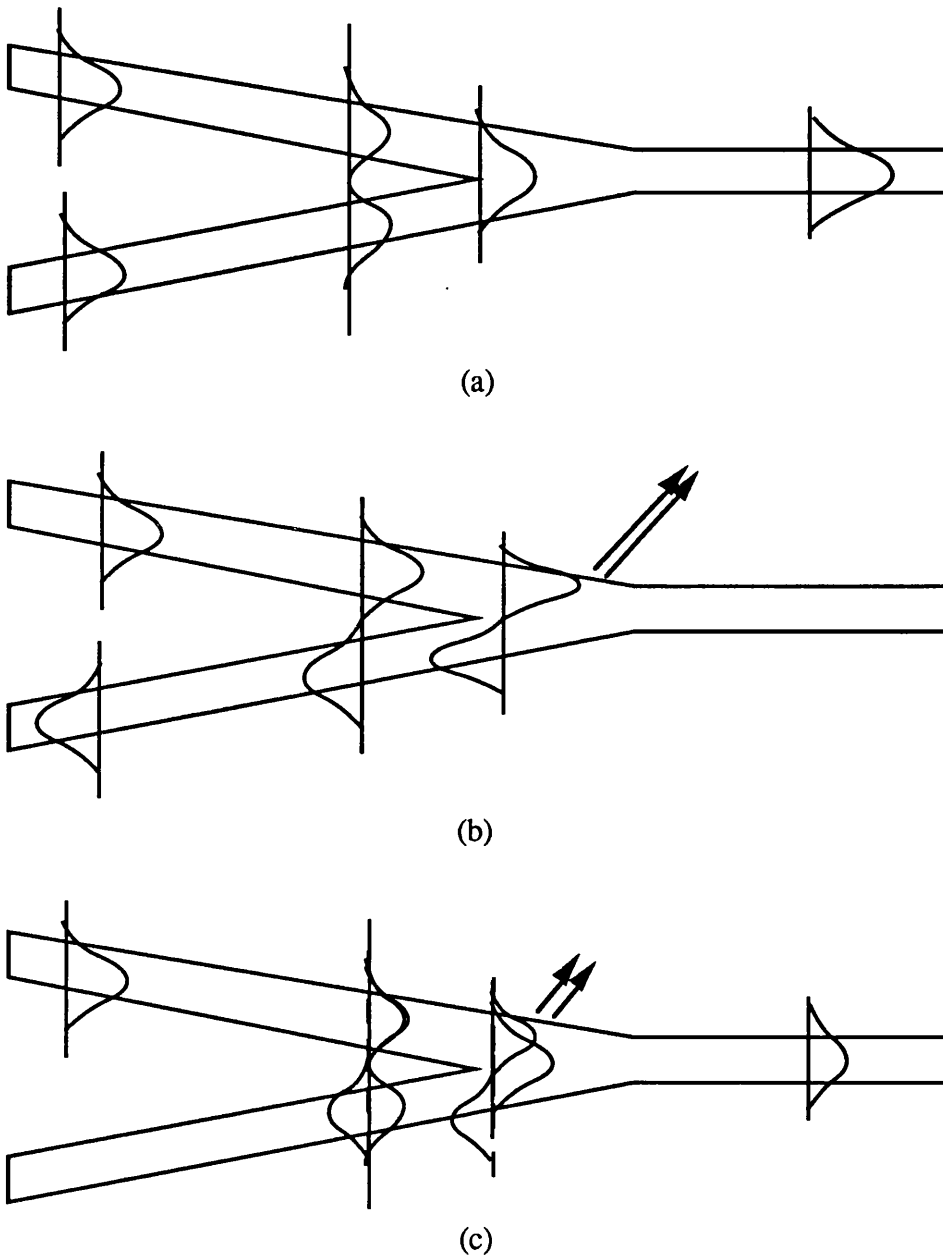
Fig. 7.3 *Schematic diagram of the basic operation of a single-mode symmetrical Y-junction as a power combiner. a) the two inputs are in phase, b) the two inputs are out of phase and c) the input is only into one arm.*

From the above description of the single mode Y-junction, the switching operation of the AM-ZI device can be achieved by introducing a relative phase difference of π between the

two arms of the single mode AM-ZI.

In the linear version of the device (e.g. electro-optic modulator), the π phase change is introduced by applying an electric field, across one arm of the Mach-Zehnder device. In the nonlinear version of the device (all-optical switch) the π phase difference between the guided modes of the two arms will be introduced by means of intensity dependent refractive index change, $n = n_0 + n_2 I$.

7.3 Theoretical Modelling of the Nonlinear Integrated AM-ZI Devices:

The scattering matrix model [5,6] has been used to model the single mode AM-ZI. This was achieved by modelling the single mode asymmetric Y-junction and using the scattering matrix model twice in the case of the AM-ZI.

Fig. 7.4 shows a schematic diagram of asymmetric Y-junction. It consists of three parts, straight, taper and branching sections. The Y-junction is taken to be a four port device which consists of a straight single-mode waveguide (port1), two single-mode branching waveguides (port2 and port3) and port4 for the modes radiated to the substrate at the taper. In this model, it is assumed that the angle is small enough to neglect the reflection loss in the Y-junction. The response of the Y-junction can be described in terms of a scattering matrix S as [5];

$$E_i = SE_i'$$ (7.1)

where

$$S = \begin{bmatrix} 0 & \sqrt{(1-\delta)} & \sqrt{\delta} & 0 \\ \sqrt{(1-\delta)} & 0 & 0 & -\sqrt{\delta} \\ \sqrt{\delta} & 0 & 0 & \sqrt{(1-\delta)} \\ 0 & -\sqrt{\delta} & \sqrt{(1-\delta)} & 0 \end{bmatrix}$$

where $\underline{E_i}$ is the input optical field in the ith port and $\underline{E_i}'$ is the output field from the ith port.

From the scattering matrix S, the following observations can be made. If a wave is propagating towards the Y-junction through either port2 or port3, then a fraction of the power will always be radiated into the substrate. In other words, if a beam light incident on port2, then only a fraction $(1-\delta)$ will leave port1. Similarly, when a light beam incident on

port3, then only a fraction of δ will leave port1.
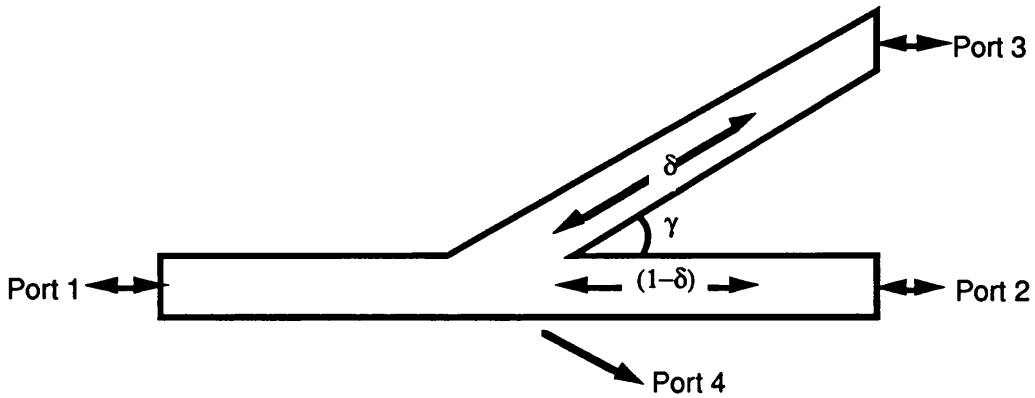
Fig. 7.4 *Schematic diagram of a single-mode asymmetric Y-junction, it is taken to be a four port device.*

The AM-ZI is considered as two Y-junctions placed back-to-back, as shown in Fig.7.5. Therefore, the response function of the AM-ZI can be obtained by applying the scattering matrix model twice [6]. Bearing in mind that a relative phase changes, ϕ_1 and ϕ_2, are introduced in arm1 and arm2, respectively. Also, the elements of the matrix for the second Y-junction are interchanged to maintain the correct definitions of the Y-junction ports shown in Fig.7.4.
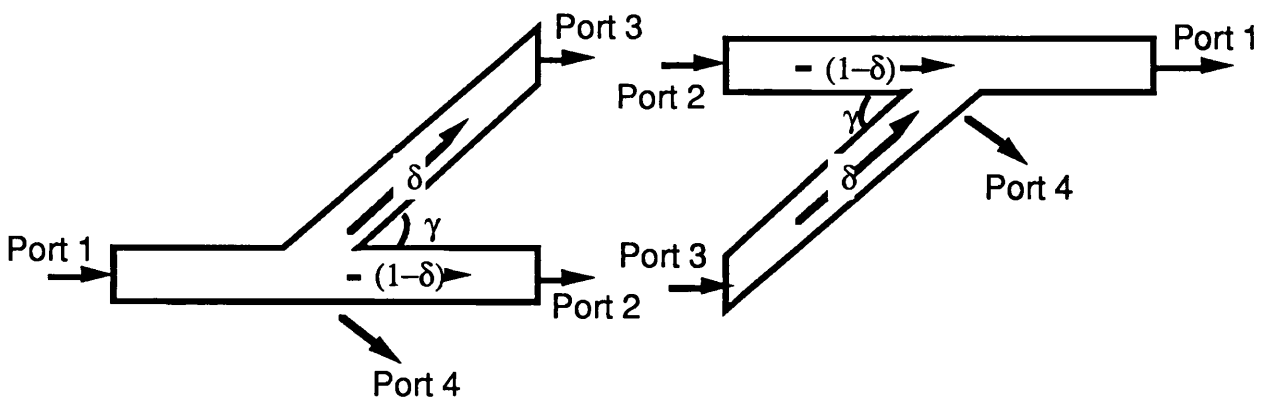
Fig. 7.5 *Schematic diagram of two single-mode asymmetric Y-junctions joint together, back-to-back, to form the asymmetric Mach-Zehnder interferometer.*

195

The output response function of the AM-ZI, as an all-optical switch, depends on the type of the nonlinearity employed to achieve the switching. In III-V semiconductor materials, the nonlinearity can be either nonresonant or resonant, depending on the operating wavelength. In the following sections each of these effects will be considered.

7.3.1 Nonresonant Nonlinear Integrated AM-ZI Device:

The intensity dependent refractive index change induced by using nonresonant nonlinearity is described in section 6.5. The operating photon energy (wavelength) is well below the semiconductor absorption edge, and it is very desirable to operate at photon energies below half the absorption edge of the semiconductor to avoid the two-photon absorption (TPA) effect which emerges at high optical intensities. In these spectral regions, the nonlinearity does not include absorption or refraction saturation effects and no photogenerated carriers are involved.

The output transmission, P_{out}, of the lossless AM-ZI is given by;

$$P_{out} = 4 P_{in} \delta (1 - \delta) \cos^2 (\Delta\varphi / 2 + \theta) \qquad (7.2)$$

θ takes account of any built-in phase difference in the device due to slightly different optical paths in the arms caused by fabrication inaccuracies. The differential phase change between the two arms ($\Delta\phi = \phi_1 - \phi_2$) due to the optical nonlinearity, is induced due to the difference in the split ratio of the input power in each arm. $\Delta\phi$ is expressed as;

$$\Delta\phi = \frac{2\pi}{\lambda_0} \Delta(nL)$$

where $\Delta(nL)$ is the differential change in the optical path length between the two arms.

$$\Delta(nL) = \frac{P_{in}}{A_{eff}} Ln_2 [(1 - \delta) - \delta]$$

$$\Delta\varphi = \frac{2\pi n_2 P_{in} L_{eff} (1 - 2\delta)}{\lambda_0 A_{eff}} \qquad (7.3)$$

where L_{eff} is the effective length of the interferometer arms ($L_{eff}=(1-\exp(-\alpha L))/\alpha$), α is the linear attenuation coefficient (scattering loss and free carriers absorption), L is the length of the arms, n_2 is the nonlinear coefficient, P_{in} is the input beam power, δ and $(1-\delta)$ are the

196

optical power split ratio between the two arms, λ_0 is the free space wavelength and A_{eff} is the waveguide effective cross sectional area. The output response of the AM-ZI from Eq. 7.2 is shown in Fig. 7.6 as a function of the input optical power.
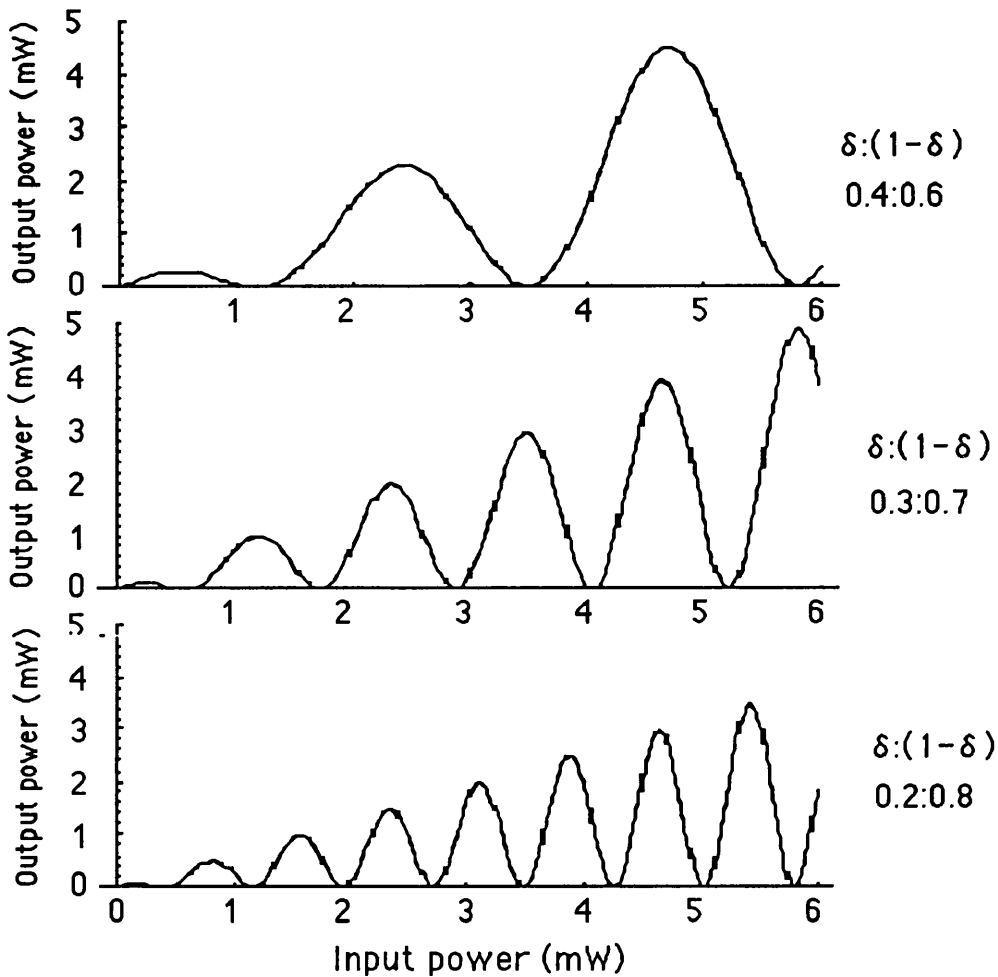
Fig. 7.6 *The output response of asymmetric Mach-Zehnder interferometer as a function of the input power, for different splitting power ratios.*

The output response of the AM-ZI is a $\cos^2$ function of the input beam power. The amplitude and oscillation strengths depend on the split ratio, δ:(1-δ), between the two arms of the Y-junction.

In our experiments, the AM-ZI was tested using the pump-probe technique, described in section 6.3.1.3. In this technique, the output transmission of the probe was monitored as a function of the pump beam intensity. Therefore, Eq. (7.2) can be written in a normalised form (P_{out}/P_{in}) as a function of the pump beam intensity, $I_{pump}=(P_{pump}/A_{eff})$;

197

$$T = 4\,\delta(1 - \delta)\cos^2(\Delta\varphi\,/\,2 + \theta) \tag{7.4}$$

and

$$\Delta\varphi = \frac{2\pi n_2 I_{pump} L_{eff}(1 - 2\delta)}{\lambda_0} \tag{7.5}$$

The response function of the AM-ZI, Eq. (7.4), is plotted in Fig.7.7 as a function of the input pump intensity for different power split ratios δ:(1-δ). The values of $n_2 = 1 \times 10^{-11}$ cm^2/W, $L_{eff} = 0.4$ cm and $\lambda = 1.55$ μm. It can be seen that for small split ratio, the modulation depth is large but the input power required to achieve switching is increased. Therefore, in the design of AM-ZI, there is a compromise between low switching power and reduction in the switching fraction.
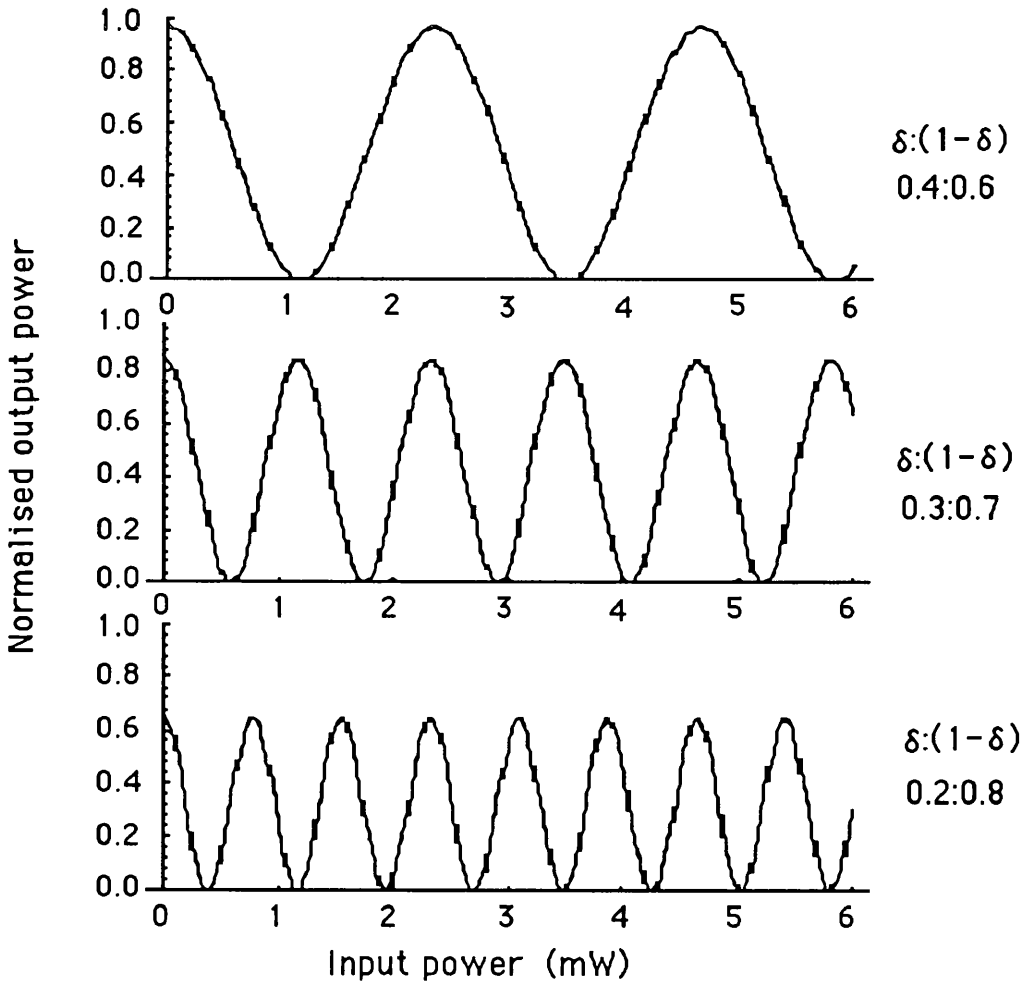
Fig. 7.7 *The normalised output response of asymmetric Mach-Zehnder interferometer as a function of the input power, for different splitting power ratios.*

7.3.2 Resonant Nonlinear Integrated AM-ZI Device:

When the AM-ZI device is operating at photon energies close to or above the semiconductor band gap, then the all-optical switching is achieved by mean of resonant nonlinear effects. Therefore, the photo-absorption and -refraction effects in the semiconductor have to be included in the device modelling.

The intensity dependent absorption and refraction saturations are considered, using a two level saturation law [9]. Therefore the intensity dependent absorption and refraction can be expressed in arm1 and arm2 as;

$$\alpha_1 = \frac{\alpha_0}{1 + \frac{(1-\delta)I_{pump}}{I_{\alpha sat}}} \qquad\qquad \alpha_2 = \frac{\alpha_0}{1 + \frac{\delta I_{pump}}{I_{\alpha sat}}} \qquad (7.6)$$

$$\varphi_1 = \frac{2\pi n_2 (1-\delta)I_{pump} L_{eff}}{\lambda_0 \left(1 + \frac{(1-\delta)I_{pump}}{I_{nsat}}\right)} \qquad \varphi_2 = \frac{2\pi n_2 \delta I_{pump} L_{eff}}{\lambda_0 \left(1 + \frac{\delta I_{pump}}{I_{nsat}}\right)} \qquad (7.7)$$

α_0 is the linear absorption coefficient and I_{pump} is the input pump light intensity, $I_{\alpha sat}$ is the absorption saturation intensity and I_{nsat} is the refractive index saturation intensity. Two different saturation intensities for the absorption and refraction are used, due to different mechanisms involved in the photo-absorption and -refraction nonlinear effects. This is confirmed by the experimental results presented later in this chapter.

The normalised output response of the resonant AM-ZI becomes;

$$T = \delta(1-\delta)\left[\exp(-\alpha_1 L) + \exp(-\alpha_2 L) \right.$$
$$\left. + 2\exp\left(-\frac{(\alpha_1+\alpha_2)}{2}L\right)\cos(\varphi_1 - \varphi_2 + \theta)\right] \qquad (7.8)$$

where α_1 and α_2 are the absorption coefficients in arm1 and arm2 respectively, and ϕ_1 and ϕ_2 are the phase changes of the guided modes in arm1 and arm2 respectively.

The absorption saturation intensity $I_{\alpha sat}$ can be estimated from the experimental results of the absorption saturation in the straight waveguide. The response function, Eq. 7.8, is used later in this chapter to model the resonant nonlinear AM-ZI.

Some of the remarks need to be made about the scattering matrix model. Because of the idealisations made about the Y-junction in the AM-ZI, the model does not give sufficiently good representation of a realistic device, but it gives a qualitative indication of the operation principles of the AM-ZI device. In the scattering matrix model, the coupling between the guided modes in each arm of the Y-junction, close to the junction of the Y, is not included, this coupling has to be included for a realistic model. Furthermore, the response function of the AM-ZI is derived from a CW theory for the operation of the device, while the experimental results were taken with a pulsed laser and there could be several effects associated with averaging over the pulse duration which may alter the operating characteristics of the device.

7.4 Design Considerations of the AM-ZI Devices:

From the theoretical modelling of the integrated AM-ZI devices, switching can be achieved when a relative phase change is introduced between the two arms of the device. This relative phase change depends on the intensity of the input light. Therefore, it is important to reduce the intensity attenuation in the device elements, e.g. Y-junction and bend waveguides. Propagation losses in the AM-ZI arise from scattering loss in the Y-junction and bend waveguides and from free carrier absorption. These losses can be reduced by optimising the design structure of the Y-junction and bend waveguides as well as the semiconductor layers structure. These loss mechanisms are investigated in section 7.6.

In the resonant AM-ZI, the photon energy is close to the semiconductor absorption edge and the losses are dominated by band-edge absorption, the required switching power is high. It is possible to reduce the switching power by designing a linear AM-ZI with a nonlinear section, of length L, in arm 1. This can be obtained by fabricating a AM-ZI with an energy band E_{g1} in arm 1 and the rest of the device with energy band E_{g2}, such that $E_{g2}>E_{g1}$. Two techniques can be used to achieve this, either by a) using the QCSE or b) selective disordering of GaAs/GaAlAs QW materials. These two techniques are out lined in the following sections.

7.4.1 Electric Field Induced Effects Technique:

Fig. 7.8 shows a schematic diagram of a resonant AM-ZI with a nonlinear section in arm 1, achieved by employing the QCSE in GaAs/GaAlAs QWs [10]. By selectively applying an electric field perpendicular to the plane of the epitaxial layers, the QW absorption edge will be shifted to lower energy, E_{g1}, (red shift). The rest of the device will have an energy band

of the as grown material E_{g2}.
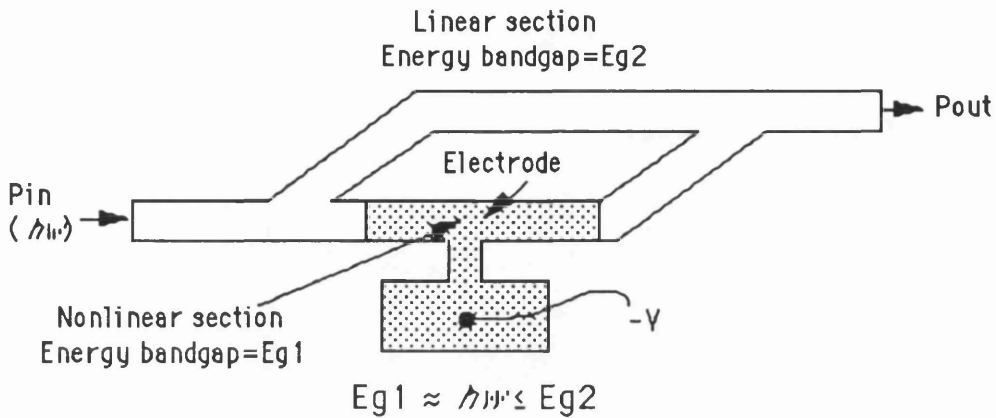
Fig. 7.8 *Schematic diagram of an active asymmetric Mach-Zehnder interferometer. The electrode (shaded area) forms the nonlinear section of the all-optical switch when a reverse bias is applied across the device.*

7.4.2 Vacancies Induced Disordering Technique:

The selective vacancy induced disordering technique, described in section 4.6.7, can be used to form a resonant AM-ZI with a nonlinear section in arm1. This is shown in Fig. 7.9, the disordered area of the device will be shifted to a higher energy E_{g2} compared to the as grown material (in the nonlinear section) E_{g1}.
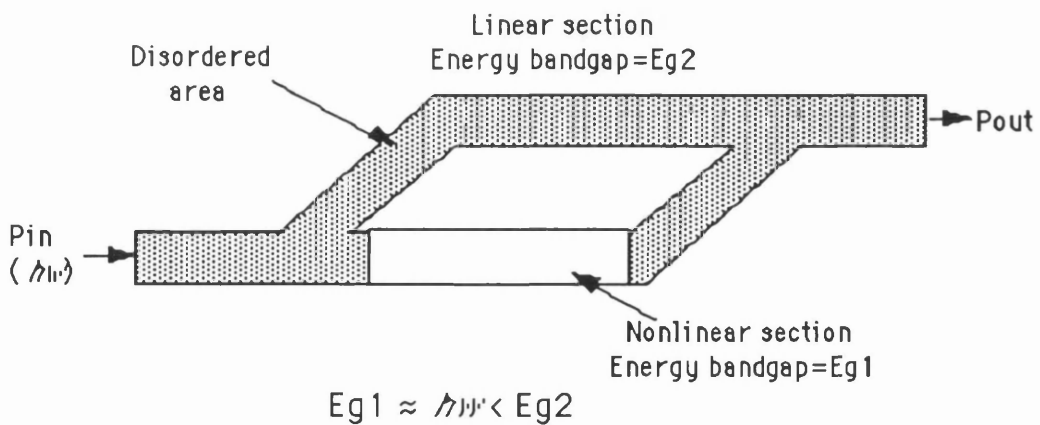
Fig. 7.9 *Schematic diagram of an asymmetric Mach-Zehnder interferometer, the shaded area is disordered by using either IID or vacancies indiffusion technique. The clear area with energy band E_{g1} play as a nonlinear section in the all-optical switch when the device operates at photon energy such that $E_{g1} \approx h\omega < E_{g2}$.*

In both versions of the resonant AM-ZI device, the energy band of the nonlinear section, E_{g1}, is smaller than the energy band of the rest of the device, E_{g2}. Therefore, by tuning the photon energy of the input light close, or equal, to E_{g1}, it is possible to enhance the nonlinear effect in the nonlinear section as well as reduce the unnecessary absorption loss in the rest of the device.

In spite of the technical difficulties in fabricating either of these devices, the two techniques have some advantages and disadvantages. The electric field induces a larger red shift in the QW absorption edge (QCSE) compared to the vaccancy disordering technique. Also the presence of the electric field across the QW reduces the relaxation time of the resonant nonlinearity [11], by sweeping the photo-generated carriers out of the waveguide. The drawback of applying electric field, is that it may broaden and weaken the QW exciton resonant peaks [10].

7.5 Theoretical Modelling of AM-ZI with Applied Electric Field:

The guided-wave intensity modulation in electro-optic devices can be obtained with either the Pockels effect or the Franz-Keldysh effect. The Pockels effect is usually obtained at an optical wavelength λ far from the fundamental absorption edge of the material. Therefore, the phase effect is strong and the associated loss is negligible. In Franz-Keldysh devices, the operating optical wavelength λ is quite close to the material absorption edge. For these modulators, the loss component is strong compared to the weak phase retardation. In quantum well material, the effect of applying an electric field across the quantum wells is known as a D.C. quantum confinement Stark effect QCSE, as described in section 2.4. In our integrated AM-ZI, shown in Fig. 7.8, the two effects are taken into account.

In the analysis of such a device, the applied electric field across the length L produces a uniform perturbation to the mode of the waveguide over that length. This perturbation produces a phase retardation and amplitude change $\Delta\beta+i\Delta\alpha/2$. The propagation coefficient ($\beta = 2\pi n_{eff}/\lambda$) and the optical power absorption coefficient ($\alpha = 4\pi k/\lambda$) are per unit length. Following the scattering matrix model and assuming that the two arms of the interferometer are phase matched in the zero field case, the throughput of the integrated interferometer is given by [12];

$$P_{out} / P_{in} = \delta(1 - \delta) \left[1 + e^{-\Delta\alpha L} + 2e^{-\Delta\alpha L / 2} \cos \Delta\beta L\right] \qquad (7.9)$$

At a given drive voltage, the relative strength of the phase versus amplitude modulation can be expressed using a parameter ρ ($\rho=2\Delta\beta/\Delta\alpha$). This parameter provides a measure of the

202

relative strength of the phase and amplitude modulation. Inserting the ρ parameter into Eq. (7.9) gives;

$$P_{out} / P_{in} = \delta(1-\delta) \left[1 + e^{-2\Delta\beta L / \rho} + 2e^{-\Delta\beta L / \rho} \cos(\Delta\beta L)\right] \qquad (7.10)$$

Assuming that ρ is constant, Fig. 7.10 shows a plot of the output transmission of the M-Z as a function of ΔβL for ρ = 3, 10 and 500. The split ratio between the two arms of M-Z δ:(1-δ) is 0.5:0.5. Fig. 7.11 shows a plot of the output transmission of a AM-ZI for ρ =10, and different split ratios δ=0.5, 0.3 and 0.2.
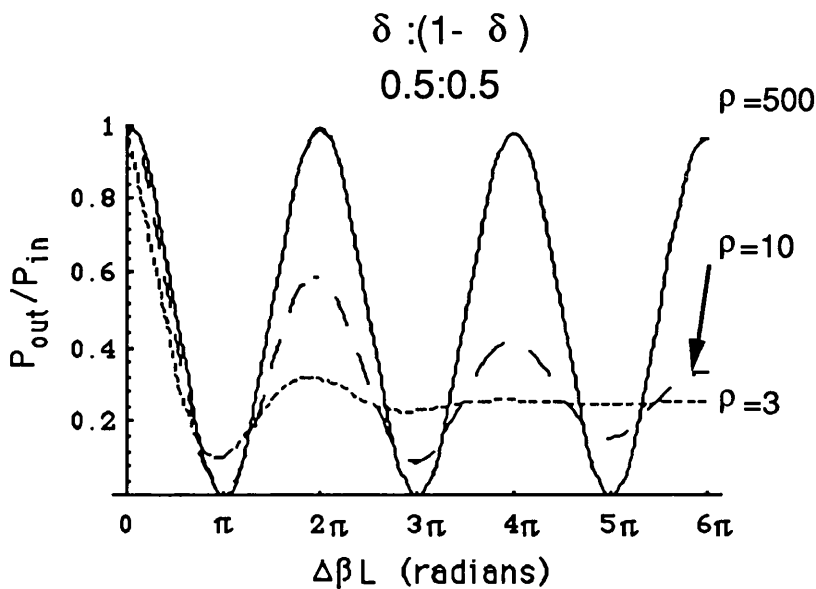
Fig. 7.10 *The output response of an electro-optic symmetrical Mach-Zehnder switch (δ=0.5) as a function of the phase change ΔβL, at different values of ρ=2Δβ/Δα.*

This analysis gives a qualitative indication of the operation principles of the device. As ρ increases, the mixed modulator (phase and amplitude changes) blend continuously into a phase modulator. The familiar raised cosine result at ρ → ∞ with perfect nulls at odd multiples of π. As the absorption coefficient α increases, i.e. ρ decreases, the modulator has non zero minima and nonunity maxima this is due to the amplitude imbalance between the two arms which washes out the peaks and valleys of the interference. As ΔβL increases, the throughput of the modulator approaches the value δ(1-δ), as it is shown in Fig. 7.11. The size of the electro-refractive and -absorptive effects depends on the wavelength. Therefore by tuning the operation wavelength, it is possible to change the

value of the ρ parameter.
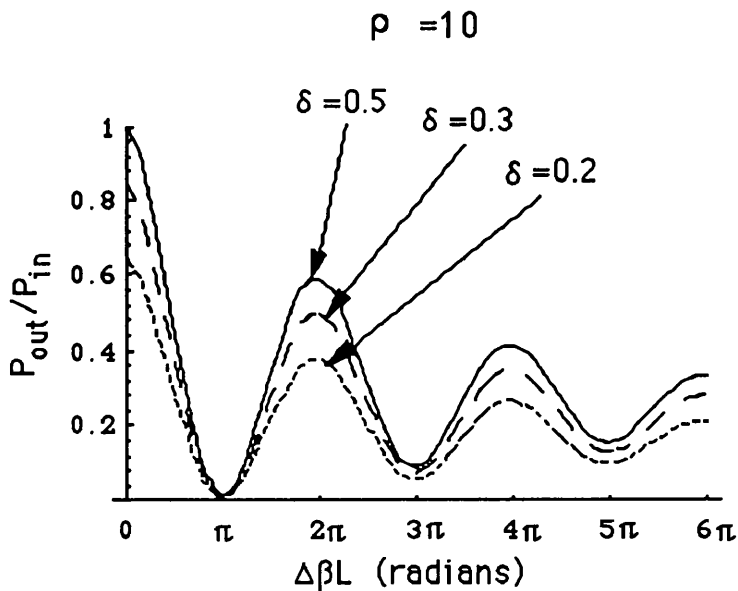
Fig. 7.11 *The output response of an electro-optic asymmetrical Mach-Zehnder switch, with ρ=10, as a function of the phase change ΔβL, at different values of power splitting ratios δ:(1-δ).*

7.6   Linear characterisation of the Integrated Mach-Zehnder Interferometer:

The linear characterisation of the single mode AM-ZI involves the investigation of the device insertion losses. This is an important parameter as far as the device performance concerned, specially when the switching operation is an input light intensity dependent.

The integrated AM-ZI device consists of a straight waveguide, input and output Y-junctions and bending corners in each arm. Therefore, it is vital, in studying the device insertion losses, to measure the losses in the straight waveguide, the Y-junction and the bend waveguides. The linear propagation losses of the straight waveguide are studied in chapter 5. Therefore, in this chapter only the Y-junction and bend waveguides propagation losses are discussed.

204

7.6.1 Bend Waveguides :

In integrated optical circuits, bending waveguides play an important role in connecting different components within one chip. The directional change in these waveguides causes some of the power propagated in the guided modes to be transferred into a radiated modes at the bends.

Fig. 7.12 shows two types of bend waveguides. In the first type, the two parallel, noncolinear single-mode waveguides are joined by a straight section which forms sharp corners at each end. In the second type, the two waveguides are joined by two smooth curved waveguides. The smooth curves are portions of a circle with same radius of curvature R. They both have equal but opposite curvature.

(a)

(b)
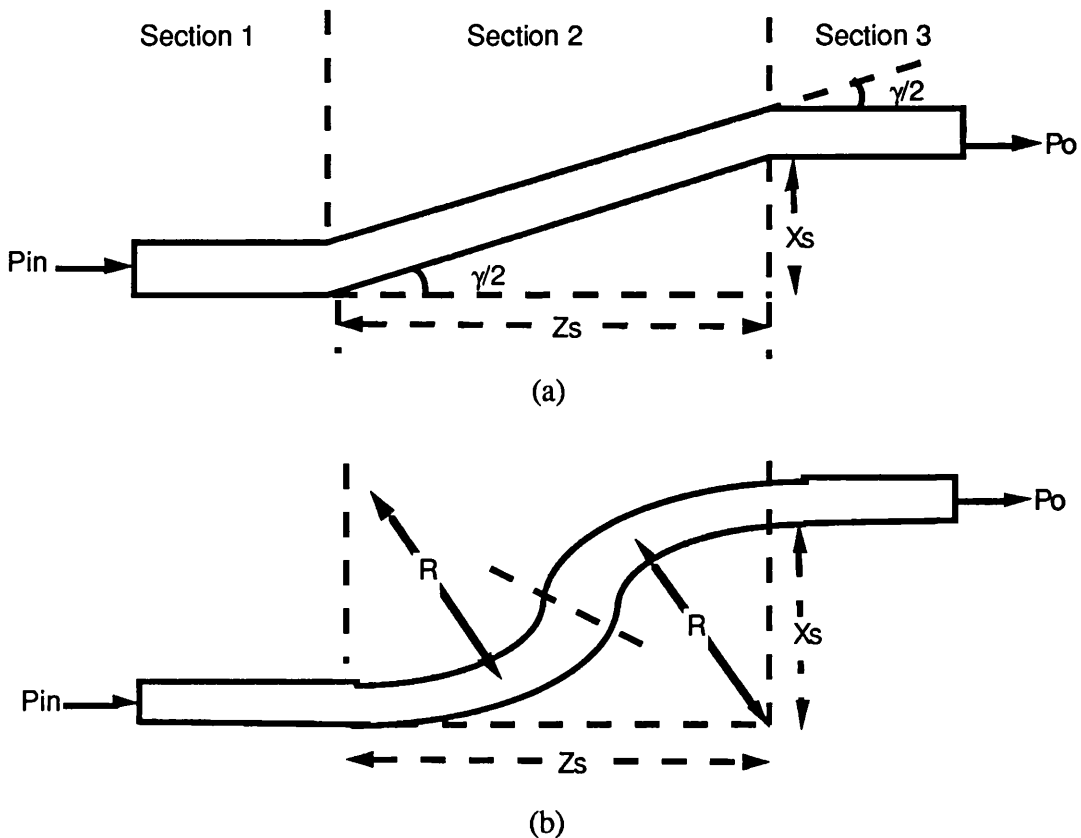
Fig. 7.12 *Schematic diagram of two types of bent waveguides,* a) *with sharp corners and* b) *with smooth corners.*

Curved waveguides have been analysed by several authors using different techniques [13,14]. In most cases, it was assumed that the refractive index difference between the

205

guiding region and the surrounding media was small. In general, the attenuation coefficient of the curved slab guide was found to be of the form [15,16]

$$Q = C_1 e^{-C_2 R}$$

(7.11)

where

$$C_2 \approx \beta \left(\frac{2 \Delta n_{eff}}{n_{eff}} \right)^{3/2}$$

(7.12)

where C_1 is a constant depending on the guide thickness and indices, Δn_{eff} is the difference between the model effective index and the cladding index. Eq. 7.11 assumes $\Delta n_{eff}/n_{eff}$ is small. The exponential behaviour means that the bending loss increases abruptly for radii below some critical value.

In a bent waveguide with two corners, the power coupled out of the second corner is given by [17];

$$P_{out} = P_{in} |a_{12}|^2 \cdot |a_{23}|^2 \cdot e^{-\gamma_0 L_0}$$

(7.13)

where P_{in} is the power incident upon the first bend, γ_0 is the attenuation coefficient that is due to absorption and scattering, L_0 is the length of the joined segment and $|a_{ij}|^2$ is the relative power-coupling coefficient for the fundamental mode between the two waveguide sections i and j. The power-coupling coefficient is given by [17];

$$|a_{12}|^2 = |a_{23}|^2 = \exp\left[-\beta^2 x_0^2 \sin(\gamma/2)/4 \right]$$

(7.14)

$\gamma/2$ is the angle of each bend, β is the propagation constant of the lowest-order fundamental mode of the waveguide and X_0 is the half-width of the mode in the plane of the bend.

Hutcheson et al [17] investigated the bending loss in the two types of bent waveguides. A great difference in the propagation loss of the two types of bent waveguides was found, for the same offset connection. In general, the corner-bend approach was better for a very small transverse separation. As the transverse separation increases, the S-bend yields the lowest loss.

In the early stage of this project, it was not possible to make a mask with smooth S-bends. Therefore, only the bends with sharp corners were investigated. The mask was designed not only to measure the bending loss but also the loss in the Y-junctions and straight waveguides. It consisted of two sets of lines with linewidths 2 μm and 3 μm. As shown in Fig. 7.13, each set had straight waveguides, sharp angled bends and sharp angled symmetrical Y-junctions. The closest distance between these optical elements was 50 μm , this was to prevent any coupling between adjacent waveguides due to the evanescent field of the guided modes. There were six Y-junctions in each set with various splitting angles. The Y-junction full angles γ were 1°, 1.5°, 2°, 3°, 4° and 6°. Adjacent to the side of each Y-junction there were two bend waveguides with bending angles half that of the neighbouring Y-junction full angle γ. Each bend waveguide had two bends so that both ends of the waveguide meet the cleaved edge of the sample at a normal angle. Six straight waveguides were distributed between the Y-junctions.
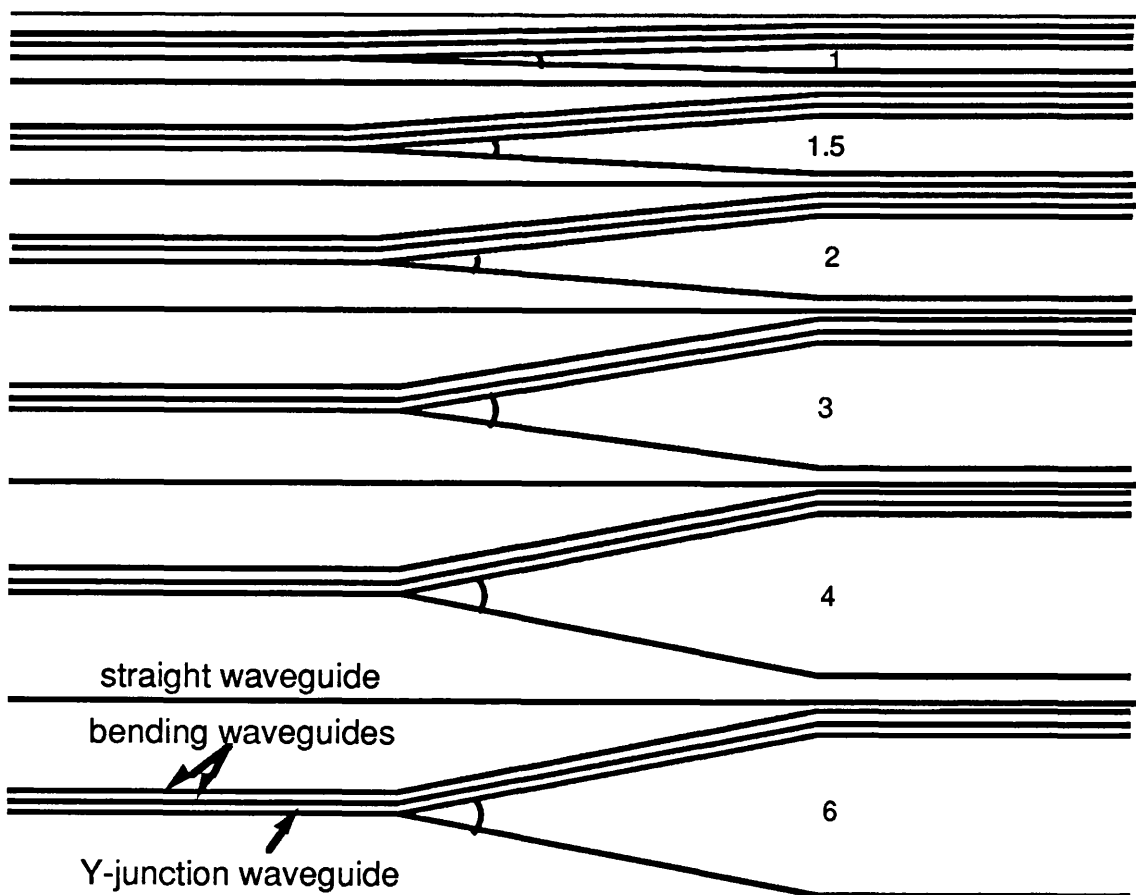
Fig. 7.13 *Schematic diagram of a chrome mask with six symmetric Y-junctions, twelve bent waveguides and six straight waveguides. The Y-junctions full angle is γ 1°, 1.5°, 2°, 3°, 4° and 6°. The mask is a dark-field.*

207

The straight waveguides were used to measure the end facets reflectivity r and r', using the technique described in section 5.7, as well as the attenuation in the straight sections. The propagation loss of bent waveguides was measured as a function of bending angle $\gamma/2$, from the combination of the losses measured in the straight and bent waveguides.

7.6.1.2 Material Description:

A GaAs/GaAlAs double heterostructure wafer was designed and grown by MBE. Fig. 7.14 shows a schematic diagram of the layers structure, it consisted of a 1.2 μm thick GaAs $(n \approx 4.5 \times 10^{14}$ cm$^{-3})$ guiding region, a 4 μm thick lower cladding layer of $Ga_{0.9}Al_{0.1}As$ $(n \approx 1.5 \times 10^{16}$ cm$^{-3})$ and a 1.5 μm thick upper cladding layer of $Ga_{0.75}Al_{0.25}As$ $(n \approx 1.5 \times 10^{16}$ cm$^{-3})$. The epitaxial layers were grown on n^+-GaAs substrate. The relatively thick lower cladding layer was to isolate the evanescent field of the guided mode from the high refractive index GaAs substrate. The reason for using a three layers structure and not a multiple quantum well, is the simplicity of growing such material with a minimum number of overgrowth defects and eliminate the possibility of increasing the optical propagation loss due to the interface roughness between the wells and barriers in MQW materials.
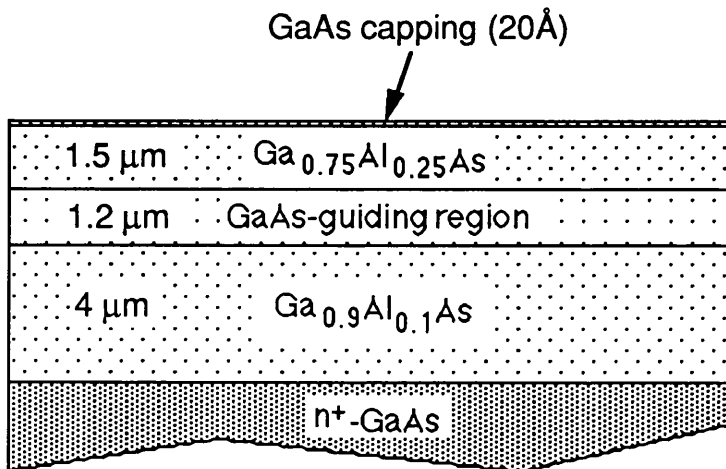
Fig. 7.14 *Schematic diagram of* GaAs/GaAlAs *double-heterostructure material, the epitaxial layers are n-doped and grown on* n^+-GaAs *substrate by MBE.*

7.6.1.3 Fabrication Details:

As we will see in the experimental measurements, strong lateral optical confinement was required to reduce the propagation loss in bent and Y-junction waveguides, this was

208

achieved by deep etch of the samples. The limited etching selectivity between the photo-resist mask and GaAs/GaAlAs substrate (during the RIE with SiCl₄ gas) may reduce the effective width of the rib waveguide, due to the deterioration of the mask edges. Therefore, a metal mask was used, which require a dark-field mask when a positive photo-resist was used.

The straight, bent and Y-junction patterns were transferred to the GaAs/GaAlAs double heterostructure material using the standard optical lithography and lift-off processes to produce 2 μm and 3 μm linewidth stripes of a 500 Å thick NiCr layer on top of the samples. A mask aligner was used to align the pattern with respect to the cleaved edge of the sample. The NiCr etching mask was subsequently removed using a wet etch of 1:1 HCl:H₂O for 45 seconds. Finally the etched samples were cleaved to produce mirror finish facets.

7.6.1.4 Experimental Results:

The experimental set-up described in section 5.7.2, was used to measure the linear propagation losses in the straight and bent waveguides. The linear propagation losses were measured, using the Fabry-Perot technique, described in section 5.7.1, at a wavelength λ=1.153 μm. Many samples were fabricated, with different etching depths. In samples with a shallow etching depth ≈1.3 μm, the bending loss at the corners of the waveguide bends was very high. The Fabry-Perot cavity resonant cycles were suppressed completely for corners with bending angle γ/2 equal to or greater than 2°. This was due to weak lateral optical confinement in these stripe loaded waveguides, where the waveguide adjacent slabs were not cut-off and a significant amount of the guided mode was penetrating in to these adjacent regions. The bending loss in these structures was reduced significantly by increasing the etching depth to ≈2.2 μm, i.e. increasing the lateral optical confinement. By increasing the etching depth, the scattering loss from the sidewalls roughness increases, due to the large overlap integral between the confined optical field and the sidewalls roughness. In spite of the increase in the scattering loss, the overall insertion losses in the bent waveguides was significantly reduced. After examining the deeply etched samples, ≈2.2 μm, the 3 μm rib width waveguides were found to be multimoded. Therefore only the 2 μm rib width waveguides were considered.

The end facet reflectivity and propagation loss of the straight rib waveguides were measured using the combination of Fabry-Perot and sequential cleaving techniques. The propagation loss of the 2 μm rib waveguides with an etching depth 2.2 μm was 2.7 dB/cm with a standard deviation of 0.5 dB/cm. The power reflection coefficient was R=27% with

standard deviation of 1.5%.

The bending loss in the 2 μm rib width single mode bend waveguides was measured as a function of the bending angle γ/2. Fig. 7.15 shows the raw data for the propagation loss as a function of the angle γ/2. The length of the sample was 7 mm. The 0° bending angle data represents straight waveguides. Some of these waveguides showed a high propagation loss, points shown as open squares. The straight and bend waveguides with high propagation loss were examined, using the scanning electron microscope. It was found that these waveguides pass through defects, as shown in Fig. 5.18. These defects are grown during the material growth process in the MBE system.
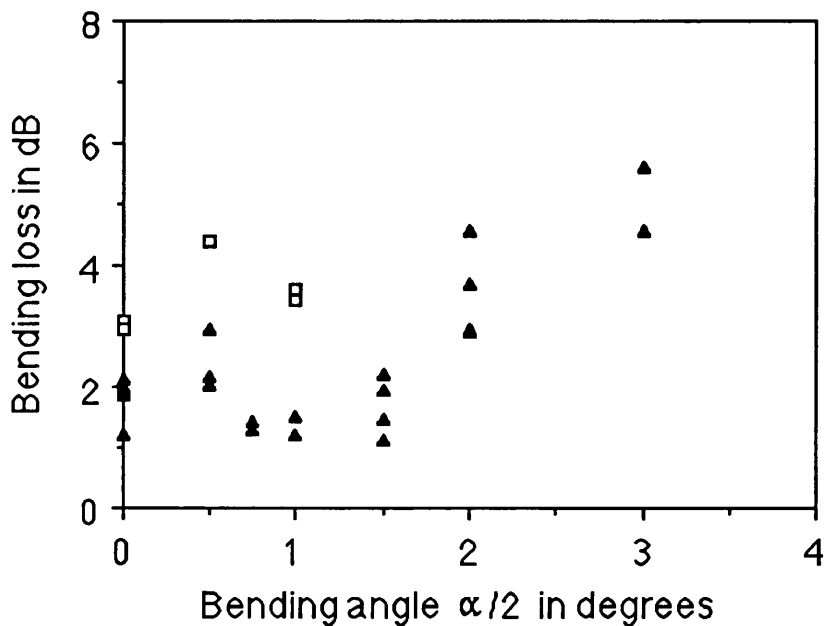
Fig. 7.15 *Bending losses in the* 2 μm *rib width bent waveguides as a function of bending angle* γ/2. *Each waveguide had two bends, in which the two ends of the waveguide met the cleaved edge at a normal angle. The* 0° *"bending" data represent straight waveguides.*

Fig. 7.16 shows the average bending loss for the 2 μm rib width bend waveguides as a function of the bending angle, derived by subtracting the average propagation loss of the straight waveguide, but ignoring points shown as open squares. The increase in the bending loss as a function of the angle γ/2 is caused by the increase in the conversion of the guided mode to a radiated mode, due to the change in the propagation direction, at the corner of the waveguide bends.
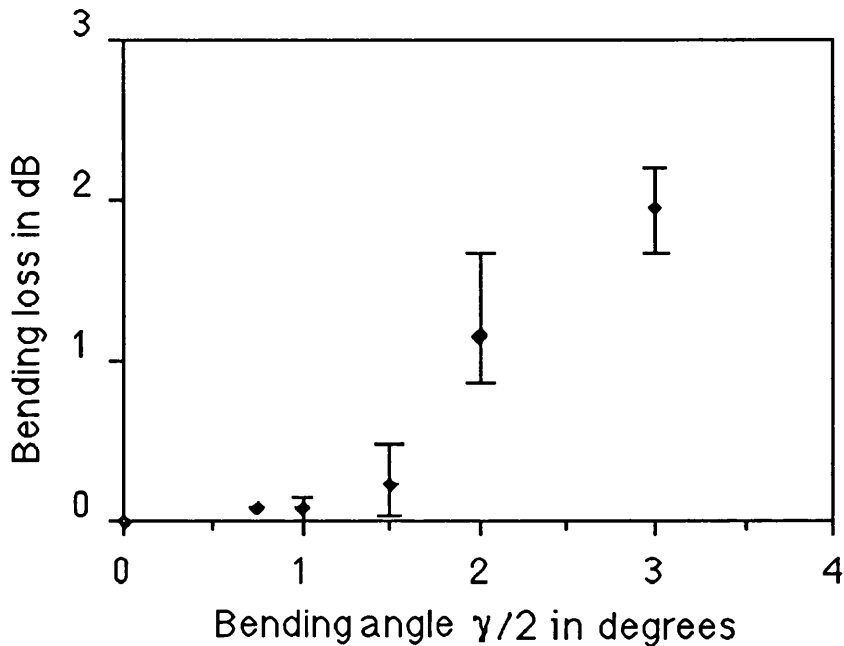
Fig. 7.16 *The average bending loss as a function of bending angle γ/2 (derived by subtracting the average of the straight guide loss, ignoring points shown as open squares in Fig. 7.15).*

7.6.2 Y-Junction Waveguides

The symmetric and asymmetric Y-junction have both been theoretically modelled [18-20] and experimentally investigated [21,22]. For purposes of design it is desirable to express the propagation characteristics of the Y-junction in term of the physical properties of the junction. In this section, the single mode symmetrical Y-junction transmission coefficient of the fundamental TE-mode is described using the theoretical model developed by Anderson [23]. The same theory was modified by Dr. J. Isaac [24] to model the TM_0 mode. The analysis is designed for a two-dimensional single-mode Y-junction formed from three identical planar waveguides, as shown in Fig. 7.17. When the lowest order TE mode incident upon the junction from z<-L, it is required to find the power transmitted to the output waveguides, the power reflected back in the input waveguide and the power radiated from the junction to the surrounding medium. In this theory, the coupling between the two output waveguides close to the junction is neglected. Also from a study carried out by Marcuse [25], the transmission coefficient for long tapers (L>>W) is close to unity, i.e. the reflection back of the propagating light along the taper is neglected.
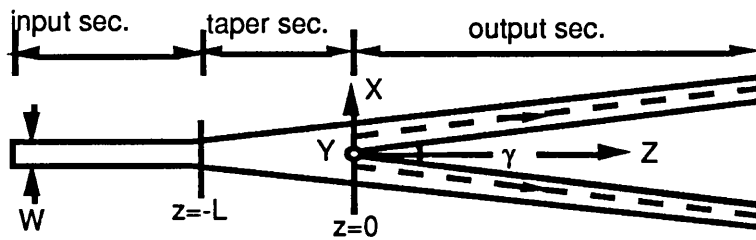
Fig. 7.17 *Schematic diagram of a single-mode symmetrical Y-junction. It consists of three parts, the input, taper and the output sections, the length of the taper is* L.

With reference to Fig. 7.17, an incident mode E_y^i on the junction at z=0 excites transmitted and radiated modes τE_y^t and E_y^+, respectively, in z>0. Due to the discontinuity presented to the incident mode at z=0, there are reflected and radiated modes rE_y^i and E_y^-, respectively, in z<0. By matching the tangential electric and magnetic field components on the plane z=0 and integrating the two equations over the z=0 plane (with respect to x) and isolating τ and r to give [23]:

$$\tau = \frac{\beta_a \beta_b}{\beta_a + \beta_b} \cdot \frac{1}{\omega\mu} \int_{-\infty}^{\infty} E_y^i (x, 0) E_y^{t^*} (x, 0) dx \qquad (7.15)$$

$$r = \frac{\beta_a - \beta_b}{\beta_a + \beta_b} \qquad (7.16)$$

where β_a and β_b are the propagation constants just before and after z=0 respectively. In other word, the propagation constants for waveguides with thickness 2W and W respectively. ω and μ are the angular frequency and permeability respectively. The integral part in Eq. (7.15) is determined in reference [23].

The fraction of the incident power transmitted, reflected and scattered are related by;

$$T = |\tau|^2 \qquad\qquad R = |r|^2 \qquad\qquad T + R + S = 1$$

To be able to apply Anderson model to a Y-junction with rib waveguide, the effective index method EIM is applied to convert the three dimensional structure to two dimensional structure. A computer program was written by Dr. J. Isaac [24] to calculate the transmission T as a function of the junction half-angle $\gamma/2$. Fig. 7.18 shows an example of two Y-junctions with their rib waveguide cross sections. The rib width was 2 μm with two different etching depths 0.5 μm and 1.2 μm. With reference to Fig. 7.18, to improve the

212

transmission of the Y-junction with relatively large angle γ/2, an increase in the optical confinement is required.
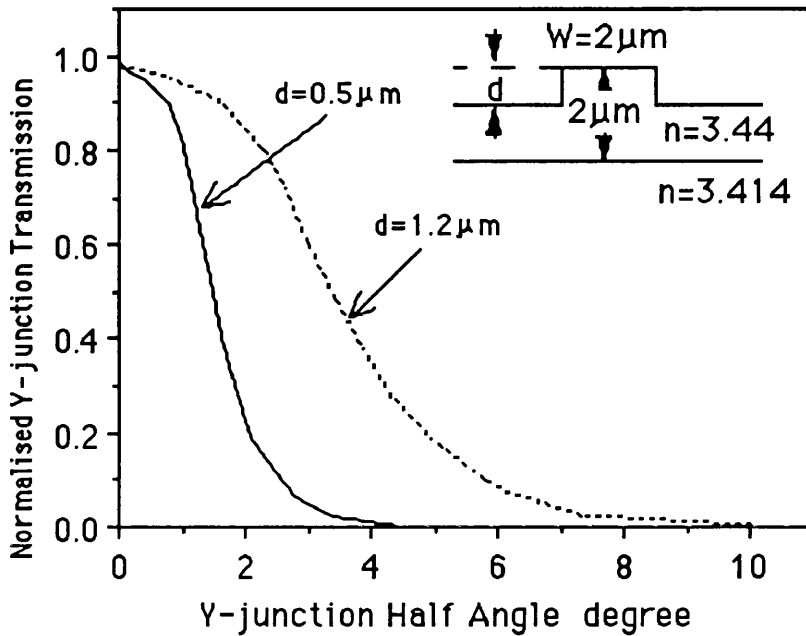
Fig. 7.18 *Normalised output transmission of a single-mode symmetrical Y-junction as a function of the Y-junction half angle, for two Y-junctions with different lateral optical confinements (i.e. different etching depths d as shown in the inset diagram).*

7.6.2.1   Theory of the Fabry-Perot Resonator with a Y-Junction Configuration:

Figure 7.19 shows a schematic diagrams of the two types of single-mode symmetrical Y-junctions investigated in this work. In each case, the Y-junction is divided into three sections. The input section is joined to the two branches in the output section through a tapered section. In Fig. 7.19a the Y-junction output branches meet the cleaved edge at an angle equal to half-angle of the Y-junction γ, while in the device shown in Fig. 7.19b the output branches always meet the cleaved edge at normal incidence.

The application of the Fabry-Perot cavity method to the Y-junction waveguide is more complicated than in the case of a straight waveguide. In the later case there is a single resonant cavity, while in a Y-junction the cavity is split into a composite cavity formed by the two output branches of the Y-junction. As a consequence, in one propagation direction the optical field is splitted into two parts of amplitudes, √δ and √(1-δ) in respective arms of the Y-junction, while in the other direction they recombined with some phase difference φ

213

due to the difference in the optical path length of the two branches. This phase difference, may be due to poor alignment of the Y-junction with respect to the sample cleaved edge, or improper cleaving of the sample or any other fabrication errors in the mask or optical lithography. The two resonant cavities formed by the output waveguide branches of the Y-junction are strongly coupled.
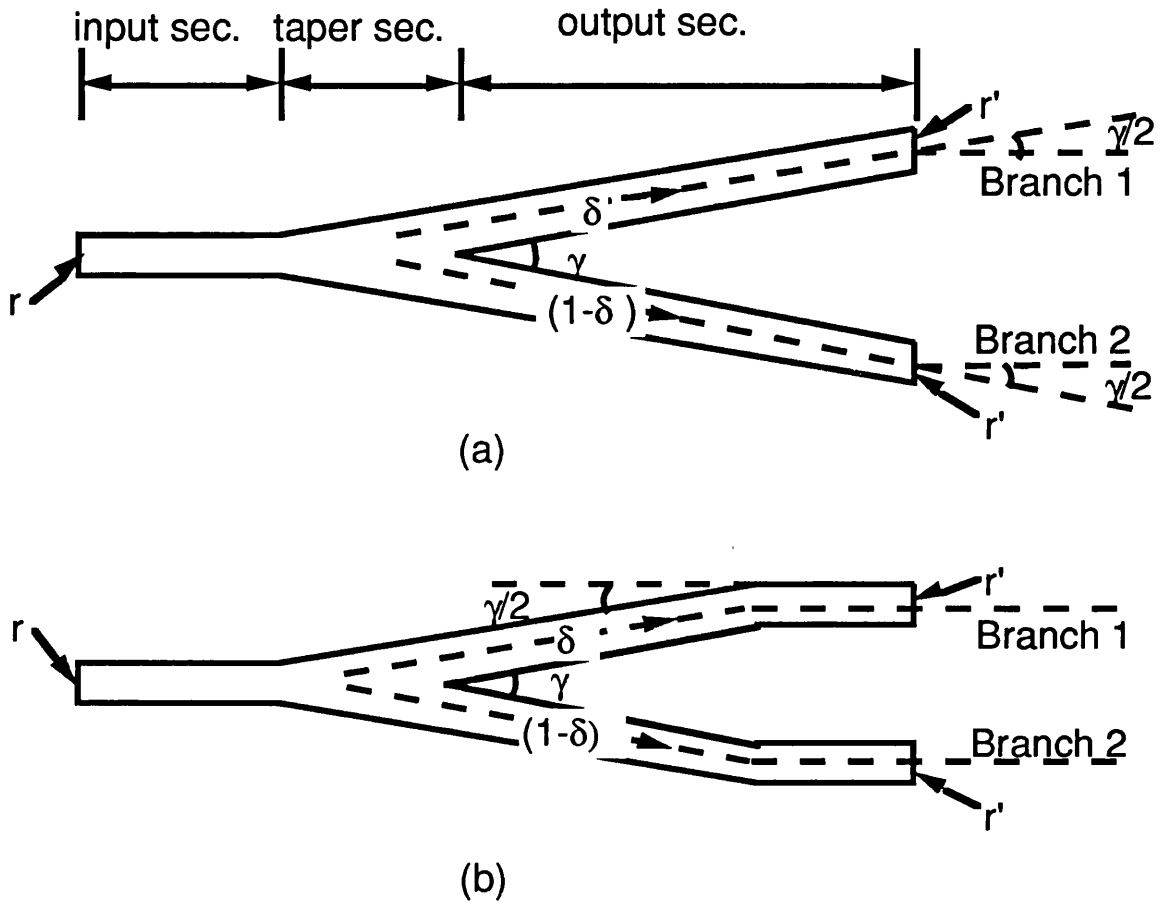
Fig. 7.19 *Schematic diagram of a single-mode symmetrical Y-junction, the output arms meet the normal to the end facets at an angle ±γ/2 in (a) and at zero angle in (b).*

In the general case where the Y-junction is asymmetric, the optical power transmission of the Fabry-Perot Y-junction cavity can be derived, in the same manner as for the case of a straight waveguide cavity described in section 5.7.1, from the convergent geometric series obtained by adding wave amplitudes due to successive reflections. Assuming perfectly coherent, monochromatic light, the resonant (T_R) and antiresonant (T_A) transmissions of branch 1 and branch 2 are:

214

$$(T_R)_1 = I_0 \left[\frac{\zeta\sqrt{\delta}}{1 - \zeta^2 |rr'| \left(\sqrt{\delta} + \sqrt{(1-\delta)} \cos^2\phi \right)} \right]^2$$

$$(T_R)_2 = I_0 \left[\frac{\zeta\sqrt{(1-\delta)}}{1 - \zeta^2 |rr'| \left(\sqrt{\delta} + \sqrt{(1-\delta)} \cos^2\phi \right)} \right]^2$$

$$(T_A)_1 = I_0 \left[\frac{\zeta\sqrt{\delta}}{1 + \zeta^2 |rr'| \left(\sqrt{\delta} + \sqrt{(1-\delta)} \cos^2\phi \right)} \right]^2$$

$$(T_A)_2 = I_0 \left[\frac{\zeta\sqrt{(1-\delta)}}{1 + \zeta^2 |rr'| \left(\sqrt{\delta} + \sqrt{(1-\delta)} \cos^2\phi \right)} \right]^2$$

where I_0 is the effective input intensity and includes terms due to input and output coupling efficiencies, r and r' are the amplitude reflection coefficients of the input and output facets of the Y-junction. ζ is a single-pass wave amplitude attenuation factor ($\zeta = \zeta_1\zeta_2\zeta_3$), where $\zeta_1, \zeta_2, \zeta_3$ are the single-pass wave amplitude attenuation factors of the input, taper and output sections of the Y-junction respectively. $\sqrt{\delta}$ and $\sqrt{(1-\delta)}$ are the amplitudes splitting of the input field between the two branches 1 and 2, respectively, of the Y-junction and ϕ is the relative phase difference between the two output branches of the Y-junction.

In this model, the co-directional coupling between the Y-junction two branches has been included. As the optical field in the Y-junction two arms are reflected back from the output facet r' with relative phase difference ϕ, the co-directional coupling between the two fields close to the junction will generate the symmetric (even) and antisymmetric (odd) modes in the taper. In the single mode straight section, only the even modes will be transformed into the fundamental mode. The odd modes will be radiated into the substrate.

The single-pass loss Γ_K (dB) of the Y-junction is obtained from the ratio

$$K_{1,2} = (T_R)_{1,2}/(T_A)_{1,2}$$

$$\Gamma_K(dB) = -20 \, \text{Log}\,\zeta = -10 \, \text{Log}\left[\frac{\sqrt{K}-1}{\sqrt{K}+1} \cdot \frac{1}{|rr'| \left(\sqrt{\delta} + \sqrt{(1-\delta)} \cos^2\phi \right)} \right] \qquad (7.17)$$

In the case of symmetrical Y-junction, K should be the same for both output branches 1 and 2, i.e. $K_1 = K_2$.

From Eq. (7.17), the assessment of the single mode Y-junction propagation losses requires the measurements of the followings;

1) The resonant and antiresonant output cycles of the transmission of the two cavities formed by the Y-junction branches.

2) The relative phase difference between the two outputs of the Y-junction.

3) The input and output facets reflectivities r and r'.

4) The split ratio between the two branches of the Y-junction.

In the early stage of this work, Y-junctions with similar configuration as the one in Fig. 7.19a were used. In these devices, the input and output facets reflectivity were assumed equal. This assumption was not valid ($r \neq r'$) as it was proved experimentally in section 5.7.3. Therefore the propagation loss in Y-junctions shown in Fig. 7.19b, was measured as a function of the angle γ.

7.6.2.2 Fabrication Details:

The fabrication procedures of transferring the chrome mask pattern (of Fig. 7.12) onto A118 GaAs/GaAlAs double heterostructure is described in section 5.3. One problem was emerged in the fabrication of the Y-junctions using a dark-field mask, namely the diffraction of UV light at the wedge of the Y-junction, which produced a blunted Y-junction tip. This was a serious problem as it increased the scattering losses of the Y-junction [18]. The diffraction of the UV light during exposure happens when there was an air-gap between the mask and the sample. Therefore, the following precautions were taken during the fabrication process:

1) Removal of the thicker photoresist at the edges of the coated sample, by rubbing the edges with a cotton pud (soaked in acetone).

2) To obtain a good contact printing, a uniform hard pressure was applied onto the sample. This was achieved by balancing heavy weights on the top of the sample.
3) Optimise the exposing and developing times of the optical lithography.

216

Fig. 7.20 shows SEM photographs of sharp and blunted tips of Y-junctions.
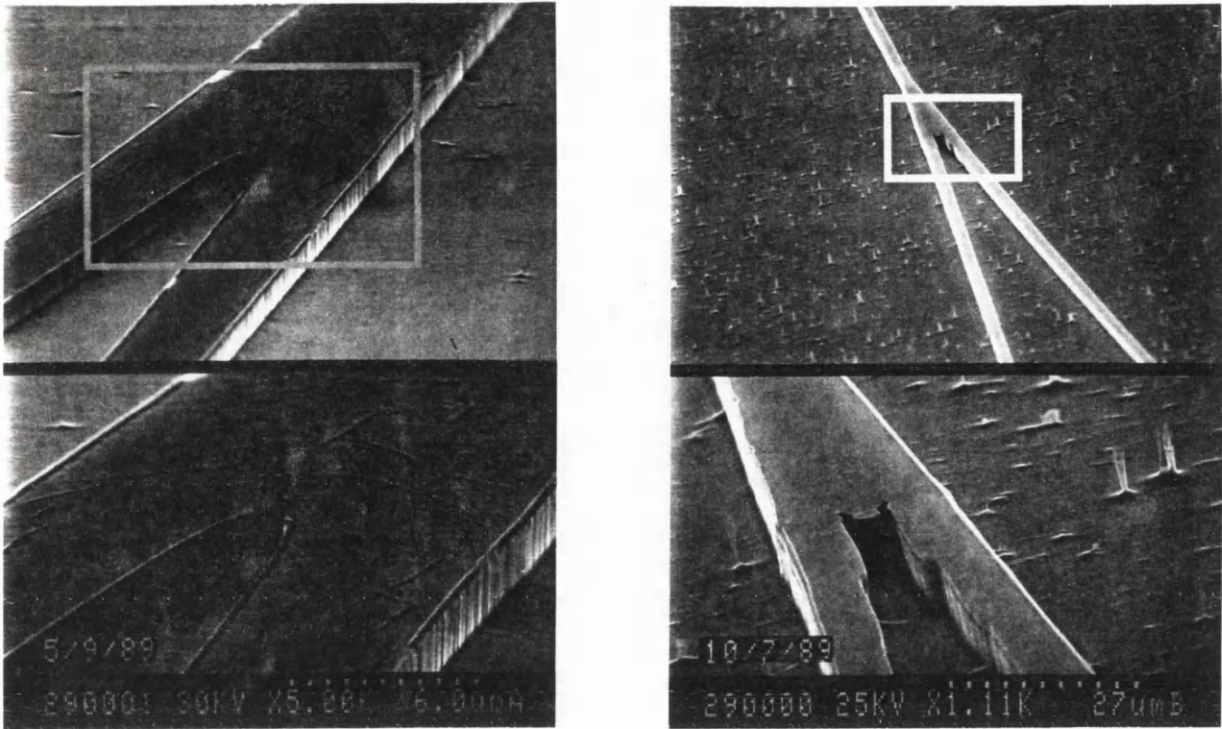
Fig. 7.20 *SEM photographs of sharp and blunted tips of Y-junctions.*

7.6.2.3 Experimental Measurements:

Single- and Multi-mode Nature of the Y-Junction:

The model field profile of the waveguides were examined using a Hamamatsu camera. The scan of the intensity profile in the transverse and lateral directions can show if the waveguide is a single- or multi-mode. This can mislead when the waveguide is highly multi-mode and/or the output is intense. In this case the output intensity profile of the waveguide will be the superposition of all the modes which may look like a Gaussian profile as that of the fundamental mode.

In Y-junction waveguides, the single- and multi-mode nature was examined by traversing the laser beam across the rib width of the input guide. By doing this, if the output intensity from the two branches of the Y-junction shows a progressive increase and decrease then the Y-junction is multi-mode. This is due to the coupling between the local normal modes in the branching waveguides. Fig. 7.21 shows the output transmission of the two branches of the Y-junction when the input beam is moved from one edge to the centre then to the other edge

of the rib width of the waveguide. In a single-mode Y-junction, the output light intensities is evenly distributed between the two output branches regardless of the input laser beam position.

Output Transmissions and Phase Measurements of the Fabry-Perot Y-Junction:

The output from the two arms of the Y-junction were detected using two identical Ge-photodiodes connected to two lock-in amplifiers, the outputs of the two lock-in amplifiers were recorded on a two channel chart-recorder. As in the case of straight and bent waveguides, the Fabry-Perot resonant/antiresonant cycles of both output cavities were recorded simultaneously during cooling of the sample. We have seen in section 5.7.2.3, that the drop in the sample temperature, after removing the heat source, with time was not linear, so that the change in the optical length was also not linear with time and the periodicity of Fabry-Perot cycles changed with time. Therefore the relative phase difference between the two arms is time dependent, this increases the experimental error. Typical results are shown in Fig. 7.22, the cycles of the Fabry-Perot were recorded during and after heating the sample. For accurate measurement of ϕ, it was important to keep the periodicity of these cycles more or less constant with time. This was achieved by recording the output intensities of the two Y-junction arms while slowly heating the sample. In this way, it was possible to measure ϕ to an accuracy of $\pm 10°$. Fig. 7.23 shows the cycles of Fabry-Perot as recorded during slowly heating the sample. The values of K_1 and K_2, the ratio of resonant to antiresonant transmissions, $K = T_R/T_A$, were calculated from the Fabry-Perot cycles of the outputs of arm 1 and arm 2 of the Y-junction respectively.

Power Split Ratios δ and $(1-\delta)$ Measurement:

One of the key parameters which influences the output response of the nonlinear integrated asymmetric Mach-Zehnder interferometer is the split ratio $\delta:(1-\delta)$ between the two arms of the device. The power split ratio δ and $(1-\delta)$ in the single mode symmetrical Y-junction was measured directly by observing the intensity of the output light from each arm. As any resonance (i.e. multi-reflections within the Y-junction cavity) would complicate such measurement, an absorbing layer was put on top of the Y-junction waveguides.
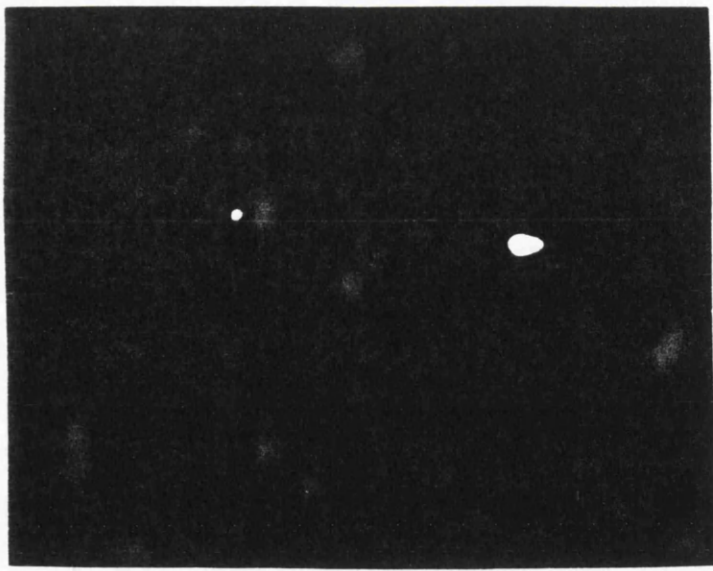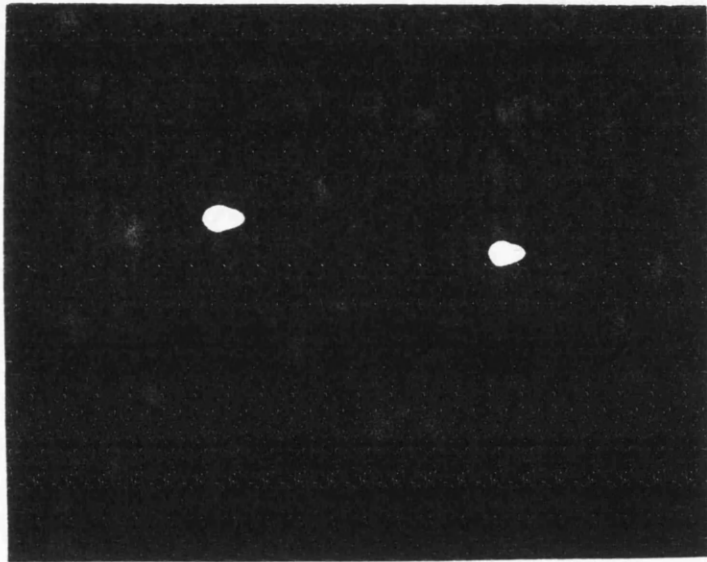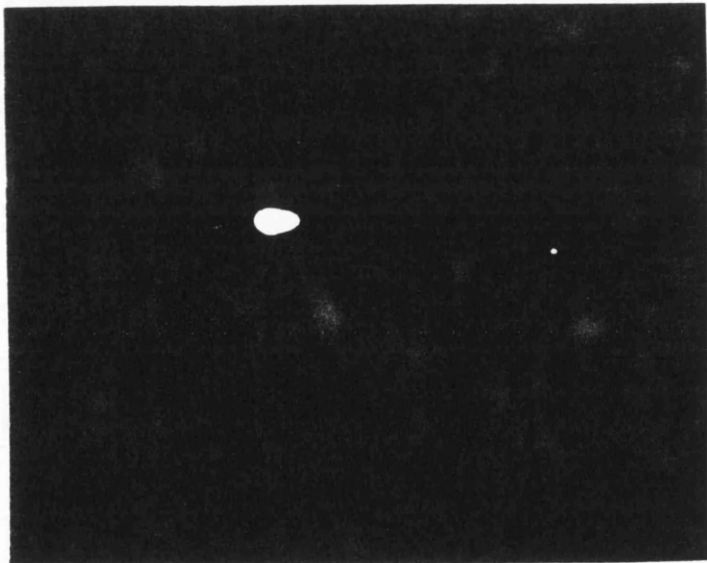
Fig. 7.21 *The variation of the intensity distribution between the two output arms of a multimode Y-junction as the input laser beam moves across the lateral axis of the input end facet of the Y-junction.*
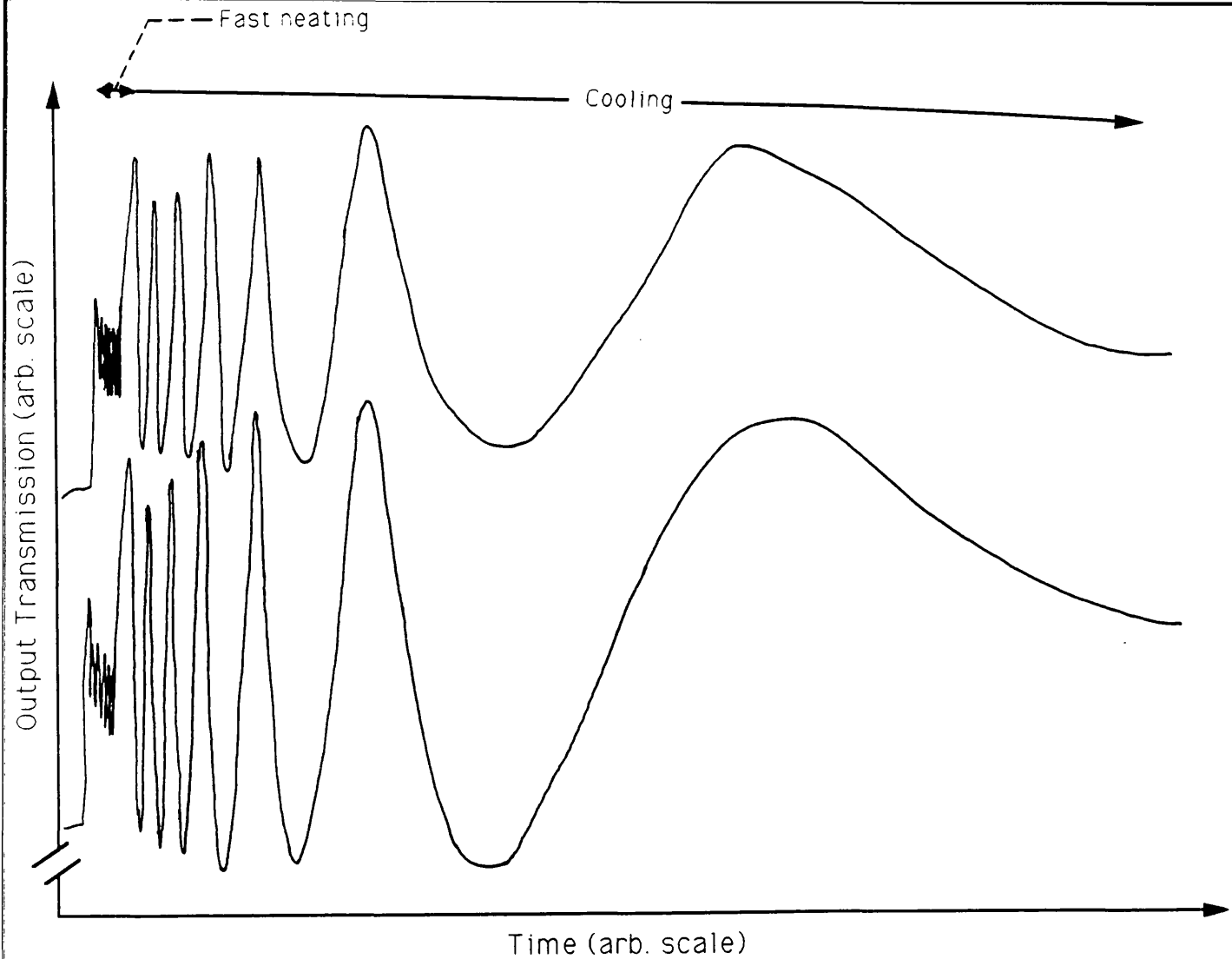
Fig. 7.22 *The resonant/nonresonant cycles of the two outputs of a single mode Y-junction, produced by fast heating of the sample.*
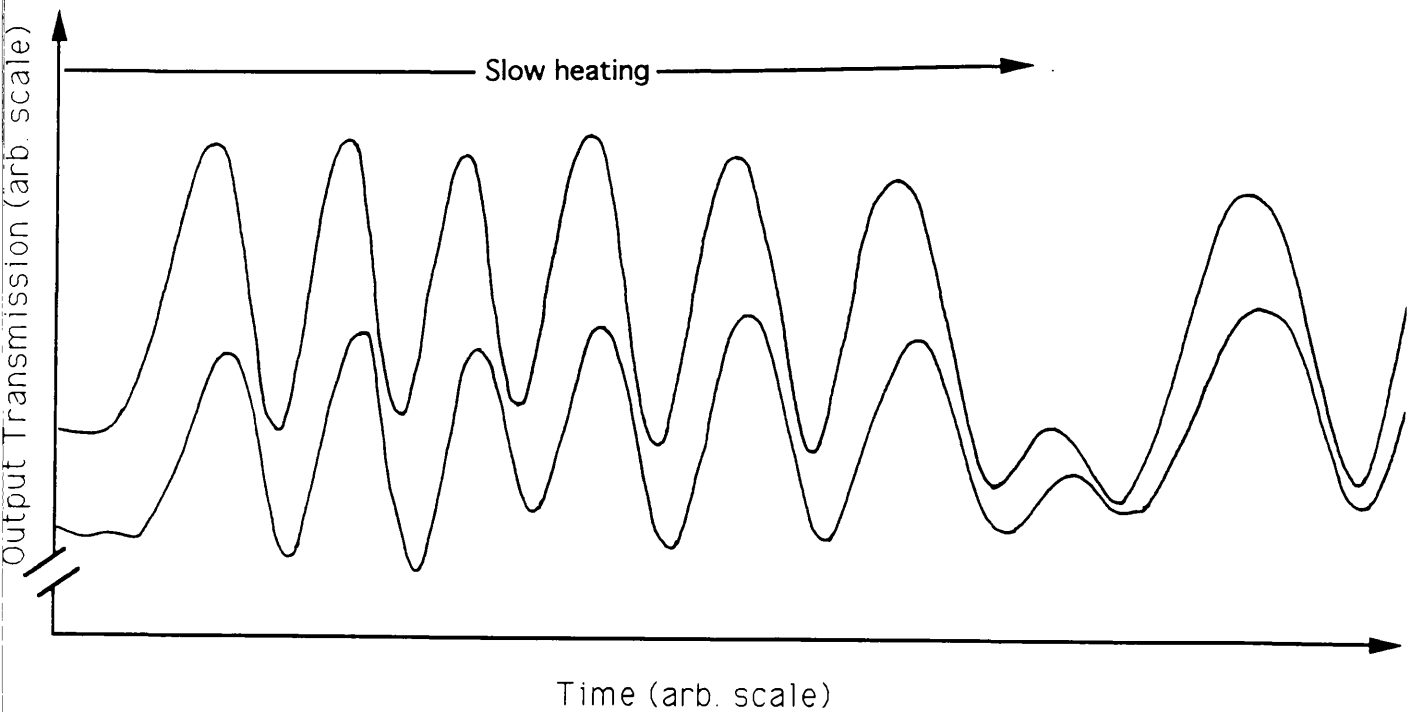
Fig. 7.23 *The resonant/nonresonant cycles of the two outputs of a single mode Y-junction, produced by slowly heating of the sample.*

The deliberate suppression of the resonance was achieved by coating the top surface of the sample with a sheet of metal by one of two techniques. Either by melting indium directly onto the sample or vacuum evaporation of NiCr, both of which were easy to remove from the sample later. The power splitting, in these single-moded waveguide Y-junctions, was less sensitive to the lateral position of the input laser beam across the rib width of the Y-junction input waveguide facet.

Experimental Results:

Only single mode Y-junction waveguides, with 2 μm rib width and 2.2 μm etching depth were considered. The Y-junction experimental measurements of the phase difference ϕ, the power split between the two arms δ and $(1-\delta)$ and the measured end facet reflectivities, r and r', of the straight waveguide were applied to Eq. (7.17). Two values for the Y-junction transmission losses were calculated from K_1 and K_2 values, i.e. the ratio of the resonant to antiresonant transmissions of arm 1 and arm 2 respectively.

Figure 7.24 shows the raw data of the losses measured for the 2 μm single mode symmetrical Y-junction as a function of the full angle γ of the Y-junction, the two values of the propagation loss, derived from K_1 and K_2, agree well. As the Y-junction angle γ increased, the propagation loss increased. This loss was due to the radiation loss at the Y-junction angle and it increases dramatically when the tip of the Y-junction is blunted [18].
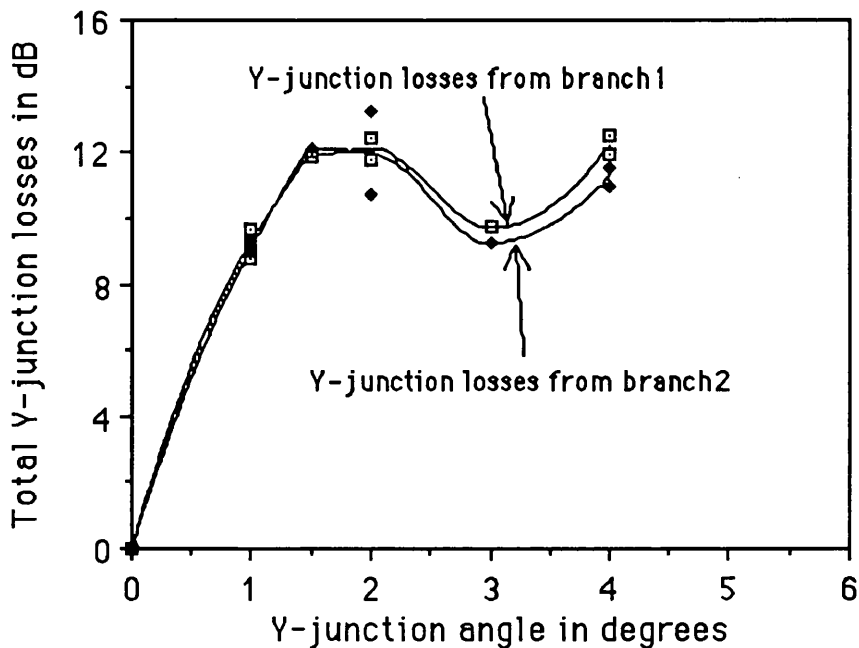
Fig. 7.24 *Propagation losses in a single-mode symmetrical Y-junction as a function of the full branching angle* g.

221

The lower propagation loss in the Y-junction with an angle γ=3° was thought to be due to the sharper wedge tip of the Y-junction compared to the rest of the Y-junctions, as confirmed by scanning electron microscope observations. Fig. 7.25 shows the same data as in Fig. 7.24 after subtracting the attenuation in the input and output sections of the Y-junction, ζ_1 and ζ_3 respectively, and the bending loss at the corners of the output arms.
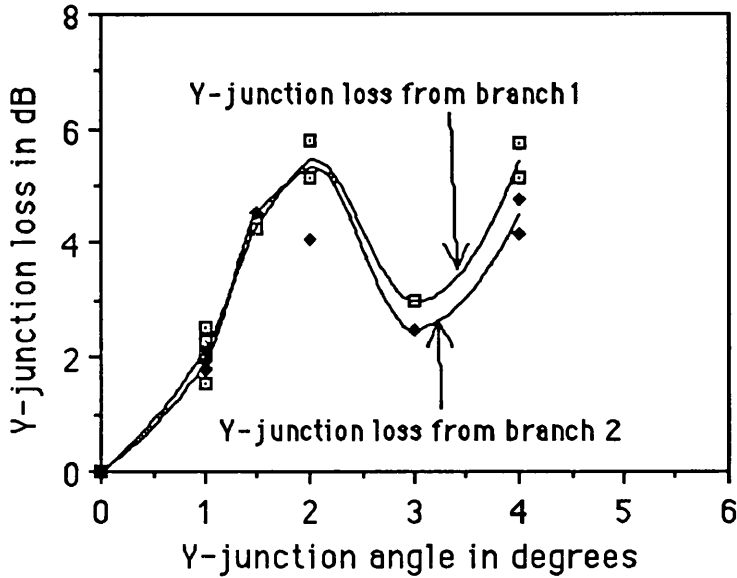
Fig. 7.25 *Same results as in Fig. 7.26 after subtracting the attenuation in the input and output sections of the Y-junction and the bending loss at the corners of the Y-junction output arms.*

7.7   Switching Operations of GaAs/GaAlAs Quantum Well Integrated Mach-Zehnder Interferometer:

As we have seen in the theoretical model of the AM-ZI, to achieve a switching in such device, a relative phase difference of π rad between the two arms of the AM-ZI has been generated. This can be achieved by two means; either using the electro-optic effects or the nonlinear intensity dependent refractive index change in GaAs/GaAlAs quantum well materials. Our main target was to achieve a switching action in such device using nonlinear all-optical switching.

222

7.7.1 Switching Operation Using the Electro-Optic Effects:

We have seen in sections 2.4 and 2.5 that in semiconductors, an applied electric field across the epitaxial layer produced a simultaneous change in the semiconductor's optical attenuation and phase retardation. At certain wavelengths, the loss and phase components are comparable in size. In this section, their sizes were examined simultaneously, this was achieved by comparing the output response of the active symmetrical Mach-Zehnder interferometer SM-ZI and that of the straight waveguide as a function of the applied electric field strength. In the active SM-ZI, the input and output Y-junctions are symmetrical, and the split ratio between the two arms of the device are equal.

7.7.1.1 Design Considerations and Fabrication Procedures:

One of the main problems in the design and fabrication of an active nonlinear integrated M-ZI was the electrical isolation of the electrodes from the rest of the device. These active devices were fabricated in GaAs/GaAlAs QT147 SQW p-i-n structure. The electrical isolation required to etch or passivate the p-doped GaAlAs upper cladding layer down to the intrinsic layer. This was achieved by two techniques, accordingly two masks were designed. Fig. 26 shows a schematic diagram of the active M-ZI used in the first mask, referred to as mask 1, and the cross section of the profile of the final device. The length of the electrodes was defined by short gaps ($t \approx 1.5$ μm). The electrical isolation of the electrodes was achieved by etching through the p-type upper cladding layer. In this case the etching depth of the gaps was equal to that of the rib height of the device. This increased the device insertion loss due to the scattering loss at the gaps. When deep etching was required to reduce the bending loss, i.e. etching through the QW guiding region, the scattering loss increased significantly.

In the second mask (referred to as mask 2), there were no gaps in either arm of the M-ZI. The electrical isolation gaps were created later in the device and isolation of the electrodes was achieved by using a combination of dry etching and hydrogen passivation of the p-type GaAlAs upper cladding layer [26]. Fig. 27 shows a schematic diagram of the fabrication steps of an active M-ZI device, using mask 2.

Selective deposition of the p-type ohmic contact on the M-ZI arms was achieved by using a copper plate with windows aligned over the required area of the sample to be metalised.

223

Hydrogen passivation was achieved by exposing the samples to a hydrogen plasma in an Electrotek 340 plasma etch under the following conditions: Hydrogen gas flow 25 sccm, pressure 10 mTorr, R.F. power 100 watts, D.C. self bias 875 V, time 20 minutes.

The samples were annealed at 360 °C for 45 sec in an Ar-ambient to form the p- and n-type ohmic contacts. Finally, the samples were cleaved to obtain mirror finished facets.

In the design structure of the p-i-n GaAs/GaAlAs QW materials, the i-region was extended to the cladding layer, as shown in the schematic diagrams of QT147 SQW and #A163 MQW in section 4.3. This allowed us to achieve electrical isolation without the need to etch through the guiding region.

Investigation of the propagation losses in M-ZI devices fabricated by using mask 1 and mask 2 showed a large difference in the results. Although the second method of fabrication (mask 2) was much more complicated than the first one, the throughput of the M-ZI device was better.
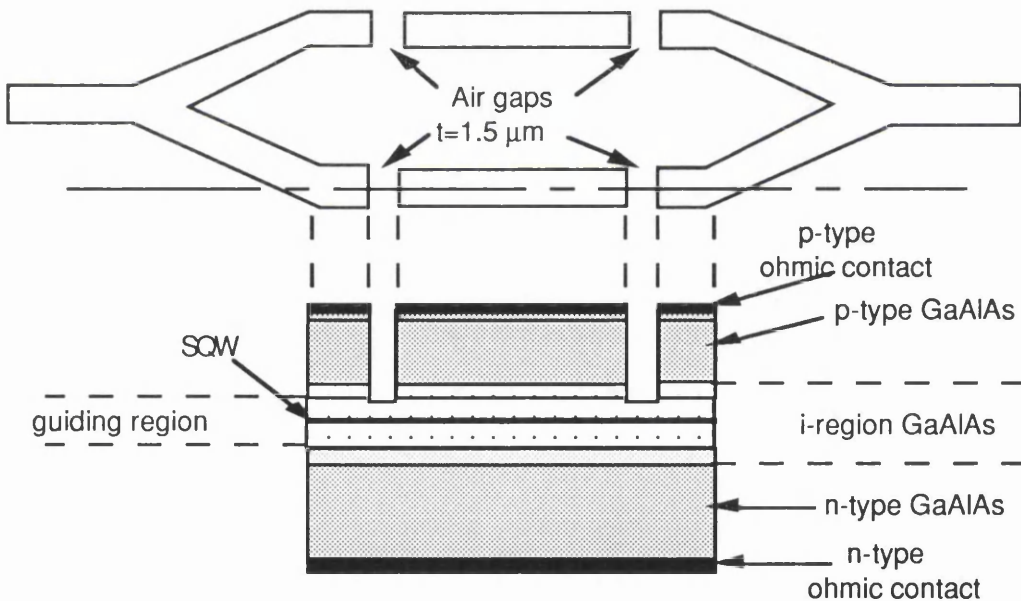
Fig. 7.26 *Schematic diagram of an active symmetric Mach-Zehnder and the cross section of the layers structure and the etching depth of the device. The air gaps depth is extended beyond the p-i junction to achieve an electrical isolation between the two arms of the device.*
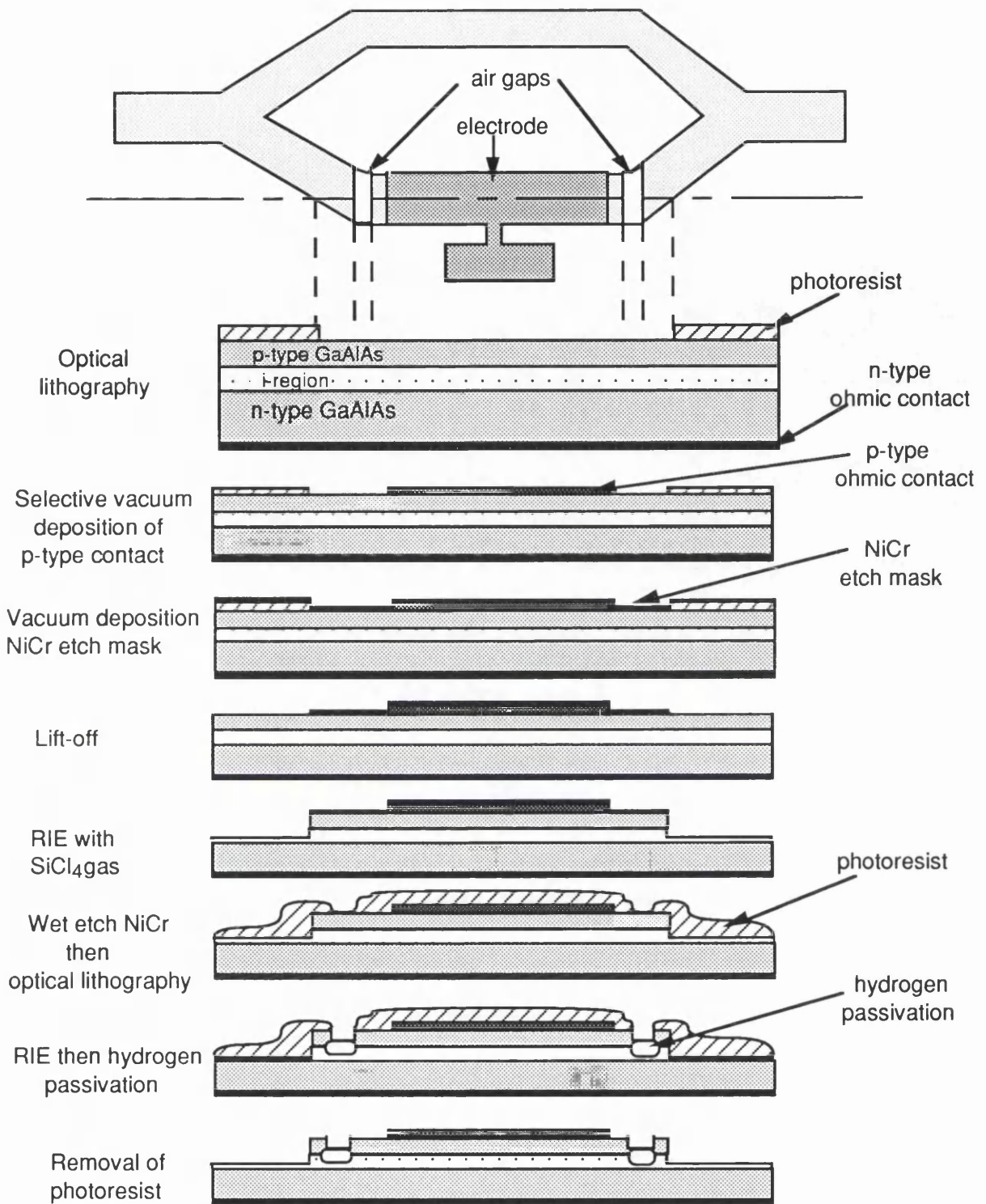
Fig. 7.27 *Schematic diagram of an active symmetric Mach-Zehnder with a selectively deposited electrode. From the fabrication stages of the device, an electrical isolation of the electrode from the rest of the device is achieved by using the combination of the dry etching and the hydrogen passivation techniques without the need to etch beyond the p-i junction.*

225

7.7.1.2 Experimental Measurements:

Integrated SM-ZIs and straight Waveguides with 2 μm and 3 μm rib width were fabricated in QT147 SQW, using mask 2. The first etching depth was ≈1.4 μm and the second etch depth was ≈0.8 μm. Therefore, the final rib height was 2.2 μm and the depth of the electrical isolation gap was only 0.8 μm. The length of the sample was 2 mm and the length of the electrode was L=400 μm.

The electrical isolation between the two arms of the integrated SM-ZI was measured using the configuration shown in Fig. 7.28. A reverse bias voltage was applied across arm 1 V_s, whilst the voltage V_m across arm 2 was monitored. The sample was exposed twice to the hydrogen plasma (each time for 10 minutes). Measurements were carried out on the sample before and after exposure to hydrogen plasma. An etching depth of 0.8 μm through the p-type GaAlAs layer followed by 20 minutes of exposing the sample to hydrogen plasma shows a complete electrical isolation between the two electrodes of the interferometer. The monitored voltage V_m was 1.5 V for an applied voltage V_s=22 V.
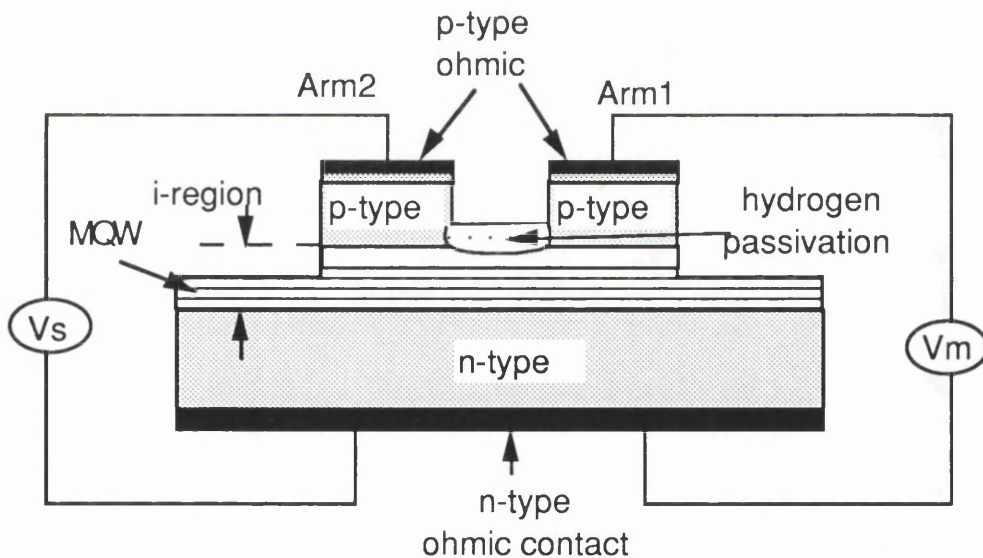
Fig. 7.28 *Schematic diagram of the circuit arrangement used to measure the electrical isolation between the electrodes of the two arms of the active Mach-Zehnder interferometer.*

The end-fire coupling system described in section 5.7.2, was used to couple the CW tuneable Ti:sapphire laser into and out of the SM-ZI. The output transmission was monitored using a Si photodiode. All the measurements were made at photon energies

226

below the e1-lh1 excitonic transition, <40 meV, for the TM-mode.

The phase and amplitude modulation in the integrated SM-ZI have been investigated as a function of the applied reverse bias voltage, at photon energies well below and close to the QT147 SQW band gap. The size of the phase and absorption coefficients have been measured. This was achieved by comparing the measurements of the output transmission of the SM-ZI with that of the straight waveguide, as a function of the applied reverse bias voltage. The length of the electrodes was the same for both the straight waveguide and the SM-ZI, L=400 μm.

7.7.1.3 Results:

The absorption change $\Delta\alpha(cm^{-1})$, in the straight waveguide and SM-ZI, was measured as a function of the reverse bias voltage V_b, at a discrete photon energies, close to the SQW absorption edge, as is shown in Fig. 7.29 and Fig. 7.30, respectively. The measured absorption change in the straight waveguide, Fig. 7.29, shows the expected increase in absorption associated with the red shift of the exciton peak via the quantum confined Stark effect (QCSE) [27]. The same effect is shown in results presented in section 6.3.2.2. Fig. 7.30 shows the same measurements for the SM-ZI device, at the same photon energies. The bias voltage was applied across one arm of the device.

From the comparison of the two above measurements, it is clear that, for a given bias voltage and photon energy, the change in absorption in the integrated SM-ZI is half that of the straight waveguide. These results shows that the modulation of the propagating light in the SM-ZI was due to only the electro-absorption effect and there was no extra modulation caused by the electro-refraction effect.

The results were confirmed by testing the electro-optic switching of the SM-ZI at photon energy well below the SQW absorption edge (λ=1.15 μm). The output transmission of the SM-ZI showed no modulation as a function of applied reverse bias voltage. Therefore, the GaAs/GaAlAs SQW material has no or very small electro-refraction effect. These results agrees with that in section 6.3.2.2, where the electro-refraction effect was measured using the external Mach-Zehnder interferometric set-up.

At photon energies close to the material absorption edge, the break down reverse bias voltage of the active M-ZI devices was reduced dramatically, depending on the intensity of the laser beam, due to the photogenerated carriers in the intrinsic region. Fig. 7.31 shows an SEM micrograph of a blown device
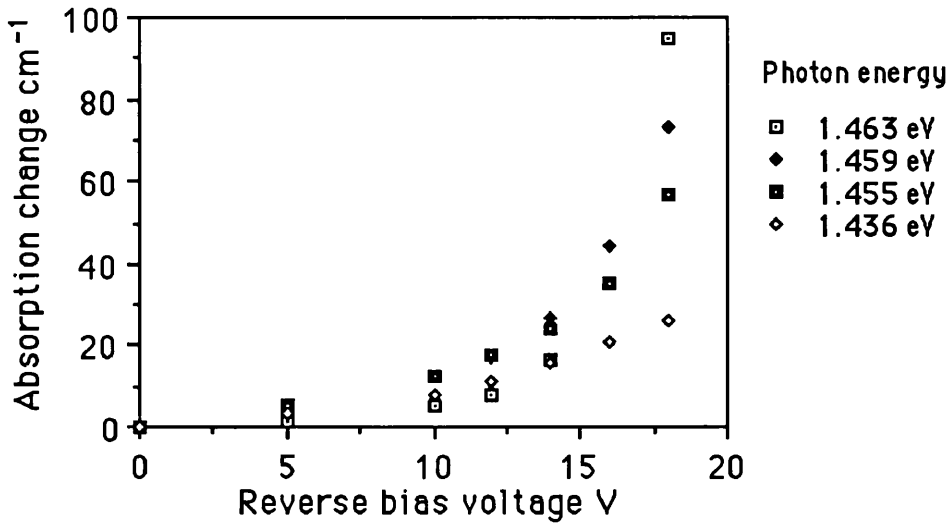
Fig.7.29 *The absorption change* Δα(cm⁻¹) *in the straight waveguide measured as a function of the reverse bias voltage* Vb, *at a discrete photon energies close to the SQW absorption edge. The rib width and etching depth were* 3 μm *and* 1.4 μm *respectively. The length of the electrode was* L=400 μm.
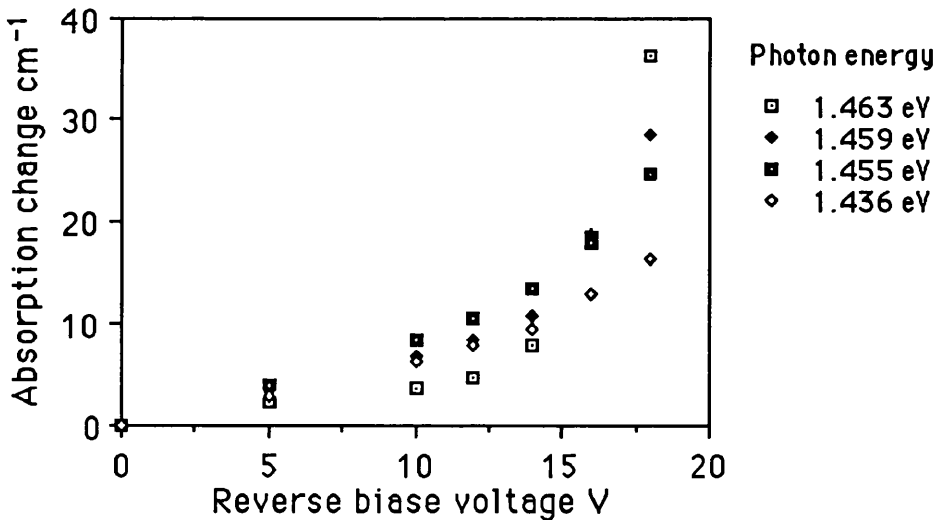
Fig 7.30 *The absorption change* Δα(cm⁻¹) *in the symmetrical Mach-Zehnder interferometer measured as a function of the reverse bias voltage* Vb, *at a discrete photon energies close to the SQW absorption edge. The rib width and etching depth were* 3 μm *and* 1.4 μm *respectively. The length of the electrode was* L=400 μm.

228
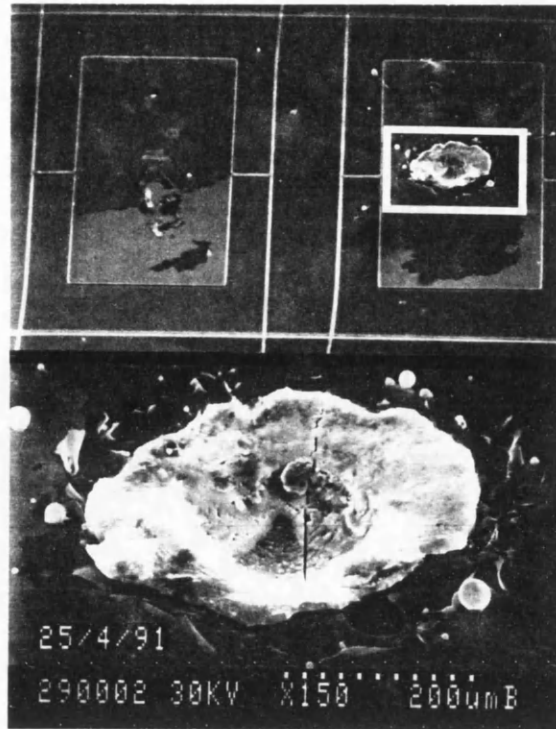
Fig. 7.31 *SEM micrograph of a blown pad of a M-ZI active device.*

7.7.2 All-Optical Switching Using the Resonant Nonlinearity in GaAs/GaAlAs Quantum Well Material:

The intensity dependent refractive index change in GaAs/GaAlAs single quantum well material has been used to achieve switching in the integrated AM-ZI. In this section, the switching performance of the AM-ZI was examined using both CW and ultra short pulse lasers.

The mask design used for these experiments consisted of straight, asymmetric Y-junctions and AM-ZIs waveguides, the linewidth of these devices was 3 μm. The mask consisted of five asymmetric Y-junctions, five AM-ZI's and four straight waveguides. In the Y-junctions and AM-ZI's, the bends were designed with two sequential bends with bending angle half the Y-junction full angle. This was to reduce the bending loss. The Y-junction full angle γ was 1°, 1.5°, 2°, 2.5° and 3°, the length of the segment 200 μm. The separation between the two arms of the AM-ZI was large enough to avoid any coupling caused by the evanescent field of the guided modes in the two arms.

229

in section 4.3, by using the standard optical lithography and lift-off processes followed by RIE, using SiCl$_4$ gas.

7.7.2.1 CW Switching Operation:

A CW pump-probe experimental set-up was used to test the switching operation of the AM-ZI, as shown in Fig. 7.32. The probe beam was a semiconductor diode laser and the pump beam was the tuneable Ti:Al$_2$O$_3$ laser. The Sharp diode laser was GaAs/GaAlAs heterostructure, the operating wavelength was λ=830 nm at a room temperature. A temperature controller with a feedback loop circuit were used to keep the temperature constant within ±0.25 °C. The probe beam was chopped at 800 Hz and the pump beam at 1 Hz. The wavelength of the tuneable Ti:Al$_2$O$_3$ laser was chosen close to the excitonic peak of the #A187 SQW material, λ=850 nm. The two beams were linearly polarised (TE) and couples into the AM-ZI device by using endfire coupling and at the output they were separated by using a diffraction grating. The probe beam was focused onto a Si-photodiode connected to a lock-in amplifier and then to a chart recorder.
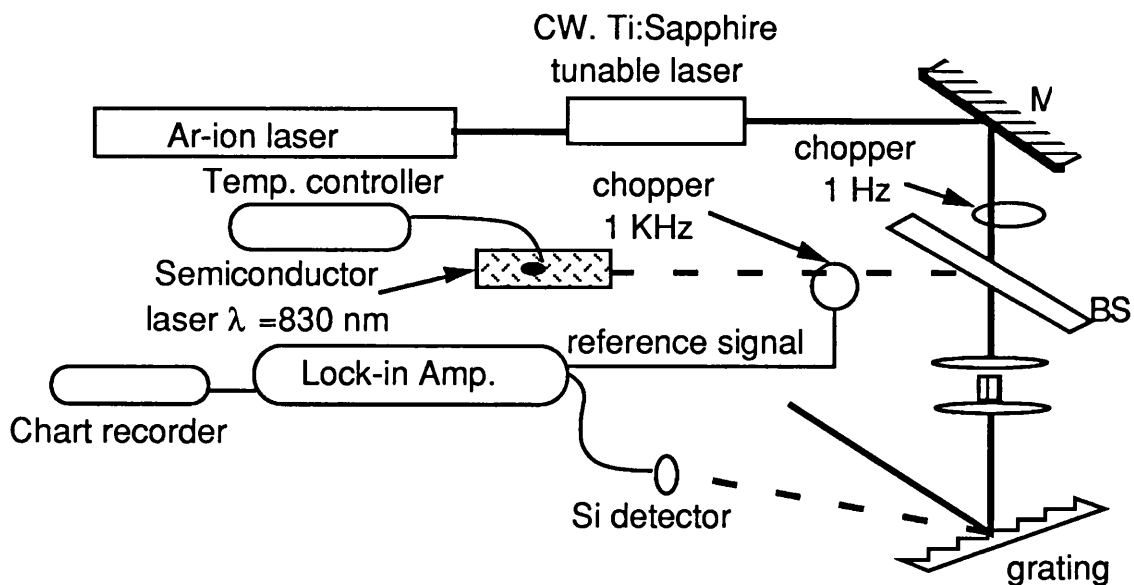
Fig. 7.32 *Pump-probe experimental set-up used to test the all-optical switching of the asymmetric Mach-Zehnder devices. The pump beam was a CW Ti:sapphire laser and the probe beam was a GaAlAs semiconductor laser, the two beam were separated at the output by using a grating.*

230

Fig. 7.33 shows the probe output transmission of the AM-ZI when the pump beam was on and off at a rate of 1 Hz. The rib width of the AM-ZI device was 3 μm, etching depth 1 μm, Y-junction full angle 3° and the split ratio δ:(1-δ) was around 0.25:0.75. As the pump beam was off (i.e. blocked), the probe output transmission was steady and when the pump beam is lunched into the AM-ZI the probe output transmission is modulated at the same rate as that of the pump beam with a 34% amplitude modulation. The intensities of the probe and pump beam were ≈50 μW and ≈70 mW respectively. The switching operation of the AM-ZI can be attributed to a combination of electronic and thermal effects.
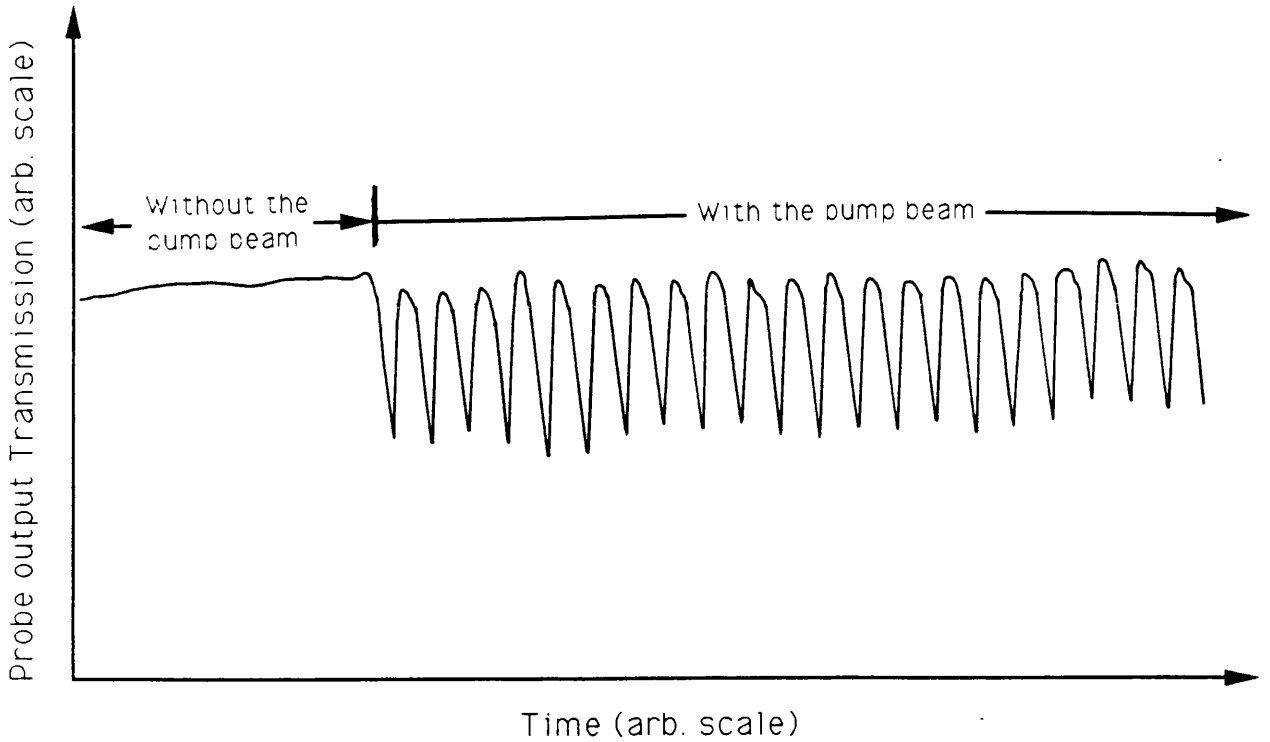
Fig. 7.33 *The probe output transmission of an AM-ZI when the pump beam was on and off at a rate of 1 Hz. The rib width of the AM-ZI device was 3 μm, etching depth 1 μm, Y-junction full angle 3° and the split ratio δ:(1-δ) was around 0.25:0.75.*

7.7.2.2 Ultrashort Pulse Switching Operation:

The investigation of the switching operation of the integrated AM-ZI using the resonant opto-electronic effects requires the elimination of the opto-thermal effects. This was achieved by testing the AM-ZI with ultrashort pulses ≈50 ps at a repetition rate of 13 ns, much longer than the recombination time of the photo-generated carriers. These pulses were generated using the actively mode-locked tunable Ti:sapphire laser.

The experimental set-up described in section 6.3.1.3 was used. The pump beam was TM polarised and orthogonal to the TE polarised probe beam. The delay time between the pump and the probe pulses was zero, and the photon energy was 1.452 eV. The intensity of the

pump beam was varied by using a combination of an electro-optic modulator and polariser, as described in section 6.3.1.2.

Fig. 7.34 shows the theoretical (solid line) and experimental (square points) of the normalised probe output transmission of the AM-ZI as a function of the pump peak intensity (W.cm^{-2}). These results can be explained in term of the intensity dependent absorption and refraction saturations in the AM-ZI. As the pump-beam intensity increases, the absorption saturates and the output transmission increases. At high pump intensity the absorption saturates completely, and the AM-ZI output transmission decreases due to the change in the relative phase difference between the two arms, via the intensity dependent refractive index change. These results follow the theoretical prediction of the response function of the resonant AM-ZI derived in section 7.3.2. As predicted by equations 7.6-7.8, the AM-ZI does not switch off completely due to the relative difference in the saturation of absorption between the two arms, caused by the difference in the intensities resulting from the asymmetric split ratio.
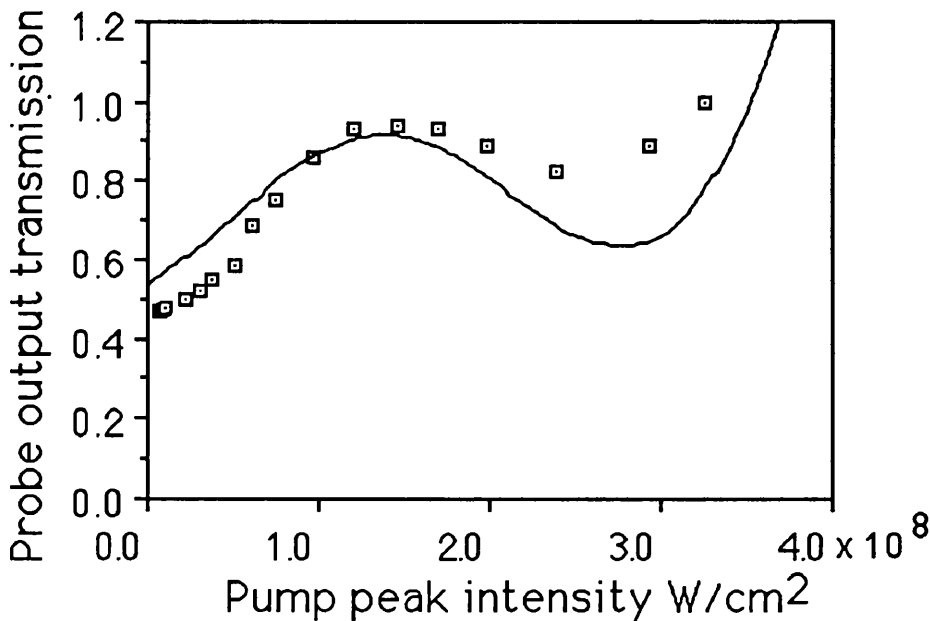
Fig. 7.34 *The solid line is the theory described in the text fitted to the experimental results of the normalised probe-beam output transmission of the integrated asymmetric Mach-Zehnder interferometer as a function of the input pump-beam intensity. The delay time between the pump and probe pulses was zero and the photon energy was 1.452 eV. The AS-MZI Y-junction full angle was 2° and the split ratio between the two arms was 0.3:0.7.*

232

The same measurement was repeated for different delay times between the pump and probe pulses ($\Delta\tau$ = 12.5 ns), the probe output transmission of the AM-ZI was constant with the pump input peak power density. This was a clear indication that the underlying mechanism was non-thermal in origin.

7.7.2.3 Comparison of Theoretical and Experimental Results:

With reference to Fig.7.34, the output response of the resonant AM-ZI, was calculated using Eq. (7.8). The parameters δ=0.3, $I_{\alpha sat}$=10^{11} W/cm^2, n_2= 1.4x10^{-8} cm^2/W length=0.2 cm, α_0=65 cm-1, λ=854 nm have been obtained experimentally. The parameter $I_{\alpha sat}$ is obtained from the absorption saturation measurements in the straight waveguide. I_{nsat} and θ are taken as adjustable parameters whose values are 4x10^5 W/cm^2 and π/10, respectively.

The plot shows qualitative agreement with the experimental results. However, the following aspects are worth noting, the I_{nsat} value is much smaller than $I_{\alpha sat}$. The small value of I_{nsat} is an unexpected result since from previous work on MQW nonlinearities [28] indicates that $I_{\alpha sat}$ and I_{nsat} arise from the same mechanism and therefore should have the same value. If the same saturation intensity as the absorption nonlinearity is used in our model then the device should go through several switching cycles in the intensity range shown in Fig. 7.34, where only one switching cycle is observed. It has been observed [29] in other waveguide devices that, for the refractive nonlinearity, even at short times the thermal mechanism competes with the electronic mechanism and this may account for the small value of I_{nsat} although clearly this aspect deserves further investigation. In this respect a significant difference between the quantum well employed here compared to [28] is that nonradiative traps, the surface states, have been introduced close to the quantum well to reduce the carrier recombination time this will result in increased heating and therefore thermal effects are expected to be more significant in our results than in [28]. Furthermore equation (7.8) was derived from a CW theory of the operation of the device, while the experimental results are from pulsed operation and there could be several effects associated with averaging over the pulse duration which may alter the operating characteristics of the device. The pulse operation of the device requires more extensive computer modelling than we have presented here. In general the model reproduces the main features of the results but does not give a detailed fit.

233

7.8 All-Optical Switching Operation Using Nonresonant Nonlinearity in GaAlAs Waveguides:

We have seen in the previous section that the AM-ZI, utilising resonant nonlinearity for all-optical switching, is not an attractive device. Due to the small throughput of the device, caused by the large absorption near the material band gap, and full switching is not possible, caused by the saturation of the nonlinear absorption and refraction effects. For these reasons, our interest was directed towards use of the nonresonant nonlinearity for all-optical switching of the AM-ZI. In spite of the high power density required to achieve relative phase difference of π, the recovery time of nonresonant nonlinearity is ultrafast (few 10's fs).

Nonresonant nonlinear AM-ZIs were fabricated and demonstrated in A293 $Ga_{0.82}Al_{0.18}As$ material, described in section 4.3. This material was fully characterised and a figure of merit η ($\eta=\beta\lambda/n_2$) ≈0.38 was obtained at a photon energy below half the band gap of $Ga_{0.82}Al_{0.18}As$, in section 6.5.3. This suggested that the material was suitable for all-optical switching of the AM-ZI ($\eta<2$). In the following sections, the design structure and operation of the nonresonant nonlinear AM-ZI below half the band gap of $Ga_{0.82}Al_{0.18}As$ are presented.

7.8.1 Mask Design:

Due to the small nonresonant nonlinearity, a high power density over a long interaction length is required to obtain a relative phase change of π rad in the AM-ZI for switching. Each arm of the device consisted of two segments, which formed two sharp corners with bending angle $\gamma/2$, where γ is the asymmetric Y-junction full angle. This was to reduce the over all bending loss. The Y-junction full angle γ was 0.5°, 1°, 1.5°, 2°, 2.5°, 3° and 4°. The length of the two segment were 0.4 mm and 1 mm. The chrome mask consisted of four sets of AM-ZI with linewidths W=2 μm and 3 μm and the effective lengths of the AM-ZI arms were L≈5 mm and 7 mm. In each set there were four straight lines for the purpose of SPM, TPA and linear absorption loss measurements.

7.8.2 Experimental Measurements:

A293 GaAlAs heterostructure material, described in section 4.3, was used to explode the nonresonant all-optical action in AM-ZI, at photon energies below half the band gap.

Optical lithography was used to transfer the chrome mask pattern into S1400-31 photoresist. The patterned samples were etched in Plasmatech RIE80 reactive ion etching RIE using $SiCl_4$ gas.

The linear propagation losses was measured in a straight waveguide using Fabry-Perot technique, described in section 5.7. In waveguides with rib width and etching depth 3 μm and 1.6 μm respectively, $\alpha=1.7\pm0.15$ cm^{-1}. The split ratio between the two arms of AM-ZI was measured, after cleaving the AM-ZI into two Y-junctions, and deliberately suppress the multireflections inside the Y-junction, by depositing an absorbing layer of NiCr, as described in section 7.6.2.3. This was achieved by directly observing the intensity of the light output from each arm of the Y-junction.

Ultrashort pulses having a duration of 330 fs, at full width half maximum FWHM, were generated using a synchronously pumped coupled-cavity mode-locked KCl:Tl colour centre laser, as described in section 5.11, at a wavelength $\lambda=1.52$ μm and a repetition rate of 82 MHz. It was also possible to operate the laser without the couple-cavity section, the pulses were then 30 ps with the same range of average power. The pulse duration was measured by using a second harmonic generation autocorrelator.

A single beam experiment was used to examine the AM-ZI as an all-optical switch, the experimental set-up is described in section 6.5.3.1. This was achieved by monitoring the output transmission of the AM-ZI as a function of the input light intensity. The peak power of the input pulses was varied by using a motor controlled attenuator wheel. The output of the waveguides was spatially filtered by focusing through a <0.5 mm diameter aperture positioned ≈1.5 m away and detected with a calibrated Ge-detector. The far field mode profile of the waveguides output was examined and plotted using a Hamamatsu C1000 camera connected to a computer for data logging. It was confirmed that these waveguides were single mode.

7.8.2.1 Results and Discussions:

Fig. 7.35 shows a plot of the experimental (dots) and theoretical (solid line) results of the normalised output transmission as a function of the average input power (i.e. the estimated input power in the device was after taking into account the coupling efficiency and input facet reflectivity). The Y-junction full-angle of the AM-ZI was $\gamma=3°$ and the length of the arms was L≈0.5 cm. The split ratio between the two arms $\delta:(1-\delta)$ was 0.18:0.82. The open circles were for the normalised output transmission of the device for input pulse duration of 30 ps while the rest of the data points were for pulse duration of 330 fs. As the peak power

235

was increased by a factor of 100 (in the case of $\tau_p \approx 330$ fs), a relative switching of more than 80 % was achieved at an average power of ≈ 8.5 mW (i.e. peak intensity≈ 3.92 GW/cm^2). From the measured nonlinear refractive index coefficient n$_2$=5.4x10^{-14} cm^2/W, the relative difference in refractive index between the two arms was Δn= ± 1.4x10^{-4}. This is equivalent to a relative phase difference of π between the two arms of the AM-ZI.
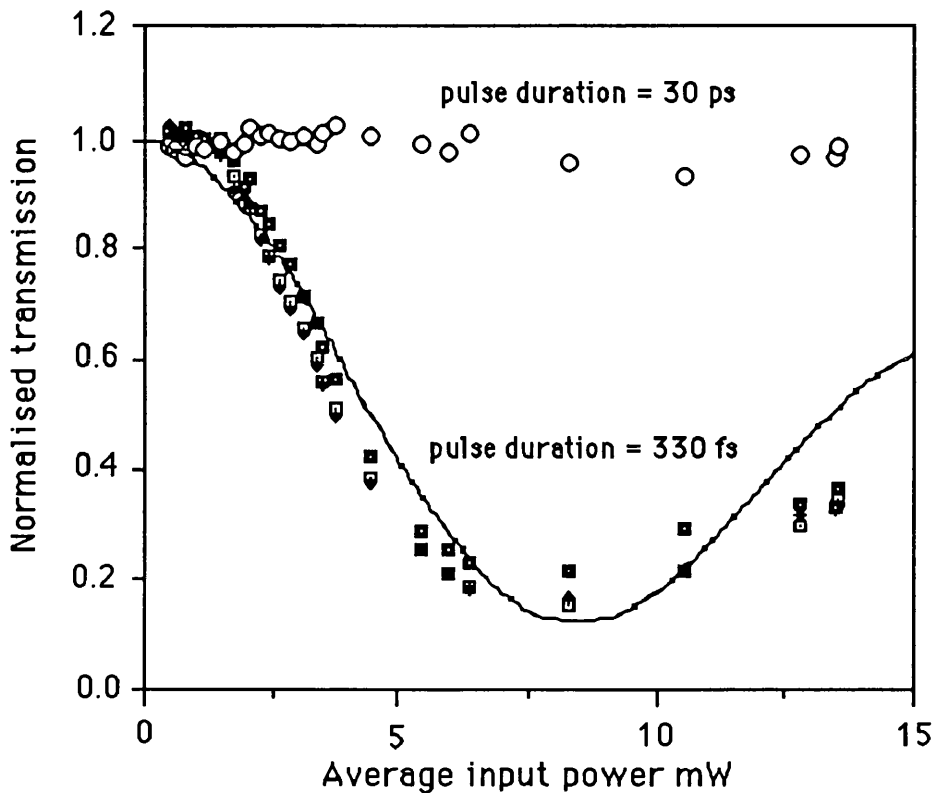
Fig. 7.35 *The experimental (dots) and theoretical (solid curve) results of the normalised transmission of the GaAlAs integrated asymmetric Mach-Zehnder interferometer as a function of the average input power in the device for both 330 fs pulses and 30 ps pulses. For the 330 fs pulses, the switching intensity in the waveguide at an average power of 8.5 mW is 3.92 GW.cm^{-2}.*

From the results of the AM-ZI, the nonlinear refractive index coefficient was estimated to be n$_2 \approx 5.86$x10^{-14} cm^2/W, which was calculated using Eq. (7.3). This value agrees well with that obtained from the SPM measurements in section 6.3.5. It is also consistent with the value of n$_2$ = 3.6 (± 0.5)x10^{-14} cm^2/W of reference [30] measured in GaAlAs waveguides with an Al concentration of 20% and at wavelength of 1.6 μm. In Fig. 7.35, the incomplete switching was due to the different parts of the recombined pulses (at the output Y-junction of the AM-ZI) experienced different effects because the response time of

236

the nonlinear optical mechanism is shorter than the pulse width. In other words, the centre of the pulse experiences destructive interference (i.e. due to a π relative phase difference caused by the SPM) while the wings of the recombined pulses remain in phase (we have observed similar pulse break up in the nonlinear directional coupler [31]). Therefore, due to the low power at the wings of the recombined pulses, the AM-ZI does not switch completely. This explanation is confirmed by our theoretical results (solid curve), which was obtained by using a sech^2 pulse profile and integrate Eq. (7.2) over the pulse width.

From Fig. 7.35, the fact that the 30 ps pulses do not induce switching at the same average power as the 330 fs pulses eliminates the possibility that the switching is due to thermally induced refractive index changes. Furthermore, this is confirmed by the symmetrical spectral broadening in the SPM measurements and the fact that n_2 measurements from the device are consistent with our SPM results and those of reference [30].

In summary, an ultrafast all-optical switching in an integrated asymmetric Mach-Zehnder interferometer has been demonstrated by exploiting the nonresonant nonlinearity in $Ga_{0.82}Al_{0.18}As$ for photon energies below half the band gap. A relative switching fraction of more than 80% has been achieved using 330 fs pulses at around 1.55 μm from a coupled-cavity mode-locked colour centre laser.

7.9 Conclusions:

In this chapter, the operation mechanism and theoretical modelling of the single-mode, AM-ZI were described, using the local normal-mode description and scattering matrix model, respectively. The linear characterisation of the AM-ZI was also investigated, this included the measurement of the propagation loss of the Y-junction and bend waveguides. Finally, the switching action of the AM-ZI was examined using the electro-optic effects and intensity dependent refractive index change in GaAs/GaAlAs materials.

The operation of the nonlinear AM-ZI switch which utilises the resonant nonlinear effects in GaAs/GaAlAs SQW and the nonresonant nonlinear effect in GaAlAs were successfully demonstrated. In the resonant device, a switching of only 10% at an input peak intensity of ≈ 0.25 GW.cm^{-2} was achieved. The poor switching performance of the device was due to the absorption saturation effect. In the nonresonant nonlinear device, a switching of more that 80% at an input peak intensity of 3.92 GW.cm^{-2} was achieved. The later device operated at a photon energy below half the band gap of the GaAlAs material, at the wavelength of the low loss telecommunication window of 1.55 μm.

References:

[1] W.E. Martin, "*A new waveguide/modulator for integrated optics*", Appl. Phys. Lett., vol. 26, p. 562 (1975).

[2] F.J. Leonberger, C.E. Woodward and D.L. Spears, "*Design and development of high-speed electro-optic A/D converter*", IEEE Trans. Circuits Syst., vol. CA-26, p. 1125 (1979).

[3] F.J. Leonberger, "*High speed operation of LiNbO$_3$ electro-optic interferometric waveguide modulators*", Opt. Lett., vol. 5, p. 312 (1980).

[4] Izutsu Masayuki, Nakai Yoshihami and Tadasi Sueta, "*Operation mechanism of the single mode optical waveguide Y-junction*", Opt. Lett., vol. 7, p. 136 (1982).

[5] R.H. Rediker and F.J. Leonberger, "*Analysis of integrated optics near 3dB coupler and Mach-Zehnder interferometric modulator using port scattering matrix*", IEEE of QE, vol. QE-18, p. 1813 (1982).

[6] B.S. Bhumbra, "*Nonlinear optical waveguide devices in GaAs/GaAlAs*", Ph.D. Thesis, University of Glasgow (1990).

[7] H. Yajima, "*Theory and applications of dielectric branching waveguides*", Presented at the Symposium on Optical and Acoustical Micro-Electronics Polytechnic Institute of New York, p. 339 (1974).

[8] H. Yajima, "*Coupled mode analysis of dielectric planar branching waveguides*", IEEE J. of Quantum Electron.,Vol. QE-14, p. 749 (1978).

[9] G.I. Stegeman, "*Nonlinear wave in solid state physics*", NATO ASI Series Plenum Press (1990).

[10] D.A.B. Miller, D.S. Chemla, T.C. Damen, A.C. Gossard, W. Wiegmann, T.H. Wood and C.A. Burrus, "*Electric field dependence of optical absorption near the band gap of quantum well structures*", Phys. Rev. B, Vol. 32, p. 1043 (1985).

[11] P. LiKamWa, A. Miller, J.S. Roberts and P.N. Robson, "*130 ps recovery of all-optical switching in a GaAs multiquantum well directional coupler*", Appl. Phys. Lett., Vol. 58, p. 2055 (1991).

[12] R.A. Soref, D.L. McDaniel, Jr. and B.R. Bennett, "*Guided-wave intensity modulators using amplitude- and -phase perturbations*", J. Lightwave Tech., Vol. 6, p. 437 (1988).

[13] M. Miyagi and S. Nishida, "*Bending losses od dielectric waveguides for integrated optics*", J. Opt. Soc. Am., Vol. 68, p. 316 (1978).

[14] H.F. Taylor, "*Power loss at directional change in dielectric waveguides*", Appl. Opt., Vol. 13, p. 642 (1974).

[15] E.A.H. Marcatili, "*bends in optical dielectric guides*", Bell Syst. Tech. j., Vol. 48, p. 2103 (1969).

[16] M. Heiblum and J.H. Harris, "*Analysis of curved optical waveguides by conformal transformation*", IEEE J. Quantum Electron., Vol. QE-11, p. 75 (1975).

[17] L.D. Hutcheson, I.A. White and J.J. Burke, "*Comparison of bending losses in integrated optical circuits*", Optics Lett., Vol. 5, p. 276 (1980).

[18] H. Sasaki and N. Mikoshiba, "*Normalised power transmission in single mode optical branching waveguides*", Electron. Lett., Vol. 17, p. 136 (1981).

[19] H. Sasaki and I. Anderson, "*Theoretical and experimental studies on active Y-junctions in optical waveguides*", IEEE J. of Quantum Electron., Vol. QE-14, p. 883 (1978).

[20] C.G. Someda, "*Simple way to understand the behaviour of an optical Y-junction*", Electron. Lett., Vol. 20, p. 349 (1984).

[21] T.J. Cullen, C.D.W. Wilkinson, "*Radiation losses from single-mode optical Y-junctions formed by silver-ion exchange in Glass*", J. Opt. Soc. Am., Vol. 10, p. 134 (1984).

[22] T.J. Cullen, "*Y-junction analysis*", Ph.D. Tesis, University of Glasgow (1986).

239

[23] I. Anderson, *"Transmission performance of Y-junctions in planar dielectric waveguide"*, Microwaves, Optics and Acoustics, Vol. 2, p. 7 (1978).

[24] J.J. Isaac, *"An integrated optical pressure sensor in the GaAs/GaAlAs ternary system"*, Ph.D. Thesis, University of Glasgow (1987).

[25] D. Marcuse, *"Radiation losses of tapered dielectric slab waveguides"*, Bell Syst. Tech. J., Vol. 49, p. 273 (1970).

[26] J.A. Jennings, *"Electro-optic effects in multiple quantum well GaAs/GaAlAs stripe waveguides"*, Ph.D. Thesis, University of Glasgow (1991).

[27] D.A.B. Miller, D.S. Chemla, T.C. Damen, A.C. Gossard, W. Wiegman, T.H. Wood and C.A. Burrus, *"Band-edge electroabsorption in quantum well structures: The Quantum Confined Stark Effect"*, Phys. Rev. Lett., Vol. 53, p. 2173 (1984).

[28] S.H. Park, J.F. Morhange, A.D. Jeffery, R.A. Morgan, A. Chaven-Pirson, H.M. Gibbs, S.W. Koch, N. Peyghambrian, M. Derstine, A.C. Gossard, J.H. English and W. Weigman, *"Measurements of GaAs/GaAlAs multiple quantum wells and bulk GaAs"*, Appl. Phys. Lett., Vol. 52, p. 1201 (1988).

[29] N. Finlayson, W.C. Banyai, C.T. Seaton, G.I. Stegeman, M. O'Neil, T.J. Cullen and C.N. Ironside, *"Optical nonlinearities in CdS_xSe_{1-x} doped glass waveguides"*, J. Opt. Soc. Am. B, Vol. 6, p. 675 (1989).

[30] S.T. Ho, C.E. Soccolich, M.N. Islam, W.S. Hobson, A.F.J. Levi and R.E. Slusher, *"Large nonlinear phase shifts in low-loss $Al_xGa_{1-x}As$ waveguides near half-gap"*, Appl. Phys. Lett., Vol. 59, p. 2558 (1991).

[31] J.S. Aitchison, A.H. Kean, C.N. Ironside, A. Villeneuve and G.I. Stegeman, *"Ultrafast all-optical switching in $Al_xGa_{1-x}As$ directional coupler in 1.55 mm spectral region"*, Electronics Lett., Vol. 27, p. 1709 (1991).

Chapter 8

Nonlinear Integrated Directional Coupler

8.1 Introduction:

In this chapter two types of nonlinear directional couplers are investigated, namely the resonant and nonresonant version. In the resonant directional coupler, an electric field was used to shorten the recovery time of the resonant nonlinearity by sweeping the photogenerated carriers from the GaAs/GaAlAs QWs region.

8.2 Operational Mechanism and Theoretical Modelling of the Directional Coupler:

When two identical, parallel waveguides are separated from each other by a small distance, the propagating electromagnetic wave in guide 1 will be coupled into guide 2 and vice-versa. The transfer of energy between the two guides occurs only if the separation is small enough for the evanescent fields of the waves in the two guides to overlap, and the phase matching condition of equal propagation constants $\beta_1=\beta_2=\beta$ is satisfied. The coupling action in a lossless linear directional coupler (LDC) can be modelled using coupled mode theory[1].

Consider to waves of amplitudes a_1 and a_2 propagating in guide 1 and guide 2, which in the absence of coupling have propagation constants β_1 and β_2. For such propagating waves we can write:

$$\frac{da_1}{dz} = -j\beta_1 a_1 \qquad \frac{da_2}{dz} = -j\beta_2 a_2$$

As the two guides are brought close to each other, such that the evanescent fields overlap, the amplitude a_1 will be altered by a_2 and vice-versa, leading to:

$$\frac{da_1}{dz} = -j\beta_1 a_1 + K_{12} a_2 \qquad (8.1)$$

$$\frac{da_2}{dz} = -j\beta_2 a_2 + K_{21} a_1 \qquad (8.2)$$

241

where K_{ij} is the coupling coefficient between the two guides. The behaviour of the LDC can be modelled by solving these two coupled mode equations. Assuming an initial conditions such that, an optical power $|a_1(0)|^2=P_0$ is coupled into guide 1 and $|a_2(0)|^2=0$. Therefore, the power emerging from guide 1 and guide 2, at a length L are given by[1]:

$$P_1(L) = P_0 \left| \frac{K}{\sqrt{(K^2 - \delta^2)}} \right|^2 . \cos^2\left[\sqrt{(K^2 - \delta^2)} . L\right] \qquad (8.3)$$

$$P_2(L) = P_0 - P_1(L) \qquad (8.4)$$

where δ is the mismatch between the two guides, $P_1(L)=|a_1(L)|^2$ and $P_2(L)=|a_2(L)|^2$. If $\delta=0$ (i.e. the two waveguides are identical $\beta_1=\beta_2=\beta$) then the optical power in guide 1 will be transfered to guide 2 after a distance L_c, known as the coupling length, where $KL_c=\pi/2$ or:

$$L_c = \frac{\pi}{2K} \qquad (8.5)$$

The optical power will be transfered back to guide 1 after a distance $2L_c$. Eqs. 3 and 4 shows that if $\delta\neq0$ (i.e. the two guides are not identical $\beta_1\neq\beta_2$) then a complete transfer of power between the two waveguides is not possible.

The coupling coefficient K between the two waveguides can be expressed in terms of the physical dimensions of the directional coupler[1]. This was achieved by evaluating the overlap integral of the fields in the two waveguides and results in:

$$K = \frac{2k_0^2\left(n_g^2 - n_1^2\right)k_1\cos^2\left(k_2W/2\right)}{\beta\left(\frac{W}{2} + \frac{1}{k_1}\right)\left(k_1^2 + k_2^2\right)} e^{-k_1(s-w)} \qquad (8.6)$$

where

$$k_1^2 = \beta^2 - n_1^2 k_0^2 \qquad\qquad k_2^2 = n_g^2 k_0^2 - \beta^2$$

where n_g and n_1 are the refractive indices of the guiding and cladding regions respectively, W is the width of the coupled waveguides and s is the spacing between them. Equation 6 shows the dependence of the coupling coefficient, K, on the separation between the two coupled guides, s, as well as the step index difference between the guiding and cladding regions ($\Delta n=n_g-n_1$). In a directional coupler with rib waveguides, the coupling coefficient can be evaluated by converting the two-dimensional, stripe waveguide, structure into one-dimensional, slab waveguide, structure using the effective index method (EIM).

8.2.1 Switching Operation of the Directional Coupler:

The coupling length, L_c of a directional coupler can be obtained by cleaving and testing the samples sequentially until the device is at a cross-over state $\otimes$ (i.e. the input light in guide1 emerges from guide2 at the output). Once a coupler which is in the crossed state is realised, it is then possible to make the device switch. This can be achieved by perturbing one of the guides, e.g. changing the refractive index, Δn, so that the phase-match condition is broken. Switching of a directional coupler has been demonstrated [2] using electro-optic effect, by applying a revers bias to one of the waveguides.

Another way of causing the directional coupler to switch is by means of intensity dependent refractive index change [3,4] $\Delta n=n_2 I$. Fig. 8.1 shows a schematic diagram of a nonlinear directional coupler. One of many application of such a device is that it can be used to control a stream of input pulses by another control pulses. When there is no control signal, the device is normally in the crossed state, however, when the control signal is present, if the intensity of the light is sufficiently high to change the refractive index then the directional coupler will switch to the bar state. If the device is designed so that the required intensity level of the control pulse is the same as that of the input pulse, then the device becomes an all-optical logic gate.
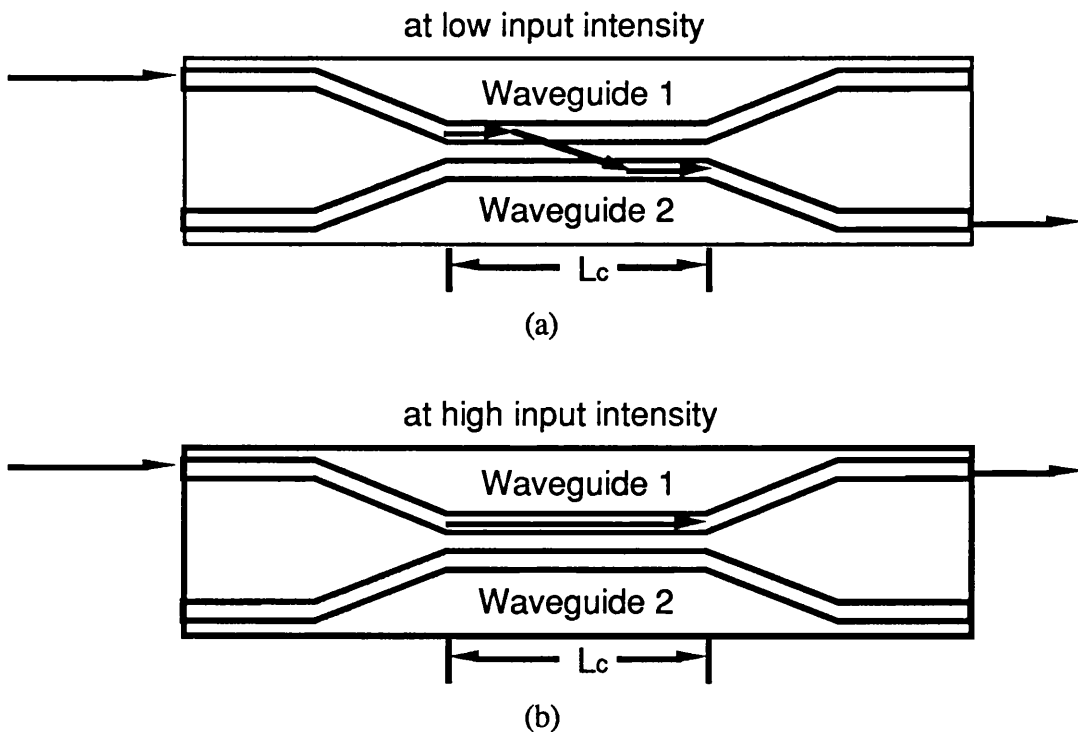
Fig. 8.1 *Schematic diagram of a nonlinear directional coupler with a coupling length* L_c a) *at low input light intensity* b) *at high input light intensity*.

243

8.2.2 Theoretical Modelling of the Nonlinear Directional Coupler:

To model the nonlinear directional coupler, extra terms representing the nonlinearity, are included in the coupled mode equations (8.1) and (8.2). The nonlinear refractive index change can be expressed as:

$$\Delta n = n_2 I \qquad or \qquad \Delta \beta = n_2 k_0 I$$

hence, replacing β by $(\beta + \Delta \beta)$ in Eq. (8.1) and (8.2) we obtain:

$$\frac{da_1}{dz} = -j\beta a_1 + K a_2 - j n_2 k_0 |a_1|^2 a_1 \tag{8.7}$$

$$\frac{da_2}{dz} = -j\beta a_2 + K a_1 - j n_2 k_0 |a_2|^2 a_2 \tag{8.8}$$

In these equations $\beta_1 = \beta_2 = \beta$, the two waveguides are identical. Jensen [5] solved these equations analytically in the form of Jacobi functions. An input critical power, P_c, required to cause the output power to split equally between the two guides of a directional coupler, with length L_c, is given by:

$$P_c = \frac{A_{eff} \lambda_0}{n_2 L_c} \tag{8.9}$$

In a resonant nonlinear directional coupler, extra terms associated with the absorption losses, α, need to be included into Eqs. (8.7) and (8.8), resulting in:

$$\frac{da_1}{dz} = -j\beta a_1 - \frac{\alpha a_1}{2} + K a_2 - j n_2 k_0 |a_1|^2 a_1 \tag{8.10}$$

$$\frac{da_2}{dz} = -j\beta a_2 - \frac{\alpha a_2}{2} + K a_1 - j n_2 k_0 |a_2|^2 a_2 \tag{8.11}$$

a_1 and a_2 have solutions of the form:

$$a_1 = A_1(z) e^{-j\phi_1(z)} \tag{8.12}$$

$$a_2 = A_2(z) e^{-j\phi_2(z)} \tag{8.13}$$

Substituting Eqs. (8.12) and (8.13) into Eqs. (8.10) and (8.11), then separating the real and imaginary parts we obtain the following equations:

$$\frac{dA_1}{dz} = -\tfrac{1}{2}\alpha A_1 + KA_2\sin(\phi_2 - \phi_1) \qquad\qquad (8.14)$$

$$\frac{dA_2}{dz} = -\tfrac{1}{2}\alpha A_2 + KA_1\sin(\phi_2 - \phi_1) \qquad\qquad (8.15)$$

$$\frac{d\phi_1}{dz} = \beta - \frac{KA_2}{A_1}\cos(\phi_2 - \phi_1) + n_2 k_0 |A_1|^2 \qquad (8.16)$$

$$\frac{d\phi_2}{dz} = \beta - \frac{KA_1}{A_2}\cos(\phi_2 - \phi_1) + n_2 k_0 |A_2|^2 \qquad (8.17)$$

Eqs. (8.16) and (8.17) can be reduced further to:

$$\frac{d}{dz}(\phi_2 - \phi_1) = \left(A_2^2 - A_1^2\right)\left[\frac{K\cos(\phi_2 - \phi_1)}{A_1 A_2} + n_2 k_0\right] \qquad (8.18)$$

These equations have been solved numerically using a 4$^{\text{th}}$ order Runge-Kutta integration method [6], taking small increments δz to construct the behaviour of the wave propagation inside the directional coupler under different conditions of input power excitation.

The accuracy of this numerical method has been checked by simulating a linear directional coupler ($\alpha=n_2=0$), i.e. linear lossless device. The width of the two coupled waveguides was 3 μm and separated by 3 μm. The input initial conditions at z=0 were $A_1(0)=1$, $A_2(0)=0$, $\phi_1(0)=0$ and $\phi_2(0)=-\pi/2$. As expected, the amplitudes A_1 and A_2 were changing as a cos and sin functions, respectively, as a function of the propagation direction, z, as shown in Fig. 8.2. The accuracy of this numerical method was confirmed by the result obtained for, L_c, which was equal to that obtained from Eqs. (8.6) and (8.5).
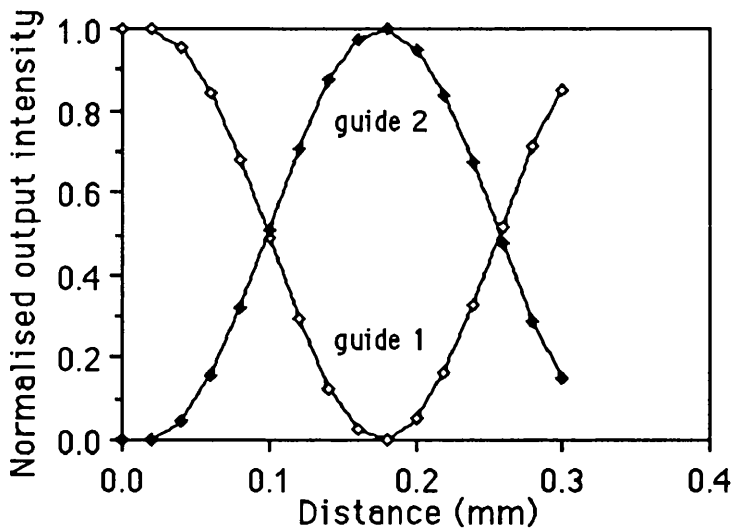
Fig. 8.2 A plot of the theoretical calculations of the normalised output transmission of waveguide 1 and waveguide 2 of a lossless linear directional coupler ($\alpha=n_2=0$) as a function of the coupling length L.

245

The nonresonant nonlinear directional coupler has been simulated by assuming $\alpha=0$ but $n_2 \neq 0$. Fig. 8.3 shows the predicted output transmission of guides 1 and 2 as a function of the coupling length, for two different input intensities, 0.5 mW and 1 mW.
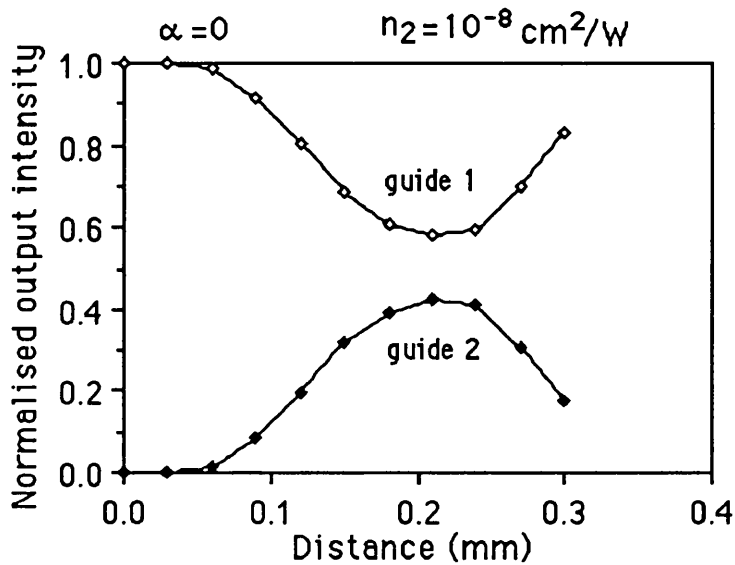
(a)
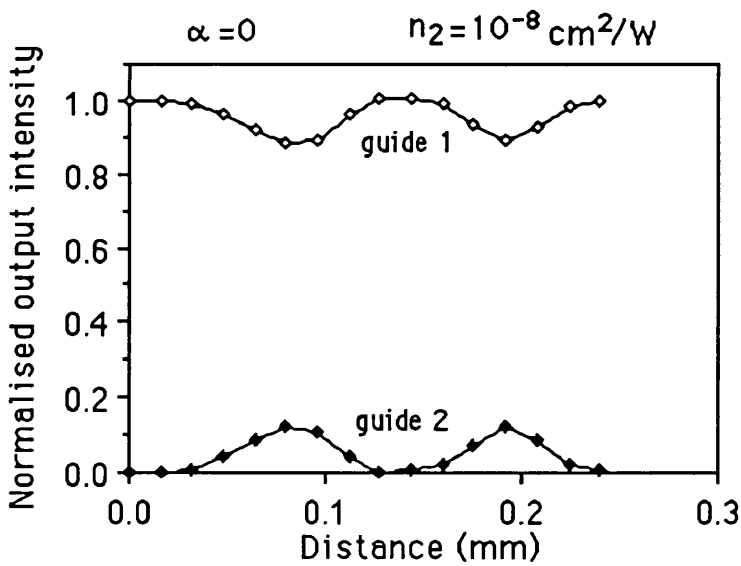
(b)

Fig 8.3 *A plot of the theoretical calculations of the normalised output transmission of waveguide 1 and waveguide 2 of a lossless nonlinear directional coupler* ($\alpha=0$, $n_2=10^{-8}$ cm²/W) *as a function of the coupling length* L, *at two different input optical beam intensities* a) 0.5 mW *and* b) 1 mW.

As the input light intensity increases a phase mismatch is introduced to the directional coupler due to the intensity dependent refractive index changes, $\Delta n = n_2 I$. For a directional coupler with a coupling length L_c the output transmission of the two coupled waveguides is extracted and plotted as a function of the input light intensity. Fig. 8.4 shows the output transmissions $|A_1(L_c)|^2$, waveguide 1, and $|A_2(L_c)|^2$, waveguide 2, as a function of the input intensity into waveguide 1 $|A_1(0)|^2$. At low input intensity the device is on a cross state, as the input intensity increases the device switch to the bar state.
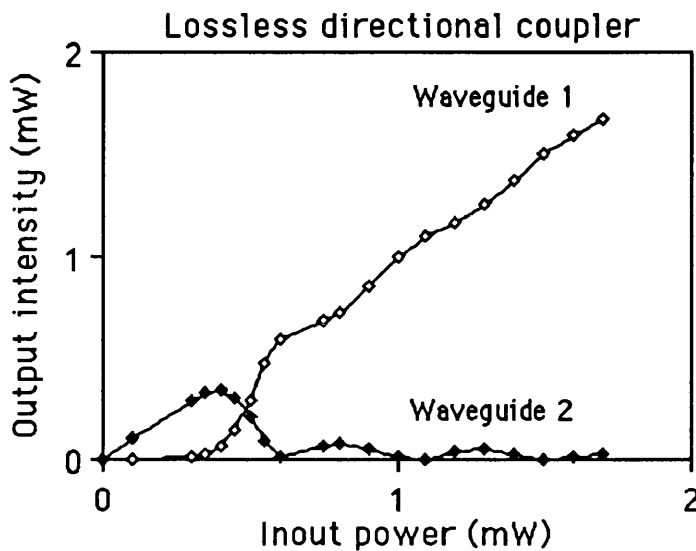
Fig. 8.4 *A plot of the theoretical calculations of the normalised output response of waveguide 1 and waveguide 2 of a lossless nonlinear directional coupler* ($\alpha=0$, $n_2=10^{-8}$ cm^2/W) *as a function of the input light intensity into waveguide 1. The device coupliong length is* L_c.

Again the numerical integration is performed on a nonlinear directional coupler with absorption ($\alpha \neq 0$ and $n_2 \neq 0$), using the same initial conditions. Fig. 8.5 shows the output transmissions of waveguide 1, $|A_1(L_c)|^2$, and waveguide 2, $|A_2(L_c)|^2$, as a function of the length L, at two different input intensities, 0.5 mW and 1 mW. Fig. 8.6 shows the extracted output transmission of the two coupled waveguides, for the coupling length L_c, as a function of the input power into waveguide 1. At low excitation power, the output power distribution of the two waveguides varies from a fully crossed-over state to an almost equal power division when the input power is increased to ≈ 1.1 mW.
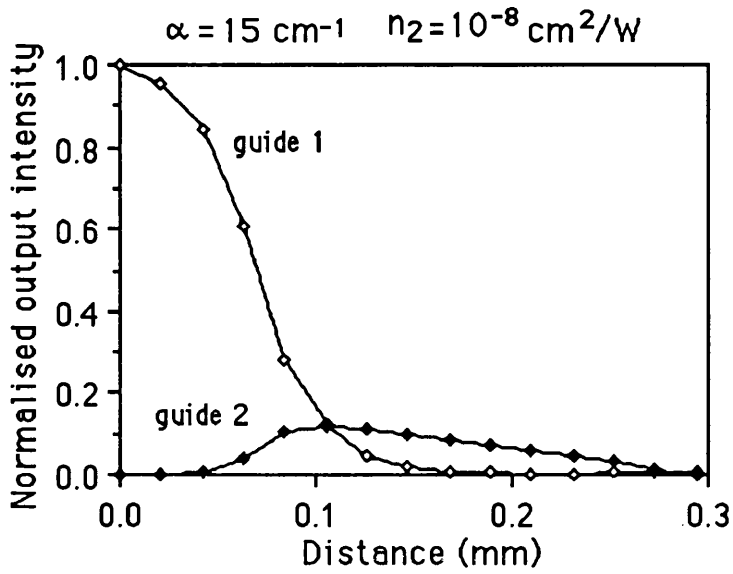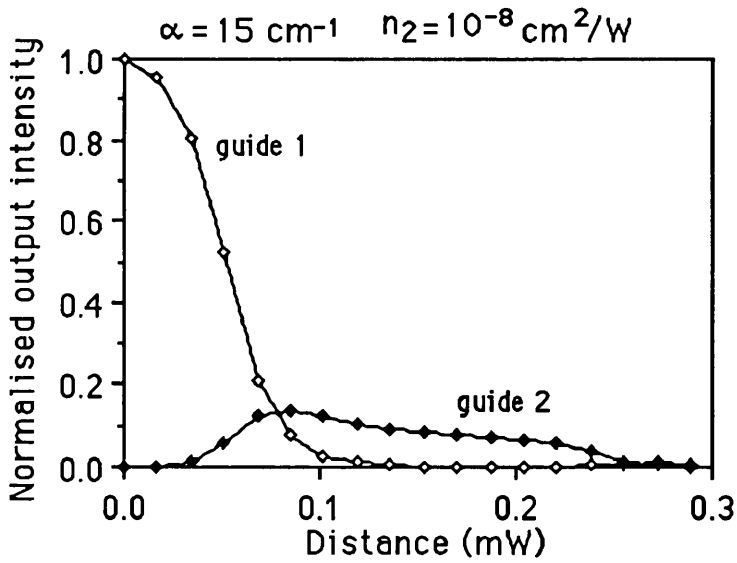
Fig. 8.5 *A plot of the theoretical calculations of the normalised output transmission of waveguide 1 and waveguide 2 of a lossly nonlinear directional coupler* (α=15 cm^{-1}, n$_2$=10^{-8} cm^2/W) *as a function of the coupling length* L, *at two different input optical beam intensities* a) 0.5 mW *and* b) 1 mW.

Fig. 8.6 *A plot of the theoretical calculations of the normalised output response of waveguide 1 and waveguide 2 of a lossy nonlinear directional coupler (α=15 cm^{-1}, n_2=10^{-8} cm^2/W) as a function of the input light intensity into waveguide 1. The device coupliong length is* L_c.

From these results it is clear that in a lossy directional coupler a higher switching power level is required than in a lossless device, having the same value of n_2. This is due to the progressive attenuation of the wave as it propagates along the device. Although the nonlinearity is large at the input, it decreases exponentially with distance from the input. Thus although the coupling is destroyed at the input section of the device, the remaining section is still coupled and some of the energy is still transferred from guide 1 to guide 2. However, because the coupling length of the remaining section is now less than L_c, the device is not fully in the cross-over state and switching effect can still be observed. On the other hand a complete switch-over is harder to achieve and according to the numerical simulation, some residual power will remain in the coupled waveguide regardless of the level of the input pumping power.

8.2.3 Theoretical Modelling of the Electro-Optic Directional Coupler:

Fig. 8.7 shows a schematic diagram of an electro-optic directional coupler, an electrode of a length L was deposited on the top of the waveguide. The switching operation of the device was obtained by means of the electro-optic effect in GaAs/GaAlAs. The idea behind employing the electro-optic effect in our all-optical nonlinear directional coupler was for two reasons: firstly to obtain the transfer coupling length (L_c=π/2K) by changing the

249

optical path length via the electro-optic effect, secondly, the applied electric field may shorten the recovery time of the resonant nonlinearity by sweeping out the photogenerated carriers in the GaAs/GaAlAs guiding region [7].
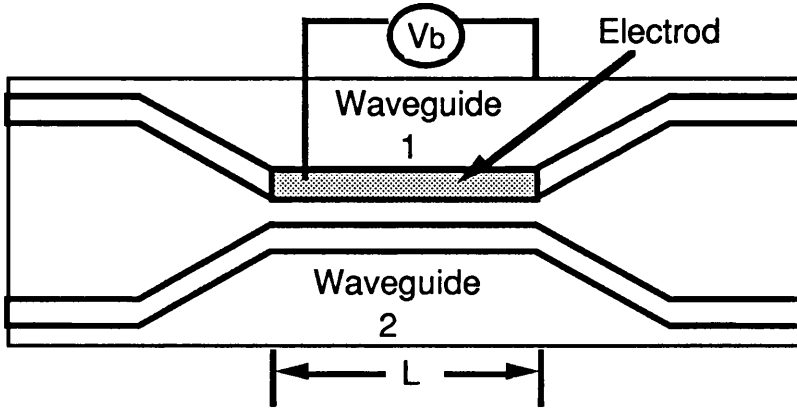
Fig. 8.7 *Schematic diagram of an electro-optic directional coupler with a coupling length* L. *The reverse bias voltage* V$_b$*is applied across waveguide 1.*

As we have seen in chapter 6, when an electric field is applied across the GaAs/GaAlAs QWs region, two effects emerge, depending on the operating wavelength. These are the Pockels effect, at photon energy well below the QWs absorption edge, and the QCSE, at photon energy close to the QWs absorption edge. The two effects can be comparable in size when the operating wavelength is between the two regimes.

In the analysis of such a device, the applied electric field across the length, L, produced a uniform perturbation to the mode of the waveguide over that length. This perturbation produces a phase retardation and amplitude change $\Delta\beta + i\Delta\alpha/2$. Therefore, the complex quantity $\Delta\beta + i\Delta\alpha/2$ has been introduced into the coupled mode equations, and result in the following response functions [8]:

$$P_1 / P_0 = e^{-\Delta\alpha L/2} \left| \cos gL + i(b/g) \sin gL \right|^2 \qquad (8.19)$$

$$P_2 / P_0 = e^{-\Delta\alpha L/2} \left| i(K/g) \sin gL \right|^2 \qquad (8.20)$$

where

$$g^2 = b^2 + K^2$$

$$b = \pm \left(\Delta\beta / 2 + i\Delta\alpha / 4 \right)$$

With reference to Fig. 8.7, the plus sign in, b, denotes a perturbation across waveguide 1 while the minus sign indicates a perturbation across waveguide 2.

As in the case of the electro-optic Mach-Zehnder interferometer in section 7.5, a parameter $\rho=2\Delta\beta/\Delta\alpha$, which provides a measure of the relative strength of the phase verses the amplitude modulation at a given drive level, is introduced in Eq. 8.19 and Eq. 8.20 and for $KL=m\pi$, this gives [8]:

$$P_1 / P_0 = e^{-\Delta\beta L / \rho} \left| \cos gL \pm [(i-1/\rho) \right.$$
$$\left. (\Delta\beta L) / (2gL)] \sin gL \right|^2 \qquad (8.21)$$

$$P_2 / P_0 = e^{-\Delta\beta L / \rho} \left| (im\pi / gL) \sin gL \right|^2 \qquad (8.22)$$

where

$$(gL)^2 = (1 + i/\rho)^2 (\Delta\beta L / 2)^2 + (m\pi)^2$$

Fig. 8.8 shows the transmission response, P_1/P_0 and P_2/P_0, as a function of the change in the optical coupling length, $\Delta\beta L$, for $\rho=3$, 15 and 500. The initial state is at the cross-over, i.e. $KL=m\pi=\pi/2$. In Fig. 8.8(a) the electric field is applied across waveguide 1 and in Fig. 8.8(b) is applied across waveguide 2. The $\rho=500$, device reaches the straight-through state at a value $\Delta\beta L=\sqrt{3}.\pi$.

Next, a directional coupler in the bar state, i.e. $KL=m\pi=\pi$, was considered. Fig. 8.9 shows the transmission P_1/P_0 and P_2/P_0 of the two coupled waveguides as a function of $\Delta\beta L$, for $\rho=3$, 15 and 500. In Fig. 8.9(a) the electric field is applied across waveguide 1 and in Fig. 8.9(b) is applied across waveguide 2. The $\rho=500$ device becomes a ≈ 3 dB coupler at $\Delta\beta L=2\pi$.

From these results the loss component $\Delta\alpha$ affects the coupled modes such that, one mode becomes more localised in the perturbed lossy guide and its attenuation increases. While the other mode becomes more localised in the more transparent unperturbed guide. The localisation of the modes within their guides is due to the phase mismatch between the two guides caused by the electro-optic refractive index change. In conclusion, applying the electric field on waveguide 2 provides more oscillations without a significant loss of the input optical power.

251

KL=mπ = π/2

Normalised output transmission

P_2/P_0

ρ=500

P_1/P_0

ρ=15

ρ=3

P_0 ⟶ ⟶ P_1
⟶ P_2

ΔβL (radians)

(a)

KL=mπ = π/2

Normalised output transmission

ρ=500

ρ=15

ρ=3

P_1/P_0

P_2/P_0

P_0 ⟶ ⟶ P_1
⟶ P_2

ΔβL (radians)
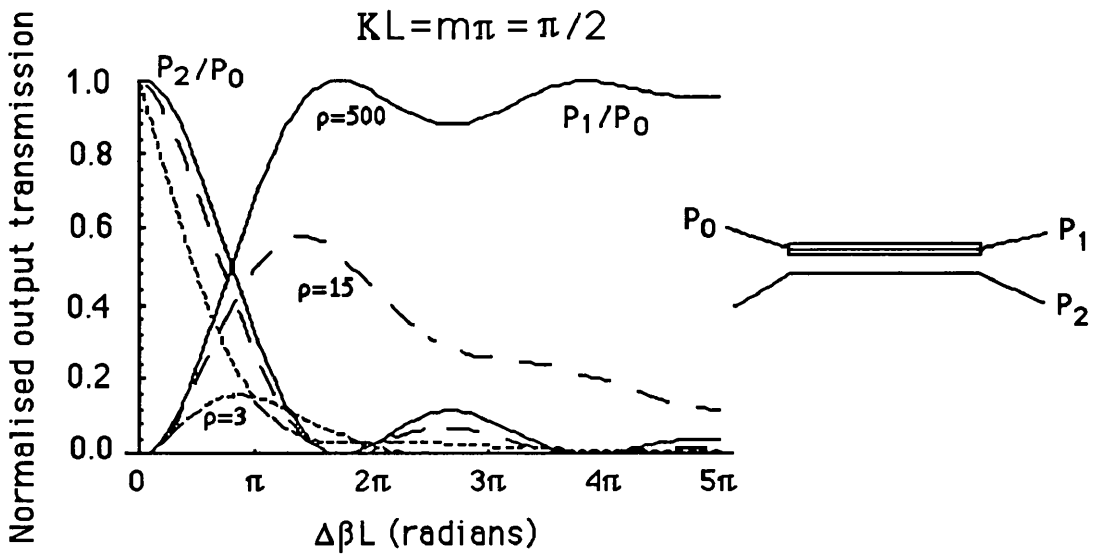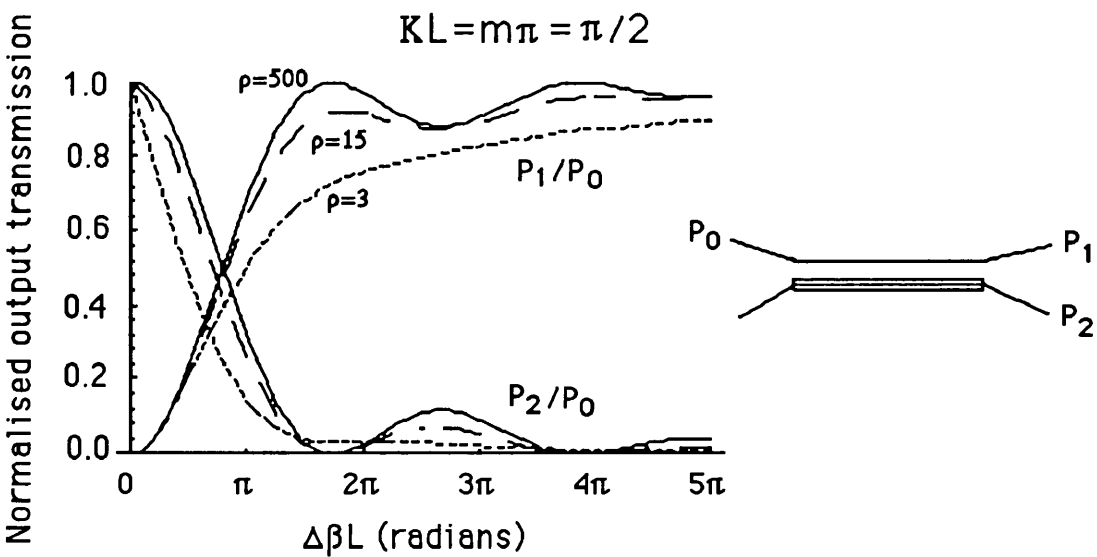
(b)

Fig. 8.8 *The normalised output response of an electro-optic directional coupler as a function of the phase change* ΔβL, *for three values of* ρ=3, 15 *and* 500 (ρ=2Δβ/Δα). a) *the electric field is applied across waveguide 1 and* b) *is applied across waveguide 2. The initial state of the device* (Vb=0) *is at the cross-state.*

252
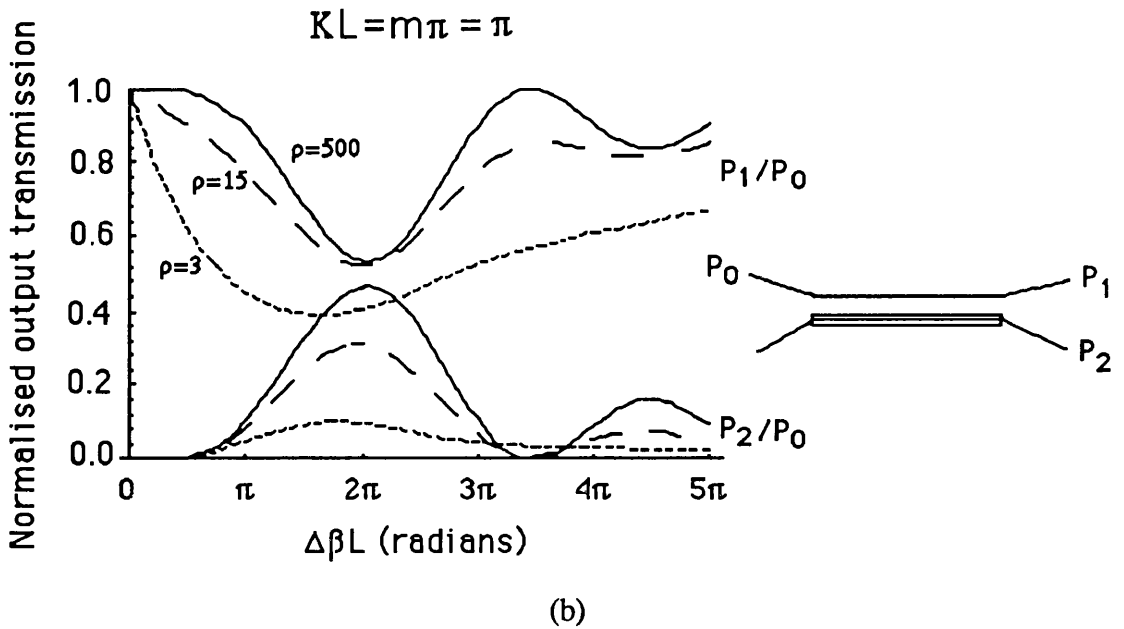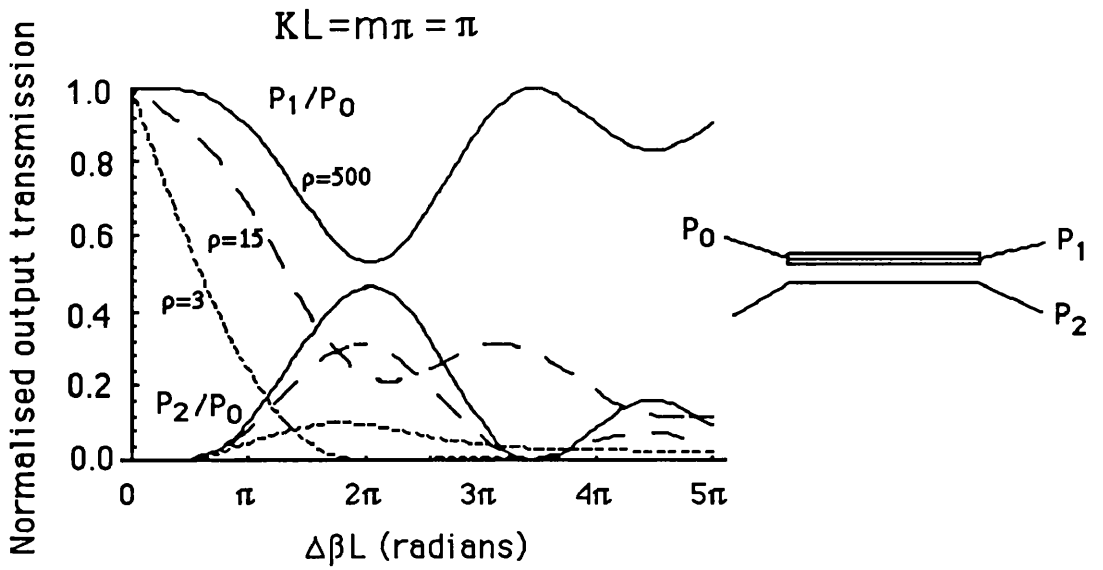
Fig. 8.9 *The normalised output response of an electro-optic directional coupler as a function of the phase change* $\Delta\beta L$, *for three values of* $\rho=3$, 15 *and* 500 ($\rho=2\Delta\beta/\Delta\alpha$). a) *the electric field is applied across waveguide 1 and* b) *is applied across waveguide 2. The initial state of the device* ($V_b=0$) *is at the bar-state.*

8.3 Fabrication of Electro-Optic Directional Coupler:

The material used to demonstrate the resonant nonlinear directional coupler was A163 GaAs/GaAlAs MQW, described in section 4.3. This wafer exhibited a good electro-optic properties, which made it sutable for the device proposed. An existing chrome mask was

used, it consisted of a set of five couplers and five straight waveguides, the directional couplers linewidth was 3 μm and separated by 3 μm spacing. The couplers were designed such that only one guide was excited at the input facet, by extending it to the edge of the mask. The second guide started at some distance from the edge of the mask. The interaction length of each coupler differing in steps of 0.25 mm. At intervals along each guide, pads of 80 μm square were in contact with the guides, to allow the fabrication of an active devices.

A positive image of the dark-field chrome mask was transfered into a S1400-17 photoresist film using standard optical lithography. A p-type ohmic contact (Au-Ge-Ni-Au) followed by a layer of NiCr film, as an etching mask, were deposited on the top of the patterned samples. Lift-off was used to leave the samples patterned with stripes of metal. The samples were etched, using RIE with $SiCl_4$ gas, to a depth of ≈ 1.75 μm, and hence, an acceptable electrical isolation between the two waveguides was obtained. The isolation was later enhanced by exposing the etched samples to a hydrogen plasma, as described in section 7.7.1. The NiCr mask was subsequently removed with wet etching, using 1:1 $HCl:H_2O$ for 45 sec. Fig. 8.10 shows an SEM micrograph of a directional coupler.
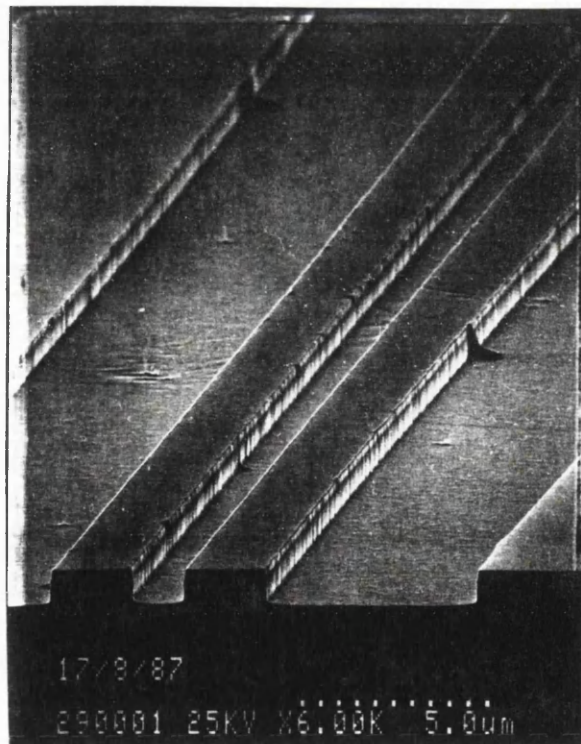
Fig. 8.10 *SEM micrograph of a GaAs/GaAlAs MQW directional coupler waveguide.*

The coupling coefficient and length, in the passive directional coupler, were calculated for both the TE and TM polarization. This was achieved by first converting the two-dimensional rib waveguides into one-dimensional slab waveguides using the EIM, and then using Eq. (8.6) and Eq. (8.5) to calculate the coupling coefficient and the coupling length. The effective refractive index of the MQWs layer was calculated using Eqs. (3.31) and (3.32), for the TE- and TM-modes respectively.

At a wavelength $\lambda=1.15$ μm, well below the MQWs absorption edge, the coupling coefficient and coupling length, for the TE-mode were K=3.97 cm $^{-1}$ and L_c=3.9 mm, and for the TM-mode were K=5.37 cm $^{-1}$ and L_c=2.9 mm.

At a wavelength $\lambda=0.857$ μm (close to the MQWs absorption edge) the coupling coefficient and coupling length, for the TE-mode, were K=6 cm $^{-1}$ and L_c=2.6 mm. For the TM-mode were K=6.8 cm $^{-1}$ and L_c=2.3 mm. The photon energy was only 60 meV below the hh-exciton for TE-mode, and 68 meV below the lh-exciton for the TM-mode.

All waveguides were fabricated with the direction of propagation along the crystalographic direction [1$\underline{1}$0], which yield in a maximum change in the electro-refractive index (see Eq. 2.29). The etched samples were then cleaved to a length of 3 mm and bonded onto a p.c.b. mount, with silver epoxy. Contacts to the individual devices were connected by ultrasonically bonded aluminium wire from the top pads to the p.c.b. mount. The coupling length of the five directional couplers were L=2.7 mm, 2.45 mm, 2.2 mm, 2mm and 1.73 mm, while the length of waveguide 1 was equal to the length of the sample.

8.4 Experimental Results and Discussions of the Directional Coupler:

The end-fire coupling system described in section 5.7.2 was used to characterise the couplers. The light sources were He-Ne, $\lambda=1.15$ μm, and the CW tunable Ti:sapphire lasers. The far-field of the outputs of the directional coupler and straight waveguides were examined using a C1000 Hamamatsu camera connected to a data logging computer. It was confirmed that they were single moded.

8.4.1 Electro-Optic Directional Coupler:

The active directional coupler was first tested at an optical wavelength $\lambda=1.15$ μm, well below the absorption edge of the MQWs of A163 material. Fig. 8.11 shows the output optical intensity distributions of the two coupled waveguides at three different reverse bias

255

voltages V_b=0, 6.5 V and 15 V. The coupling length was L=2.7 mm, and the bias voltage was applied across waveguide 2. With reference to Fig. 8.11, the initial state of the coupler (V_b=0) showed a power split ratio of 0.37:0.63 in waveguide 1 and waveguide 2 respectively. Equal splitting 0.49:0.51 was achieved with V_b=6.5 volts, and a switching of 30%, in both guides, was obtained at V_b=15 volts.
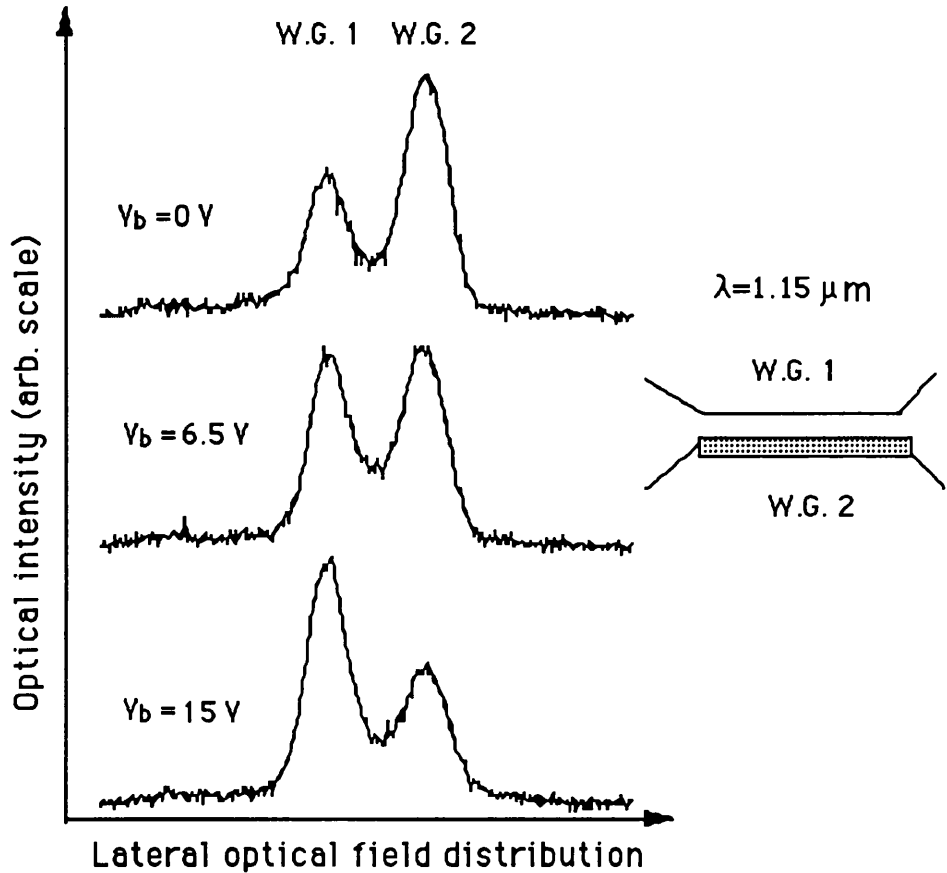
Fig. 8.11 *The output transverse field distribution of waveguide 1 and waveguide 2 of an electro-optic directional coupler at three different bias voltages* V_b=0, 6.5 V *and* 15 V. *The bias voltage was applied across waveguide 2 and the optical beam (λ=1.15 μm) was fed into waveguide 1. The waveguide rib width and height were 3 μm and 1.75 μm respectively and the coupling length L=2.7 mm.*

Similar switching results were obtained when the bias voltage V_b was applied across waveguide 1, but with less drive voltage. This was due to the difference in the length of the electrodes, waveguide 1 was longer than waveguide 2. The similar switching results confirm that there was no absorption change, i.e. $\Delta\alpha$=0 and only phase change via the Pockel's effect.

At a wavelength λ=0.857 μm (1.448 eV), close to the absorption edge of the MQWs of A163 material and ≈60 meV below the hh-exciton, the electro-absorption and refraction effects were both significant in the directional coupler with applied voltage V_b. Fig. 8.12 shows the optical intensity distribution of the output transmission of the two coupled waveguides at two bias voltages V_b=0 and 15 V. The bias voltage was applied across waveguide 2. The initial state of the device (V_b=0) showed a power split ratio of 0.485:0.515 in waveguide 1 and waveguide 2 respectively. A switching of ≈35% was achieved at V_b=15 volts.
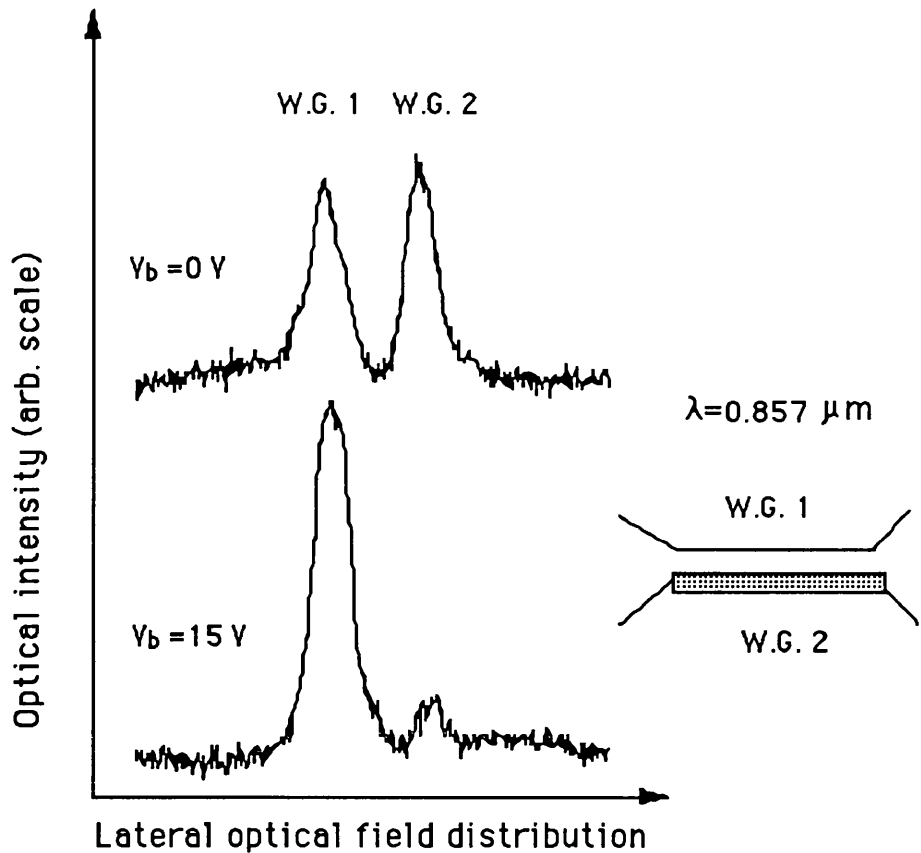
Fig. 8.12 *The output transverse field distribution of waveguide 1 and waveguide 2 of an electro-optic directional coupler at two different bias voltages* V_b=0, *and* 15 V. *The bias voltage was applied across waveguide 2 and the optical beam* (λ=0.857 μm) *was coupled into waveguide 1. The waveguide rib width and height were 3* μm *and* 1.75 μm *respectively and the coupling length* L=2.7 mm.

These measurements were repeated, but this time the bias voltage was applied across waveguide 1. Fig. 8.13 shows the intensity distributions of the two coupled guides, at two bias voltages. At V_b=5 volts, the split ratio was changed to 0.56:0.44 in waveguide 1 and

waveguide 2 respectively. A switching of ≈20% was obtained when the bias voltage increased to V_b=15 volts.
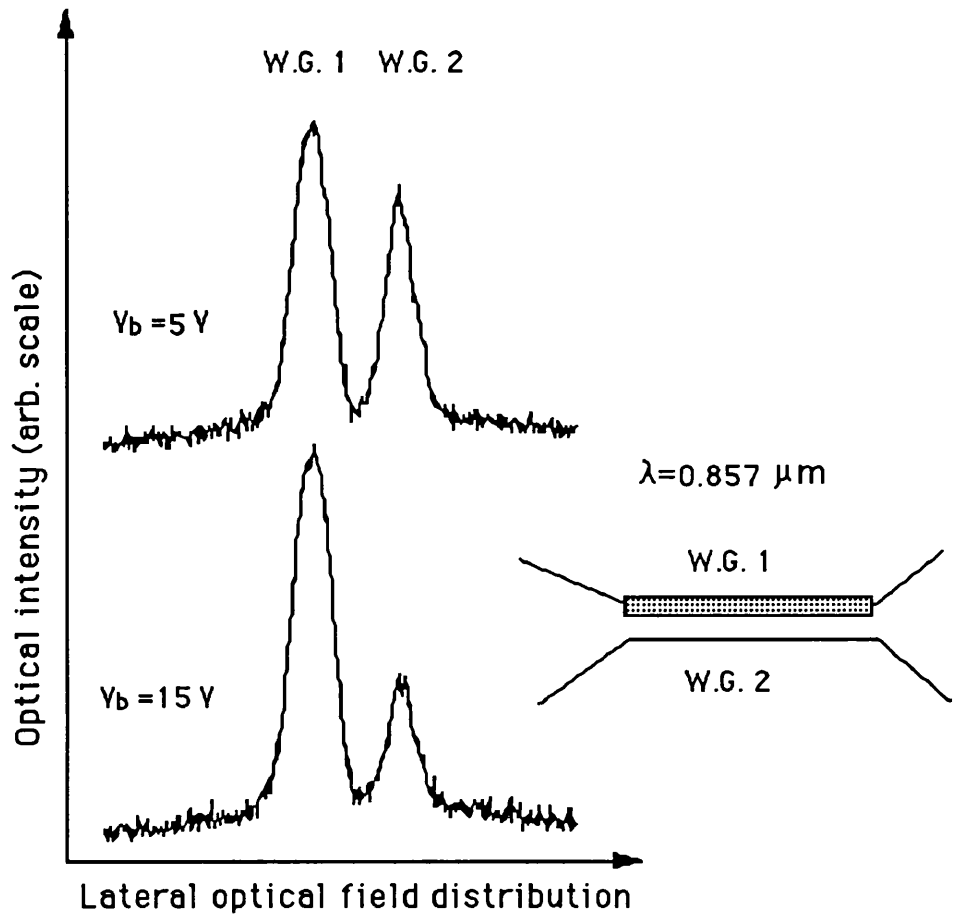
Fig. 8.13 *The output transverse field distribution of waveguide 1 and waveguide 2 of an electro-optic directional coupler at two different bias voltages* V_b=0, *and* 15 V. *The bias voltage was applied across waveguide 1 and the optical beam* (λ=0.857 μm) *was coupled into waveguide 1. The waveguide rib width and height were 3 μm and 1.75 μm respectively and the coupling length* L=2.7 mm.

Compaing the results of Fig. 8.12 and Fig. 8.13 it is clear that a smaller modulation depth was obtained when waveguide 1 was perturbed. This was due to the extra absorption loss, via electro-absorption effect, in the input section of the device before the two waveguides become close enough to be coupled.

A full characterisation of the switching operation of two electro-optic directional couplers are presented in the rest of this section. This was achieved by recording the output transmission of waveguide 1 and waveguide 2 simultanously, while the bias voltage V_b

258

was varied continuously across waveguide 2. The two outputs of the coupler were separated using an edge mirror to reflect each beam onto a Si-detector, after they were specially filtered.

Fig. 8.14 shows the normalised output transmission of waveguide 1 (P_1/P_0) and waveguide 2 (P_2/P_0) as a function of the bias voltage V_b, at a wavelength $\lambda=0.857$ μm. The square points are the experimental measurements and the sum of the two outputs is equal unity at all values of V_b. The solid lines are the calculated output response of the two coupled waveguides as a function of $\Delta\beta L$, top scale. They were obtained by using Eq. (8.21) and Eq. (8.22), the two parameters $\rho=2\Delta\beta/\Delta\alpha$ and $m=KL/\pi$ were adjusted to fit the experimental results; $\rho=25$ and $m=1.254$. From the m parameter, the coupling coefficient was $K=14.6$ cm^{-1}, for the coupling length of $L=2.7$ mm. This value of K is two times larger than the calculated $K=6$ cm^{-1} for the TE-mode, using Eq. (8.6). The calculated value of K is less accurate, for two reasone. Firstly, the estimated effective refractive index of the MQWs region, using Eq. (3.31) and Eq. (3.32), exclude the excitonic effect of the QWs. Secondly, Eq. (8.6) is applicable to a slab directional couplers and using EIM to convert the rib waveguide to a slab waveguide is an approximate method, see section 3.3.1.
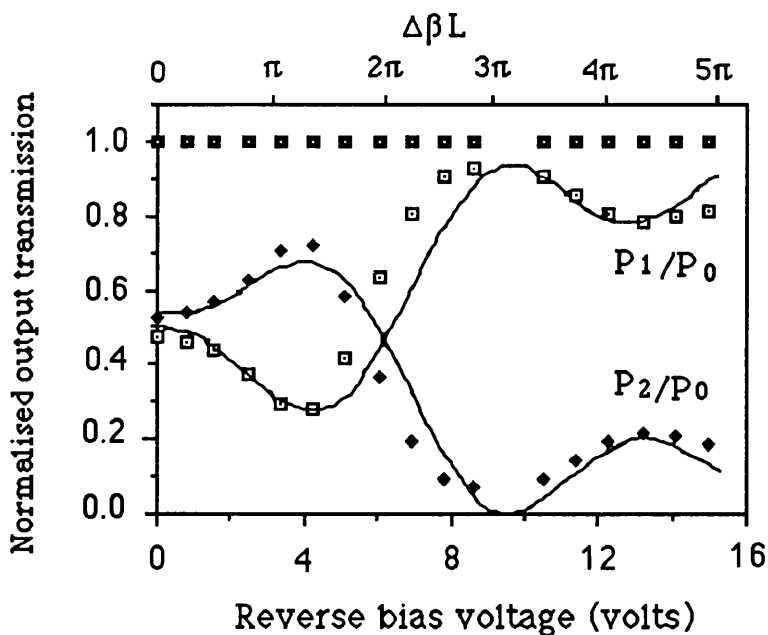
Fig. 8.14 *Normalised outout transmission of waveguide 1* (P_1/P_0) *and waveguide 2* (P_2/P_0) *as a function of the reverse bias voltage* V_b. *The square points are the experimental results and the solid lines are the theoretical results.* V_b *was applied across waveguide 2 and the optical beam* ($\lambda=0.857$ μm) *was coupled into waveguide 1. The waveguide rib width and height were* 3 μm *and* 1.75 μm *respectively and the coupling length* $L=2.7$ mm.

Further measurements of the switching operation of the electro-optic directional coupler were carried out on another device. The coupled waveguides width and spacing were 3 µm, with a rib height 1.75 µm and coupling length L=2 mm. Fig. 8.15 shows the output response of the device as a function of bias voltage V_b, at a wavelength λ=0.857 µm. The bias voltage was applied across waveguide 2. The square points are the experimental measurements, the sum of the two outputs is equal unity at all values of V_b. The solid lines are the calculated output response of the two coupled waveguides as a function of $\Delta\beta L$, top scale. The two parameters ρ and m were taken to be 25 and 0.87, respectively. From the m parameter, the coupling coefficient was K=13.6 cm $^{-1}$ (for the coupling length of L=2 mm). This value is in good agreement with that of the first device, where K=14.6 cm $^{-1}$.

Qualitatively, the theorectical model of the electro-optic directional coupler in reference 8 was in good agreement with our experimental results presented in Fig. 8.14 and Fig. 8.15.
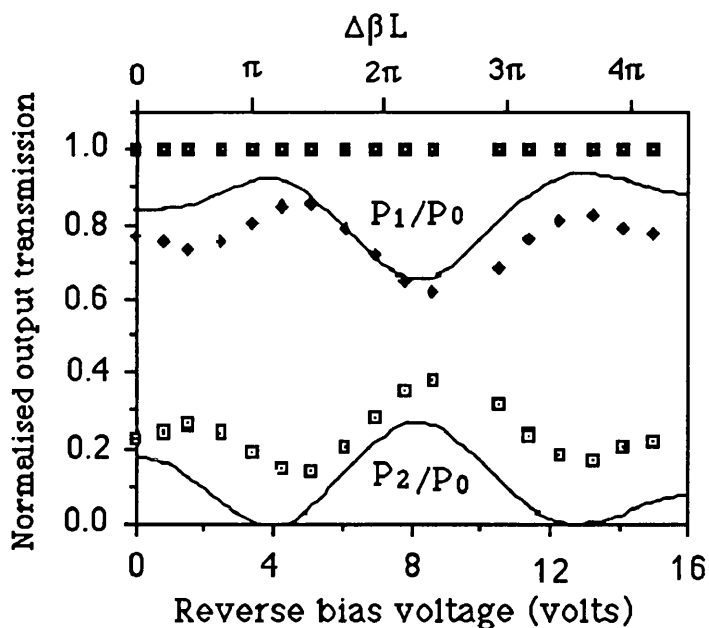
Fig. 8.15 *Normalised outout transmission of a directional couper similar to that in Fig. 8.14, but the coupling length L=2 mm.*

8.4.2 Resonant Nonlinear Directional Coupler:

A single beam experiment was used to examine the resonant nonlinear directional coupler as an all-optical switch. In this experiment, the output transmission of the two coupled waveguides was monitored as a function of the input light intensity. The light source was

an actively mode-locked Ti:sapphire laser pumped with a CW Ar$^+$-ion laser, this system is described in section 5.10.2. The laser output consisted of a train of pulses of ≈50 ps at a repetition rate of 76 MHz with an average power ≈350 mW. Therefore, the pulse energy was 5 nJ and the peak power 100 W. The peak power of the input pulses was varied by using a motor controlled attenuator wheel. The polarisation of the incident beam was set to TE or TM polarisation, using a halfwave plate and polariser. These pulses were chopped at a rate of 1 KHz and coupled into the waveguides using a ×40, N.A. 0.65, microscope objective lens. The output response of the two coupled waveguides was monitored and recorded using the set-up described in the previous section, with two Si-detectors.

Measurements were performed at a range of photon energies (1.41 eV-1.46 eV), i.e. at a range of ≈100 meV to 50 meV below the hh-excitonic resonance of the MQW of A163 material. At photon energies up to 1.45 eV, there was no sign of all-optical switching in the device response. As the photon energy brought closer to the MQW absorption edge (above 1.45 eV) miscoupling of the incident light into the device was experienced, at an average powers just below 50 mW. This was due to the generated heat in the sample as a result of the large MQW absorption coefficient. This problem was reduced by replacing the input objective lens with a ×20, N.A. 0.4, which made coupling of the incident light less sensitive to heat expantsion. As the input power was increased above ≈70 mW, the input facet of the couplers damaged, due to the large absorption in the MQWs region, this is shown in Fig. 8.16. Unfortunatley, the length of these samples did not allow further cleaving for fresh input facets. The failure of these devices to switch all-optically was due to the long life time of the photogenerated carriers, longer than the laser pulses repetition rate, τ≈14 ns. This was measured by using the time resolved PL spectroscopy, obtained at Heriot Watt University.

8.4.3 Nonresonant Nonlinear Directional Coupler:

A nonresonant nonlinear directional coupler was successfully demonstrated by Dr. S. Aitchison [9], of this Department, in GaAlAs below half the band gap. In this section only the device description and performance are outlined, for completness.

A single mode passive directional couplers were fabricated in A293 GaAlAs wafer. This material was later used to demonstrate the successful nonlinear AM-ZI described in section 7.8. The layers structure and the linear and nonlinear optical properties of this wafer are presented in section 4.3.
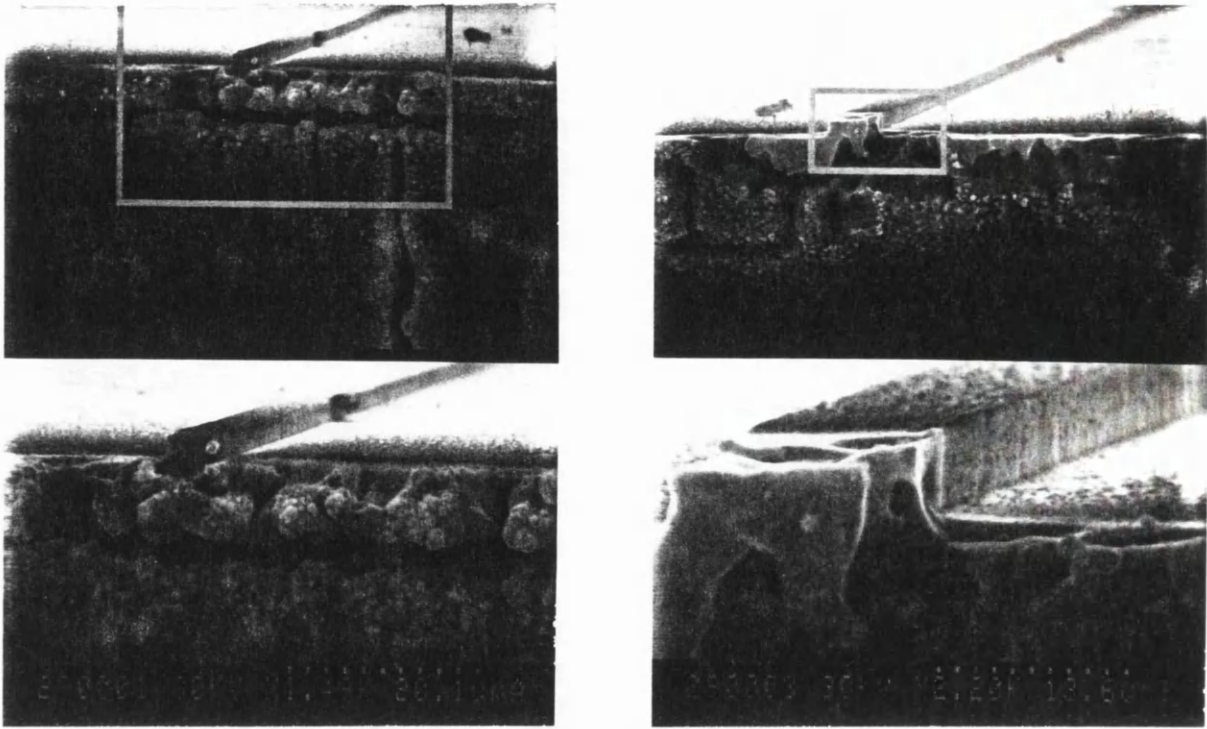
Fig. 8.16 *SEM micrograph of a directional coupler input end facet damaged by a focused laser beam due optothermal effect.*

The directional couplers consisted of 4 μm stripe loaded coupled waveguides with an etching depth varied from 1.2 μm to 1.45 μm, and separated by 5 μm spacing. These devices were fabricated using the standard optical lithography and RIE using SiCl$_4$ gas. The etched samples were cleaved to achieve a coupling length of 6.25 mm.

The ultrafast (<<100fs) all-optical switching of the device was demonstrated below half the band gap of the Ga$_{0.82}$Al$_{0.18}$As, at a wavelength λ=1.6 μm. The light source was a synchronously pumped mode-locked NaCl:OH$^-$ colour centre laser, which generated a train of pulses of 10 ps duration.

Fig 8.17 shows the normalised output transmission of the two coupled waveguides as a function of the total output peak intensity (after ref. 9). The total output power was the sum of the outputs of the two coupled waveguides, this allowed to neglect the coupling efficiency to the device. With reference to Fig. 8.17, the split ratio between the two coupled waveguides, at low power (i.e. initial state) was 0.3:0.7.
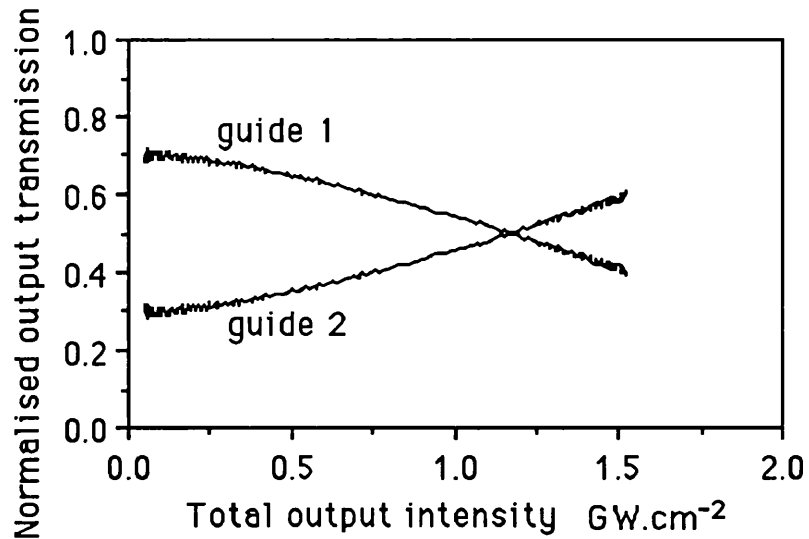
Fig. 8.17 *Normalised output transmission of waveguide 1 and waveguide 2 of a nonresonant nonlinear directional coupler as a function of the total output peak intensity. The waveguide rib width and height were* 4 μm *and* 1.3 μm *respectively and coupling length* L=6.25 mm.

A relative switching of ≈25% was achieved at a peak pumping intensity of ≈1.6 GW.cm^{-2}, assuming the effective mode area $A_{eff}=6\times10^{-8}$ cm^2. The switching intensity takes onto account the device insertion losses and the coupling losses.

The intensity dependent refractive index coefficient was estimated from these results to be $n_2 \approx 6\times10^{-14}$ cm^2/W. This value is slightly higher than that estimated from our SPM measurements, for the same material presented in section 6.5.3.2, and that esitmated value from the switching operation of the nonlinear AM-ZI device in section 7.8.2.1.

8.5 Conclusions:

In this chapter, we presented the theoreticall modelling of the directional coupler switch, this included the all-optical and electro-optic switching. The operation of the electro-optic directional coupler has been successfully demonstrated in GaAs/GaAlAs MQW structure, the experimental results agreed well with the theoretical model. These devices fail to switch all-optically due to the longe life time of the photogenerated carriers, longer than the repetion rate of the pumping laser pulses, in the MQW region. This was confirmed by the lift time photoluiminescence measurement. At high pumping intensities, the input facets of

263

these waveguides were damaged due to the large thermal effect induced in the MQW absorption region.

In the last section of this chapter, we outlined the ultrafast nonresonant nonlinear directional coupler which has been sucessfully demonstrated in GaAlAs material at 1.55 μm spectral region, by Dr. S. Aitchison of this Department. The photon energy was below half the band gap of the GaAlAs guiding region to avoid the TPA effect. A relative switching of ≈25% was achieved at a peak pump intensity of ≈1.6 GW.cm^{-2}.

References:

[1] H.A. Haus, *"Wave and fields in optoelectronics"*, Prentice-Hall, Englewood Clifts, New Jersey (1984).

[2] T.M. Benson, T. Morotani, P.N. Robson and P.A. Houston, *"A novel electro-optically controlled directional coupler switch in GaAs epitaxial layers at 1.15mm"*, IEEE Trans. Elect. Dev., Vol. 19, p. 1477 (1982).

[3] P. Likam Wa, J.E. Sitch, N.J. Mason, J.S. Roberts and P.N. Robson, *"All-optical multiple-quantum well waveguide switch"*, Electron. Lett., Vol. 21, p. 26 (1985).

[4] R. Lin, J.P. Sokoloff, P.A. Harten, C.L. Chuang, S.G. Lee, M. Warren, H.M. Gibbs, N. Peyghambarian, J.N. Polky and G.A. Pubanz, *"Ultrafast modulation with subpicosecond recovery time in GaAs/GaAlAs nonlinear directional coupler"*, Appl. Phys. Lett., Vol. 56, p. 993 (1990).

[5] S.M. Jensen, *"The nonlinear coherent coupler"*, IEEE J. Quantum Electron, Vol. QE-18, p. 1580 (1982).

[6] C.F. Gerald and P.O. Wheatley, *"Applied numerical analysis"*, 3rd ed., Wesley Publishing Company, p. 306 (1984).

[7] P. LiKam Wa, A. Miller, J.S. Roberts and P.N. Robson, *"130 ps recovery all-optical switching in a GaAs multiquantum well directional coupler"*, Appl. Phys. Lett., Vol. 58, p. 2055 (1991).

[8] R.A. Soref, D.L. McDaniel, Jr. and B.R. Bennett, *"Guided-wave intensity modulators using amplitude and phase perturbations"*, J. Lightwave Tech., Vol. 6, p. 437 (1988).

264

[9] J.S. Aitchison, A.H. Kean, C.N. Ironside, A. Villeneuve and G.I. Stegeman, *"Ultrafast all-optical switching in AlGaAs directional coupler in 1.55 mm spectral region"*, Electron. Lett., Vol. 27, p. 1709 (1991).

Chapter 9

Conclusions and Future Work

Linear Optical properties of Semiconductor Waveguides:

The linear optical properties of GaAs/GaAlAs rib waveguides were investigated, it included the propagation losses as well as the end facets reflectivity. It was found that the propagation loss was higher for deeply etched waveguides. This was due to the increase in the scattering loss from the roughness in the sidewalls of the waveguide, where the overlap integral between the optical guided light and the sidewall roughness was higher. The facet reflectivity of GaAs/GaAlAs single mode rib waveguides was measured as a function of the tilting angle between the longitudinal axis of the waveguide and the normal to the facet and also as a function of the lateral optical confinement. The lateral confinement was controlled by changing the etching depth of the waveguide adjacent slabs (rib height). It was found from the experimental results, that the facet reflectivity of the single mode waveguide change dramatically with the facet tilting angle as well as the lateral optical confinement. In other words, the mirror reflectivity of the waveguide end facet was a strong function of the waveguide parameters and the consequent modal field parameters.

The linear propagation losses in bent and Y-junction waveguides were investigated. Experimental results have been presented for the propagation loss of bent waveguides as a function of the bending angle. As expected an over all losses (scattering and bending losses) of bent waveguides was reduced significantly by increasing the lateral optical confinement in the waveguide. In single mode Y-junction waveguides, the propagation losses were measured as a function of the full branching angle. It has been shown that the radiation loss increases as the Y-junction angle increases.

Nonlinear Optical properties of Semiconductor Waveguides:

The nonlinear optical properties of the semiconductor waveguides were investigated, it included the resonant nonlinear properties of GaAs/GaAlAs single and multiple quantum wells (SQW and MQW) and the nonresonant nonlinear properties of GaAlAs waveguides. The absorption spectra of GaAs/GaAlAs SQW waveguides were measured for the TE and TM modes; a well resolved hh and lh exciton peaks were observed at room temperature. The relative absorption strength of the hh and lh excitons were 3/4 and 1/4 for the TE mode

266

and 0 and 1 for the TM mode, respectively. The intensity dependent absorption saturation of these excitonic peaks were measured for the TE and TM modes. A maximum change in absorption was achieved at photon energies equal to the excitonic transitions of the SQW. This was due to the screening effect of the excitons caused by the photogenerated carriers.

The intensity dependent refractive index change in GaAs/GaAlAs SQW waveguides was measured, a negative change (electronic effect) was observed at photon energies close to the SQW exciton peak, and a positive (thermal effect) was observed at photon energies above the SQW exciton peak. The value of the unsaturated electronic refractive nonlinear coefficient, n_2, was 1.4×10^{-8} cm^2/W, calculated from the negative part of the intensity dependent refractive index change. These measurements were achieved by using the external Mach-Zehnder interferometer and a CW tunable Ti:sapphire laser source. The recovery time of the resonant nonlinearity, in these waveguides, was measured using a conventional pump-probe scheme, at different photon energies. The laser source was an actively mode-locked Ti:sapphire laser, and produced pulses with a duration of ≈ 50 ps at a repetition time of 13 ns. The measured recovery time (1/e) was ≈ 125 ps. The short recovery time is believed to be due to the reduction of the recombination time of the photogenerated carriers caused by the surface recombination where the SQW was only 40 nm below the surface of the material. The process may well be assisted by a built-in electric field due to depletion layer associated with the proximity of the surface.

The nonresonant nonlinear optical properties of $Ga_{0.82}Al_{0.18}As$ waveguides were measured at photon energy below half the band gap. These measurements were performed, at St. Andrews University/Department of Physics, using a coupled-cavity mode-locked CCML KCl:Tl colour centre laser. The pulse width was ≈ 330 fs at a repetition rate of 12 ns. The nonlinear refractive index coefficient, n_2, of the $Ga_{0.82}Al_{0.18}As$ waveguides was obtained from the spectral broadening measurement, via the self-phase modulation SPM effect, of the transmitted pulses. This was carried out for both the TE and TM modes which showed that the spectral broadening via the SPM was polarisation independent. The measured corresponding value of the nonlinear refractive index, n_2, was $(5.4 \pm 0.5) \times 10^{-14}$ cm^2/W. A figure of merit ($\eta = \beta\lambda/n_2$), where β is the two photon absorption coefficient and λ the wavelength in vacuum, is used to characterise the suitability of a material for all-optical switching. For our $Ga_{0.82}Al_{0.18}As$ waveguides, a value $\beta = 0.14$ cm/GW was deduced from the transmission measurements of the waveguides as a function of the input intensity, for the 330 fs pulse width. The figure of merit took a value of $\eta = 0.38$ at $\lambda = 1.52$ μm. This thus satisfied the criterion for an all-optical AM-ZI switch in that $\eta < 2$.

The electro-optic effects in GaAs/GaAlAs p-i-n single and multiple quantum well waveguide structures have been investigated, it included the electro-absorption and refraction effects. The idea behind applying an electric field across the QWs, in all-optical switching devices, was to reduce the recovery time of the resonant nonlinearity by sweeping the photogenerated carriers out of the QWs region.

Nonlinear Asymmetric Mach-Zehnder Interferometer:

All-optical operation of an integrated AM-ZI was successfully demonstrated employing the resonant and nonresonant nonlinearities. The resonant nonlinear integrated AM-ZI was fabricated in GaAs/GaAlAs SQW structure and a pump-probe experiment was used to examine the device performance as an all-optical switch. The laser source was an actively mode-locked Ti:sapphire laser, and produced pulses with a duration of ≈ 50 ps. The results qualitatively agree with a simple model of the device operation. The differential saturation of the absorption means that the device cannot switch off completely because at the second Y junction there is different relative intensities in each arm compared to how the split at the first Y junction. The saturation of the absorption is inherent to the nature of the resonant optical nonlinearity although its relative significance can be reduced by operating at longer wavelengths. The resonant optical nonlinear device discussed here is therefore unsuitable for all-optical switching applications where large depths are required. It may find an application in passive mode-locking of semiconductor lasers where large modulation are not necessary.

The nonresonant nonlinear AM-ZI was fabricated in $Ga_{0.82}Al_{0.18}As$ heterostructure and its operation as an all-optical switch was examined at photon energy below half the band gap of $Ga_{0.82}Al_{0.18}As$. A single beam experiment was used where by the output transmission of the AM-ZI was monitored as a function of the input light intensity. A relative switching of more that 80% has been achieved using 330 fs pulses at around 1.55 μm from a coupled-cavity mode-locked KCl:Tl colour centre laser. The recovery time of the switching operation was ultrafast, in femtosecond regime, this was confirmed by the symmetry of the spectral broadening in the straight waveguide via the SPM.

Nonlinear Integrated Directional Coupler:

The switching operation of an integrated directional coupler was examined using the resonant nonlinearity in GaAs/GaAlAs p-i-n MQW structures. Active devices were fabricated in an attempt to reduce the recovery time of the resonant nonlinearity by applying

268

an electric field across the intrinsic region to sweep the photogenerated carriers out of the MQWs. A switching action was observed, using the electro-optic effects in MQWs, and the theoretical model fitted well with the experimental results. These devices fail to switch all-optically due to the long life time of the photogenerated carriers (≈ 14 ns) measured using the lifetime photoluminescence spectroscopy. This experiment was carried out at Heriot Watt University.

An integrated ultrafast all-optical directional coupler switch was successfully demonstrated, by Dr. S. Aitchison of this Department, using the nonresonant nonlinearity in $Ga_{0.82}Al_{0.18}As$ at photon energies below half the band gap. A synchronously pumped mode-locked NaCl:OH colour centre laser was used, the pulse width was 10 ps at 1.6 µm spectral region. A relative switching of $\approx 25\%$ was achieved at a peak pump intensity of 1.6 GW/cm^2.

Future Work:

Figure 9.1 shows a proposed all-optical switching device based on a symmetric Mach-Zehnder interferometer, utilizing the resonant nonlinearity in GaAs/GaAlAs MQWs. Implementing either impurities induced or vacancies indiffusion disordering techniques will provide a linear device with a nonlinear section in one of the M-Z arms. This will reduce the device insertion loss close to the MQW absorption edge of the nonlinear section and enhance the output modulation depth.
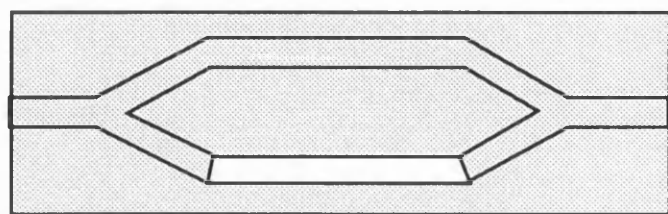
Linear section
Impurities induced or Vacancies indiffusion disordering

Nonlinear section
As grown area

Fig. 9.1 *Schematic diagram of AM-ZI, the shaded area is disordered with energy gap larger than the clear area (as grown material).*

Recent studies of the nonresonant nonlinear optical properties of GaAs/GaAlAs MQWs

below half the band gap showed an increase in the value of n_2 by a factor of 2.4 over that of the bulk GaAlAs. Therefore, demonstrating our all-optical switching devices (AM-ZI and directional coupler) using GaAs/GaAlAs MQW structures may reduce the required switching power of these devices.

A target device for logic operations is shown in Fig. 9.2, this device was demonstrated by A. Lattes et al. [1] using LiNbO3 substrate. This device can operate as an XOR gate, AND gate and inverter.
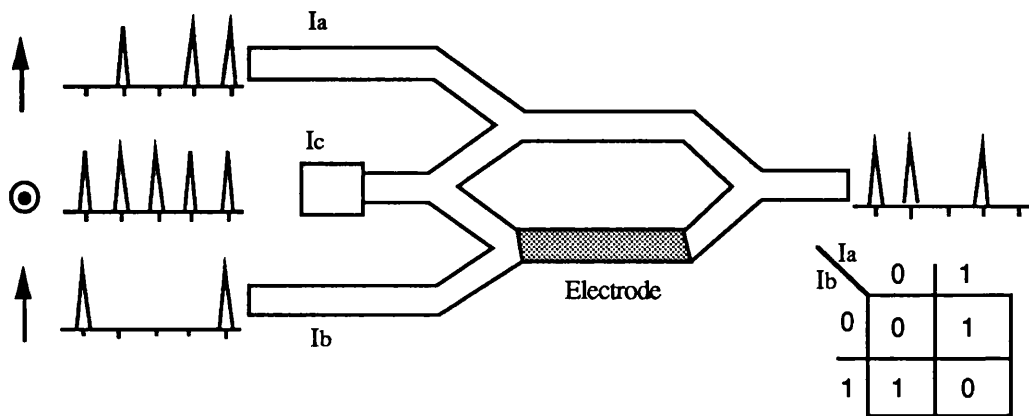
Fig. 9.2 *Schematic diagram of the optical logic gate. A continuous stream of pulses is modulated by the information carrying pulses incident in waveguides a and b.*

References:

[1] A. Lattes, H.A. Haus, F.J. Leonberger and E.P. Ippen, *"An ultrafast all-optical gate"*, IEEE J. Quantum Electron., Vol. QE-19, p. 1718 (1983).